Micromechanical and Probabilistic Approaches to Improve Asphalt Concrete Rutting Performance Prediction Procedures

By

ERDEM COLERI
B.S. (Middle East Technical University, Ankara) 2005
M.S. (Middle East Technical University, Ankara) 2007

DISSERTATION

Submitted in partial satisfaction of the requirements for the degree of

DOCTOR OF PHILOSOPHY

in

Civil and Environmental Engineering

in the

OFFICE OF GRADUATE STUDIES

of the

UNIVERSITY OF CALIFORNIA

DAVIS

Approved:

_____
Prof. John T. Harvey, Chair

_____
Prof. Boris Jeremić

_____
Prof. Carl L. Monismith

Committee in Charge
2011

i

UMI Number: 3482112

UMI

Dissertation Publishing

UMI 3482112

ProQuest®

Erdem Coleri
September 2011
Civil and Environmental Engineering

Micromechanical and Probabilistic Approaches to Improve Asphalt Concrete

Rutting Performance Prediction Procedures

ABSTRACT

Rutting is the load induced permanent deformation of pavements with asphalt concrete (AC) layers. Rutting can occur in the unbound layers of the pavement and in the AC surface layers, the latter of which is the focus of this thesis. The risk of rutting in the AC layers is highest just after construction and then generally diminishes as the materials harden due to traffic and environmental aging. AC rutting has a large impact on life cycle cost because it mostly occurs at the beginning of the life cycle and because failure by rutting often requires removal and replacement of the affected layers or other costly remedial construction, which makes rutting a crucial consideration. Although rutting performance of AC pavements has been characterized by various studies, there has been little study of the effects of AC micromechanical structure on in-situ rutting deformation accumulation mechanisms. In addition, the analysis of the predicted pavement performance variability and the development of a reliability-based design method considering all significant sources of variability have been lacking.

The goal of this thesis was to explain the rutting accumulation mechanisms for pavements with conventional and modified asphalt mixes and develop a comprehensive rutting performance prediction procedure considering the fundamental material properties, in-situ deformation accumulation mechanisms and the effects of various sources of variability, based on investigation of the fundamental problems in current test methods, structural models and performance prediction procedures.

An innovative method was developed to quantify the precision and bias in repeated simple shear test at constant height (RSST-CH) laboratory test results for specimens with different dimensions and to determine the effects of variability on predicted rutting performance. Specimen size requirements for two different asphalt mix types were proposed based on the results of the analysis. The effects of test temperature and specimen volume on test variability were also investigated.

A reliability based rutting performance prediction procedure was developed that considers the variability in laboratory test results, layer thicknesses, stiffnesses, and measured in-situ performance. The effects of input design parameter variability on predicted performance were determined using the calculated distributions of calibration coefficients. By using these calibration coefficient distributions, asphalt layer design thicknesses for different reliability levels can be predicted without performing computationally intensive calculations, such as Monte Carlo simulations, facilitating incorporation of reliability into design software. The general procedure developed for specific tests and AC rutting in this thesis can be applied to other distresses.

iii

The use of X-ray computed tomography (CT) images was extended from previous work in a new empirical approach developed to investigate the changes in AC microstructure caused by full-scale accelerated pavement testing with a Heavy Vehicle Simulator (HVS), by using images taken before and after HVS rut tests. A viscoelastic micromechanical finite element model was also developed to investigate effects of binder and aggregate properties on shear resistance using the microstructural model developed from the imaging process with laboratory specimens. The approach was used to investigate the differences in performance under full-scale loading of two mixes, one dense graded with polymer modified binder and the other gap-graded with rubberized binder. It was found that shear related deformation appeared to control the long term rutting performance of the AC pavement layers while densification was primarily an initial contributor at the very early stages of the trafficking. A high concentration of aggregate interlock in the polymer modified mix, as a result of the dense gradation and larger aggregate sizes, appears to have resulted in greater dissipation of shear stresses and therefore greater shear resistance. The lack of this interlocking effect for the rubberized gap-graded mix is proposed to have caused the earlier failure in the full-scale HVS test sections. Important differences in aggregate movement and air-void changes were also observed between different overlay thicknesses indicating the depth of the rut phenomenon, important information for the design of overlays on aged AC as well as for asphalt overlays on concrete pavements.

Recommendations are proposed to improve design and construction of asphalt surfaced pavements based on these findings.

To my wife Selin

v

ACKNOWLEDGEMENTS

First, I would like to express my deepest appreciation and gratitude to my advisor, Professor John Harvey, whose expertise, understanding, and patience, added considerably to my graduate experience. I appreciate his support in times of struggling, his guidance in times of pondering, and for enabling me to learn many lessons independently. His unique combination of vision, technical knowledge and kindness will be an inspiring role model in both my academic and personal lives.

I would also like to thank the other members of my committee (Professor Boris Jeremić and Professor Carl L. Monismith) who generously shared their time and encouragement. Their insightful comments and questions have immensely improved this study.

I am grateful to Professor John M. Boone and Professor Kai Yang of the University of California Davis Medical Center for providing the computed tomography images for this study. I would also like to thank Dr. Michael Paddy of University of California Davis Molecular and Cellular Biology Department for providing the image processing tools.

Finally, I would like to thank my wife Selin for her encouragement, unwavering support and intellectual advice. She has been my inspiration for all potential successes for which I strive.

TABLE OF CONTENTS

x

LIST OF FIGURES

xvi

xviii

LIST OF TABLES

ABBREVIATIONS

AASHTO	The American Association of State Highway and Transportation Officials
AC	Asphalt Concrete
ANOVA	Analysis of Variance
APA	Asphalt Pavement Analyzer
APT	Accelerated Pavement Testing
ATIRC	The Advanced Transportation Infrastructure Research Center
CalME	California Mechanistic-Empirical Design Software
Caltrans	California Department of Transportation
COV	Coefficient of Variation
CSIR	The Council for Scientific and Industrial Research
CT	Computed Tomography
DEM	Discrete Element Method
FEM	Finite Element Method
FFST	Flexural Frequency Sweep Test
FMLC	Field Mix Laboratory Compacted
FOSM	First Order Second Moment
FSCH	Shear Frequency Sweep Test at Constant Height
FWD	Falling Weight Deflectometer
GLWT	Georgia Loaded Wheel Test
HMA	Hot Mix Asphalt
HVS	Heavy Vehicle Simulator
HWTT	Hamburg Wheel Tracking Test
IR	Incremental Recursive
LET	Linear Elastic Theory
MDD	Multi-Depth Deflectometer
ME	Mechanistic-Empirical
MEPDG	Mechanistic-Empirical Pavement Design Guide
NMAS	Nominal Maximum Aggregate Size
PCC	Portland Cement Concrete
PEM	Point Estimate Method
PG	Performance Grade
PM	Polymer Modified
RHMA-G	Rubberized Gap-Graded Asphalt Mix
RSST-CH	Repeated Simple Shear Test at Constant Height
RVE	Representative Volume Element
UCDMC	The University of California Davis Medical Center
UCPRC	The University of California Pavement Research Center

CHAPTER 1   INTRODUCTION

1.1   IMPORTANCE OF RUTTING IN PAVEMENT DESIGN

Highways are an important component of our civil infrastructure; they are essential to the economy and consume large amounts of natural and financial resources. Therefore, the most effective design and construction methods and the most efficient materials need to be used in order to minimize the expenditures while maximizing the social benefits of mobility. Asphalt surfaced pavements make up the vast majority of the pavement in California and the US, and therefore have great importance in terms of roadway construction, rehabilitation and maintenance. Asphalt surfaced pavements include flexible pavements with granular bases, semi-rigid pavements with cement treated soil bases and composite pavements with underlying concrete. Asphalt surfaced pavements make up more than 25 percent of the state-owned highway network in California, and more than 5 million miles of highway across the United States. More than 500 million

tons of hot mix asphalt (HMA, another term for asphalt concrete [AC]) with the cost of nearly 18 billion dollars is used annually to improve and preserve the existing networks in the United States and to a lesser extent for the construction of new roadways (Epps et al., 2002). Even minor improvements in current design and construction methods can lead to large economic savings for the entire country, and decreases in undesirable effects for the environment.

The general trend in truck tire technology for heavy freight trucks is to reduce rolling resistance and improve fuel economy, including the switch from bias-ply to radial tires beginning 45 years ago, and continuing with the movement to wide-base single tires over the last 20 years. At the same time, tire inflation pressures have generally been increasing for the same reasons. The combined effects of each of these tire technology changes and increasing inflation pressures and truck traffic volumes have increased the risk of rutting of AC and a need for high performance pavement structures (Al-Qadi and Elseifi, 2008). Therefore, new pavement design and construction specifications have been developed to reduce the risk of early failure of pavement structures (White et al., 2002). Three other trends affecting the design and construction of asphalt mixes are:

- Change of focus from designing and constructing new pavements adding traffic volume capacity to the road network to rehabilitation and maintenance of the existing network;

- Increasing use of modified asphalt binders and gap-, open- and stone matrix type aggregate gradations in addition to dense-gradations, as specialized mixes are

developed for specific performance requirements in different layers of the pavement and different functional requirements; and

- Increasing use of specifications to reward or penalize the contractor for performance-related construction quality or performance (Epps et al., 2002).

Together, these trends require the use of design methods that consider material properties, structural design (particularly the use relatively thin modified asphalt overlays on concrete and aged existing asphalt layers), and the effects of traffic and climate to deliver the required future performance of the constructed structure.

In recent years, the focus of pavement engineering has changed from designing and constructing new pavements to the rehabilitation and maintenance of existing pavements (Caltrans, 2007). According to California Department of Transportation (Caltrans) "State of the Pavement" report (Caltrans, 2007), preventive maintenance (also called "pavement preservation") conducted on one lane-mile highway structure costs an average of $60,000 whereas allowing the structure to further deteriorate requires rehabilitation for the same section which has a commensurate cost of $1.1 million. For this reason, failure of the pavement structure should be avoided by conducting preventive maintenance at regular time intervals. Many preventive maintenance treatments consist of thin asphalt overlays on existing aged asphalt or concrete pavements using mixes that are optimized for surface performance, including mixes with polymer modified or rubber modified binders and gap-graded or open-graded aggregate gradations. Design methods should be developed

to evaluate the expected in-situ performance of these types of treatments in order to develop effective maintenance alternatives.

Rutting in the AC layers (White et al., 2002), appears to be a crucial part of the pavement failure problem. The risk of rutting of the AC is usually greater early in the life of the new asphalt surface layers before hardening occurs due to oxidation and trafficking, resulting in major increases in life cycle cost. Prediction of rutting performance is important to determine the most cost-effective design alternatives. Understanding of in-situ deformation accumulation mechanisms is needed to develop effective performance prediction models and associated laboratory materials characterization tests in order to effectively design mixes to the appropriate level of risk for a given project. Effective tests and models are also needed to understand the reasons behind differences in the rutting performance of different asphalt mix types so that design methods can be improved.

Surface rutting also introduces a significant safety problem. Ruts in the wheelpaths of asphalt-surfaced roads trap rainfall increasing the risk of hydroplaning and skid-related accidents. Severe rutting can contribute to loss of steering control accidents when the pavement is dry. Accident cost data for 1994 recommended by Federal Highway Administration (FHWA) for use in cost-benefit analysis indicated that the cost for a rutting related fatal accident is $2.6 million. The costs for a rutting related personal injury and property damage accidents were given as $78,000 and $2,000, respectively (FHWA, 1994). Based on the FHWA data, the average cost per rut-related accident was calculated

to be $202,806. Start et al. (1998) indicated that rutting creates a significant safety problem when rut depths exceed 7.6 mm. This result suggests that although the failure rut depth is specified as 12.5 mm for the California Department of Transportation, rut-related safety problems can start to be observed at rut depths that are less than the actual failure standard.

1.2   RUTTING PERFORMANCE PREDICTION

1.2.1   *Mechanistic-empirical pavement design*

Mechanistic-empirical (ME) design is a method of designing highway pavements by integrating the empirical relations relating distress to pavement response obtained from the field data with the theoretical predictions of pavement response from structural models (MEPDG, 2004). The structural models are developed based on the generally accepted theories and methods (linear elastic theory [LET], finite element [FE] method etc.) to determine the response of the pavement to the environmental conditions, traffic levels and material properties. A general framework for mechanistic empirical pavement analysis and design is given in Figure 1.1. Material characteristics, traffic and climatic information are entered as inputs to predict pavement responses, such as strain, stress and displacement at critical locations, by using the theoretical structural models developed for predicting cracking or rutting distress potential. These responses are used as input to empirical transfer functions, which are generally developed from accelerated pavement testing and/or field test results (Ullidtz, 2006; MEPDG, 2004), to predict in-situ distress distribution and pavement performance. Once it is established that the pavement

responses calculated by the theoretical models sufficiently match measured pavement response, the transfer function models are calibrated based on in-situ performance measurements.
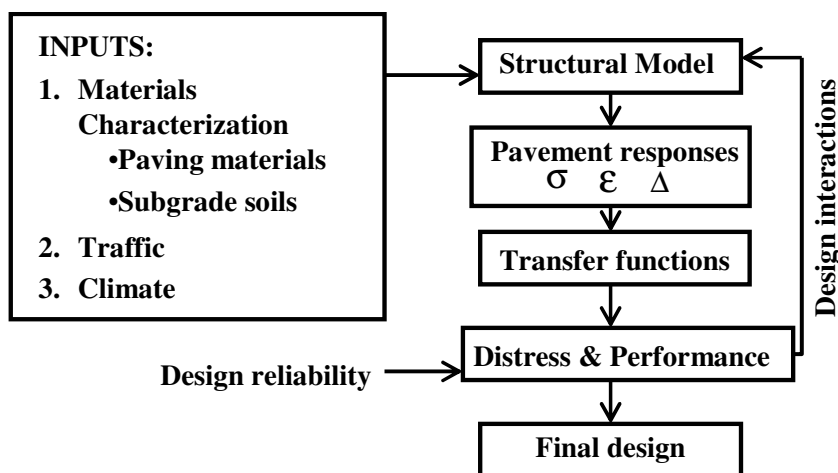
Figure 1.1 General framework for the mechanistic-empirical (ME) pavement analysis and design.

The process of using a mechanistic-empirical pavement design method consists of selecting a trial design and analyzing it to determine whether it meets the specified design criteria (MEPDG, 2004). If the trial design does not meet the specified requirements, it should be modified and reanalyzed, and the costs of acceptable designs calculated, in order to achieve the optimal design which satisfies all the required criteria at lowest cost. Traffic, climate, material properties and foundation (subgrade support) characteristics are considered to be the fundamental inputs which will directly affect the life time performance of the pavements. Trial design strategy is evaluated by using pavement analysis and distress prediction models based on a specific damage accumulation mechanism.

CalME (California mechanistic empirical) and MEPDG (Mechanistic empirical pavement design guide) are two design programs that have been developed for mechanistic-empirical analysis that include models for various distress types (Ullidtz, 2006; MEPDG, 2004).

Accelerated pavement tests appear to be the most important initial sources of information for development and checking of ME models because the long term performance of the pavement can be simulated in a short period of time (Brown, 2004). However, because accelerated pavement testing is very expensive (although not as expensive as long-term field testing) and cannot be performed for all possible design alternatives, structural models and laboratory tests must be developed and/or improved to simulate the actual pavement performance with a reasonable cost. Thus, results of the accelerated pavement tests should be used to improve these structural models and laboratory tests, rather than for development of empirical design criteria directly from the accelerated pavement tests themselves.

1.2.2   Theoretical modeling for rutting performance evaluation

Pavement rutting can be divided into two parts: rutting of the asphalt surfacing and rutting of the unbound layers. Unbound layers rutting is caused by subsidence caused by the shearing and densification in unbound base, subbase and subgrade layers, and directly affects the total rutting accumulated at the surface. However, on existing pavements that are rehabilitated and where water has not been allowed to pass to the unbound layers, the major part of the rutting (85 to 95 percent) is generally accumulated in the AC layers

(Coleri et al., 2008). Rutting in the asphalt layers accumulates with increasing number of load applications and is highly sensitive to variations in the temperature and traffic levels (Metcalf, 1996). AC mixtures consist of aggregates bound together by viscoelastic binders which impart time of loading and temperature sensitivity to the general material characteristics. Volume change (densification) and shape distortion are the two deformation modes that control the rutting accumulation. Volume change is the deformation of a material with equal principal strains in all dimensions. Bulk modulus (K) is the resistance of a material to volume change. Shear distortion can be defined as the deformation without any change in volume. The resistance of a material to shear distortion is represented with the shear modulus (G) (Kim, 2009). Figure 1.2 illustrates the possible cases for volume change and shape distortion.

a.   b.   c.
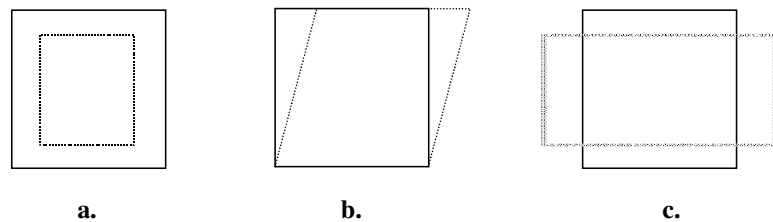
Figure 1.2 Schematic representations of (a) Volume change (b,c) Shape distortion (Kim, 2009).

Typically, the rate of rutting accumulation under repeated loading is higher under initial loading due to the combined effect of densification and shear distortion. The deformation accumulation rate starts to decrease as the layers become stiffer with the reduction in air-voids and reorientation of aggregates. Shear resistance of asphalt mixes also increases

with aging due to the effect of the binder hardening from oxidation and volatilization of lighter constituents in the asphalt (Zhou et al., 2006). A typical curve representing the rutting accumulation over time is given in Figure 1.3.
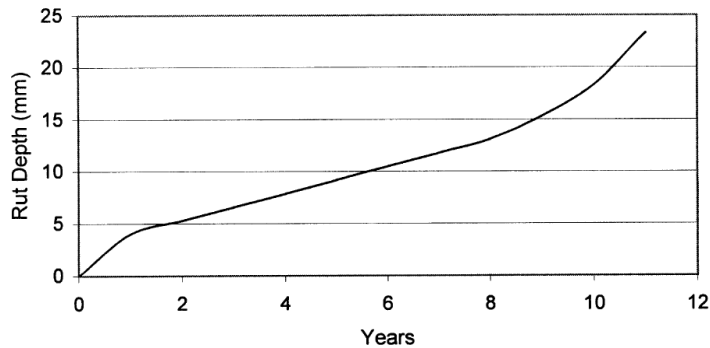
Figure 1.3 Classic rutting behavior over time (White et al., 2002).

Sousa et al. (1994) indicated that strain caused by the volume change will be recovered more than the strain due to the shape distortion when a transient load is released. Thus, the shear distortion component of the total deformation will be more than the portion related to the volume change. However, results of the analysis conducted by using the profilometer measurements indicated that the contribution of densification to total accumulated rutting can be up to 45 percent even after the structure is failed by rutting (White et al., 2002). This result suggests that prediction of the AC rutting performance by only considering the shear resistance of the material can be misleading under specific circumstances. Therefore, the fundamental phenomenon behind the movement of the aggregates and reduction in air voids at high temperatures under repeated loading should be determined in order to improve use of layered elastic theory for rutting performance

prediction, and to provide fundamental experimental data for calibration of multi-phase finite element models (such as used in this thesis) and discrete element models.

AC mixes exhibit different performance characteristics at different temperature levels. AC pavement layers start to behave as particulate structures at elevated temperatures, while their behavior tends to approach that of a continuum with decreasing temperature. Weissman et al. (1999) indicated the possible problems in the use of the continuum assumption for rutting performance prediction at high temperatures due to the differences between the stiffness of the aggregate, which is not sensitive to temperature, and the mastic (asphalt binder and fine aggregates), which is. Two-dimensional, plane strain, finite element simulations indicated that asphalt pavement layers function as united load carrying systems at lower temperatures when the asphalt and mastic (or binder) stiffnesses are similar. However, increasing temperature will make the asphalt layer to act more like a particulate structure than a continuum. Figure 1.4(a) presents the results of the axial deformation for the case where $E_{\text{aggregate}} = E_{\text{mastic}} = 100$ MPa, and Figure 1.4(b) presents results for $E_{\text{aggregate}} = 100$ MPa and $E_{\text{mastic}} = 1$ MPa, where E represents the Young's modulus of the material. It can be observed from Figure 1.4(a) that the axial deformation is relatively uniform when the mastic and the aggregate have the same stiffness. However, when the stiffness of the mastic and aggregate are different, $E_{\text{aggregate}} = 100$ MPa and $E_{\text{mastic}} = 1$ MPa, large variations start to occur in the axial deformation. Therefore, at high temperatures the use of continuum mechanics without considering the aggregate and mastic properties separately for the simulation of the stress and strain fields throughout the AC pavement sections appears to be questionable.
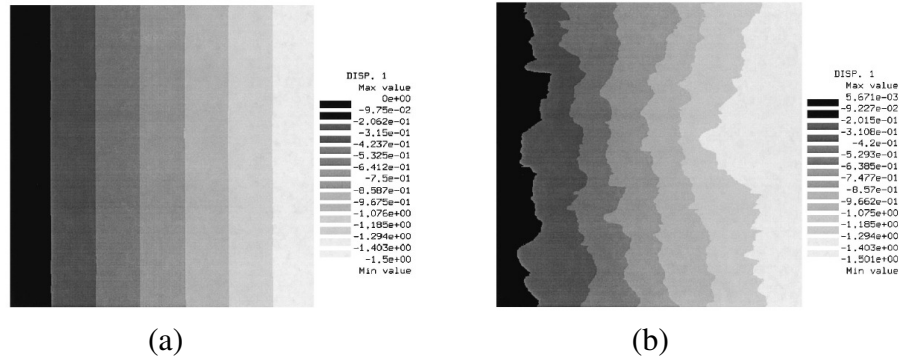
Figure 1.4 Distribution of the axial displacements at different stiffness levels
(a) Contours of axial displacements (*y* direction): Pleasanton aggregate,
$E_{\text{aggregate}}$ =100 MPa and E_{mastic} = 100 MPa. (b) Contours of axial displacements
(*y* direction): $E_{\text{aggregate}}$ = 100 MPa and E_{mastic} = 1 MPa (Weissman et al., 1999).

Figure 1.5 illustrates the accumulated deformation after a specific full-scale accelerated

pavement test (in this case using a Heavy Vehicle Simulator [HVS]) conducted with a

low stiffness (300 MPa at 50°C) AC overlay on top of a previously trafficked AC layer

with relatively higher stiffness (1100 MPa at 50°C). It can be observed from Figure 1.5(a)

that most of the deformation is accumulated in the underlying AC layer with higher

stiffness. However, predictions performed by using Layered Elastic Theory (LET)

indicated that most of the deformation should be accumulated at the top layer with low

stiffness, which does not match the actual response of the pavement (Figure 1.5[b]).

Further investigation based on the profilometer measurements indicated that the loss of

air-voids during the previous trafficking produced a layer which is highly sensitive to

dilation under additional truck wheel repetitions. This result for that particular case

suggests that asphalt pavement layers start to behave as particulate structures at high

temperatures which avoids the effective simulation of the actual stress and strain

distributions in the layers based on LET without considering the aggregate and mastic

properties separately. Thus, interactions between the particles and the effect of binder

viscosity at high temperatures on the overall structural performance of the pavement should be determined in order to improve models and design methods.

(a)

(b)
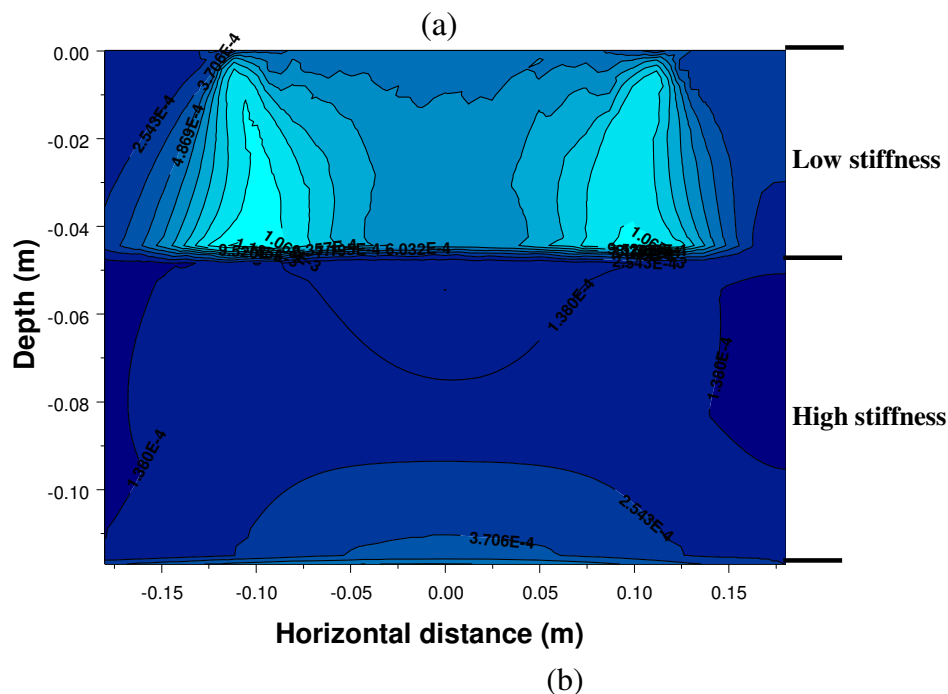
Figure 1.5 Rutting deformation accumulation mechanism (a) Accumulated deformation after the HVS test (b) Elastic strain field for the section developed by using LET (lighter colors indicate higher strain levels).

It should be noted that most of the current rutting performance prediction procedures rely on the assumption that the distribution of elastic strain values for an asphalt pavement layer calculated by using continuum mechanics is highly correlated with the distribution

of the in-situ permanent strains (MEPDG, 2004; Ullidtz et al., 2006; Sousa et al., 1994). In addition, because of the fact that AC layers start to behave as particulate structures at high temperatures, dilation in the AC structure might occur due to the effect of the shear forces. Because dilation is primarily controlled by the percentage of air-void in the asphalt mix and the interaction of aggregates along the contact surfaces, it is not possible to simulate the actual dilation phenomenon by using the continuum mechanics without considering the aggregate and mastic properties separately (Cross and Brown, 1992).

1.2.3   Variability and reliability in pavement design

Estimating the variability in fundamental pavement design inputs and integrating this variability into the general performance prediction procedures is generally considered a required component of modern ME pavement design. Since pavement owners would like to have an understanding of risk and be able to control risks that they take, design reliability levels and the corresponding costs for each level of reliability should be determined. This kind of risk control may require increasing the initial costs in order to decrease the risk of early failure for critical highway construction projects (Lea, 2009). For this reason the full distribution of expected performance with the likelihood of early failure should be determined and considered in design.

Reliability does not imply validity (Kutner et al., 2005). In many cases, the bias incurred during the consideration of possible external factors cannot be evaluated or identified based on reliability analysis. For this reason, potential bias that may occur due to the deficiencies in data collection procedures should also be evaluated based on comparisons

between measured and calculated performance variability by considering the variability in input parameters.

The thickness and stiffness of pavement layers are two fundamental design inputs with significant impact on the variation of rutting performance within a design section. Therefore, their spatial variability within a section should be quantified based on suitable distribution types for these parameters (Jiang et al., 2003; Lea, 2009). These distributions should be used in pavement design to provide an estimate of the range of performance estimates, rather than only averaged inputs (deterministic analysis).

1.2.4   *Representative volume element and laboratory test specimen size considerations*

Laboratory tests are generally developed to measure a specific material property that can be associated with the in-situ performance of the material. ME models are often developed based on characterization of the material based on laboratory test results. The fundamental question for a laboratory test is whether a specific test under consideration is applicable to the theory underpinning the model (Weissman et al., 1999). Most of the models used for performance prediction of composite materials rely on the assumption that properties of the heterogeneous media can be homogenized by using the right specimen size and geometry.

AC is a composite material which consists of aggregates, air-voids and mastic. All of the constituents of AC are large enough to be regarded as continua and they are bonded together at the interfaces. With its composite structure, AC can be considered to exhibit

heterogeneous characteristics due to the large number of composite microheterogeneities (aggregates, air-voids, mastic [asphalt and fine aggregate], etc.) in its structure. However, AC specimens can be assumed to exhibit homogeneous characteristics when the volume of the specimen is increased to a minimum level, the dimensions of which are referred to as a representative volume element (RVE). A necessary characteristic of the RVE is the statistical homogeneity that must be constituted in its media (Hashin, 1983).

There are two major disadvantages for using specimen sizes that are smaller than the RVE for the material. First, the number of tests must be increased to avoid bias throughout the averaging process. Large number of tests may increase the testing cost and time spent for testing. Thus, it may not be practical to keep the specimen dimensions at a level that is smaller than the actual RVE (Weissman et al., 1999). Second, if the required number of replicates for a specimen with dimensions smaller than the RVE cannot be achieved, a significant level of bias maybe introduced into test results (Gitman et al., 2007). Biased test results will consequently reduce the effectiveness of the developed model while minimizing the reliability of the predicted in-situ performance. RVE requirements should be developed by performing tests with various specimen dimensions to determine the minimum specimen volume which results in an acceptable level of variation in the test results.

Although variability in laboratory test results can be reduced by using specimen sizes that are larger than the RVE, it is not possible to achieve zero variability by any means due to the composite structure of AC, as well as other sources of variability in the testing

process and equipment. Thus, a method quantifying the effects of laboratory test results variability on predicted performance should be developed. This quantified variability should be incorporated into current design procedures to be able to develop a reliability based design approach that can provide different design alternatives for various confidence levels. In this way, it will be possible to design pavements with a specific reliability level which can be determined by considering the importance of the project under consideration.

1.2.5   Accelerated pavement testing - Heavy Vehicle Simulator

Full scale accelerated pavement tests (APT) are performed by applying a full scale wheel load at or above field load levels to a full scale pavement (Figure 1.6) (Metcalf, 1996). The Heavy Vehicle Simulator (HVS) operated by the University of California Pavement Research Center for the California Department of Transportation is an example of a full scale APT device.

Estimates of long-term pavement performance can be determined in a short period of time by evaluating the response of the pavement system to applied loads. The duration of the testing can be reduced by performing the tests under critical conditions. For instance, for rutting performance evaluation, accelerated tests can be conducted at continuously critical high temperatures expected in the field without including the lower nighttime or cold season temperatures during which there is little or no rutting increase. The rate of deformation can also be increased by decreasing the wheel speed. Variables which affect

the rutting performance of the pavement can be more accurately controlled and monitored during the accelerated tests (Ullidtz et al., 2006).

Profilometer readings are taken at specific intervals during HVS tests to determine the changes in surface profiles with increasing repetitions. Although surface deformation measured by profilometer provides a great deal of insight into the rutting performance manifested at the surface of asphalt pavements, particle movement and displacement field in asphalt layers under HVS trafficking cannot be acquired. Because AC pavement layers start to behave as particulate structures at elevated temperatures due to the low binder stiffness, changes in microstructure need to be analyzed to describe the actual failure phenomenon (Weissman, 1997). Changes in air void distributions under trafficking should also be investigated to explain densification related deformations within the asphalt layers.

Although the HVS appears to provide important information for the reliability check, the effects of the absence of long term aging in the AC layers, realistic rest periods after each load application and the constant temperature and load levels maintained throughout the test should be corrected during the model development to achieve effective performance predictions (Ullidtz et al., 2008). For this purpose, HVS tests should be conducted at various load levels with varying temperatures to simulate the effects of the daily and seasonal temperature variations and variable traffic loads. Laboratory RSST-CH tests should also be conducted with variable temperatures and shear stresses that are close to the levels applied during a HVS test (Coleri et al., 2008). Variability in the materials,

structure, loads, and climate for the accelerated pavement tests should be compared with the in-situ variability to develop models and procedures which simulate the actual in-situ pavement performance.
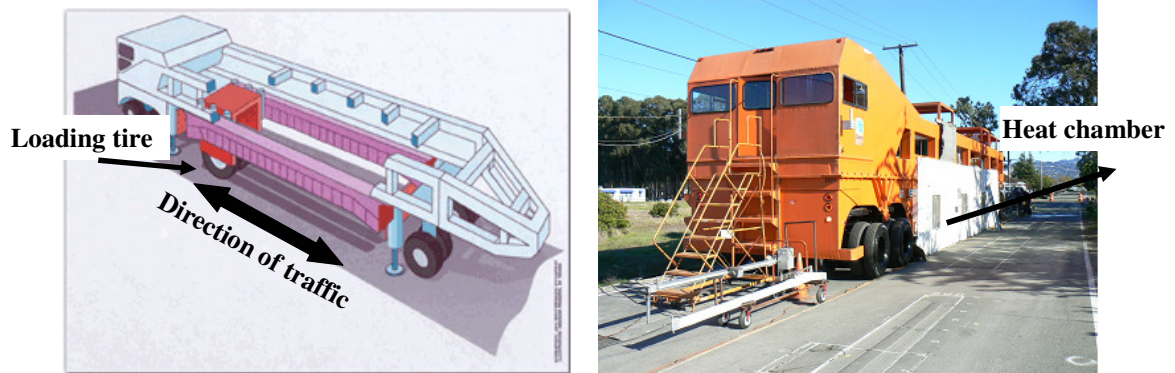
Figure 1.6 Heavy Vehicle Simulator (HVS).

1.3   OPPORTUNITIES PROVIDED BY MICROMECHANICS

Micromechanics is simply the analysis of composite materials on the level of the individual phases that form the composite. AC is also a composite material which consists of aggregates, air-voids and mastic. The mastic phase consists of fine aggregates, sand and other particles (rubber, polymer, etc.) embedded in asphalt binder, or at times the asphalt is embedded in a media of polymer. Performance and physical properties of the asphalt mixtures are controlled by the properties of the aggregate (shape, texture, gradation, modulus, etc.), properties of the asphalt binder (grade, complex modulus, cohesion, etc.), asphalt-aggregate interactions and distribution of air voids (Dai and You, 2007).

In this study, changes in the micromechanical structure of asphalt mixes under laboratory and HVS testing were investigated to explain the rutting failure mechanisms for different structure and mix types. A viscoelastic micromechanical finite element model was developed to simulate the laboratory shear performance of asphalt mixes based on the mastic properties measured by laboratory testing. Changes in the micromechanical structure of asphalt layers under HVS trafficking were also measured with before and after-trafficking X-ray computed tomography (CT) imaging to investigate the in-situ failure phenomenon.

1.3.1 Micromechanical finite element modeling

The properties of particular interest in identifying the shear resistance of asphalt mixes and binders are the dynamic shear modulus and phase angle (Papagiannakis et al., 2002). Various test methods were proposed for measuring these properties under the testing conditions that are similar to the in-situ case. Although most of the mixture test methods provided a great deal of insight into the identification of asphalt mix rutting performance, it is not possible to evaluate the individual effects of binder and aggregate properties on shear performance. In addition, effects of air void distributions on measured shear performance cannot be directly determined based on the asphalt mixture tests.

Laboratory tests developed to understand the individual binder and aggregate properties are also incapable of providing information about the interactions between those two phases. For example, an AC mix with soft binder maybe expected to exhibit early shear failure under laboratory testing. However, superior aggregate properties, such as shape,

texture, gradation and modulus, may cause the mix to show good shear performance. Although the Superpave mix design method, used by many states, estimates the asphalt mix performance by considering the aggregate and binder properties separately, interactions between aggregate, air-void and binder phases are not considered in the procedure. For that reason, a micromechanical finite element modeling framework simulating the individual constituents of the AC mix by considering interactions between each phase can provide crucial information for understanding the shear failure phenomenon leading to rutting.

1.3.2 *Investigation of the micromechanical changes under HVS trafficking*

Although micromechanical finite element models can provide important information about the dynamic interactions between different phases of a composite material under laboratory testing, the actual in-situ failure phenomenon cannot be simulated at this time due to excessive computational runtimes and resource requirements. Based on the experience gained from laboratory micromechanical shear testing models, possible computational time (for a new generation computer with 12 CPUs) for a 3D viscoelastic micromechanical finite element model simulating the HVS trafficking was estimated to be around four months for a single case with one load level, temperature and loading frequency. This result suggests that it is not computationally efficient to identify the 3D micromechanical response of HVS test sections by micromechanical finite element modeling.

In this study, changes in AC microstructure with HVS trafficking were determined by comparing the X-ray CT images taken before and after HVS testing. Deformed and un-deformed 3D air-void and aggregate distributions were compared to determine the changes in air-void content distributions and aggregate positions. The primary purpose is to investigate rutting failure phenomenon by analyzing the interactions between aggregate, binder and air void phases. Viscoelastic micromechanical finite element models developed for a laboratory shear test were also used to evaluate the shear resistance of different mix types.

1.4   OBJECTIVES OF THIS STUDY

The primary purpose of the study documented in this thesis is to identify the deficiencies in current rutting performance prediction procedures and propose possible modifications to improve the accuracy and precision of predictions. For that purpose, the in-situ behavior of asphalt mixes and the rutting failure phenomenon under trafficking were investigated based on micromechanical principles, laboratory and HVS test results. The contribution of each chapter of the thesis to improvement of the general rutting performance prediction procedure is illustrated in Figure 1.7. The major objectives of the study are given as follows:

Chapter 3:

- Develop guidelines for the required size for the RVE for AC mixes at high temperatures (45°C and 55°C) that are critical for rutting performance evaluation.

- Quantify the effects of specimen size induced bias and precision in laboratory shear test results on predicted pavement rutting performance using statistical methods and incorporate this bias and precision into the general performance prediction procedure.

Chapter 4:

- Develop a method to quantify the individual effects of laboratory test results, layer thicknesses, stiffnesses and measured in-situ performance variability on predicted rutting performance.

- Develop a reliability based asphalt pavement rutting design procedure which considers the variability in laboratory test results, layer thicknesses, stiffnesses and measured in-situ performance used for calibration.

Chapters 5 and 6:

- Develop a micromechanical finite element model from X-ray CT images to investigate the shear resistance and particle movement of different asphalt mix types at a scale level considering aggregates, air-voids and mastic.

- Use the X-ray CT imaging method to identify changes in microstructure caused by the rutting process, namely aggregate displacements and changes in air-void content and distribution, under full-scale loading and for different thicknesses of overlay on very stiff underlying layers.

- Use the experimental measurements to perform a first-level assessment of the micro-mechanical phenomena to provide insight into mix performance for mix design and development and understanding of laboratory tests, and information regarding the

mechanics of rutting that can be used to improve micro-mechanical analysis approaches.

• Integrate the findings from in-situ experimental measurements and micromechanical finite element modeling to explain the rutting failure mechanisms of rubberized gap graded and polymer modified dense graded AC mixes.

All chapters:

• Provide recommendations to engineering practice based on the findings of this study.
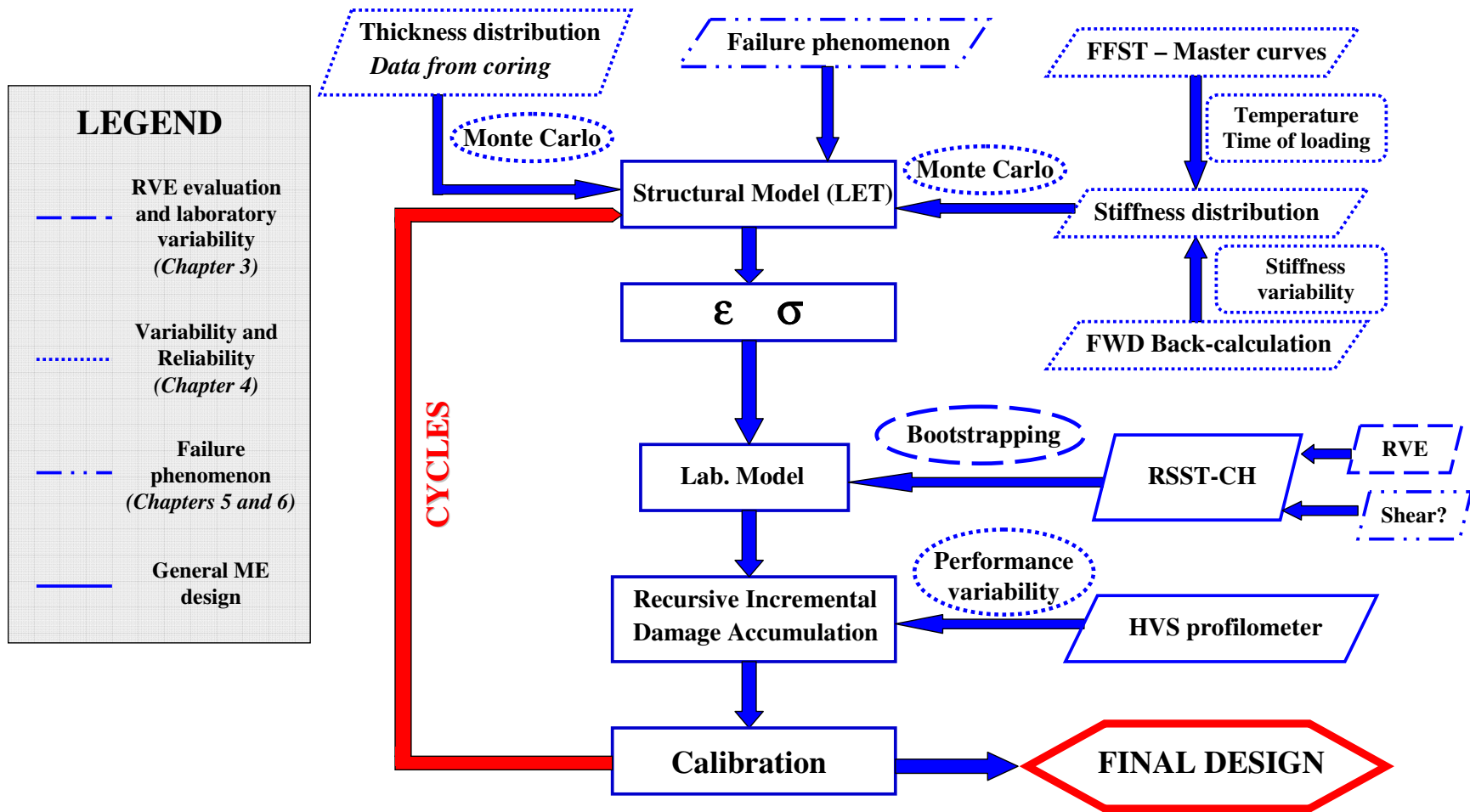
Figure 1.7 Contribution of the study documented in this thesis to the general rutting performance prediction procedure.

1.5   ORGANIZATION OF THE THESIS

Chapter 2 summarizes the test methods used in this study.

Chapter 3 presents the analyses performed to develop a procedure to quantify the precision and bias in repeated simple shear test at constant height (RSST-CH) laboratory test results for different sized specimens and determine the effects of this precision and bias on predicted rutting performance.

Chapter 4 presents an innovative reliability based asphalt pavement rutting design procedure which evaluates reliability by considering the variability in laboratory test results, layer thicknesses, stiffnesses and measured in-situ performance. The method proposed in Chapter 3 for the incorporation of laboratory test results variability into the general rutting performance prediction procedure is also used to develop the reliability based design approach.

Chapter 5 describes the procedure followed for the development of 2D and 3D micromechanical finite element models to predict the shear resistance of dense graded polymer modified and rubberized gap graded asphalt mixtures.

Chapter 6 investigates the changes in AC microstructure with HVS loading by comparing the X-ray CT images taken before and after HVS testing to explain the in-situ failure phenomenon. The micromechanical finite element model developed in Chapter 5 is used

to identify the interactions between aggregate, air void and binder phases under shear loads.

Chapter 7 summarizes the conclusions and contributions to the knowledge, and makes recommendations to engineering practice.

CHAPTER 2   **TEST METHODS**

2.1 LABORATORY SHEAR TESTING

2.1.1 Repeated simple shear test at constant height

Various types of tests are recommended in the literature to evaluate the rutting performance of asphalt concrete pavements. The most effective tests are accepted to be repeated simple shear test at constant height (RSST-CH) and triaxial tests (Figure 2.1) (Weissman, 1999; Zhou et al., 2003). The major difference between these two tests is the mode of shearing used to accumulate permanent deformation (Sousa et al., 1994). The type of shear stress for an RSST-CH test is similar to the theoretical shear stress on the xz plane (ε_{xz}). The horizontal load applied to the test specimen is assumed to simulate the effect of traffic load. However, in a cyclic triaxial test, stress applied in the vertical and horizontal directions produce a non-hydrostatic stress state including shear stress. The shearing effects of applied vertical and horizontal loads are explained by the principal

shear stress and strain values. Although critical principal and vertical shear stress and strain values are close to each other for pavements with thick asphalt concrete layers, there can be extreme differences between these values for sections with thin asphalt concrete layers. In addition, because results of the triaxial tests provide information about the combined resistance of the material to shape (shear) and volume change (densification), it is not possible to directly determine the critical shear resistance of the material without using theoretical calculations.

(a)   (b)
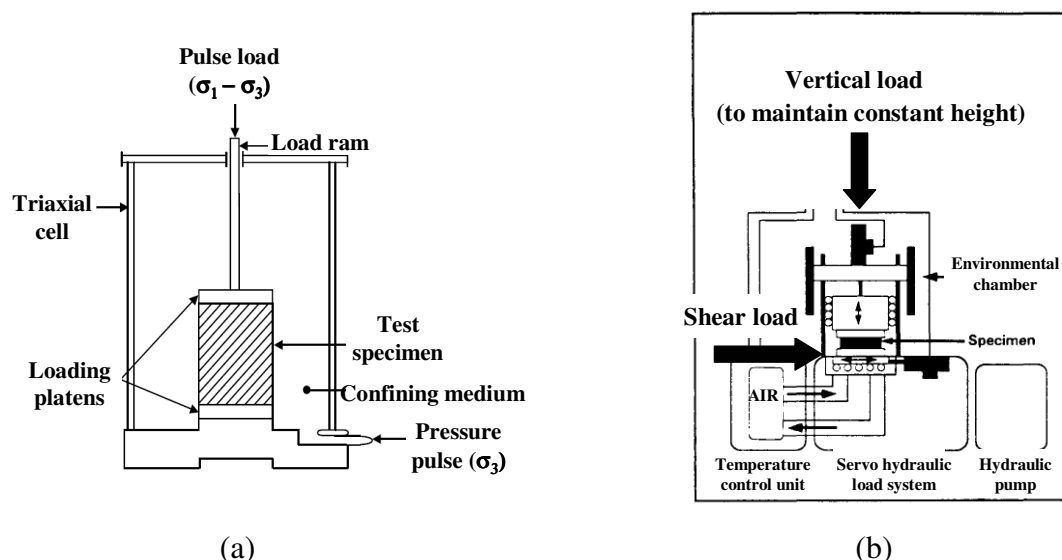
Figure 2.1 Laboratory tests for asphalt concrete rutting performance evaluation (Sousa, 1994) (a) Triaxial (b) RSST-CH.

Simple shear tests are commonly used in geotechnical engineering for the measurement of soil properties. The simplicity of shear tests relative to the triaxial testing resulted in a widespread use for in-situ performance prediction. General principles of the asphalt shear testing are similar to the direct simple shear test which is generally used for conducting undrained tests on soft clays and silts.

Procedures for the RSST-CH tests are given in AASHTO T 320 (AASHTO, 2003). Specimens for the tests are prepared by rolling wheel compaction. Circular specimens are cored and prismatic specimens are cut from the prepared ingots. RSST-CH tests are generally conducted at shear stresses varying between 70 and 130 kPa at temperatures between 40 and 60°C. Maximum shear stress amplitude was maintained at a constant value throughout a specific test. Shear load is applied at 0.1 second with a rest period of 0.6 second to simulate the in-situ loading conditions which were specified by Sousa et al. (1994).

Zhou et al. (2003) compared the results of various laboratory tests including the diametral resilient modulus, asphalt pavement analyzer (APA), Hamburg wheel tracking test (HWTT), repeated simple shear test at constant height (RSST-CH), dynamic modulus test, and repeated load triaxial permanent deformation test, with the field performance measurements of specific pavement sections. It was concluded that RSST-CH tests can be effectively used to differentiate the in-situ performance of different pavement sections. Epps Martin and Park (2003) compared the results from RSST-CH with the downward rut depths measured under full-scale trafficking and concluded that it can be effectively used to predict rutting performance. Monismith et al. (2000) also conducted RSST-CH for specimens from WesTrack test sections and developed rutting performance models to be used for performance-related construction quality specifications.

Although results of the RSST-CH can be used to evaluate in-situ performance, the effect of test results precision and bias on predicted in-situ performance is still an issue, both for testing for design and construction quality assessment and for the effects on performance predictions noted by Prozzi et al (2005). For this reason, determination of bias and precision as a function of specimen size and the effects of RSST-CH results bias and precision on predicted in-situ performance is important.

2.1.2   *Frequency sweep at constant height test*

The frequency sweep at constant height (FSCH) test is used to measure the dynamic shear modulus (G^*) and phase angle (δ) for asphalt mixes to predict the permanent deformation potential. FSCH tests are conducted by applying a sinusoidal cyclic shear load at the upper loading platen that is glued to asphalt sample while maintaining the sample height constant during this loading. Constant height is preserved during the FSCH tests to avoid volume change and isolate the effects of change in specimen volume on test results. In this way shear performance of the material can be directly measured without using any conversion equations. Phase angle and shear modulus parameters were measured based on a stress-strain relationship that is recorded during the test. Measured complex shear modulus is generally separated into two components: (1) the shear storage modulus and (2) the shear loss modulus or viscous modulus. Standard test is conducted without a confining pressure. Procedures for the FSCH tests are similar to RSST-CH and given in AASHTO T 320 (AASHTO, 2003).

2.2 HEAVY VEHICLE SIMULATOR TESTING

The Heavy Vehicle Simulator is a mobile load frame that uses a full-scale wheel (dual or single) to traffic the pavement test section. The trafficked test section is 8 m (26.4 ft) long, of which 1 m (3.3 ft) on each end are used for turnaround of the wheel and are generally not included in analysis and reporting of results. This wheelpath length permits the testing of one slab of jointed PCC of up to approximately 6 m (19.8 ft) with the trafficking including both joints and the entire slab. The specifications and a photograph of the HVS are shown in Figure 2.2.

Overall weight	59,646 kg
Load weight of the test wheel tire	20-100 kN with truck tire
	20-200 kN with aircraft tire
Dimensions of tested area of pavement	1.5 m × 8 m maximum
Velocity of the test wheel	10 km/hr maximum
Maximum trafficking rate	1000 repetitions/hr
Average trafficking rate	750 repetitions/hr
Average daily repetitions	16,000

Dimensions:

	Length	22.56 m
	Width, overall	3.73 m
	Height	3.7 m
	Wheel base	16.7m

Number of axles	3 (1 in rear, 2 in front)
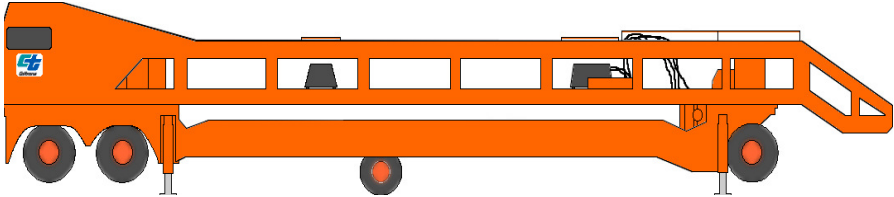
Figure 2.2 Specifications and photograph of HVS.

HVS, designed in South Africa by the Council for Scientific and Industrial Research (CSIR), is accepted to be one of the most effective accelerated test methods. The effects of the heavy truck axle loads on rutting performance can be simulated under controlled temperatures. Constant or variable loads can be applied in a unidirectional or bidirectional manner with a maximum speed 10 km/h. Critical temperature levels within the HVS can be maintained by using a heat chamber. Depending on the purpose of the test, the HVS is capable of simulating 15 to 20 year heavy truck traffic within 1 to 2 months (Jones et al., 2006).

2.2.1 *Pavement instrumentation and monitoring methods*

Instrumentation for the HVS rutting tests included the following types and collection intervals:

- Laser profilometer, a portable beam with a traveling laser collecting 260 points across its 2.3 m length, used to measure transverse surface profile across the wheelpath, with measurements taken at each 0.5 m station and at load repetition intervals selected to provide characterization of the rut development.
- Thermocouples, to measure ambient and pavement temperature, with measurements taken at Stations 4 and 12 and for ambient temperature at one-hour intervals during HVS operation.
- AC strain gauges to provide characterization of the rut development.

2.2.2 Test section failure criterion

The failure criterion was defined as an average maximum rut of 12.5 mm (0.5 in.) over the full monitored section (Station 4 to Station 12). Testing was continued past a 12.5 mm average rut depth until the rutting accumulation rate stabilized.

2.2.3 Environmental conditions

The pavement temperature at 50 mm (2.0 in.) depth was maintained at 50°C±4°C (122°F±7°F) for all HVS tests of this study to assess rutting potential under typical pavement conditions. Heaters were operated inside the temperature control box to maintain the pavement temperature. The pavement surface received no direct rainfall as it was protected by the temperature control unit. The sections were tested predominantly during the wet season, however, measures were taken to keep water from entering the pavement structure inside the temperature control box, and there was an extensive drainage system placed around the entire set of pavement test sections. In addition, plastic sheets were placed on the surface to keep water out of the pavement.

CHAPTER 3   ANALYSIS OF REPRESENTATIVE VOLUME ELEMENT FOR ASPHALT CONCRETE LABORATORY SHEAR TESTING

3.1   INTRODUCTION

Rutting is the load induced permanent deformation of pavements with asphalt concrete layers (White et al., 2002). Rutting is a critical pavement failure problem that can control the design life of the pavement. Due to its importance, prediction of rutting performance is important to determining the most cost-effective design alternatives. Effective performance prediction models and associated laboratory materials characterization tests are needed to simulate the in-situ deformation accumulation mechanism.

Mechanistic-empirical (ME) design methods are developed by calibrating critical mechanistic responses of pavement structures calculated using theoretical models with those measured in the field, and then correlating those responses with empirical performance data. The structural model is developed based on generally accepted theories

and methods (such as linear elastic theory [LET], finite element [FE] method, etc.), with specific constitutive relations that consider the effects of environmental conditions and traffic loads, and dimensions. The structural models use laboratory test results to characterize the damage in the materials (usually loss of stiffness or permanent deformation) resulting from the pavement response (stress and/or strain). Structural models are calibrated based on measured pavement performance that is generally determined from accelerated pavement testing and/or less commonly field test results (Ullidtz et al., 2006). The simulated performance is then calibrated based on correlation with observed distresses, again using accelerated pavement tests or field results.

Estimating the variability in fundamental pavement design inputs and integrating this variability into the performance prediction procedures is generally considered a required component of modern ME pavement design methods. There are two major sources of variability in a ME pavement design procedures: in-situ performance and laboratory test results. Variability in in-situ performance can be determined by either using the measured in-situ performance data or including the effects of expected field variability of input parameters, such as thickness, stiffness, air-void content etc. in the structural model simulations. Actual variability in in-situ performance should be directly included in pavement design procedures to be able to evaluate the design at various reliability levels. In addition, the effects of the bias and variability in laboratory test results used to characterize the material responses should be minimized by using appropriate laboratory tests and test configurations (Weissman et al., 1999).

This chapter discusses the effects of specimen dimensions on the precision and bias of RSST-CH results. Nonlinear regression models were developed for the test results of each specimen size group and their bootstrap samples. Accumulated asphalt concrete rutting was predicted at specific repetitions by using the nonlinear regression model coefficients for each bootstrap sample. Distributions of predicted rut depths for each laboratory model of specimen size were used to evaluate the effects of laboratory test results variability on predicted performance. Bias and precision problems caused due to the use of small size laboratory specimens were investigated to determine RVE for a specific material type.

3.1.1 Representative volume element

Fundamental properties of composite materials have been investigated since the late 19th century (Rayleigh, 1892). Mechanical properties of composite materials were first investigated by Albert Einstein (1906), in a study in which he calculated the effective viscosity of a fluid containing rigid spherical particles. The technology of composite materials started to emerge in early 1960s with the advent of modern fiber composites (Hashin, 1983).

Asphalt concrete is a composite material, which consists of aggregates, air-voids and mastic. All of the constituents of asphalt concrete are large enough to be regarded as continua and they are bonded together at the interfaces. With its composite structure, asphalt concrete can be considered to exhibit heterogeneous characteristics due to the large number of composite microheterogeneities (aggregates, air-voids, mastic [asphalt

38

and fine aggregate], etc.) in its structure. However, asphalt concrete specimens can be assumed to exhibit homogeneous characteristics when the volume of the specimen is increased to a minimum level, the dimensions of which are referred to as a Representative Volume Element (RVE). A necessary characteristic of the RVE is the statistical homogeneity that must be constituted in its media (Hashin, 1983). This statistical homogeneity can be quantified based on the global geometrical characteristics such as volume fractions, two-point correlations, etc.

Although quantified statistical homogeneity is important for analysis, it is not possible to use it as a unique property to determine the size for RVE of asphalt concrete materials. Weissman et al. (1999) investigated the dimensions for RVE of asphalt concrete specimens for repeated simple shear test at constant height (RSST-CH) based on finite element simulations and concluded that the RVE dimensions for asphalt concrete depend not only on material homogeneity but also on the test temperature and rate of loading. Two-dimensional, plane strain, finite element simulations indicated that asphalt concrete specimens act as united load carrying systems at lower temperatures when the asphalt and mastic stiffnesses are close. However, increasing temperature will make the composite act more like a particulate structure than a continuum. As the difference between aggregate and mastic stiffness increases at high temperatures, variability in laboratory test results also starts to increase. Thus, RVE sizes determined by using quantified statistical homogeneity parameters can be misleading at these high test temperatures. RVE is also often dependent on stress state, with the result that different dimensions of a specimen relative to the stress directions are often critical for determining RVE rather than the

overall volume, when the test does not produce the same stresses in all directions in the specimen.

Dimensions for laboratory specimens should satisfy RVE requirements in order to achieve test results that can represent the in-situ characteristics of the asphalt concrete pavements. Tests conducted with specimens that are smaller than the RVE can give random results that can be higher or lower than the expected values of the property. However, specimens with large volumes sometimes are difficult to test due to practical limitations. For this reason, a large number of replicate tests must be conducted with small size specimens to eliminate possible bias that might originate from the randomized nature of the test results. However, it is noteworthy that it will not be possible to determine the bias in the test procedure when the variations in the test results are higher than a specific level (Weissman, 1997). Thus, the size of the laboratory specimen for any type of test should satisfy the minimum limits that are specified based on the RVE studies. Statistically reliable and repeatable test data can only be obtained by considering this minimum size requirement that can change related to the mixture characteristics, analyzed property and testing conditions. For this reason, RVE requirements should be established for different asphalt mix types before conducting tests whose results are going to be used for performance model development.

The RVE can be determined by performing tests with various specimen sizes to determine the minimum specimen volume that results in no further reduction in the variation in the test results, and no change in the mean result.

If the RVE requires impractically large specimen dimensions, then such a study can identify specimen dimensions resulting in an acceptable level of variability, and understanding of any bias. Tests conducted with specimens smaller than the RVE will often require a large number of replicates to obtain sufficient reliability for materials characterization, which is further complicated if there is bias introduced by using less than RVE dimensions. Velasques (2009) indicated that RVE should be large enough to satisfy statistical homogeneity within the material. This statistical homogeneity will minimize the fluctuations in measured physical and mechanical properties. Figure 3.1 illustrates the theoretical variation of a specific material property with increasing RVE size. It can be seen that a specific material property can be measured with maximum accuracy and precision without conducting various tests when specimens larger than V_3 are used for testing. This minimum volume (V_3) is the size of the RVE required to achieve a desirable level of variability in the measured material property.
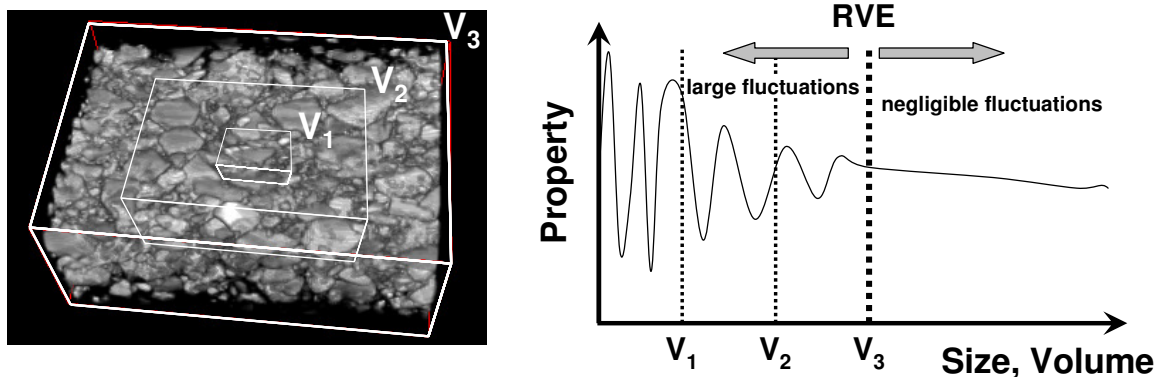
Figure 3.1 The representative volume element for a three dimensional composite material.

It is noteworthy that high variability in laboratory test results will introduce high levels of bias in predicted performance because of the averaging process used during model development (Prozzi et al., 2005). The probability of measuring the actual material property decreases with increasing variability in test results and decreasing number of measurements. If this occurs, models using laboratory characterization of the materials will fail to simulate the in-situ rutting performance of pavements.

Gitman et al. (2007) introduced a combined numerical-statistical method to determine the RVE size. For different sample sizes, finite element computations for a tension test were performed and results were presented in terms of stress/strain curves. The average stress parameters of the different size samples were used to perform Chi-square statistical tests to determine the RVE size. Although this method of RVE size estimation appears to be more effective than using statistical and numerical methods independently, it is of extreme importance that the parameter that is chosen for statistical evaluation should reflect the overall variability in test results. The appropriate parameter, and the RVE, may vary depending on the stress states in the test, thus differing between tests.

3.2 OBJECTIVES AND SCOPE

The primary purpose of the study presented in this chapter is to develop an effective method for RVE evaluation. RVE of two asphalt concrete mixes were determined by evaluating the effects of precision and bias in RSST-CH results for four specimen sizes for one mix, and three for the other mix. The effect of laboratory test results precision and

bias was quantified using a statistical sampling method called "bootstrapping". Bootstrapping is a resampling technique to estimate the properties of an estimator by calculating these properties for many samples that are generated by random sampling with replacement from the original dataset (Efron, 1979). In this study, variability and bias in laboratory test results were quantified by using the distributions of model coefficients that were calculated for randomly generated bootstrap samples. The contribution of this quantified variability and bias to overall variability and bias in predicted in-situ performance was determined by performing Monte Carlo simulations using a shear based incremental-recursive (IR) rutting design procedure developed by Deacon et al. (2002). Monte Carlo simulation is a computational algorithm that is used to simulate the variability of a specific output by repeated calculations with replacement from the complete distributions of the input parameters. Other objectives of the study are given as follows:

1. Identify the levels of variability in laboratory test results for different mixes and specimen sizes based on predicted in-situ rutting.

2. Determine the reasonableness of the general theory regarding specimen size induced variability for asphalt concrete mixtures under RSST-CH testing.

3. Evaluate the effects of possible specimen size-related bias on permanent shear strain in the RSST-CH test after 100, 200, 500, 1,000, 2,000 and 5,000 repetitions, to determine the most effective parameter for performance evaluation.

4. Determine the required number of replicates to minimize bias in RSST-CH measurements based on a specific test parameter: permanent shear strain after

5,000 load repetitions.

5. Evaluate the effects of specimen size induced bias in RSST-CH results on predicted pavement rutting performance using the bootstrapping method.

6. Develop guidelines for the required size of RVE for dense graded asphalt concrete mixes at high temperatures (45°C and 55°C) that are critical for rutting performance evaluation.

7. Evaluate the effect of temperature on the variability of RSST-CH results.

Although analyses were performed by using RSST-CH laboratory test results and rutting models used for design in California, the general procedure can be used to identify specimen size-related bias and precision for any type of laboratory test and distress model.

3.3 METHODOLOGY FOR INVESTIGATING THE EFFECTS OF LABORATORY TEST RESULTS PRECISION AND BIAS

In the first part of this study, the effects of possible specimen size-related bias was evaluated on the permanent shear strain after 100, 200, 500, 1,000, 2,000 and 5,000 repetitions measured in the RSST-CH by using the analysis of variance (ANOVA) approach, with the result at each number of repetitions treated as a different parameter. The parameter permanent shear strain after 5,000 repetitions (PSS5000), which contains minimum size-related bias, was selected to be the most effective parameter for performance evaluation. The required number of replicates to minimize the size-related bias on the variability of PSS5000 was also determined. Later, the effects of specimen

size-related bias and variability on predicted in-situ performance were evaluated by using Monte Carlo simulations with variability in laboratory test results considered by using bootstrapping. The steps followed for precision and bias evaluation are described as follows:

1. Conduct RSST-CH with different sized asphalt concrete specimens.

2. Generate various data samples for each size group by random sampling with replacement from the original data set (bootstrap sampling).

3. Calculate the regression coefficients of the nonlinear performance model for each bootstrap sample.

4. Create an example in-situ case with layer thicknesses, stiffnesses, load levels, tire pressures, etc.

5. Predict accumulated asphalt concrete rutting at specific repetitions by using the calculated model coefficients for each bootstrap sample and the shear based IR procedure developed by Deacon et al. (2002).

6. Evaluate the distribution of predicted rut depths for each specimen size to determine which specimen size meets RVE requirements.

Bias and precision problems caused due to the use of small size laboratory specimens were evaluated to determine RVE for a specific mix type.

3.4   MATERIALS AND EXPERIMENTAL DESIGN

Asphalt concrete specimens used in this study were cut from pavement sections in Brentwood, California (Contra Costa County) on the State Route 4 Bypass. The experimental design for the RSST-CH tests conducted in this study is given in Table 3.1. Specimens were cut in the shape of rectangular prisms with different dimensions. All specimens were cut with a length to height ratio of 3:1 determined from preliminary investigations of RVE for RSST-CH (Weissman et al., 1999). Specimens were tested at two temperatures, 45 ^{o}C and 55 ^{o}C, at a shear stress of 130 kPa with five replicates for each case. Specimens for four size groups are given in Figure 3.2(a) with the standard cylindrical RSST-CH specimen (AASHTO, 2003). It can be observed that Size 2 specimens are closest in surface area and volume to standard cylindrical specimens that have height of 50 mm and diameter of 150 mm.

Two mix types were used for testing. The viscosity grade for the binders in both mixes was AR4000 per Section 92 in Caltrans Standard Specifications (1999) (similar to PG 64-10 in the current Performance Grade specifications). Nominal maximum aggregate sizes for Mix 1 and Mix 2 were 9.5 mm and 19 mm, respectively. Computed tomography (CT) images of Mix 1 and Mix 2 are shown in Figure 3.2(b), which show the difference between aggregate size distributions. The target air-void content for both mixes was 4 percent. The actual average air-void content for Mix 1 were measured to be 3.62 percent with standard deviation of 0.91 percent, and 4.04 percent with standard deviation of 0.76 percent for Mix 2. Target binder contents for both mixes were 5 percent by mass of aggregate based on Hveem mix design.

Table 3.1 Experimental design for RSST-CH RVE testing

NMAS (mm)	Specimen Size	Ave. Length (mm)	Ave. Width (mm)	Ave. Height (mm)	Shear Stress (kPa)	Temp. (^{o}C)	Repl.	Total Tests
9.5	S1	115	100	39				$5\times2 = 10$
	S2	151	125	51				$5\times2 = 10$
	S3	172	143	58				$5\times2 = 10$
19	S1	116	104	38	130	45, 55	5	$5\times2 = 10$
	S2	153	127	49				$5\times2 = 10$
	S3	179	147	56				$5\times2 = 10$
	S4	229	192	77				$5\times2 = 10$

NOTE: NMAS = Nominal maximum aggregate size; Ave. = Average; Repl. = Replicate; Temp. = Temperature.
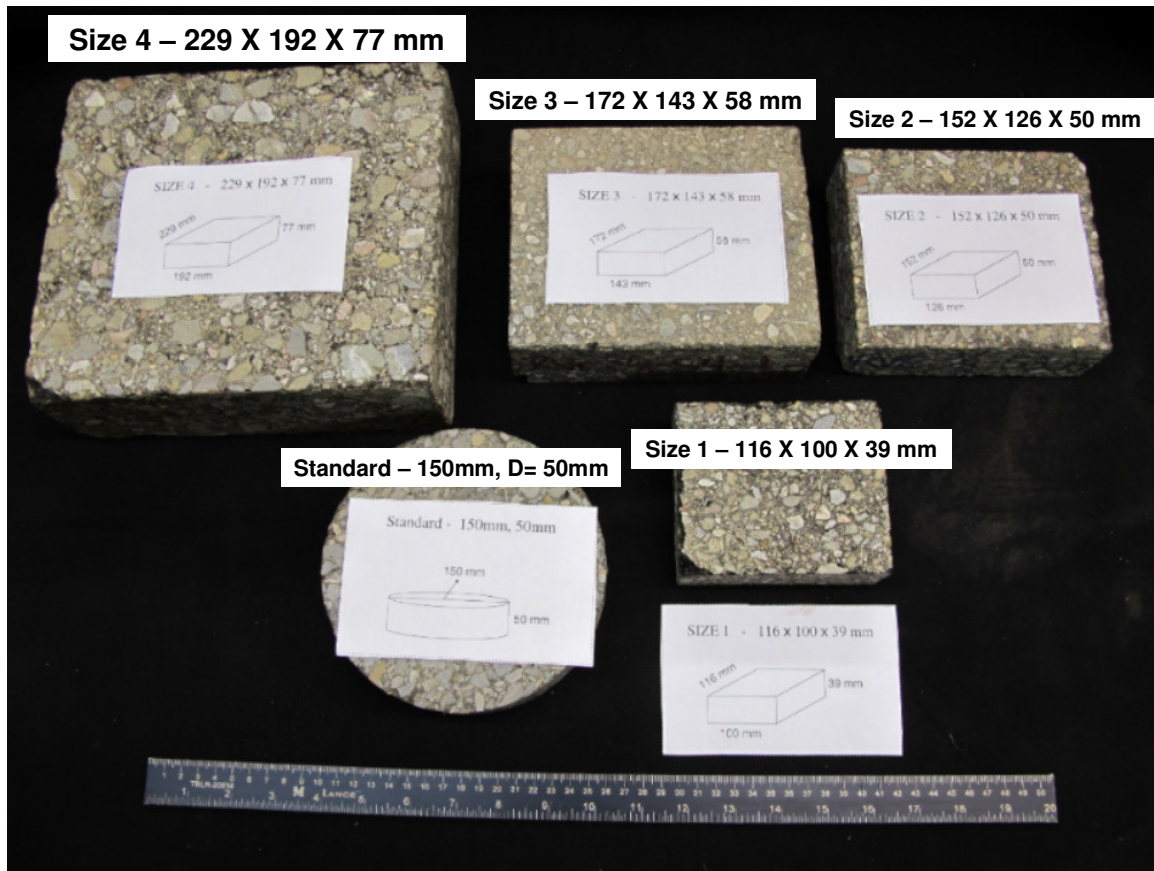
(a)
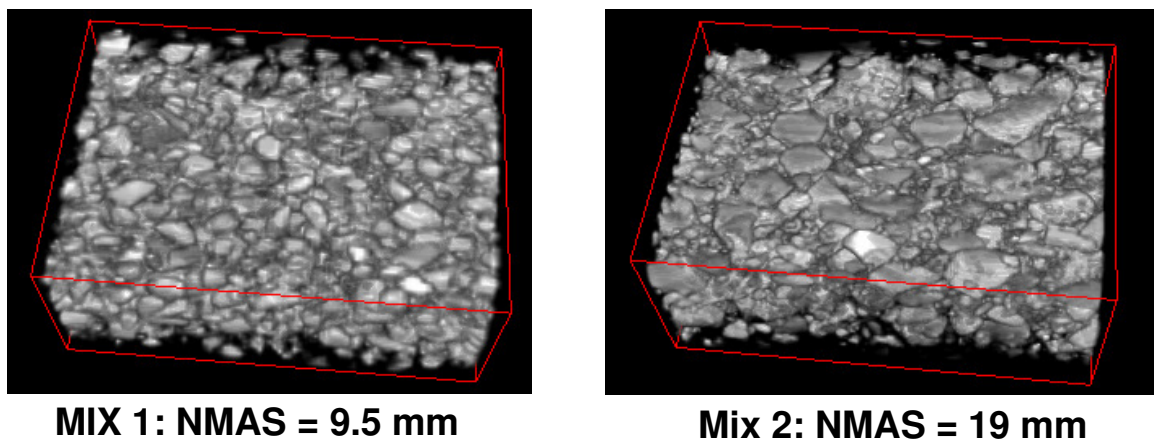
(b)

Figure 3.2 Specimen dimensions and aggregate size (a) Specimen size groups with the standard cylindrical RSST-CH specimen (b) Computed tomography (CT) images of Mix 1 and Mix 2 showing the difference between aggregate size distributions.

3.5   EVALUATION OF PRECISION AND BIAS IN LABORATORY
TEST RESULTS

Results of the RSST-CH results (repetition versus permanent shear strain) for all specimen sizes at two different temperatures (45°C and 55°C) are given in Figure 3.3. The average permanent shear strain and its standard deviation at 10,000 repetitions for both 45°C and 55°C tests are also given in Figure 3.3. Without performing any analysis, it can be observed from the results that increasing specimen size decreases the variability in test results. In addition, it can be seen that the tests conducted at 45°C always exhibit less variability in measured permanent shear strain than the tests conducted at 55°C, which is a result of increased difference between aggregate and mastic stiffness at high temperatures.
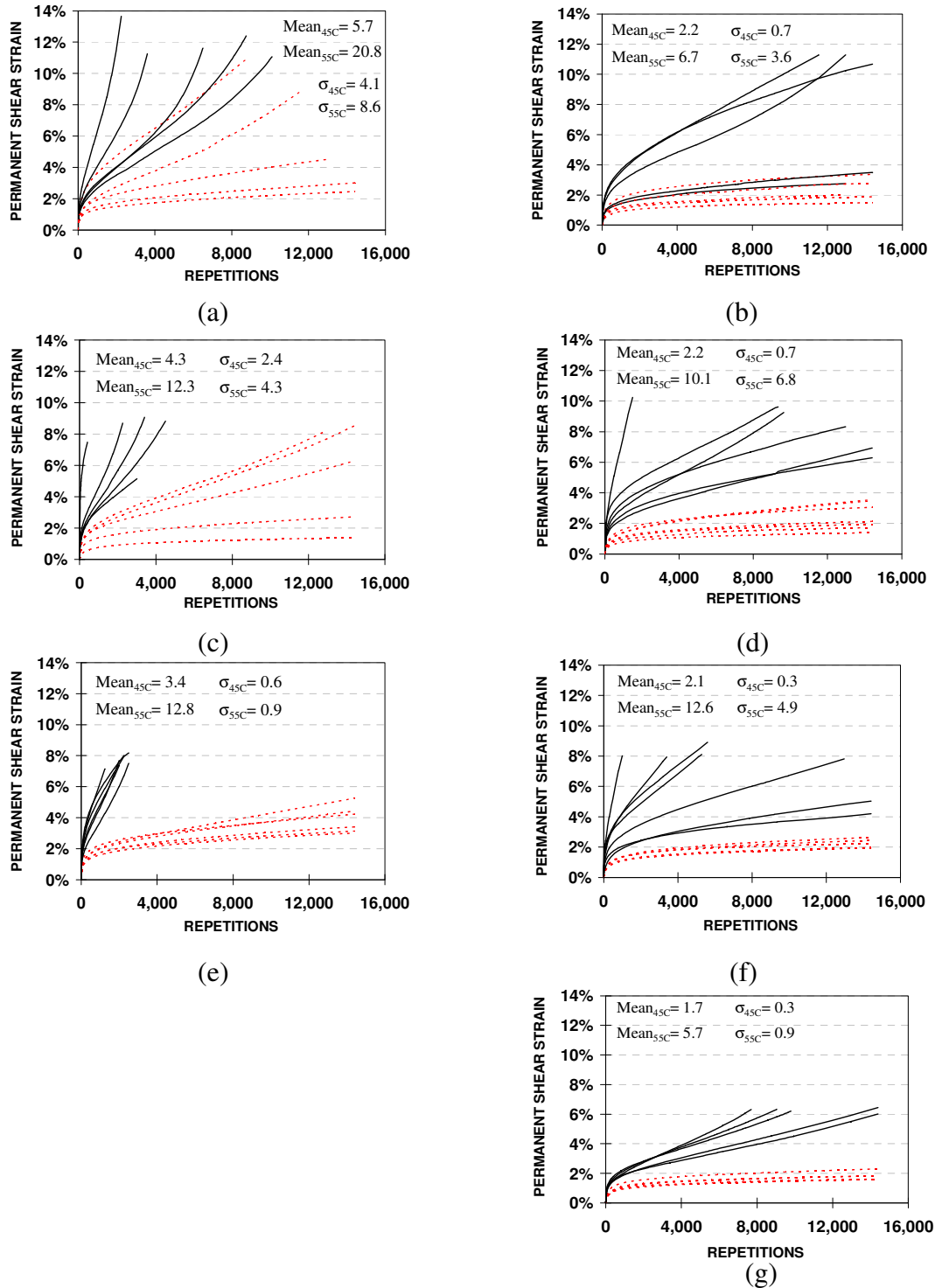
Figure 3.3 RSST-CH test results (a) Size 1 – NMAS = 9.5mm (b) Size 1 – NMAS = 19mm (c) Size 2 – NMAS= 9.5mm (d) Size 2 – NMAS = 19mm (e) Size 3 – NMAS = 9.5mm (f) Size 3 – NMAS = 19mm (g) Size 4 – NMAS = 19mm (Dashed line: Tests conducted at 45°C, solid line: tests conducted at 55°C) NOTE: NMAS=Nominal maximum aggregate size, σ = Standard deviation for PSS at 10,000[th] repetition, Mean=Average for PSS at 10,000[th] repetition.

3.5.1 Determination of minimum bias rutting performance parameter by ANOVA approach

In this study, the ANOVA approach was used to identify the most effective minimum bias parameter for rutting performance evaluation. In addition, the number of replicates required to avoid bias in laboratory models was determined by performing ANOVA analyses with various randomly selected test results. ANOVA analyses were performed by using the permanent shear strains after 100, 200, 500, 1,000, 2,000 and 5,000 repetitions as the dependent variables and specimen size (Size), air-void content (AV), test temperature (Temp) and nominal maximum aggregate size (NMAS) as the independent variables.

In the initial experimental design, four sizes for each mix type were planned to be tested. However, limitations of the test equipment prevented conducting tests with the fourth size for Mix 1. In order to avoid complications related to an unbalanced ANOVA, data for Mix 2-Size 4 were excluded from the ANOVA dataset.

The ANOVA approach is used to test the null hypothesis that sample means of two or more groups are equal or their difference is not significant based on a prescribed level of significance (Natu et al., 2002). In this study, a significance level of 5 percent was used. The null hypothesis (H_0) tested to determine the significance of "Size" variable on the description of dependent variable is given as follows for the parameter permanent shear strain after 5,000 repetitions (PSS5000) :

H_0 = Mean PSS5000 is the same for all "Size" categories (Size1, Size2 and Size3)

The results of the ANOVA are given in Table 3.2. Independent variables with p-values larger than 0.05 can be regarded as insignificant variables. Based on this decision rule, the null hypothesis (H_0) is accepted and concluded that "Size" differences do not create any bias in the measured PSS5000 parameter. On the other hand, Temp and NMAS appear to be significant variables in identifying the variability in PSS5000 measurements, as expected. Air-voids (AV) also appear to have a small effect on the variation of PSS5000 measurements, with a p-value of 0.077, which can be explained by the narrow interval for the AV of tested specimens.

Table 3.2 ANOVA results for the complete PSS5000 dataset

Variable	Type	Df	SS	F Value	p - value
Size	S1, S2, S3	2	0.00104	0.73	0.489
AV	Variable	1	0.00235	3.27	0.077
Temp	45°C and 55°C	1	0.06005	83.74	0.000
NMAS	9.5mm,19mm	1	0.01291	18.00	0.000
Size:AV	Interaction	2	0.00429	2.99	0.059
Size:Temp	Interaction	2	0.00100	0.70	0.503
Size:NMAS	Interaction	2	0.00069	0.48	0.620
AV:Temp	Interaction	1	0.00070	0.97	0.330
AV:NMAS	Interaction	1	0.00136	1.90	0.174
Temp:NMAS	Interaction	1	0.00602	8.39	0.006

NOTE: S1 = Size 1, AV=air-void content, Temp=test temperature, NMAS=nominal maximum aggregate size, Df = degrees of freedom, SS = sum of squares.

Results of the ANOVA analysis for PSS5000 parameter were further checked to identify whether the general assumptions of ANOVA were satisfied. Assumptions were checked based on Figure 3.4 and Figure 3.5 as follows:

- *The expected values of the residuals equal to zero*: the average of the residuals for the ANOVA model was calculated to be zero (3.736327E-019).

- *Independence of variables:* the independence of variables NMAS, AV, Temp and Size was checked by pairs plot given in Figure 3.4. It can be observed that only a small correlation exists between AV and NMAS. However, excluding the AV parameter from the analysis does not change the general rank for the p-values while the p-value for the Size variable increases from 0.489 to 0.568.

- *Residuals are normally distributed:* the distribution of residuals is compared to the normal distribution that was obtained by using the average and standard deviation of the residuals in Figure 3.5(a). It can be observed that the distributions are close to each other. The two sample Kolmogorov-Smirnov test was used to compare these two distributions and it was concluded that two distributions show similarities, with a p-value that is significantly higher than 0.05 (p-value=0.25).

- *Homoscedasticity - the variance of data in groups should be the same:* Figure 3.5(b) shows the fitted values versus residuals for the ANOVA test. It can be observed that the width for the cluster of points for the residuals is slightly increasing with increasing fitted values. However, since the difference between residual variances for the two ends of the fitted values does not appear to be extremely different, it was assumed that the Homoscedasticity assumption holds.
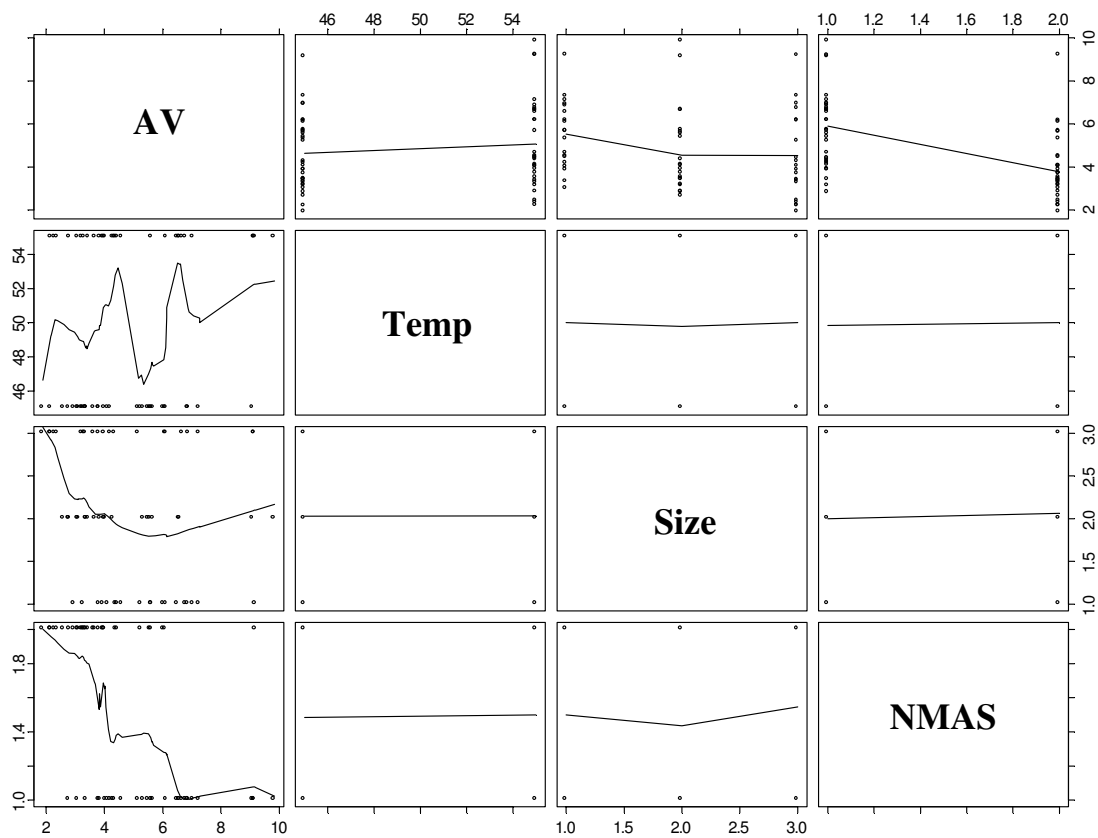
Figure 3.4 Pairs plot to evaluate independence of variables.
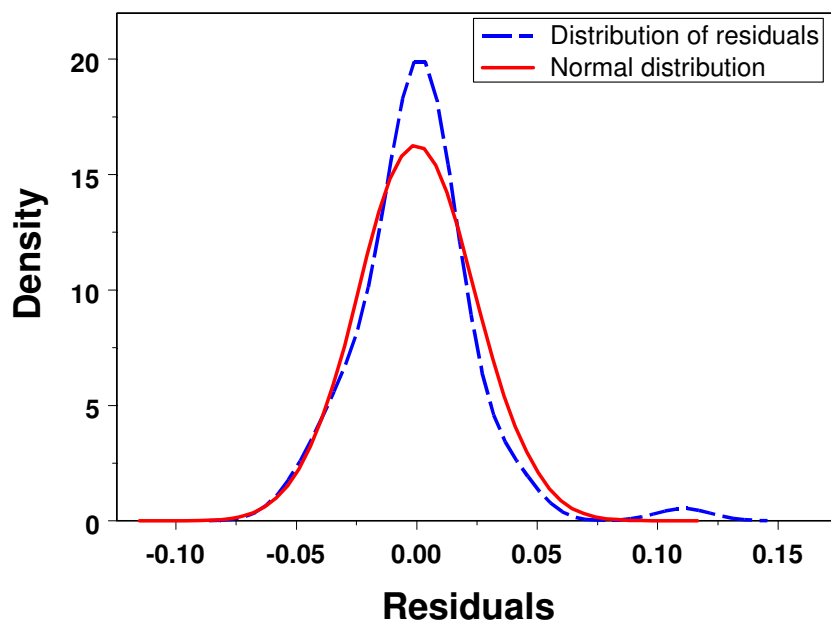
(a)
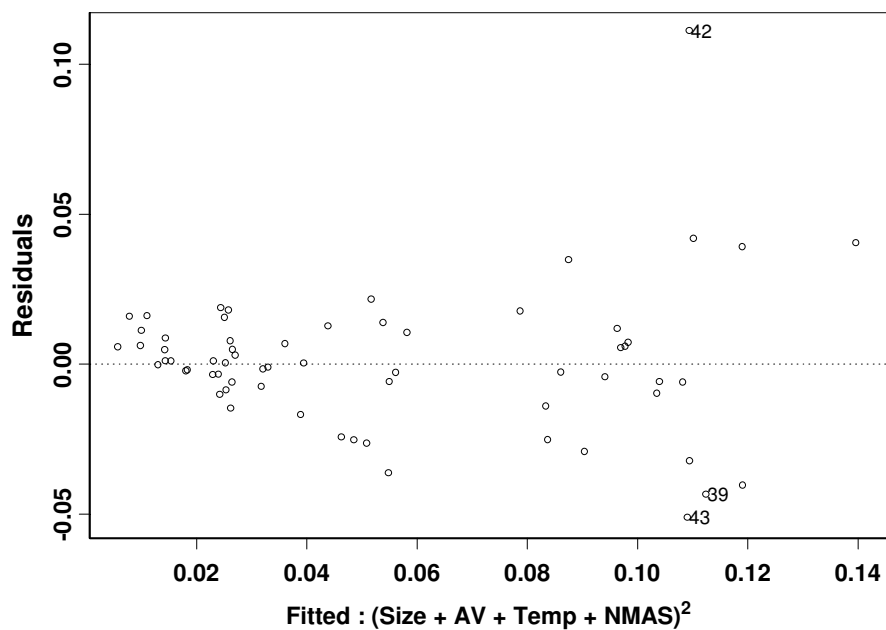
(b)

Figure 3.5 Residual plots to evaluate the general assumptions of ANOVA (a) residual distribution vs. normal distribution for the mean and standard devaiation of the residuals (b) Fitted data vs. residuals.

When the ANOVA analyses were performed with dependent variables permanent shear strain after 100, 200, 500, 1,000 and 2,000 repetitions, it was observed that decreasing repetitions increases the risk of having size-related bias with lower p-values. This result is illustrated in Figure 3.6(a). This result suggests that the size of the tested specimens appears to be an important factor at the initial stages of the RSST-CH tests whereas this size-related bias starts to disappear after 2,000 repetitions based on a significance level of 5 percent (Figure 3.6[a]). For this reason, PSS5000 was selected to be the minimum bias parameter for rutting performance evaluation.

Although mean PSS5000 appears to be the same for all size categories, validity of this conclusion should be checked when less than five replicate tests are used for the analysis. The use of less replicates will likely result in lower p-values when the variability in test results is higher. This reduction in p-values with decreasing number of replicates may change the decision for the null hypothesis. In order to determine the level of reduction in p-values with decreasing number of replicates, an iterative procedure is proposed, as follows.
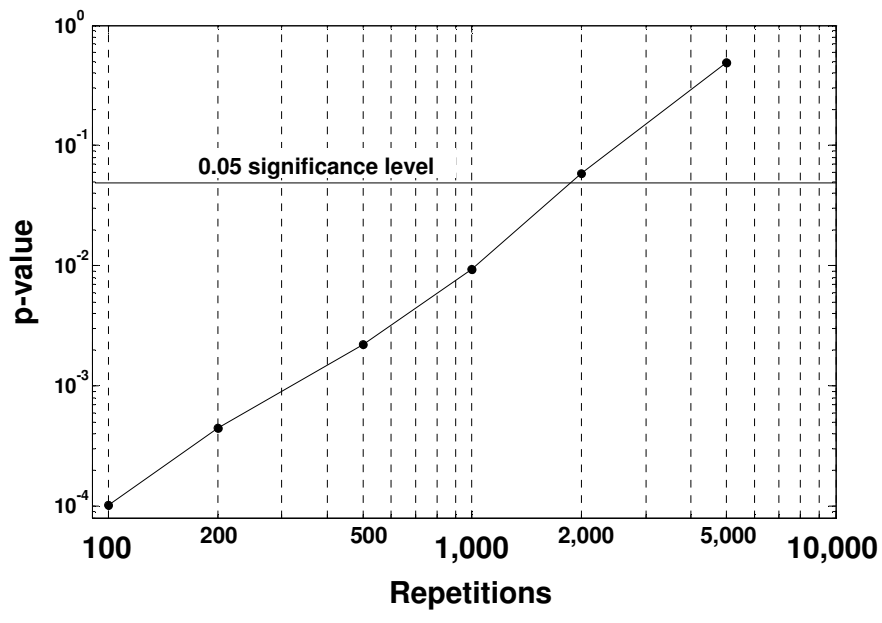
(a)
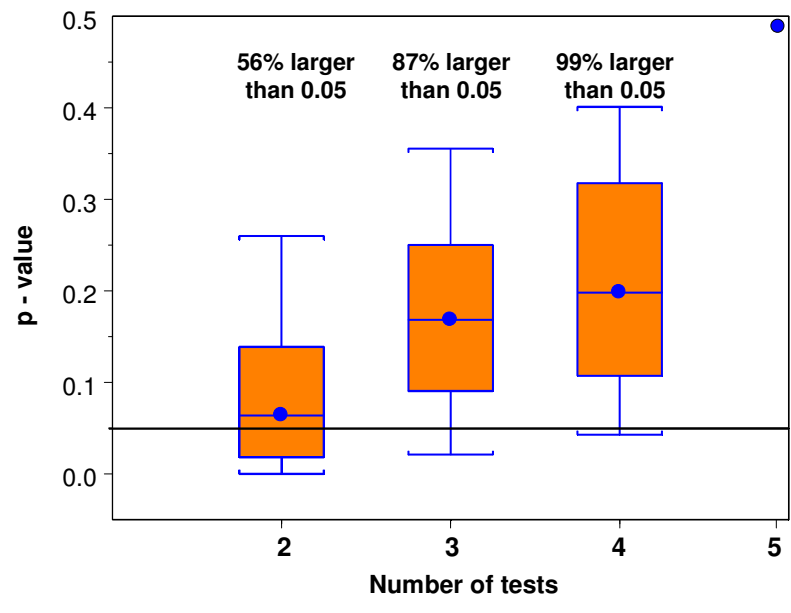
(b)

Figure 3.6 Results of ANOVA analyses (a) Variation of Size variable's p-values for parameters permanent shear strain after 100, 200, 500, 1,000, 2,000 and 5,000 repetitions (b) Distribution of Size variable's p-values for cases with different number of replicates for parameter PSS5000.

For each NMAS, Size and Temp, less than 5 replicates (2, 3 or 4) were randomly selected and a new dataset was created. The ANOVA test was conducted for that new dataset and the calculated p-value was recorded after every iteration. The number of iterations was selected to be 1,000 because it was observed that the difference between p-value distributions for cases with 1,000, 2,000 and 5,000 iterations appeared to be negligible. This iterative algorithm was used for cases with two, three and four replicates and p-value distributions were developed for each case.

These distributions are given in Figure 3.6(b). It can be observed from the box-plot that 99 percent of the randomly generated datasets do not have size-related bias (with a significance level of 5 percent) when four replicate tests were conducted. On other hand, in 44 percent of randomly generated dataset sets with two replicate tests, size differences appeared to cause bias in measured PSS5000 values. It should be noted that ANOVA analysis with the complete dataset (five replicates) resulted in a p-value of 0.489 for the Size variable which is higher than all p-values calculated with replicates less than five (see Figure 3.6[b]).

Results of the ANOVA analyses performed by using parameters permanent shear strain after 100, 200, 500, 1,000, 2,000 and 5,000 repetitions indicated that test results bias related to specimen size increases with decreasing repetitions. Thus, PSS5000 appears to be an unbiased parameter when compared to other parameters (PSS100, PSS200, PSS500, PSS1000 and PSS2000) according to the ANOVA results. In addition, when

three or more replicate tests were used for the analysis, the effect of size-related bias on the variability of parameter PSS5000 will be at acceptable levels.

3.5.2 *Investigating the effects of laboratory test results precision and bias on predicted pavement performance by Monte Carlo simulations and Bootstrapping method*

Most of the laboratory RVE studies for asphalt concrete shear testing in the literature have focused on the evaluation of variability in test results based on specific parameters, such as the complex shear modulus (Weissman et al., 1999; Romero and Masad, 2001), number of repetitions to 5 percent shear strain (Harvey et al., 1999) and permanent shear strain after 5,000 load repetitions (Romero and Masad, 2001). Although these parameters can give useful insight into the general performance of the material, they do not reflect the complete performance of the material throughout the test. Materials with similar critical parameters may exhibit more varied results when the full time history of the test is used in the performance prediction, as it is in mechanistic-empirical incremental-recursive (IR) approaches for simulating rutting performance. For instance, two time histories of load repetition versus permanent shear strain intersecting at a specific repetition will have equal permanent shear strain at that particular point, although the curves can diverge from each other due to differing rates of increase in permanent shear strain with increasing load repetitions. In other words, although these two materials have the same permanent shear strain parameter at that specific repetition, their performance in the rest of the test may be completely different. Therefore, the effect of the laboratory test results precision and bias on predicted in-situ rutting performance in IR procedures should be evaluated to determine the critical RVE size for the test materials.

In this study, precision and bias in laboratory test results was quantified by using the bootstrapping method with Monte Carlo simulations. Various data samples for each size group were generated by random sampling with replacement from the original data set. Coefficients of the nonlinear IR rutting model for each sample were calculated by minimization of the sum of squared differences between measured and calculated permanent shear strain. These model coefficients were used to predict rutting at three different repetitions for an example highway section. Distributions of predicted rut depths were used to identify the differences between the levels of precision and bias arising from the use of different sized specimens for laboratory testing. In addition, RVE size requirements for the two different asphalt concrete mixes were proposed based on the results of this study.

Procedure for Rutting Performance Prediction

The shear based IR procedure developed by Deacon et al. (2002) was used to predict accumulated rut depth in asphalt concrete layers of an example highway section by considering the effects of temperature, material properties, load levels and speed. In the IR procedure, material properties are updated for each time increment by considering the changes in environmental conditions and traffic characteristics. Calculated damage (permanent deformation for rutting) for each time increment is recursively accumulated using the time hardening principle to be able to predict the pavement condition at any point in time. The IR approach has been found to be effective for simulating damage accumulation, and has been implemented in the California Mechanistic-Empirical (CalME) software, which is an ME analysis and design program for new asphalt-surfaced

pavements and their rehabilitation (Ullidtz et al., 2006), and to a partial extent in the MEPDG (NCHRP, 2004).

The gamma function used to calculate permanent shear strain by using elastic shear strain, number of repetitions and shear strain as the independent variables is (Ullidtz et al., 2008):

$$\gamma^i = \exp\left(A + \alpha \times \left[1 - \exp\left(-\frac{\ln(N)}{\gamma}\right) \times \left(1 + \frac{\ln(N)}{\gamma}\right)\right]\right) \times \exp\left(\frac{\beta \times \tau}{\tau_{ref}}\right) \times \left(\gamma^e\right)^\delta \qquad (3.1)$$

where

γ^i = permanent shear strain

γ^e = elastic shear strain

τ = shear stress at 50 mm depth

N = number of load repetitions

τ_{ref} = reference shear stress (0.1MPa = atmospheric pressure)

A, α, β, γ and δ are model coefficients determined from the RSST-CH results.

Properties of an example highway section were used for rutting simulation. The thickness of the asphalt concrete and aggregate base layers were assumed to be 150 mm and 400 mm, respectively. Stiffnesses of aggregate base and subgrade layers were assumed to be constant at 230 MPa and 100 MPa, respectively. General conditions assumed for rutting performance prediction were as follows:

- Tire Pressure = 720 kPa

- Wheel Load = 60 kN

- Speed = 15 km/hr

- Center to center tire distance = 360 mm

- Temperature = randomly selected between 40°C and 55°C

Stiffnesses for the asphalt concrete layer were determined for a specific loading frequency and randomly generated temperatures ranging between 40°C and 55°C by using the elastic modulus master curve application methodology developed by Tsai et al. (2004). Shear stresses at 50 mm depth at the edge of the tire were calculated by using the calculated stiffnesses, wheel load characteristics and material properties as inputs to a layered elastic program. Elastic shear strain values for each repetition interval were calculated by using the following equation (Ullidtz et al., 2008):

$$\gamma^{e} = \frac{\tau}{E_i / (1 + \nu_i)} \qquad (3.2)$$

where

E_i = modulus of layer i

ν_i = Poisson's ratio for layer i (assumed to be 0.35 for all layers)

Calculated elastic strain values for the corresponding repetition interval were used in equation (3.1) to calculate plastic shear strain. The coefficient for the shear stress variable (β) was assumed to be equal to zero because all laboratory tests in this study were

conducted at constant 130 kPa shear stress level. Rut depths in CalME are calculated for the upper 100 mm of the asphalt layers (Ullidtz et al., 2008), therefore calculated plastic shear strains (from equation [3.1]) for each repetition interval were multiplied by 100 mm to calculate corresponding rutting deformation. Calculated rut depths for each repetition interval were accumulated based on the IR procedure to develop the final rutting curve. Calculated rut depths at repetitions 50,000, 100,000 and 200,000 were used for the analyses.

Bootstrapping Method and Monte Carlo Simulations for Variability Evaluation

As mentioned previously, bootstrapping is a resampling technique to estimate the properties of an estimator by calculating these properties for many samples that are generated by random sampling with replacement from the original dataset (Efron, 1979). The general theory relies on the assumption that there is high probability of reoccurrence of an event that has previously created a single data point in the original dataset. In many situations, such as when robust regression estimation is used or when the model is highly nonlinear for which the linear approximation methods do not work, standard methods to evaluate the precision of sample estimates may not be available. For these complex cases, precision can be determined by bootstrapping methods (Bates and Watts, 1988).

In this study, bootstrapping was used to identify the variability in coefficients of the nonlinear rutting model for every specimen size group. The original dataset for each specimen size group was randomly resampled with replacement to create 5,000 bootstrap samples. The sizes of the resamples were equal to the size of the original dataset.

Coefficients of the nonlinear rutting model were determined for each bootstrap sample. Variability in calculated model coefficients reflects the variability in laboratory test results for each specimen size group. Model coefficients calculated by the least squares fitting method for the original laboratory test results are given in Table 3.3 with the mean and standard deviation values for the bootstrap model coefficient distributions. Bootstrap model coefficients for each specimen size were separately used to predict rut depths at three different wheel load repetitions, 50,000, 100,000 and 200,000, for the given example case in a Monte Carlo simulation procedure. Calculated rut depth distributions were used to evaluate precision and bias for laboratory test results. With this method, the effects of the laboratory test results variability on predicted rutting performance can be determined for each specimen size group. RVE size requirements can also be established based on the results of these simulations. It should be noted that all the coefficients of one bootstrap sample were used for each rut depth prediction other than random selection from the coefficient distributions because linear correlation was observed between the distributions of some coefficients.

Table 3.3 Mean and standard deviation values for the Bootstrap coefficient distributions
and model coefficients for the original datasets

		Mix Type	Mix 1 Size 1	Mix 1 Size 2	Mix 1 Size 3	Mix 2 Size 1	Mix 2 Size 2	Mix 2 Size 3	Mix 2 Size 4
ORIGINAL DATA SET		A	1.672	1.670	1.334	1.965	1.672	1.760	0.575
		α	7.738	16.727	3.177	4.659	3.067	3.269	7.865
		β	0.000	0.000	0.000	0.000	0.000	0.000	0.000
		γ	7.824	13.186	3.244	5.689	2.958	3.389	8.836
		δ	1.000	1.000	1.000	1.000	1.000	1.000	1.000
		R^2	*0.82*	0.90	*0.89*	*0.89*	*0.93*	*0.93*	*0.95*
BOOTSTRAP SAMPLES	*MEAN*	A	1.670	1.669	1.333	1.963	1.671	1.758	0.574
		α	7.813	17.206	3.179	4.720	3.073	3.277	7.912
		β	0.000	0.000	0.000	0.000	0.000	0.000	0.000
		γ	7.923	13.349	3.246	5.743	2.968	3.396	8.858
		δ	1.000	1.000	1.000	1.000	1.000	1.000	1.000
	STANDARD DEVIATION	A	0.051	0.031	0.045	0.061	0.075	0.063	0.029
		α	1.195	3.426	0.026	0.430	0.026	0.039	0.717
		β	0.000	0.000	0.000	0.000	0.000	0.000	0.000
		γ	0.988	1.721	0.109	0.595	0.147	0.162	0.653
		δ	0.000	0.000	0.000	0.000	0.000	0.000	0.000

NOTE: R^2 = coefficient of determination

Rut depth distributions for each mix type and size group are given in Figure 3.7 for the three different repetitions. It can be observed that there is significant bias in predicted rut depths for a specific mix type at a particular repetition related to the specimen size differences. Predicted rut depths for specimens with Size 3 (172 x 143 x 58 mm) for Mix 1 (NMAS = 9.5 mm) and Size 4 (229 x 192 x 77 mm) for Mix 2 (NMAS =19 mm) are 2 to 5 times lower than the rut depths predicted for smaller specimen sizes. This result points out the existence of increased measured shear resistance for materials with larger volume.

(a)

(b)

(c)

(d)

(e)

(f)
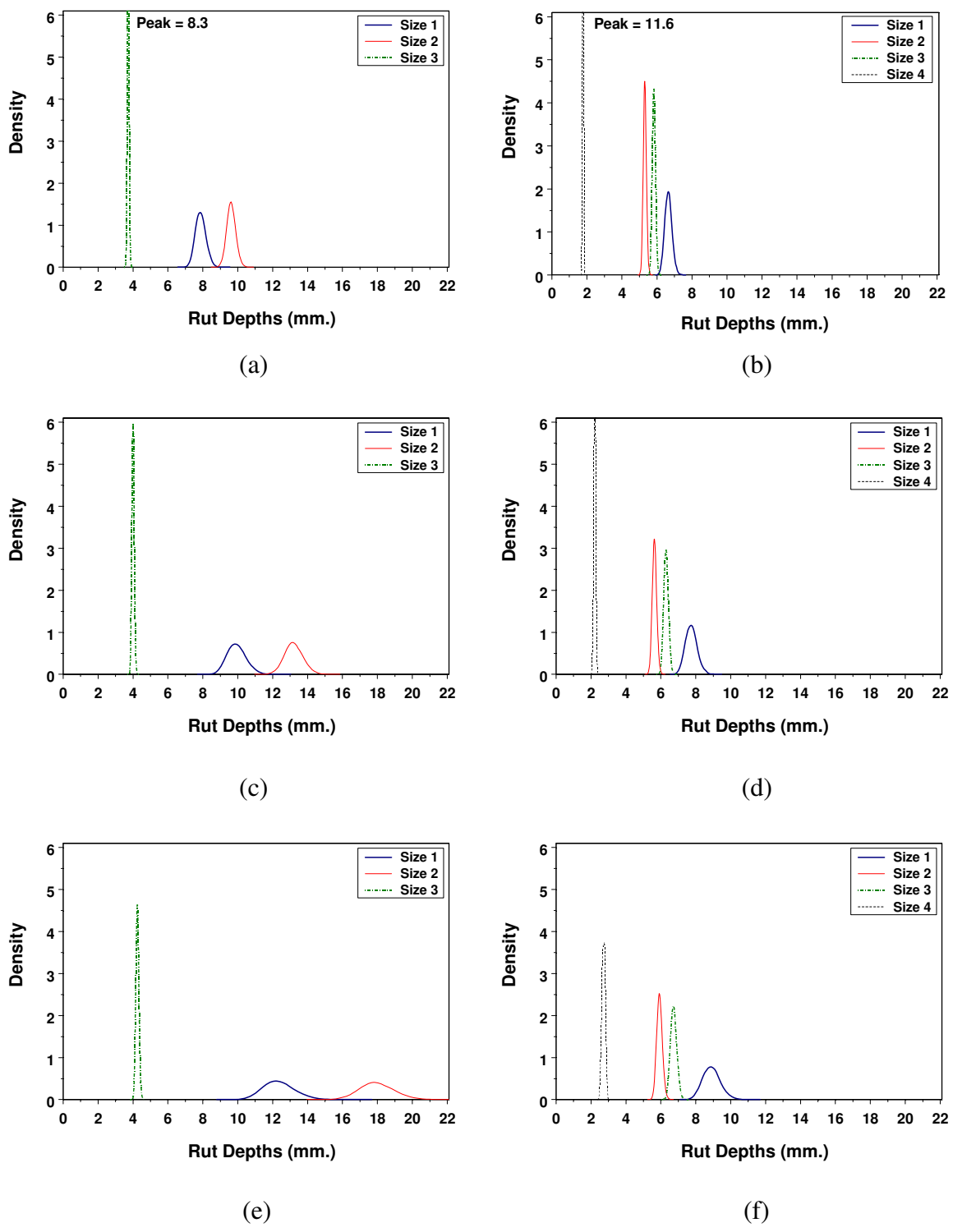
Figure 3.7 Calculated rut depth distributions for each mix type and size group (a) Nom. Max. = 9.5 mm, Repetition = 50,000 (b) Nom. Max. = 19 mm, Repetition = 50,000 (c) Nom. Max. = 9.5 mm, Repetition = 100,000 (d) Nom. Max. = 19 mm, Repetition = 100,000 (e) Nom. Max. = 9.5 mm, Repetition = 200,000 (f) Nom. Max. = 19 mm, Repetition =200,000.

It can also be observed that rut depths predicted by using test results for specimens with Size 3 (172 x 143 x 58 mm) for Mix 1 (NMAS = 9.5 mm) and Size 4 (229 x 192 x 77 mm) for Mix 2 (NMAS = 19 mm) have significantly lower variability than models developed by using test results for smaller material volumes. This is a result of the reduction in the variability of test results for larger size specimens (Figure 3.3). Rut depths predicted by using the test results for Size 1 (116 x 100 x 39 mm) always have the highest level of variability when compared to predicted rut depths of larger specimen sizes, which is a result of the high levels of variability in test results for smaller sized specimens.

3.6   SUMMARY OF FINDINGS AND CONCLUSIONS

In this study, the effects of the specimen size-related precision and bias of laboratory test results on predicted rutting performance were evaluated by using bootstrapping and Monte Carlo simulations. In addition, the required number of replicates in an experimental design for RSST-CH testing was also determined based on the parameter PSS5000. Several findings of this study are addressed as follows:

1. Significant bias exists between predicted rut depths of different specimen sizes for a specific mix type at a particular repetition. Predicted rut depths for specimens with Size 3 (172 x 143 x 58 mm) for Mix 1 (NMAS = 9.5 mm) and Size 4 (229 x 192 x 77 mm) for Mix 2 (NMAS =19 mm) are 2 to 5 times lower than the rut depths predicted for smaller specimen sizes. This result points out the existence of increased measured

shear resistance for materials with larger volume.

2. Variability in predicted rut depths for specimens with Size 3 (172 x 143 x 58 mm) for Mix 1 (NMAS = 9.5 mm) and Size 4 (229 x 192 x 77 mm) for Mix 2 (NMAS =19 mm) is significantly lower than rut depths predicted by using laboratory test results of smaller specimen sizes. On the other hand, rut depths predicted by using the test results for Size 1 (116 x 100 x 39 mm) always have the highest level of variability when compared to predicted rut depths of other size groups, which is a result of the high levels of variability in test results for smaller sized specimens. This result indicates the repeatability of RSST-CH results for larger sized specimens while it also follows the general theoretical background on specimen size induced variability for composite materials.

3. Results of the ANOVA analyses performed by using parameters permanent shear strain after 100, 200, 500, 1,000, 2,000 and 5,000 repetitions indicated that test results bias related to specimen size increases with decreasing repetitions. Thus, PSS5000 appears to an unbiased parameter when compared to other parameters (PSS100, PSS200, PSS500, PSS1000 and PSS2000) according to the ANOVA results. In addition, when three or more replicate tests were used for the analysis, the effect of size-related bias on the variability of parameter PSS5000 will be at acceptable levels.

4. Variability in laboratory test results depends on both material homogeneity and size, and also on test temperature. Tests conducted at 45°C always exhibit less variability in measured permanent shear strain than the tests conducted at 55°C, which is a result of increased difference between aggregate and mastic stiffness at high temperatures.

5. Based on the test results presented here, specimen size requirements for dense graded mixes can be determined. For mixes with NMAS 9.5 mm, RSST-CH specimens should be close to Size 3 (172 x 143 x 58 mm) with length-to-height ratio of at least 3. An acceptable level of variability at temperatures 45°C and 55°C can only be achieved with Size 3 specimens. For mixes with NMAS 19 mm, Size 4 (229 x 192 x 77 mm) is recommended for RSST-CH testing at temperatures 45°C and 55°C. However, Size 3 specimens can also be used at 45°C since the level of variability for these specimens is tolerable at that temperature. For both the laboratory and field, specimens can be obtained by either coring or saw-cutting while coring is more typical. Size 3 requires approximately a 200 mm (8 inch) diameter core and Size 4 requires approximately a 300 mm (12 inch) diameter core, which is about the maximum practical core diameter. Core specimens can be trimmed at the sides with a laboratory saw to obtain rectangular specimens. When the diameter of the available core does not allow getting the recommended specimen length and width, recommended dimensions can be modified without decreasing a length to height ratio of 3:1 while trying to achieve the maximum possible specimen volume. Saw-cutting is often more effective to meet minimum requirements and obtain replicate specimens at the same location in the field. A longitudinal strip can be cut between the wheelpaths with the middle dimension (width) and then transversely cut in the laboratory or before field extraction at the longest dimension (length). In the field, specimens with 19 mm NMAS may not meet the recommended minimum height because of field constructed lift thicknesses. In that case, the maximum height possible should be obtained and larger number of replicate tests should be conducted

to achieve statistically meaningful results.

The procedure, with Monte Carlo simulations and bootstrapping method, proposed in this study appears to be an effective way to evaluate the effects of size-related bias and precision in laboratory test results. Although analyses were performed by using RSST-CH laboratory test results and rutting models used for design in California, the general procedure can be used to identify specimen size-related bias and precision for any type of laboratory test and distress model.

CHAPTER 4   INCORPORATION OF RELIABILITY INTO RUTTING PERFORMANCE PREDICTION PROCEDURES

4.1 INTRODUCTION

Mechanistic-empirical (ME) design is a method of designing highway pavements by integrating the empirical relations obtained from field performance data with theoretical response predictions from structural models (NCHRP, 2004). The structural model is developed based on the generally accepted theories and methods (such as linear elastic theory [LET], finite element [FE] method, etc.) to determine the response of the pavement structure and materials, with their specific constitutive relations and dimensions, to the environmental conditions and traffic loads. Pavement responses, stresses, strains and deformations, determined by the mechanistic structural model should be calibrated and/or validated based on measured pavement responses, which are generally developed from instrumented accelerated pavement tests and/or field tests (Ullidtz et al., 2006). Although the general ME design procedure appears to be straightforward, differences between the transfer functions relating pavement

performance to pavement response, structural models, damage accumulation mechanisms and calibration procedures may result in considerable differences in the predicted performances.

Estimating the variability in fundamental pavement design inputs and integrating this variability into the general performance prediction procedures is generally considered a required component of modern ME pavement design. Since all public agencies would like to have control over the risk that they take, design reliability levels and the corresponding costs for each level of reliability should be determined. This kind of risk control may require increasing the initial costs in order to decrease the risk of early failure for critical highway construction projects (Lea, 2009). For this reason the full distribution of expected performance with the likelihood of early failure should be determined and considered in design.

In the study presented in this chapter, Monte Carlo simulations were performed to simulate "within section" variability for reliability evaluation and compare with actual variability for Heavy Vehicle Simulator (HVS) test results. In addition to the within section variability considered here, it is recommended that sensitivity analysis be used to assess the effects of different materials supplied to the project to determine "between section" variability, which is the performance variability caused due to differences between material source and contractor (Harvey et al., 2010). The design factors that can be controlled by the designer and constructer should be used to provide an indication of the variability of the design separating within section and between section variability.

The thickness and stiffness of pavement layers can be considered to be two fundamental design inputs with significant impact on the variation of the rutting performance within a design section. Therefore, their spatial variability within a section should be quantified based on suitable distribution types with the corresponding parameters (Jiang et al., 2003; Lea, 2009). These distributions should be used in pavement design to provide an estimate of the range of performance estimates, rather than only averaged inputs (deterministic analysis).

Thickness and stiffness variability can also be used to incorporate reliability analysis into the design procedure (Timm et al., 2000). The probability of achieving a satisfactory design for a specific time period can be determined based on the calculated reliability level (Prozzi et al., 2005). The analyst can also make cost estimates for various reliability levels which can provide useful insight into the tradeoffs between initial cost and design reliability, as well as between initial costs and future maintenance costs. However, it must be noted that reliability does not imply validity (Kutner et al., 2005). The bias incurred during the measurement of the thickness and stiffness data cannot be evaluated or identified based on reliability analysis. For this reason, potential bias that may occur due to the deficiencies in stiffness back-calculation procedures or thickness measurements should also be evaluated based on comparisons between measured and calculated performance variability by considering the variability in thickness and stiffness of pavement layers. In addition, model bias due to the assumptions of a pavement design procedure and statistical error related to the lack of fit in regression models should be

investigated as systematic errors to identify their impact on predicted performance variability (Kim and Lee, 2002).

Although the influence of laboratory test results variability on predicted pavement performance was investigated in some studies (Harvey et al., 1997; Kandhal and Cooley, 2003), the effects of that variability on predicted pavement performance was not included in comprehensive design procedures. Although thickness and stiffness distributions give valuable insight into the rutting performance of the pavement, high levels of variability in the laboratory test results might introduce high levels of bias in predicted performance as a result of the averaging process during model development. Therefore, it is proposed that the variability in laboratory test results should be introduced into the current rutting performance prediction procedures. One method of decreasing variability in laboratory test results is by increasing the specimen size requirements (Weissman et al., 1999) in the current test protocols (AASHTO, 2003). However, in many cases, increasing specimen size does not appear to be a practical solution to decrease test results variability due to funding and time concerns.

Harr (1987) divided reliability analysis methods into three categories: first-order second-moment (FOSM), point-estimate (PEM) and exact methods. Exact methods are accepted to be the most widely used methods in Civil Engineering due to their simplicity and accuracy. The term "exact" is used when complete distributions for the input variables are entered rather than discrete values (Timm et al., 2000). Monte Carlo simulation is one of the exact methods used for reliability evaluation. Monte Carlo simulation is a

computational algorithm that is used to simulate the variability of a specific output which is calculated by entering the complete distributions of the input parameters. Although Monte Carlo simulation appears to be a simple and accurate method for mechanistic pavement model evaluations, it may not be computationally efficient due to large numbers of simulations necessary to produce a robust predicted outcome distribution. For this reason, the optimum number of repetitions to achieve an acceptable level of precision should be determined before evaluating the complete system (Timm et al., 2000). In this study, Monte Carlo simulations are used to evaluate the effects of construction and laboratory test results variability on predicted rutting performance, and also to develop distributions for calibration coefficients to use as inputs for reliability based pavement rutting design. Although the proposed method is used for rutting performance evaluation, it can be applied to other distress types.

4.2 OBJECTIVES AND SCOPE

The primary purpose of this study is to develop a reliability based asphalt pavement rutting design procedure which evaluates reliability by considering the variability in laboratory test results, layer thicknesses, stiffnesses and measured in-situ performance. With the proposed method, the effects of input design parameters variability on predicted performance can be determined by evaluating the calculated distributions of calibration coefficients. By the use of calculated calibration coefficient distributions, the need for performing computationally intensive calculations within the design software for reliability evaluation is eliminated. Other objectives of the study are to:

1. Identify the levels of variability in laboratory test results for different mixes.

2. Evaluate the effect of laboratory test results variability on predicted rutting performance.

3. Evaluate the relative effects of construction variability (stiffness and thickness) on predicted performance.

4. Characterize and quantify the effect of measured in-situ rut depths (performance) variability on predicted rutting performance.

5. Investigate the effectiveness of using thickness and stiffness variability to simulate measured performance variability.

4.3 EXPERIMENT DESIGN

The analyses in this study are based on the test results of the California Department of Transportation (Caltrans) Partnered Pavement Research Center Strategic Plan Element 4.10. The goal of the project was to evaluate the rutting and reflective cracking performance of overlays with conventional asphalt and modified binder mixes. Sections were tested to assess the susceptibility of overlay mixes with five binder types to high-temperature rutting; AR4000, conventional asphalt concrete; RAC-G, asphalt rubber; and three modified binders containing both recycled tire rubber and polymers, MB4, MB15, and MAC15. AR4000 binder was used in a dense-graded asphalt concrete mix, the asphalt rubber binder was used in a gap-graded rubber asphalt concrete mix (RAC-G), and the modified binders were all used in gap-graded mixes (Coleri et al., 2008). The MB4 has 4% crumb rubber modifier (CRM) by weight of binder mixed in the wet

process (the rubber particles were mixed with the asphalt cement prior to adding the resulting binder to the aggregates) without agitation to keep the rubber particles uniformly distributed in the hot mix; similarly, the MB15 has 15% CRM by weight of binder. The MAC15 has 15% (by weight of binder) CRM added as part of the aggregate to the mix in the dry process (the crumb rubber was mixed with the aggregates prior to the addition of the asphalt). The experimental design for the laboratory shear tests is given in Table 4.1 with the corresponding PG grades for each mix.

Table 4.1 Experimental design for shear testing of GOAL 9 project

Mix	PG	Grad.	AC (%)	AV (%)	Temp.(^{o}C)	Sts. (kPa)	Repl.	Total tests
AR4000	64-16	DG	5.0	6.1				2 x 3 x 3=18
RAC-G	64-16		8.0	7.7		70		2 x 3 x 3=18
MAC15	70-28	GG	7.4	5.6	45	100	3	2 x 3 x 3=18
MB15	58-28		7.1	5.3	55	130		2 x 3 x 3=18
MB4	64-28		7.2	6.2				2 x 3 x 3=18

Note: PG = performance grades; grad. = gradation; AC = asphalt content; AV = air-void content; Temp. = temperature; Sts. = shear stress; Repl. = replicate; DG = dense graded; GG = gap graded

In this study, rutting test results at high temperatures from six HVS test sections were used for model calibration. Cross sections of the HVS test sections with the average thicknesses and standard deviations determined from cores taken at various locations are given in Figure 4.1. The general test conditions for the HVS rutting tests are as follows:

- Tire Pressure = 720 kPa
- Wheel Load = 60 kN
- Speed = 8.7 km/hr
- Center to center tire distance = 360 mm

- Temperature $= 50 \pm 4^{\circ}$C at 50 mm depth
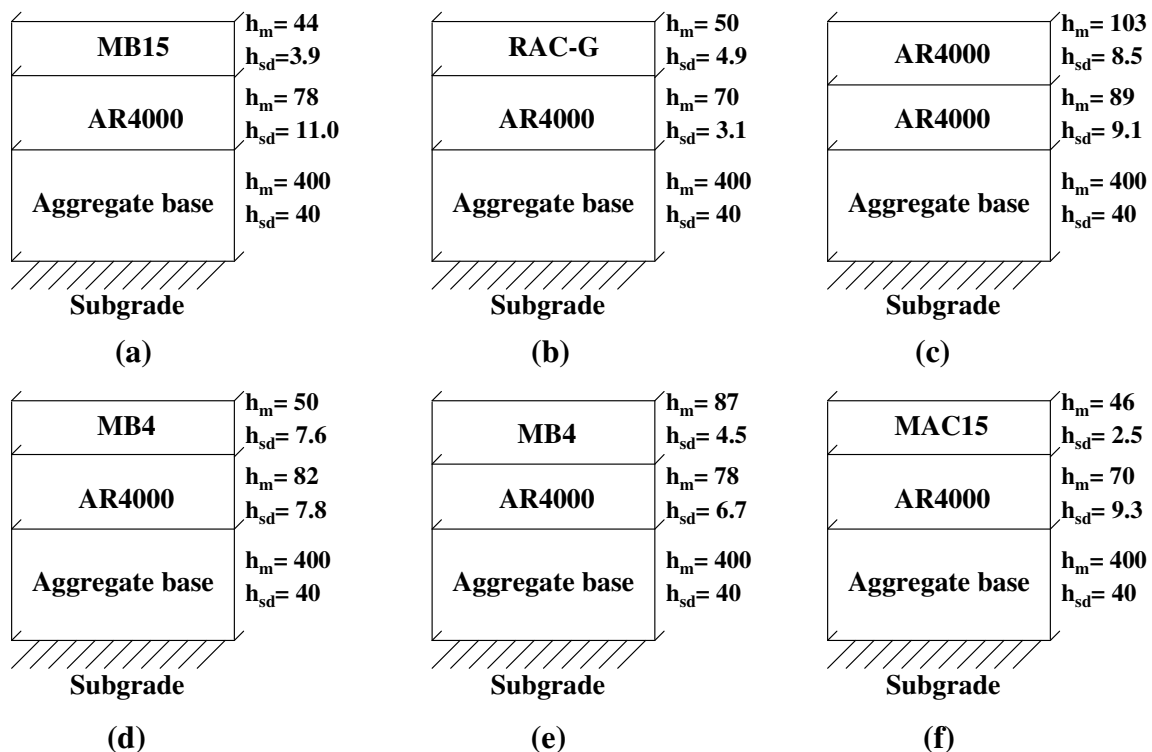
Figure 4.1 Cross sections of HVS test sections: (a) Section 580RF (MB15), (b) Section 581RF (RAC-G), (c) Section 582RF (AR4000), and (d) Section 583RF (MB4), (e) Section 584RF (MB4), (f) 585RF (MAC15) (h_m=mean thickness, h_{sd}=thickness standard deviation). Note: Dimensions are in millimeters.

Caltrans standard specifications and procedures were followed to design the overlays and the underlying pavement structures of the HVS test sections, except for the MAC15 mix which met southern California Greenbook specifications. Laboratory tests were conducted on samples collected during construction to determine binder content, binder properties and air-void contents. According to the tests performed by Caltrans, all binders met the specifications (Bejarano et al. 2005).

Repeated simple shear test at constant height (RSST-CH) was used for laboratory performance evaluation of asphalt concrete mixes. Procedures for the RSST-CH tests are given in AASHTO T 320 *(*AASHTO, 2003) and Chapter 2 of this dissertation. Specimens for the tests in this study were prepared in the laboratory by rolling wheel compaction. Cylindrical specimens with the diameter of 150 mm and 50 mm height were cored from the prepared ingots. RSST-CH tests in this study were conducted for five mix types at three shear stress levels, 70 kPa, 100 kPa and 130 kPa at temperatures of 45 ^{o}C and 55 ^{o}C with three replicates (Table 4.1).

4.4   INCORPORATION OF VARIABILITY INTO GENERAL RUTTING PERFORMANCE PREDICTION PROCEDURE

A shear based incremental- recursive (IR) procedure developed by Deacon et al. (2002) was used to estimate development of rutting in asphalt layers of HVS test sections by considering the effects of temperatures, material properties, load levels and speed. In the IR procedure material properties are updated for each time increment by considering the changes in environmental conditions and traffic characteristics. Calculated damage (permanent deformation for rutting) for each time increment is recursively accumulated to be able to predict the pavement condition at any point in time. A similar approach is used for rutting performance prediction in CalME, which is an ME analysis and design program for new flexible pavements and rehabilitation (Ullidtz et al., 2008). Although the reliability approach proposed in this study was developed using RSST-CH laboratory test results and rutting models used in CalME, the general procedure can be applied to any pavement design software for any type of distress.

4.4.1 General procedure

The general framework for the application of simulations for rutting performance prediction is given in Figure 4.2. Steps illustrated with dashed ellipses describe the incorporation of variability into the procedure by different methods. To asses the contribution of each input parameter's variability to variability of calculated calibration coefficients, various cases were created by including and excluding the variability in these parameters throughout the calibration process.
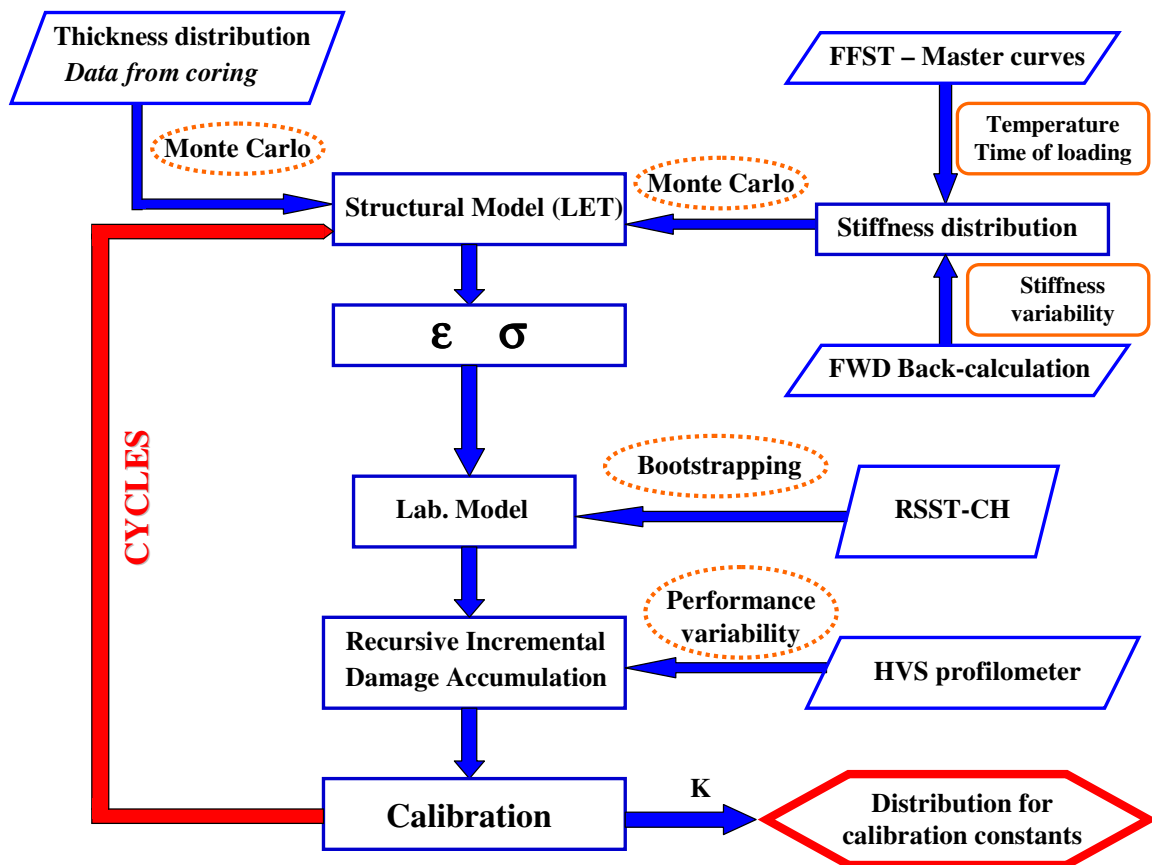
Figure 4.2 The general framework for the application of simulations for rutting performance prediction. NOTE: FFST = Flexural frequency sweep test

The steps followed for model calibration are described as follows:

PART1: Preparation of input distributions for variability evaluation

1. *Thickness variability:* Determine thickness variability for each asphalt (existing and overlay) and aggregate base layer for all test sections using the data from coring and trenching.

2. *Stiffness variability for unbound layers:* Perform falling weight deflectometer (FWD) tests at various locations on HVS test sections and determine unbound layer stiffness variability along the test sections using the backcalculated stiffness values.

3. *Stiffness variability for asphalt concrete layers:*

   a. Perform FWD tests at various locations on HVS test sections and determine asphalt concrete stiffness variability along the test sections at temperatures that are close to HVS rutting test levels $(50 \pm 4^{o}C)$

   b. Perform flexural frequency sweep test (FFST) to determine stiffnesses for each asphalt concrete layer at loading frequencies and temperatures used for HVS rutting tests by using elastic modulus master curve application methodology developed by Tsai et al. (2004).

   c. Develop distributions for asphalt concrete layer stiffnesses by setting the stiffnesses determined from master curves as the mean values and incorporating the stiffness variability using the coefficient of variation (COV) values from backcalculation.

4. *Laboratory test results variability:* Determine the effect of laboratory test results variability on model coefficients by bootstrapping method (Details of the bootstrapping method will be explained later in this chapter).

The gamma function used to calculate permanent shear strain is given as follows:

$$\gamma^i = \exp\left(A + \alpha \times \left[1 - \exp\left(-\ln(N)/\gamma \right) \times \left(1 + \ln(N)/\gamma \right) \right] \right) \times \exp\left(\beta \times \tau / \tau_{ref} \right) \times \left(\gamma^e \right)^\delta \quad (4.1)$$

where

γ^i = permanent shear strain

γ^e = elastic shear strain

τ = shear stress

N = number of load repetitions

τ_{ref} = reference shear stress (0.1MPa = atmospheric pressure)

A, α, β, γ and δ are coefficients determined from the RSST-CH results

5. *Performance variability:* Determine variability in collected transverse profilometer data at 13 different stations at 0.5 meter longitudinal positions along each 6 meter HVS test section after subtracting deformation in unbound layers that was calculated from measured multi-depth deflectometer (MDD) data.

PART2: Model calibration

1. Randomly select thickness and stiffness values for each layer in the test section (the effect of the temperature variation on stiffnesses throughout the HVS tests is included after this random selection).

2. Calculate shear stress at 50mm depth at the edge of the tire (per assumptions of the CalME rutting model, equation [4.1]) using layered elastic theory and randomly selected stiffness and thickness values.

3. Calculate shear strain by the following linear elastic equation given in CalME (Ullidtz et al., 2008):

$$\gamma^e = \frac{\tau}{E_i / (1 + v_i)} \tag{4.2}$$

where

E_i = modulus of layer i

v_i = Poisson's ratio for layer i (assumed to be 0.35 for all layers)

Because the effect of Poisson's ratio on predicted rutting performance is insignificant when compared to the effects of thickness and stiffness, a reasonable value of 0.35 is assumed for all layers without any variation.

4. Randomly select coefficients of the gamma function from the bootstrap distributions of model coefficients.

5. Perform IR deformation accumulation (Coleri et al., 2008; Monismith et al., 1975) for a randomly selected location (station) of the HVS test section using the calculated shear stress, elastic shear strain and the gamma function.

6. Calculate optimum calibration coefficient (K) by relating calculated permanent shear strain values to measured rut depths using the following equation and optimization:

$$dp_i = K \times h_i \times \gamma^i \tag{4.3}$$

where

K= calibration coefficient

h_i= thickness of layer i (above a depth of 100mm)

dp_i = rut depth (from profilometer measurements)

7. Record the calibration coefficient and go to PART 2 step 1 for another cycle.
8. Evaluate the distribution for the calibration coefficients after performing a predetermined number of cycles.

4.4.2   *Evaluation of variability in laboratory test results – Bootstrapping method*

Bootstrapping is a resampling technique to estimate the properties of an estimator by calculating these properties for many samples which are generated by random sampling with replacement from the original dataset (Efron, 1979). In many situations, such as when a robust regression estimation is used or when the model is highly nonlinear for which linear approximation methods do not work, standard methods to evaluate the precision of sample estimates may not be available. For these complex cases, precision can be determined by bootstrapping methods (Bates and Watts, 1988).

In this study, bootstrapping was used to determine the precision of estimated model coefficients of the gamma function used to calculate permanent, or inelastic, shear strains in the asphalt layers in CalME. 10,000 resamples of the laboratory (RSST-CH) test results were generated by random sampling from the observed laboratory dataset with replacement. Sampling with replacement implies that duplicate data points may occur in the bootstrap sample and some data points may not exist in the generated sample (Kutner et al., 2005). The general theory relies on the assumption that there is high probability of reoccurrence of an event that has previously created a single data point in the original dataset. Model coefficients, A, α, β, γ and δ for each bootstrap sample were determined using an optimization procedure. The estimated standard deviation of the distributions for the model coefficients generated by the sampling is an estimate of the variability of the sampling distribution for these coefficients. For this reason, these standard deviations reflect the precision of predicted coefficients for the original dataset.

High variability in RSST-CH results will result in high standard deviations for the bootstrap coefficients. Variability in these coefficient distributions were used to simulate the effects of laboratory test results variability on the predicted rutting performance in the HVS tests. All the coefficients calculated for each sample were recorded to use in the calibration process. Random selection from these coefficient distributions was performed for performance model calibration. It should be noted that all the coefficients of one bootstrap sample were randomly selected for a specific cycle in the calibration process because linear correlation was observed between the distributions of some coefficients. For that specific cycle permanent shear strain was calculated by using these coefficients

in equation (4.1). Equation (4.3) is used in the IR deformation accumulation procedure to calculate the calibration coefficient (K value) that gives the best fit to measured HVS rut depths. Permanent shear strain values were multiplied by asphalt concrete layer thicknesses to calculate rut depths (equation [4.3]). This way, optimum calibration coefficients for each bootstrap sample model were determined. Calculated calibration coefficients for each cycle were saved throughout the Monte Carlo simulations to develop distributions that would describe the variability in various factors, such as laboratory test results, thickness, stiffness, etc.

All distributions for the bootstrap model coefficients for all the mix types converged to normal distributions because sufficiently large numbers of independent random coefficients (10,000) were calculated from the bootstrap distributions. This phenomenon can be explained by central limit theorem in probability theory (Rice, 1995).

4.4.3 *Evaluation of construction variability*

While rutting performance of asphalt concrete layers is highly sensitive to the levels of traffic loads and temperatures, rutting can also be a direct result of high variability in material properties and their distribution during the construction. Gradation, binder content, in-place compaction (density) and air-void content are the major material properties that affect the rutting performance of the pavements. In this study, it is assumed that the effects of variability in these properties can be simulated using the stiffness variability. FWD test results were used to determine the spatial variability in layer stiffnesses (Bejarano et al., 2005). FWD tests were conducted at the end of

construction of the asphalt concrete layer at 22.2 kN, 40 kN and 60 kN loads. FWD testing was conducted every 2 meters along five 80 meter lines at different temperatures with the purpose of studying the effect of temperature on the behavior of the pavement. The data do not include the damage produced by accelerated pavement testing on the six HVS sections. Moduli was calculated from FWD deflections by using the computer program ELMOD 5.0 (Dynatest International, 2001). The backcalculation routine was run assuming a non-linear subgrade and no bedrock. The non-linear parameter would consider any non-linearity including bedrock and water table locations. For unbound layers, subgrade and aggregate base, lognormal distribution functions were observed to provide best fits to the distributions of backcalculated stiffnesses (Figure 4.3a, b).

Stiffnesses for each unbound layer were randomly selected from these lognormal distributions throughout the Monte Carlo simulations for rutting performance prediction. Lognormal distributions are defined by $\text{mean}_{\log}$ (mean of the logarithm with base 10 of stiffness vector) and $\text{stdev}_{\log}$ (standard deviation of the logarithm with base 10 of stiffness vector) parameters:

$$\text{mean}_{\log} = \frac{1}{N} \sum_{i=N}^{i=1} \log(x_i) \qquad (4.4)$$

where

N = sample size

x_i = variable (stiffness)

$$\text{stdev}_{\log} = \frac{1}{N} \sqrt{N \sum_{i=N}^{i=1} \log(x_i)^2 - \left(\sum_{i=N}^{i=1} \log(x_i) \right)^2} \qquad (4.5)$$
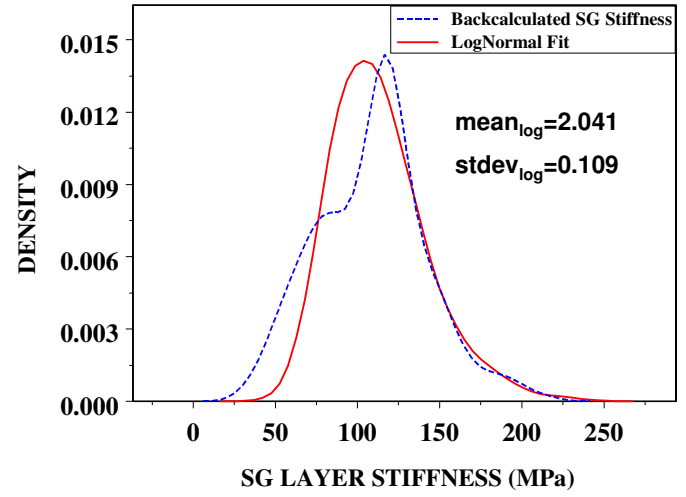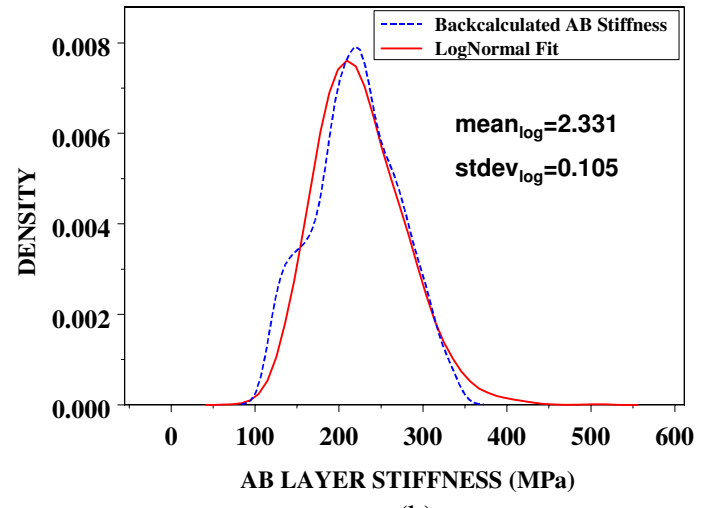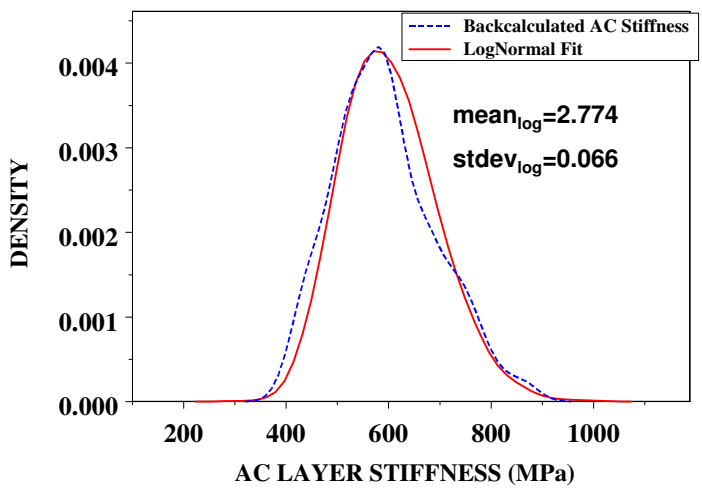
Figure 4.3 Lognormal distributions fitted to backcalculated layer stiffnesses (a) SG (subgrade) layer (b) AB (aggregate base) layer (c) AC (asphalt concrete) layer.

To determine the variability in existing AR4000 asphalt concrete layer stiffnesses, results of the FWD tests conducted at high temperatures (higher than 35°C) were used. FFST results were modeled by elastic modulus master curve application methodology (Coleri et al., 2008) to develop master curves that can reflect the effect of temperature and loading time on asphalt concrete stiffness. By using these master curves, all backcalculated stiffnesses at various temperatures were transformed to their equivalent at 50°C, which is the target temperature for HVS testing. The resulting distribution was fit by lognormal distribution function to determine its COV ($stdev_{log}/mean_{log}$). Calculated COV was assumed to represent the stiffness variability for all asphalt concrete layers. Stiffness of asphalt concrete layers (overlay and underlying asphalt concrete) for the corresponding repetition intervals were determined by integrating master curves with measured temperatures and loading times for a specific repetition interval. Lognormal distribution was formed using the average of these stiffnesses as the average for the lognormal distribution with previously calculated COV. For each Monte Carlo cycle, a number was randomly selected from this lognormal distribution and all stiffnesses calculated for all repetition intervals of the HVS test were multiplied by the ratio of this number to the average stiffness. By this means, the effect of stiffness variability was simulated without ignoring the effect of temperature on the stiffnesses.

The effects of thickness variability were also included in Monte Carlo simulations using the data from cores taken at various locations of HVS test sections. It was observed that distributions for layer thicknesses can be most effectively described by normal

distribution functions. Standard deviation and mean thickness values for all layers of the HVS test sections were given in Figure 4.1.

4.4.4   *Determination of required number of Monte Carlo cycles*

It is always of great importance to determine the required number of cycles that will be used for Monte Carlo simulations because of the high computational cost. The changes in calibration coefficient distributions as a function of the number of cycles must be determined. For this reason, 20,000 cycles were performed for the calibration of the rutting model for HVS test section 580RF. It was observed based on the results of the simulations that after 5,000 Monte Carlo cycles, the changes in the shapes of the distributions, which were evaluated using the percentile values, were negligible. Figure 4.4 shows the distributions of the calculated calibration coefficients for cases developed by performing different numbers of Monte Carlo cycles. In this study, 5,000 Monte Carlo cycles were performed to develop distributions for calibration coefficients for each case because this number provides an acceptable level of precision with reasonable computational cost.
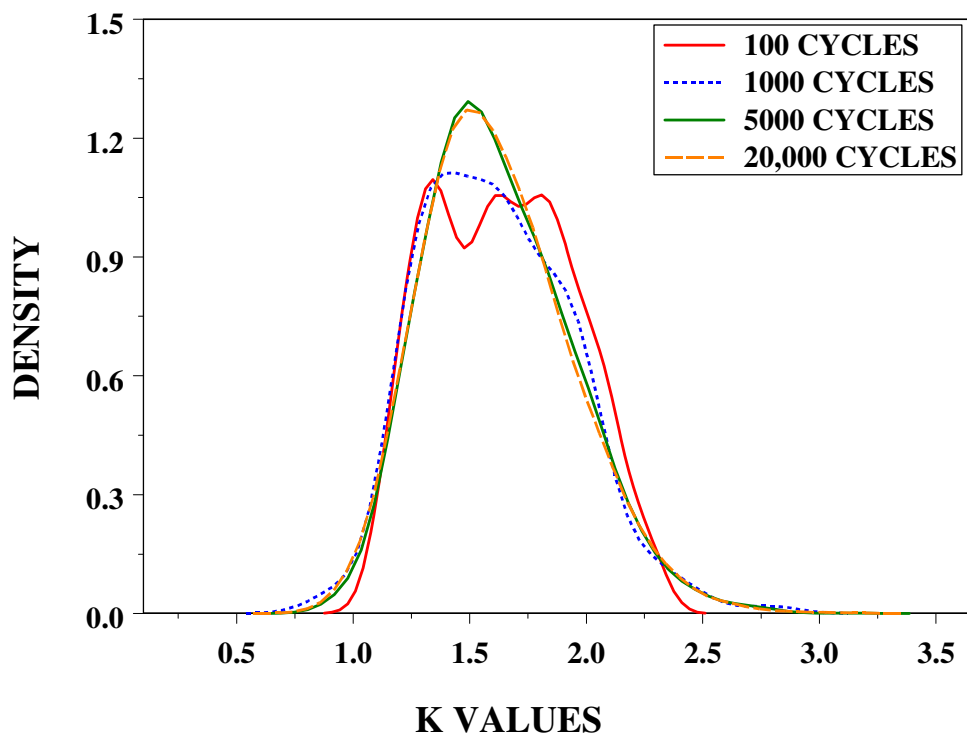
Figure 4.4 Comparison of the distributions of calculated calibration coefficients (K values) for cases developed by performing different numbers of Monte Carlo cycles.

4.5   CASES ANALYZED FOR VARIABILITY EVALUATION

The effects of construction, laboratory test results and performance variability on the distribution of calibration coefficients were determined by analyzing six different cases (Table 4.2). The effects of construction variability were simulated using predetermined stiffness and thickness distributions for each layer. Laboratory variability is included by using model coefficient distributions developed by the bootstrapping method. In Cases 1 and 2, data from the 13 stations were randomly selected at each repetition of the Monte Carlo simulations to evaluate their effect on the distribution of calibration coefficients.

Table 4.2 Cases analyzed for variability evaluation

Case number	Construction variability	Laboratory variability	Performance variability	Output form
1	NO	YES	YES	K value distribution
2	NO	NO	YES	13 K values
3	NO	YES	NO	K value distribution
4	NO	NO	NO	1 K value
5	YES	YES	NO	K value distribution
6	YES	NO	NO	K value distribution

NOTE: K value = calibration coefficient (Equation [4.3])

Because performance variability is not independent from construction variability and it is likely to be a result of the construction variability in thickness and stiffness for each pavement layer, cases with both construction and performance variability were not included in the analysis (Table 4.2). However, because the effects of performance and construction variability were individually analyzed in Case 1 and Case 5, respectively, the ability of construction variability to define performance variability can be determined by comparing calibration coefficient distributions for these two cases. Similarly, different cases from Table 4.2 were separately compared to identify their effects on predicted rutting performance variability through their influence on the calibration coefficient, K, in equation (4.3). Cases used for that comparison are given as follows:

- *The effect of performance variability:* Compare distributions for *Case 1 and Case 3*

- *The effect of laboratory test results variability:* Compare distributions for *Case 5* and *Case 6*

- *The effect of construction variability:* Compare distributions for *Case 3* and *Case 5*

- *The ability of construction variability to define performance variability:* Compare distributions for *Case 1* and *Case 5*

4.6   SUMMARY OF RESULTS FOR ALL HVS TEST SECTIONS

Monte Carlo simulations were performed for the six cases described above for all HVS test sections. Distribution plots illustrating the variation of calibration coefficients for each case and the effect of performance, construction and laboratory test results variability on predicted rutting performance are shown in Figure 4.5. Because the number of data points for Case 2 and Case 4 are not enough to illustrate by distributions, calibration coefficients for these cases are shown by vertical lines. Because variability for Case 3 is relatively lower than distributions for all other cases, part of the distribution greater than 2.5 is not shown in Figure 4.5 to better emphasize distributions for other cases. However, peak density values for Case 3 are given in corresponding plots of all HVS test sections to indicate the variability level for the distributions.

The two sample Kolmogorov-Smirnov test is used to compare the calibration coefficient distributions for the given cases (Insightful, 2001). Suppose F_1 and F_2 are two distributions. Possible hypotheses and alternatives concerning these distributions are:

H_0: $F_1(x) = F_2(x)$

H_A: $F_1(x) \neq F_2(x)$

Decision rule: Reject H_0 if p-value<0.05

Fail to reject H_0 if p-value≥ 0.05

Table 4.3 shows the results of the tests (p-values) for all four calibration coefficient distribution comparisons. All cases are compared based on the results of this statistical test in the following sections.

Table 4.3 The Kolmogorov-Smirnov test p-values for distribution comparison

Compared distributions	The Kolmogorov-Smirnov test p-values					
	580RF	581RF	582RF	583RF	584RF	585RF
Case 1 – Case 3	0.00	0.00	0.00	0.00	0.00	0.00
Case 5 – Case 6	0.93	0.97	0.91	0.99	1.00	1.00
Case 3 – Case 5	0.00	0.00	0.00	0.00	0.00	0.00
Case 1 – Case 5	0.08	0.00	0.37	0.14	0.18	0.33
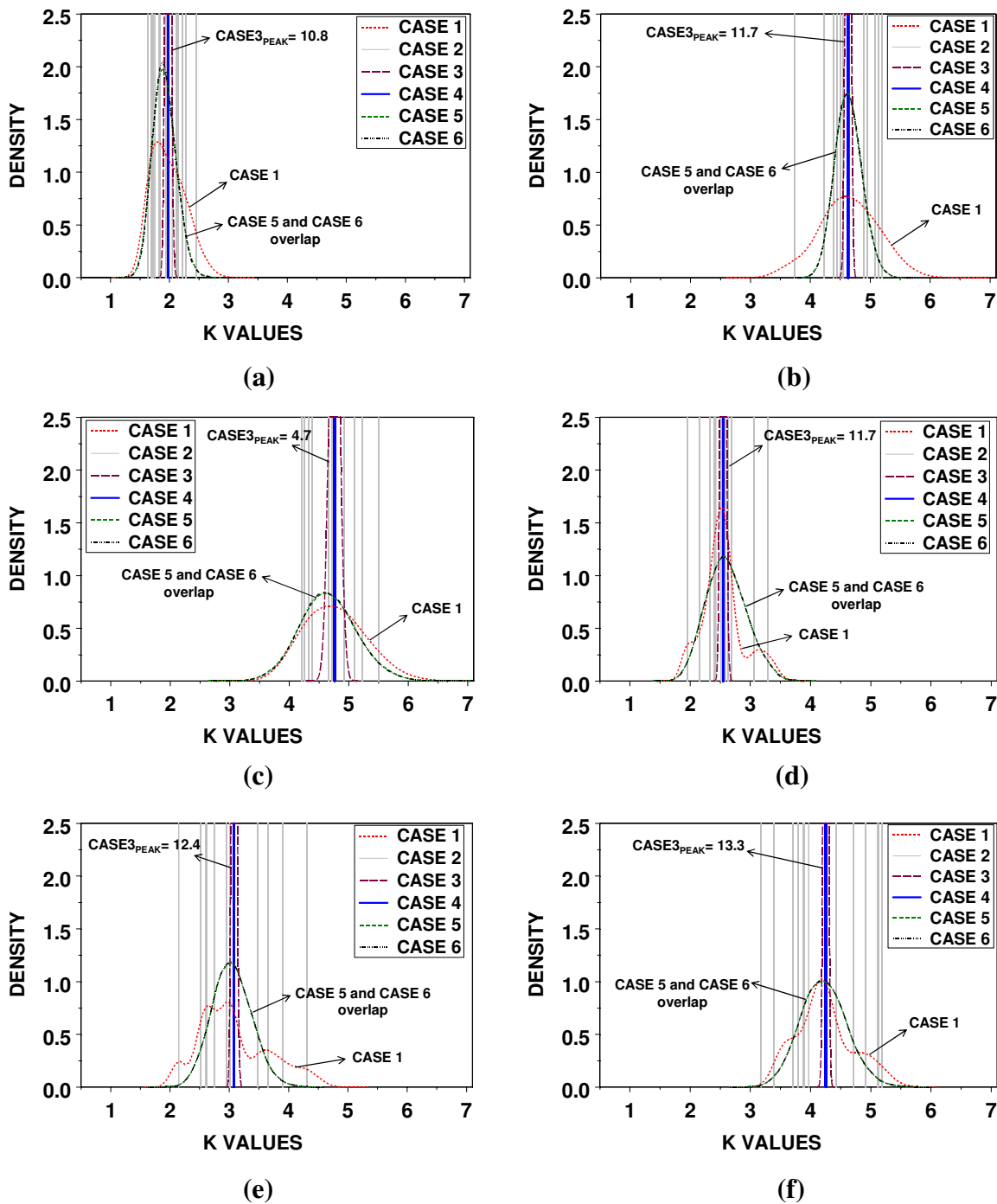
Figure 4.5 Distribution plots illustrating the variation of calibration coefficients for equation (4.3)(a) Section 580RF (MB15), (b) Section 581RF (RACG), (c) Section 582RF (AR4000), (d) Section 583RF (MB4), (e) Section 584RF (MB4), (f) Section 585RF (MAC15).

Note: Because the number of data points for Case 2 and Case 4 are not enough to illustrate by distributions, calibration coefficients for these cases are shown by vertical lines.

4.6.1   The effect of performance variability

Distributions for Case 1 and Case 3 should be compared to evaluate the contribution of performance variability to overall variability of calibration coefficients. Because only the variability in laboratory test results was simulated in Case 3, distributions for Case 1 will always have higher standard deviations due to the added variability introduced by performance variability. It can be inferred from Figure 4.5 that peak density for Case 3 distributions are 5 to 20 times higher than the peak for Case 1 distributions for all HVS test sections. This result indicates that performance variability in the HVS test sections is causing high levels of variability in predicted rutting performance, as expected. In addition, results of the Kolmogorov-Smirnov test for Case 1 and Case 3 distributions show that p-values for all sections are equal to zero (Table 4.3). This result suggests that two distributions are significantly different.

4.6.2   The effect of laboratory test results variability

Construction and laboratory test results variability were included in Case 5 by Monte Carlo simulations whereas only construction variability was included for Case 6. Due to the added variability introduced by the laboratory test results, Case 5 will always have higher variability when compared to Case 6. However, this added variability caused negligible difference between distributions of Case 5 and Case 6 for all HVS test sections according to the Kolmogorov-Smirnov test with all p-values significantly higher than 0.05 (Table 4.3). Thus, the precision of laboratory test results do not appear to have a considerable effect on predicted rutting performance because the high level of

construction variability, similar to that of field sections even over a distance of only 6 m, is masking the effect of laboratory test results variability.

Case 3 also illustrates the effects of variability only due to laboratory test results. Relatively low standard deviations for Case 3 distributions point out that the contribution of laboratory test results variability to overall variability is lower than other sources of variability. However, rutting predictions performed by using the maximum point of Case 3 distributions can be 7 percent to 12 percent higher than predictions performed with the minimum calibration coefficient.

4.6.3   The effect of construction variability

The effect of construction variability on predicted rutting performance can be determined by comparing Case 3 and Case 5. Due to the added variability introduced by the construction variability, Case 5 will always have higher variability when compared to Case 3. It can be inferred from Figure 4.5 that peak of Case 3 distributions are 5 to 13 times higher than the peak for Case 5 distributions for all HVS test sections. In addition, results of the Kolmogorov-Smirnov test for Case 3 and Case 5 distributions show that p-values for all sections are equal to zero (Table 4.3). This result suggests that two distributions are significantly different. Similar to the performance variability, this result indicated that construction variability is causing high levels of variability in predicted rutting performance.

4.6.4   The ability of construction variability to define performance variability

It was determined that construction and performance variability are the two major factors that affect the overall variability in the calibration coefficients for predicted rutting performance. However, because these two sources of variability are not independent of each other, only one of them should be included in Monte Carlo simulations to avoid exaggerated variability distributions.

In an ME design procedure it should be theoretically possible to simulate performance variability by construction variability. In other words, variability distributions for Case 1 and Case 5 should overlap if performance variability can be perfectly considered by construction variability. It can be observed from Figure 4.5 that distributions for Case 1 and Case 5 are close to each other for sections 580RF, 582RF, 583RF, 584RF and 585RF with the Kolmogorov-Smirnov test p-values higher than 0.05 (Table 4.3). This result suggests that variability in measured rut depths can be effectively explained by stiffness and thickness variability for these sections.

Because stiffness distributions were determined by using FWD test results from various locations of the test sections and thickness distributions were determined by using cores from these locations, construction variability can be accepted to reflect possible in-situ variability for HVS test sections. However, results of this study should also be validated by performing a field performance study. Based on the results of field study, the levels of variability in pavement rutting performance for a highway section can be identified. In addition, the effectiveness of using stiffness and thickness variability to evaluate overall

in-situ performance variability can be determined. A reliability based design procedure can be developed by combining the results of this field performance study with the results given in this chapter.

4.7   RELIABILITY

One very simple definition of reliability is that it is one minus the probability of failure (Timm et al., 2000). Timm et al. (2000) expressed this definition by

$$R = probability \ [N>n] \hspace{4cm} (4.6)$$

where N is the number of allowable repetitions, and n is the actual number of repetitions.

In this study, the level of reliability was determined using the cumulative frequency distributions of Case 5 calibration coefficients. Cumulative probabilities for these distributions correspond to different levels of reliability for design. This approach is illustrated in Figure 4.6 for HVS test section 584RF. Calibration coefficients for 99%, 95%, 50%, 5% and 1% reliability levels were determined from the cumulative frequency distribution developed by Monte Carlo simulations (Figure 4.6[a]). Predicted rutting performance curves for these reliability levels are given in Figure 4.6(b). It should be noted that Monte Carlo simulations were performed during the calibration process. Thus, rut depths for different reliability levels can be predicted without performing any computer intensive calculation within the design software.
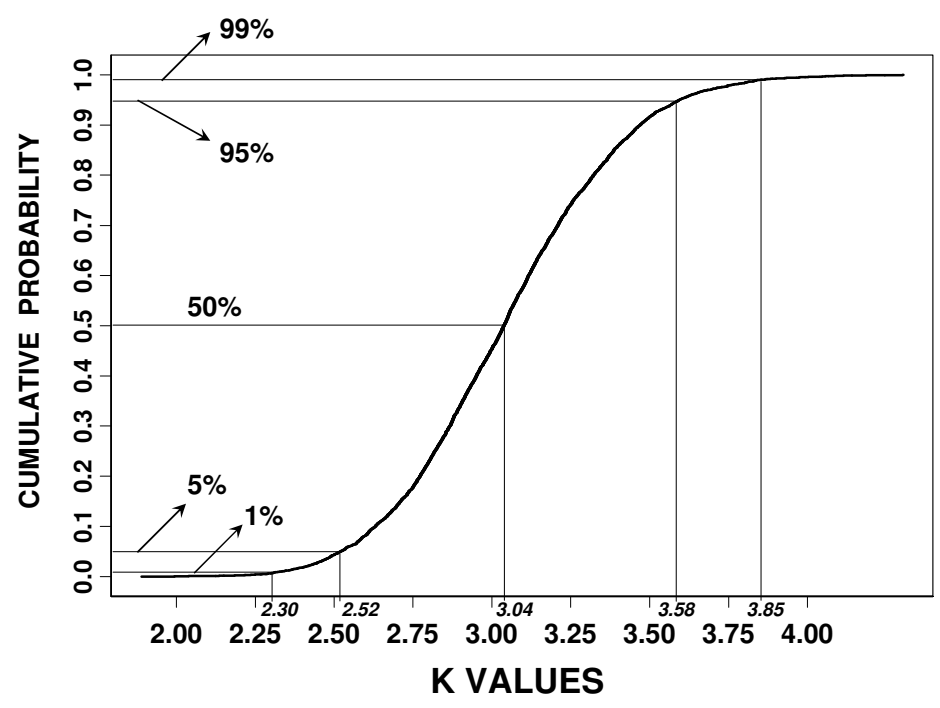
(a)
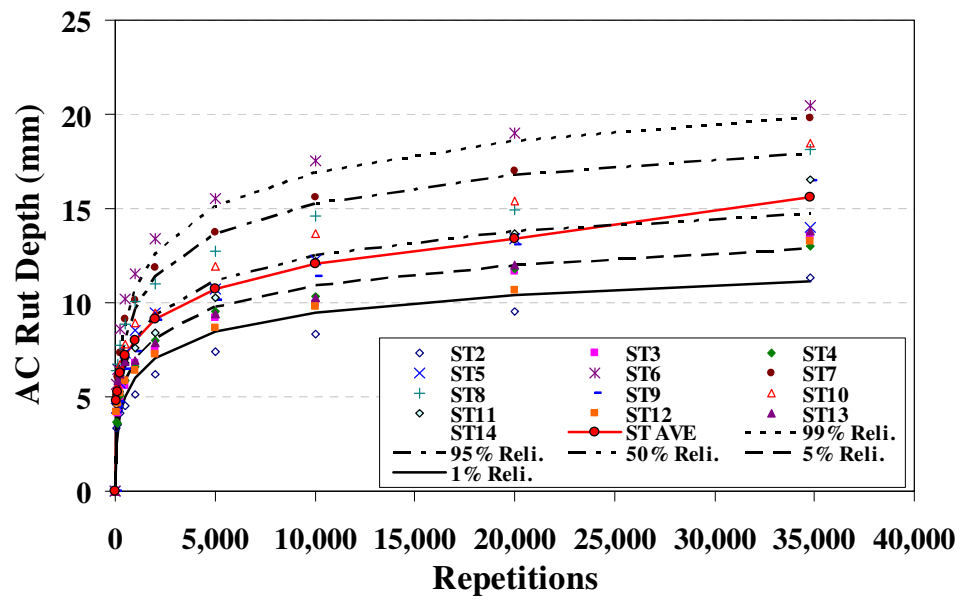
(b)

Figure 4.6 Application of reliability approach for Section 584RF (a) Cumulative frequency distribution for Case 5 (b) Predicted rutting performance for different reliability levels, (ST=Station, AVE=average, Reli.=Reliability level).

4.8 FINDINGS AND CONCLUSIONS

In this study, a reliability based design procedure is developed by evaluating the reliability based on the variability in laboratory test results, layer thicknesses, stiffnesses and measured in-situ performance. The importance of various variability inputs on predicted performance was tested by running Monte Carlo simulations for six different cases and comparing predicted variability based on the distributions of calculated calibration coefficients for each case. Key findings are as follows:

1. Variability in measured rut depths (performance variability) of the HVS test sections causes high levels of variability in the calculated calibration coefficients.

2. Computational cost for running excessive number of Monte Carlo cycles should be avoided by determining the optimum number of cycles that give acceptable level of accuracy. In this study, it was observed that after 5,000 Monte Carlo cycles, the changes in the shapes of the distributions, which were evaluated by using the percentile values, were negligible.

Major conclusions of this study are given as follows:

1. Distributions of calibration coefficients calculated by using measured rut depths (performance variability) are very similar to calibration coefficient distributions calculated by using thickness and stiffness (construction) variability for sections 580 RF, 582RF, 583RF, 584RF and 585RF whereas performance variability is significantly higher than construction variability for section 581RF. This result

suggests that variability in performance can be effectively predicted by using the variability in thickness and stiffness for HVS test sections.

2. Precision of laboratory test results did not have much effect on predicted rutting performance when the effect of laboratory variability is simulated with construction or performance variability. In other words, high level of variability in measured performance, thickness and stiffness mask the effect of laboratory variability on calculated calibration coefficient distributions. However, rutting predictions performed by using maximum point of Case 3 (only laboratory variability) distributions can be 7 percent to 12 percent higher than predictions performed with the minimum calibration coefficient.

3. Distributions of calibration coefficients determined by performing Monte Carlo simulations can be effectively used as inputs to estimate the reliability of pavement rutting design. Because Monte Carlo simulations were performed only during the calibration process, rut depths for different reliability levels can be predicted without performing any computer intensive calculation within the design software.

Although the reliability approach proposed in this study is developed by using RSST-CH laboratory test results and rutting models used in CalME, the general procedure can be applied to any pavement design software for any type of distress.

CHAPTER 5   DEVELOPMENT OF MICROMECHANICAL FINITE ELEMENT MODEL FROM COMPUTED TOMOGRAPHY IMAGES FOR SHEAR PERFORMANCE SIMULATION

5.1   INTRODUCTION

Asphalt concrete is a composite material which consists of aggregates, air-voids and mastic. All of the constituents of asphalt concrete are large enough to be regarded as continua and the aggregate and mastic are bonded together at their interfaces. Performance and physical properties of asphalt mixtures are controlled by the properties of the aggregate (shape, texture, gradation, modulus, etc.), properties of the asphalt binder (complex modulus, cohesion, etc.), asphalt-aggregate interactions and the distribution of air voids (Dai and You, 2007). The mastic phase consists of fine aggregates, sand and other particles (rubber, polymer, etc.) embedded in asphalt binder. The mastic part appears to be the most challenging phase to model due to its complex properties that depend on loading time and temperature. Dai and You (Dai and You, 2008) modeled the mastic properties by using the results of creep tests that were conducted with mastic

samples. Dai (2010) developed a microstructure-based computational approach for stone based materials to predict both phase angle and complex modulus under cyclic loadings with different frequencies. Papagiannakis et al. (2002) also developed a 2D micromechanical FE model to predict dynamic shear modulus and phase angle for asphalt mixtures tested with the Superpave shear tester. Rothenburg et al. (1992) also introduced a discrete element model for asphalt mixtures to evaluate pavement rutting performance. The model evaluated the effects of both aggregate-binder interaction and inter-granular interactions. Li et al. (1999) developed a two-phase micromechanical FE model to predict asphalt mixture elastic modulus based on measured aggregate and mastic properties.

Asphalt mixtures exhibit different performance characteristics at different temperature levels. Asphalt mixtures act as continuum materials at low temperatures when the stiffness of the asphalt binder and the aggregate are similar (Weissman et al., 1999). However, at high temperatures, i.e. the critical conditions for rutting deformation accumulation, the aggregate can be two orders of magnitude stiffer than the asphalt binder. As a result, as temperature increases or load duration decreases the asphalt concrete pavement layers start to act as particulate structures where the contact points between the aggregates become more important in terms of rutting deformation accumulation (Weissman, 1997). Therefore, at high temperatures permanent deformation accumulation mechanism in asphalt concrete layers predicted by using continuum mechanics may not reflect the actual mechanism under in-situ truck traffic. Thus, interactions between the particles and the effect of binder viscosity on the asphalt mixture performance should be evaluated to identify the rutting performance at high temperatures.

Kandhal and Mallick (2001) showed that aggregate shape, surface texture, gradation and skeletal structure significantly affect asphalt mixture rutting performance at high temperatures. Thus, micromechanical models that are developed by preserving the actual aggregate geometry and surface texture must be used to simulate laboratory tests in order to identify this proposed effect for different mix types. Zhu and Nodes (2000) investigated the effects of aggregate angularity on asphalt pavement response and concluded that increased angularity significantly increases the stiffness of the asphalt mixture. Dai and You (2007) used 2D microstructures of asphalt concrete that were obtained by optically scanning smoothly sawn asphalt mixture specimens to predict their mixture complex and relaxation modulus at -20°C. Dai and You (2007) preserved the actual 2D aggregate shape and angularity for particles larger than 1.18 mm to identify their effects on predicted material properties. You et al. (2008) developed a 3D discrete element model by combining a number of 2D discrete element models to determine the improvement in predictions caused by the realistic interactions in the third dimension. Although the 3D model resulted in better predictions for mixture modulus at temperatures lower than 0°C, actual aggregate geometry and texture and its effects on predicted modulus were not simulated. You et al. (2009) compared predicted asphalt mixture stiffnesses at temperatures -18°C, -6°C and 4°C with those predicted by 2D and 3D discrete element models generated from X-ray CT images. Results of the study indicated that 3D prediction results are very close to the measured data for all loading frequencies and temperatures. It was further concluded that 2D models under predicted the asphalt mixture stiffness in all cases.

In the study presented in this chapter, the micromechanical FE method was used for shear modulus simulation for asphalt mixtures at high temperatures. The micromechanical FE model was developed to simulate the conditions for a standard frequency sweep at constant height (FSCH) test (AASHTO, 2003). Predicted shear modulus values at various loading frequencies and temperatures were compared to laboratory measured values to evaluate the effectiveness of the developed model. Prediction accuracies of 2D and 3D micromechanical models were determined separately to identify the applicability of each model type for rutting performance prediction. Because the 3D model was developed from X-ray CT images taken at a 1 mm interval distance, geometric characteristics of the aggregates in the finite element model appeared to closely match with the aggregates of the actual asphalt concrete sample. The FE model developed in this study will be the first 3D micromechanical model used for evaluating shear resistance of asphalt mixtures at high temperatures. This model will be used for rutting performance evaluation of different asphalt mixtures under various temperatures and loading frequencies.

5.2 OBJECTIVES AND SCOPE

The primary objective of this study is to develop a micromechanical FE model from X-ray CT images for shear modulus simulation of asphalt mixtures at high temperatures. The 3D geometry of the aggregate was preserved during model development by using high pixel resolution X-ray CT images reconstructed at every 1 mm. The asphalt mixture was divided into three phases, air-voids, mastic and aggregates, by image processing and meshed for FE simulations. The aggregate and mastic phases were meshed so that they

share nodes on aggregates. The air-void volumes were left as empty voids in the model because they would not be able to resist any kind of stress applied throughout the simulation. Elastic and viscoelastic assumptions were used for modeling aggregate and mastic subdomains, respectively. Shear modulus predictions for 2D and 3D models were compared to measured values to determine the effectiveness of each model type for the simulation of the FSCH test.

The study presented in this chapter focuses on the results for model development and validation stages. However, with the proposed model, deficiencies of Superpave shear tester can be identified and modifications can be proposed based on the results of further simulations. The effects of the missing shear couple (Weissman et al., 1999) and confining pressure on measured mixture performance can be investigated by using the FE model developed in this study. In addition, the effects of specimen size and geometry on predicted mixture performance can be determined to identify possible deficiencies in the current AASHTO T 320 (2003) testing procedure.

5.3 MATERIALS

Two asphalt mixture types were used in this study, a dense-graded mixture with PG 64-28 polymer modified (PM) binder and a gap-graded mixture with asphalt rubber binder (PG 64-16), RHMA-G. Both mixes met Caltrans specifications (Caltrans, 2006a; Caltrans, 2006b) for both mix and binder. Nominal maximum aggregate sizes (NMAS) for the PG 64-28 PM and RHMA-G mixtures were 19 mm and 12.5 mm, respectively.

Table 5.1 shows the aggregate gradations, asphalt binder contents and air-void contents of the asphalt mixtures and the mastic used in this study. NMAS for the mastic samples was selected to be 1.18 mm because particles smaller than the 1 mm scanning interval may not be captured as aggregates during the X-ray CT imaging process. The air-void content for the mastic was assumed to be zero because of the high binder content and small aggregate size.

Table 5.1 Aggregate gradations for asphalt mixtures and mastic

Sieve size (mm)	Percentage passing (%)			
	Mix PG 64-28 PM	Mastic PG 64-28 PM	Mix RHMA-G	Mastic RHMA-G
25.4	100	100	100	100
19	99	100	100	100
12.5	87	100	98	100
9.5	74	100	84	100
4.75	50	100	34	100
2.36	36	100	21	100
1.18	27	75	14	67
0.6	21	58	10	48
0.3	16	44	7	33
0.15	10	28	5	24
0.075	6.2	17.2	3.5	16.7
Asphalt binder content (%)	5.10	11.6	7.6	16.7
Air void content (%)	4.2	0.0	10.0	0.0

Shear frequency sweep specimens were prepared for asphalt mixture and mastic materials for modeling. Field-mixed, laboratory-compacted (FMLC) specimens were prepared adjacent to a construction site for Heavy Vehicle Simulator (HVS) test sections by using jigs, molds, and a rolling-wheel compactor. Loose mix was taken from the trucks with a skip loader immediately prior to it being tipped into the paver and then dumped next to

the preparation area. The required volume of material, based on the densities determined earlier in the laboratory, was weighed and then compacted into molds at the same temperatures as those recorded on the HVS test sections. Asphalt mixtures used in this study were sawed from those ingots. Binders and aggregates for mastic sample preparation were taken from the plant which produced the asphalt mixtures. Because NMAS for mastic samples was 1.18 mm and the binder contents are very high in the mastic, mechanical compaction was not performed. However samples were manually compacted in the laboratory with small size 7 kg cylinders.

Asphalt mixtures and mastic samples for shear testing had rectangular prism shapes. The width and length of the asphalt mixture samples were 130 mm while the height was 48 mm. Standard cylindrical specimens with 150 mm diameter were not used in this study to avoid complications related to the variable length-to-height ratio along the circular surface area (Weissman et al., 1999). In addition, it would not be possible to develop circular 2D numerical shear samples due to the direction of applied shear load. The width and length for the mastic samples were selected to be 100 mm while the height was 15 mm. Aggregate modulus tests were not performed since the effect of aggregate stiffness on shear deformation would be negligible due to the effect of the low modulus values for the mastic at high temperatures. The aggregate modulus was assumed to be 55 GPa (You, 2003). It should be noted that aggregate modulus would have a significant effect on the asphalt mixture modulus when the testing temperatures are low (You et al., 2008).

5.4   GENERAL PROCEDURE FOR MODEL DEVELOPMENT

The general framework for the development of the micromechanical FE model is given in
Figure 5.1.
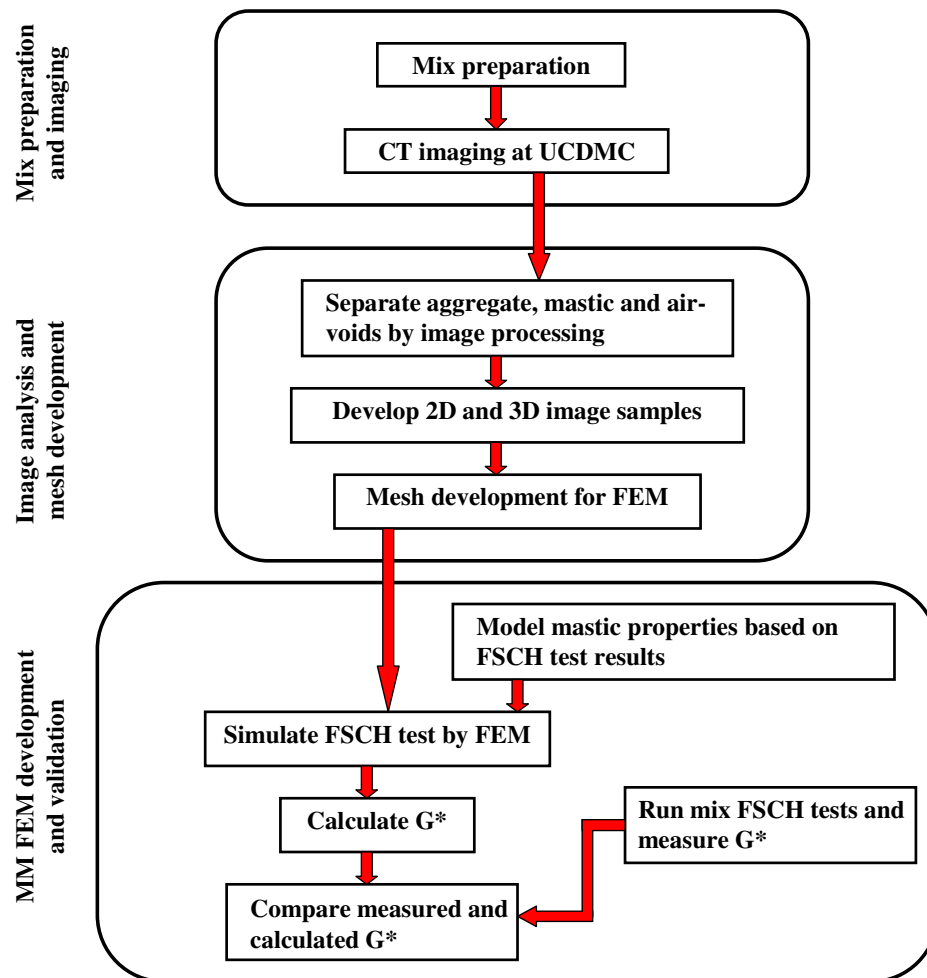
Figure 5.1 The general framework for the development of micromechanical FE model.

The steps followed for model calibration are as follows:

STEP 1: Asphalt mixture preparation and imaging

- Mix preparation: Prepare FMLC asphalt mixture samples and cut them to final dimensions.

- Mastic preparation: Prepare mastic samples for viscoelastic performance evaluation.

- Acquire the 3D internal structure of the asphalt mixture samples by X-ray CT imaging at the University of California Davis Medical Center (UCDMC).

STEP 2: Image analysis and mesh development

- Determine mixture air-void content by standard CoreLok method (AASHTO, 2009).

- Process the X-ray CT images based on the measured air void content to create the air void volumes.

- Determine aggregate threshold index (the intensity range for aggregate images) by analyzing the processed images.

- Subtract air void and aggregate domains from the complete image to obtain mastic domain.

- Exclude the air void domain from the mix (after exclusion, volume occupied by air voids will be empty).

- Create the high quality tetrahedral mesh for the aggregate and mastic domains while preserving the empty air void domain.

- Export the meshed structure to the FE modeling program.

STEP 3: Micromechanical FE model development

- Run mastic FSCH tests at 7 loading frequencies and 3 temperatures.

- Develop viscoelastic model for the mastic phase using mastic FSCH test results.

- Develop FE model for the asphalt mixture for the corresponding boundary conditions, material properties, loading type and temperature.

- Predict shear modulus (G*) at 7 loading frequencies and 3 temperatures that were used for mastic testing (21 simulations).

- Run asphalt mixture laboratory tests at 7 loading frequencies and 3 temperatures and measure G* for each test.

- Compare measured and predicted asphalt mixture G* values for both 2D and 3D models.

5.5 X-RAY CT IMAGE ACQUISITION, ANALYSIS AND MESH DEVELOPMENT

5.5.1 *Image acquisition and processing*

The internal structure of the asphalt mixture was measured by X-ray CT imaging at the University of California Davis Medical Center (UCDMC). The X-ray CT scanner reconstructs the 3D spatial distribution of the attenuation coefficients of the materials that were scanned. Three dimensional images of the specimen are generated by combining a series of 2D images generated by the scanner. The quality of the 3D image depends on

the X-ray CT image resolution. In this study, horizontal planar images were acquired at 1 mm intervals while the resolution cell for the other two dimensions was determined to be 0.24 mm. At each sampling point within the sample volume, each pixel from a CT image measures a value that is related to the density and atomic number of the material at that particular point. These measured values are then converted to grayscale values (Simpleware, 2010a). The gray scale intensities for the aggregates, air voids and mastic range from -1000 to 3095, but these values were rescaled to the range from 0 to 255. Because aggregates are denser than mastic and air voids, they occupy the higher portion of the intensity scale. On the other hand, low density air voids are at the lowest intensity portion while mastic intensity is between aggregate and air void intensities.

Simpleware software (Simpleware, 2010a) was used in this study to create masks for each domain based on measured intensity groups. Air void percentages for each asphalt mixture are shown in Table 5.1. The total volume of the asphalt mixture sample was calculated for the complete intensity range, 0 to 255. The upper limit for the air void intensity range was determined by trial and error to match the measured air void contents. The range for the PG 64-28 PM mix was determined to be 0-124 for a specimen with a calculated air void content of 4.3 % while the range for RHMA-G mix was 0-99 with a calculated air void content of 10.0 %. These air void contents are close to those measured with the CoreLok test (Table 5.1). The volumes for aggregate and mastic were calculated to be 58.2% and 37.5% for the PG 64-28 PM mix, respectively. For the RHMA-G mix, aggregate and mastic volumes were calculated to be 50.2% and 39.8%, respectively.

After the thresholds for each domain were determined, masks with different colors were assigned to clearly visualize the boundaries between each domain. Because densities for the aggregates and mastic were close to each other at some locations that are close to the aggregate boundaries, aggregates appeared to be connected at those boundaries. This segmentation problem may create a 3D structure in which all the aggregates are interconnected at the interface. This unrealistic material structure will result in over prediction of stiffness as a result of those strong bonds. In order to avoid that problem, images were first filtered with the software and then manually processed to separate mastic from aggregate. The 3D image for the PG 64-28 PM mix obtained after image processing is given in Figure 5.2 with the 3D air void distribution. In order to present the achieved 3D image accuracy in terms of aggregate shape, texture and angularity, four aggregates were selected from the processed 3D image structure and compared to the aggregates extracted from the actual tested laboratory sample. Figure 5.3 shows the comparisons between 3D virtual image structures and actual shapes for those four aggregates. It can be observed that the shapes of the 3D aggregate structures closely match with the actual shapes of the aggregates. For 2D model development, three slices were randomly selected from the 3D structure for each mix type. Predictions for the three 2D models were averaged and compared to 3D model simulation results and laboratory measured shear modulus values.

(a)   (b)
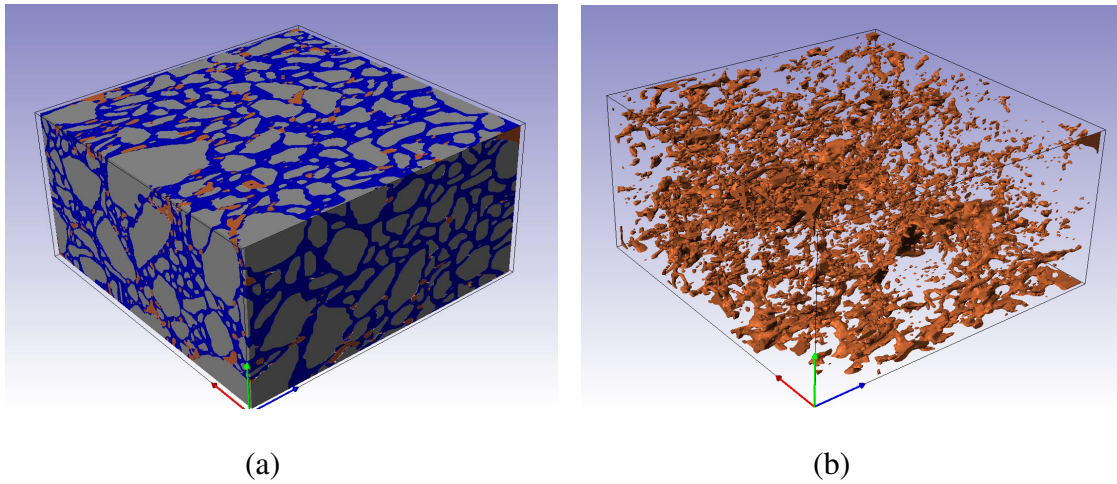
Figure 5.2 Three dimensional image of asphalt mixture PG 64-28 PM generated from X-ray CT images (a) Image with all three domains, air void, mastic and aggregate (b) Air void distribution within the asphalt mixture.
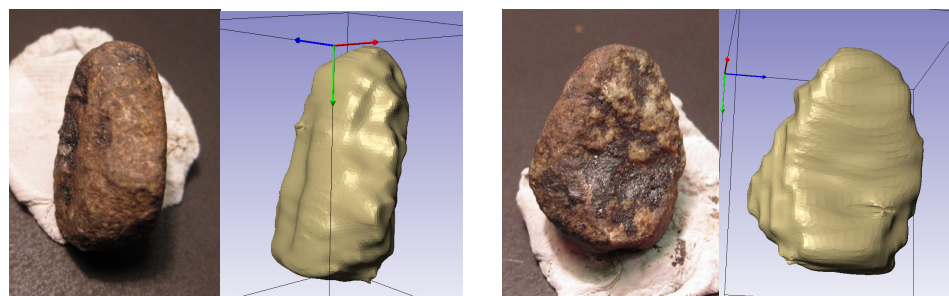
(a)
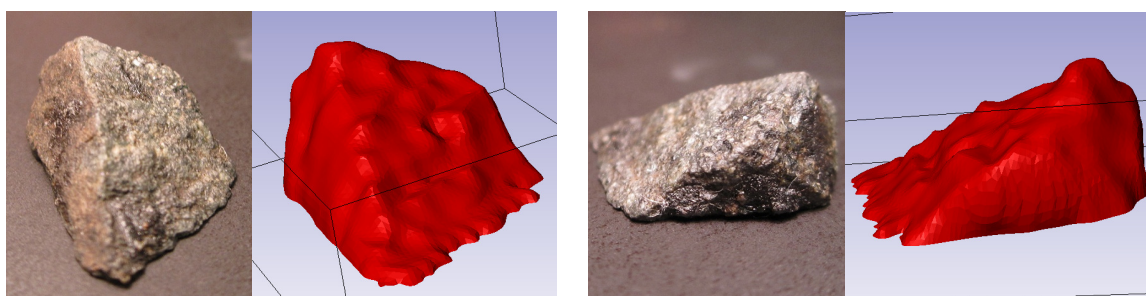
(b)
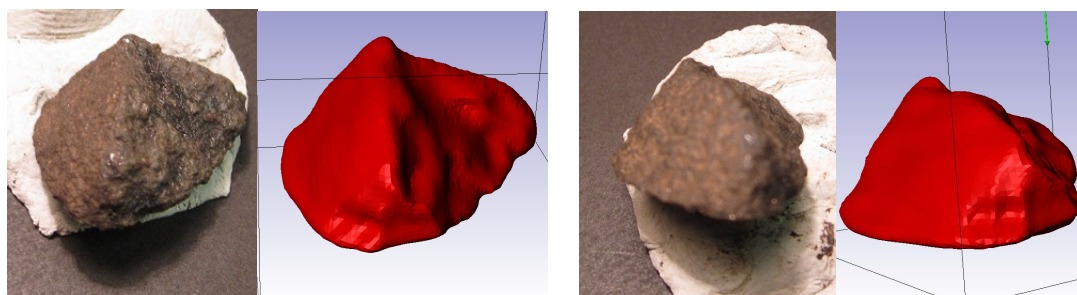
(c)
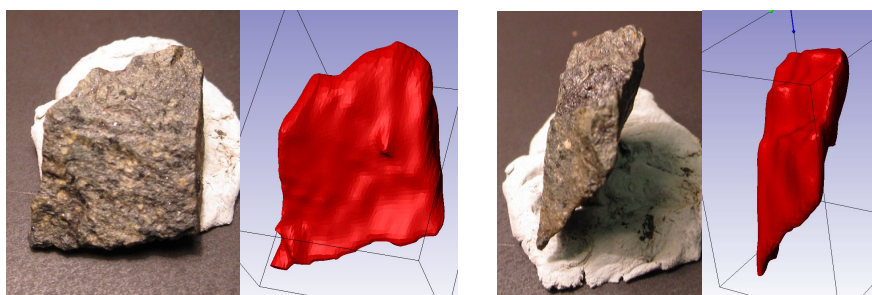
(d)

Figure 5.3 Comparisons between 3D virtual image structures and actual shapes for four aggregates (a) Aggregate 1 from two perspectives (b) Aggregate 2 from two perspectives (c) Aggregate 3 from two perspectives (d) Aggregate 4 from two perspectives.

5.5.2   *Mesh development*

The mask created for the air void domain was excluded from the material structure because it has no stiffness. Before meshing, both the aggregate and the mastic domains were slightly smoothed while preserving the element quality and volume. This pre-smoothing stage allows the software to create more realistic meshes. High quality (triangles that are "as equilateral as possible") tetrahedral meshes were created for the aggregate and mastic domains while preserving the empty air void domain. The size of surface and volume elements were adjusted based on the topological complexity of the object. To ensure high quality triangulations, i.e. to generate equilateral triangles, surface optimization was also performed before the meshing procedure (Simpleware, 2010b). Figure 5.4 illustrates a 2D asphalt mixture structure before and after mesh generation. It can be observed that triangle elements in the mastic and aggregate domains are perfectly bonded on the boundaries (Figure 5.4b). Meshed structures were exported to FE analysis software ABAQUS (2004) for modeling.
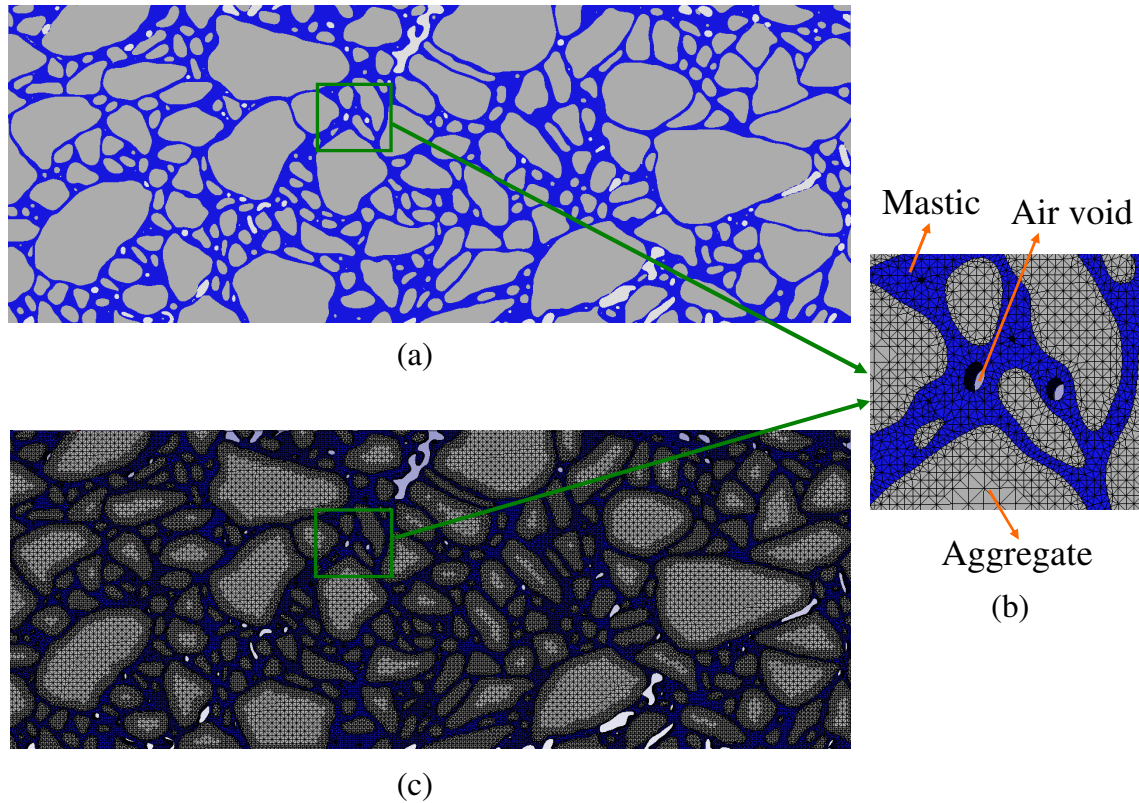
Figure 5.4 Two dimensional asphalt mixture (PG 64-28 PM) image before and after mesh generation (a) Before mesh generation (b) Enlarged image with all three domains (c) After mesh generation.

5.6   MICROMECHANICAL FE MODEL DEVELOPMENT

5.6.1   *Testing and viscoelastic model for asphalt mastic*

FSCH tests were conducted with mastic samples at 7 loading frequencies, 0.1 Hz, 0.2 Hz, 0.5 Hz, 1 Hz, 2 Hz, 5 Hz, and 10Hz, and 3 temperatures, 30°C, 40°C and 50°C under a controlled shear strain level of 0.2 %, with two replicates. It was observed that due to the small NMAS of mastic samples (1.18 mm), differences between replicate test results appear to be negligible.

The temperature dependency of the mastic was defined by using the Williams-Landel-Ferry (WLF) equation (William et al., 1955), given as follows:

$$\log(aT) = \frac{-C_1(T - T_{ref})}{C_2 + (T - T_{ref})} \tag{5.1}$$

where

aT = the time-temperature shift factor,

C_1 and C_2 = regression coefficients,

T_{ref} = the reference temperature, ($40^{o}C$ in this study), and

T = test temperature.

To optimize the regression coefficients C_1 and C_2, the shear modulus data were first fitted to a sigmoid function, in the form of (AASHTO, 2002):

$$\log(G(\xi)) = \delta + \frac{\alpha}{1 + \exp(\beta + \gamma \log(\xi))} \tag{5.2}$$

where

α, β, γ, δ = regression coefficients, and

ξ = reduced time.

Shift factors were calculated by fitting the measured shear modulus to the sigmoidal function (Equation [5.2]). One shift factor was calculated at each test temperature while the shift factor for the reference temperature ($40^{o}C$) was set at zero. The Excel Solver routine was used to optimize the regression coefficients α, β, γ, δ and shift factors for

temperatures 30°C and 50°C. Regression coefficients C_1 and C_2 were calculated by simply fitting the WLF equation to the calculated shift factors.

The generalized Maxwell-type viscoelastic model was used in this study to simulate the mastic time dependency. The schematic of the generalized Maxwell model is given in Figure 5.5. The model consists of two basic units, a linear elastic spring and a linear viscous dash-pot.
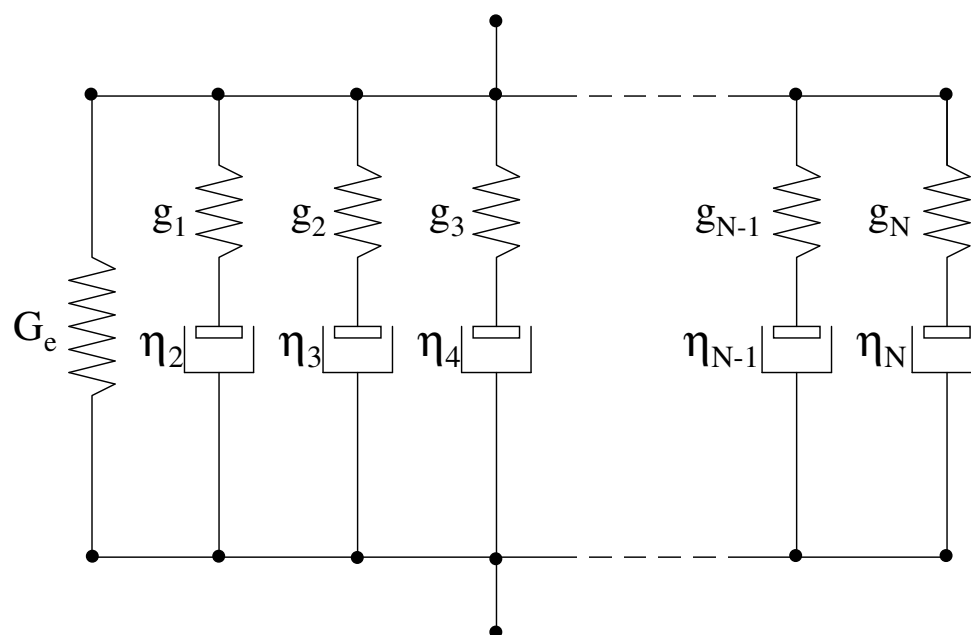
Figure 5.5 Schematic of the generalized Maxwell model.

Various combinations of these spring and dashpot units define the type of viscoelastic behavior. In this study, one spring and five Maxwell elements in parallel were used for the mastic model. Measured shear modulus (G*) values were separated into storage modulus [G'(ω)] and loss modulus [G''(ω)] components based on the measured phase angles (δ) using the following equations (Papagiannakis et al., 2002):

$$G'(\omega) = |G * (\omega)| \cos(\delta) \qquad (5.3)$$

$$G''(\omega) = |G * (\omega)| \sin(\delta) \qquad (5.4)$$

where

ω = loading frequency in rad/s,

$G*(\omega)$ = complex shear modulus in MPa, and

δ = phase angle between strain and stress.

Storage modulus and loss modulus can be expressed as follows (Baumgaertel and Winter, 1989):

$$G'(\omega) = G_e + \sum_{i=1}^{N} g_i \frac{(\omega\lambda_i)^2}{1 + (\omega\lambda_i)^2} \qquad (5.5)$$

$$G''(\omega) = \sum_{i=1}^{N} g_i \frac{\omega\lambda_i}{1 + (\omega\lambda_i)^2} \qquad (5.6)$$

where

N = number of Maxwell units,

G_e = equilibrium modulus,

g_i = relaxation strengths (spring constants of Maxwell units), and

λ_i = relaxation times.

$$\lambda_i = \frac{\eta_i}{g_i} \tag{5.7}$$

where

η_i = dashpot constants of Maxwell units (Figure 5.5)

By fitting equations (5.5) and (5.6) to measured G' and G" data, the parameters of a discrete relaxation spectrum can be determined. A genetic algorithm was used to optimize these model parameters (G_e, g_i and λ_i) by minimizing the calculated residual sum of squares (RSS) (Tsai et al., 2004). In this study, the following fitness function was used to calculate the RSS for optimization:

$$RSS = \sum_{j=1}^{m} \left(\left[\frac{G'(\omega_j)}{\hat{G}'_j} - 1 \right]^2 + \left[\frac{G''(\omega_j)}{\hat{G}''_j} - 1 \right]^2 \right) \tag{5.8}$$

where $\hat{G}'_j$ and $\hat{G}''_j$ are the measured data at m frequencies.

To predict the global viscoelastic behavior of the asphalt mixture, time-temperature dependent FE analysis was conducted by combining the elastic aggregate, viscoelastic mastic and empty air void subdomains.

5.6.2   Prediction of shear modulus by FE modeling

Micromechanical viscoelastic FE simulation was conducted on meshed 2D and 3D samples that were exported to FE analysis software ABAQUS (2004). FSCH tests were simulated for all computer generated image samples at the same loading frequencies and temperatures that were used for viscoelastic mastic model development. The purpose of the tests was to predict asphalt mixture shear modulus at all temperature and loading frequency couples. Asphalt mixture tests were also conducted in the laboratory to compare the numerical predictions to laboratory measured shear modulus values.

FSCH tests are conducted by applying a cyclic shear load at the upper loading platen that is glued to asphalt sample while maintaining the sample height constant. The bottom loading platen was fixed in the test setup that was used for this study. For the FE simulation and laboratory tests, a constant sinusoidal shear strain of 0.2% was applied. Since the specimen height was 48 mm for all 2D and 3D asphalt mixture samples, cyclic displacement-based loading (strain controlled) was applied by fixing the upper platen movement at 0.096 mm for all cases. Because the standard FSCH is an unconfined test, confining pressures were not applied around the sample walls (AASHTO, 2003).

For 2D model simulations, three slices were randomly selected from the 3D structure for each mix type. Predictions for the three 2D models were averaged and compared to 3D model simulation results and laboratory measured shear modulus values. Because slices were randomly selected from the 3D structure, air void contents for the 2D samples maybe different from the 3D sample air void content. Although more than three 2D

samples would be needed to get a representative sample of predicted shear modulus, only three 2D samples were used for each mix type due to time constraints.

Figure 5.6 illustrates the distribution of vertical displacement (U2) vectors for both mixture types at 50°C under a loading frequency of 0.2 Hz with the cyclic shear load applied at the top of the samples in positive direction 1 (left to right). Although the sample height was kept constant to avoid the sample volume change during the tests, there were significant vertical movements in the sample microstructure. It can be observed that asphalt mixture RHMA-G was exposed to higher levels of vertical displacement than the mixture PG 64-28 PM. In addition, vectors in the positive and negative 2 directions were more uniformly distributed in mixture RHMA-G while localization of positive and negative direction vectors was observed for mixture PG 64-28 PM.
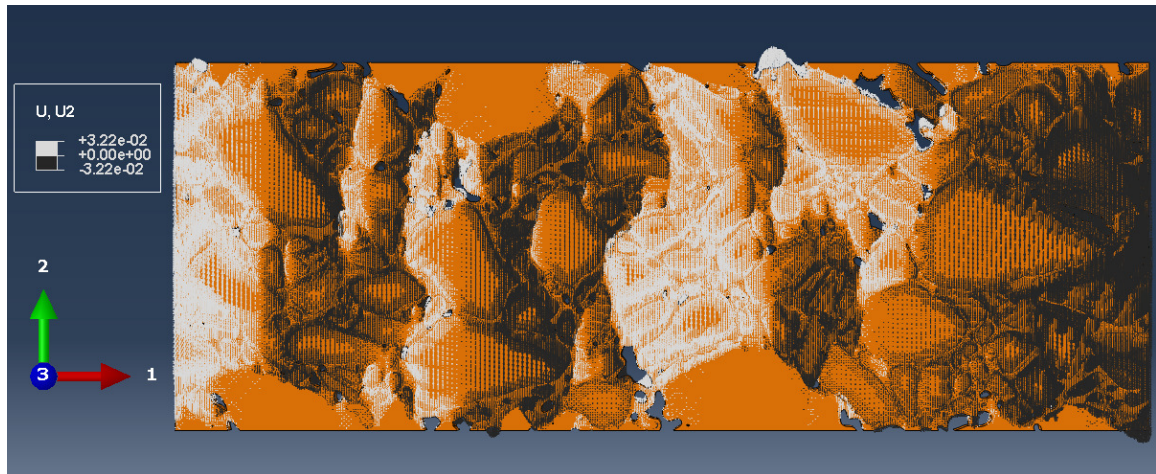
(a)
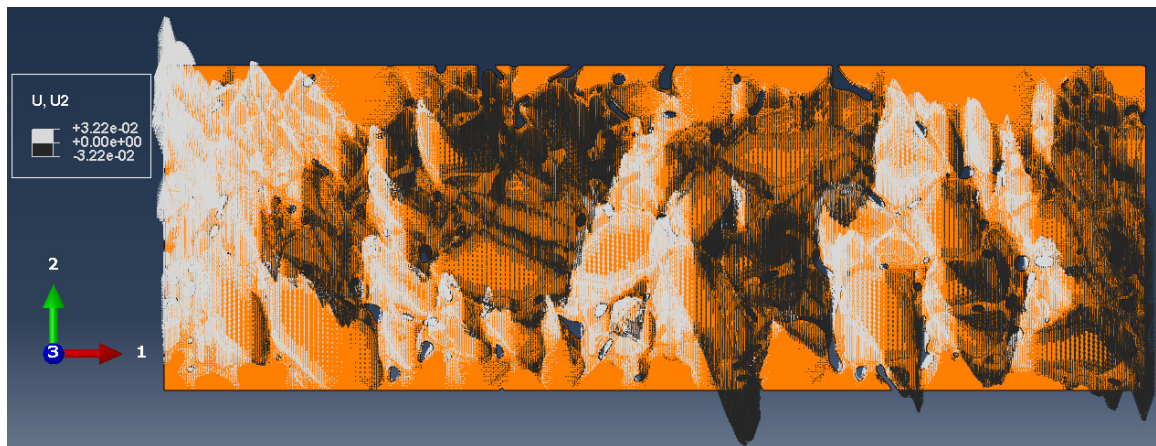
(b)

Figure 5.6 Vertical displacement (U2) distribution of 2D models at 50°C under a loading frequency of 0.2 Hz (a) Asphalt mixture PG 64-28 PM (b) Asphalt mixture RHMA-G.

Figure 5.7 shows the distribution of horizontal displacement for the mixture PG 64-28 PM for both 2D and 3D simulations at 40°C under a loading frequency of 0.2 Hz. Because the load was applied at the top of the sample, highest level of horizontal displacement was observed at that part. Similarly, no displacement was observed at the bottom of the sample since it was fixed.
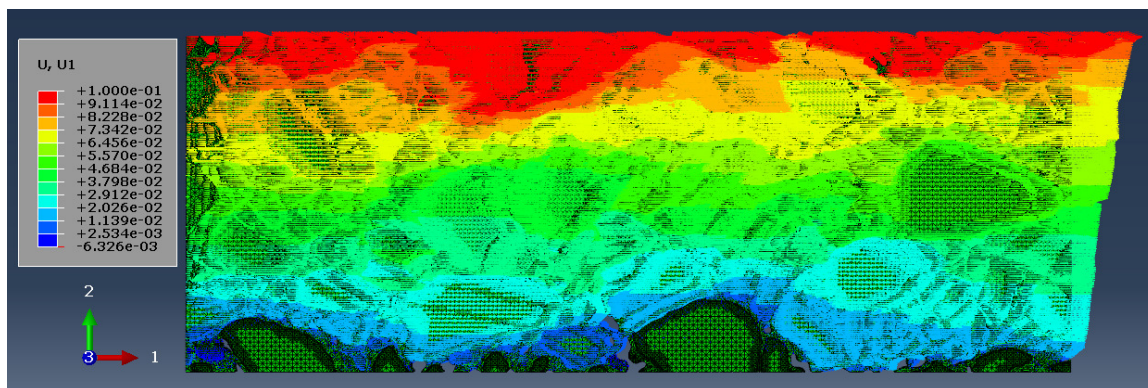
(a)
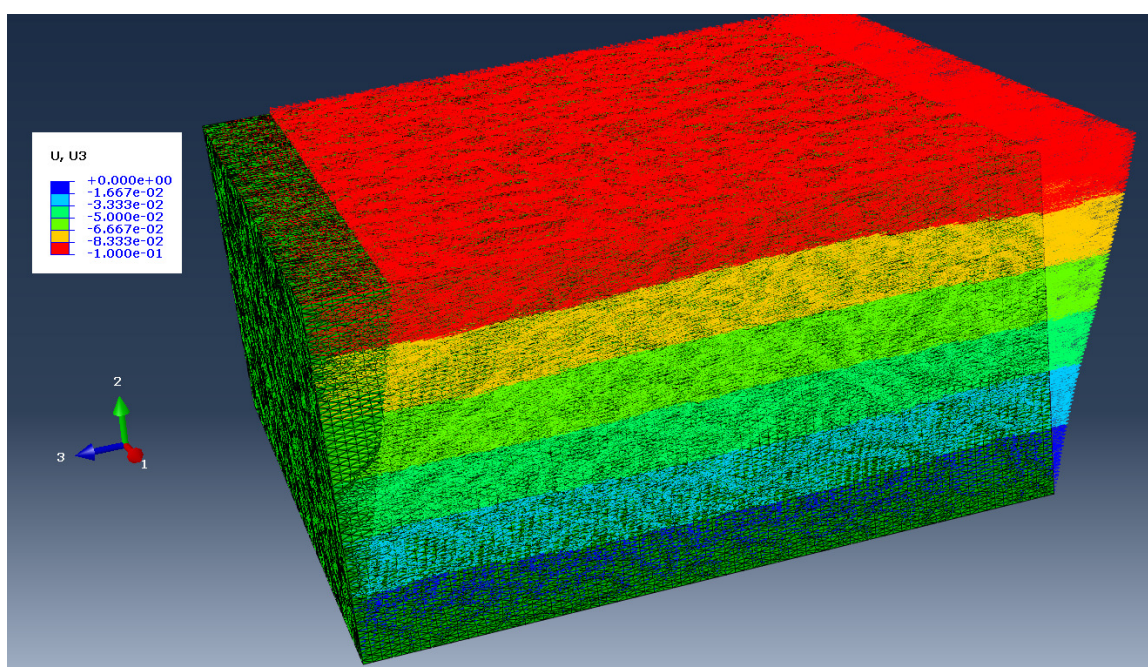
(b)

Figure 5.7 The distribution of horizontal displacement for the mixture PG 64-28 PM (a) 2D model structure (b) 3D model structure.

5.6.3   *Comparison of predicted and measured shear modulus*

Numerical samples prepared for the two asphalt mixture types were tested at 7 loading frequencies, 0.1 Hz, 0.2 Hz, 0.5 Hz, 1 Hz, 2 Hz, 5 Hz, and 10Hz, and 3 temperatures, 30°C, 40°C and 50°C under a controlled shear strain level of 0.2 %. For 2D and 3D numerical shear test samples, asphalt mixture shear modulus values were predicted for each temperature and loading frequency couples. For both asphalt mixture types, calculations were performed by using the shear stress-strain curves of simulation results that were calculated from shear load and horizontal displacement. Figure 5.8 shows the comparisons of measured and 2D numerical model predicted shear modulus values for the two asphalt mixtures. It can be observed that the 2D numerical models always underpredicted the shear modulus values. Comparison of laboratory measured and 3D numerical model predicted shear modulus values are given in Figure 5.9. Results of the analysis indicated that the shear modulus values predicted by the 3D numerical model are close to the laboratory measured shear modulus values and the prediction of shear modulus with the developed 3D model is reasonable. It can be concluded that inability to capture the 3D microstructure with the 2D models decreases the accuracy of numerical predictions.
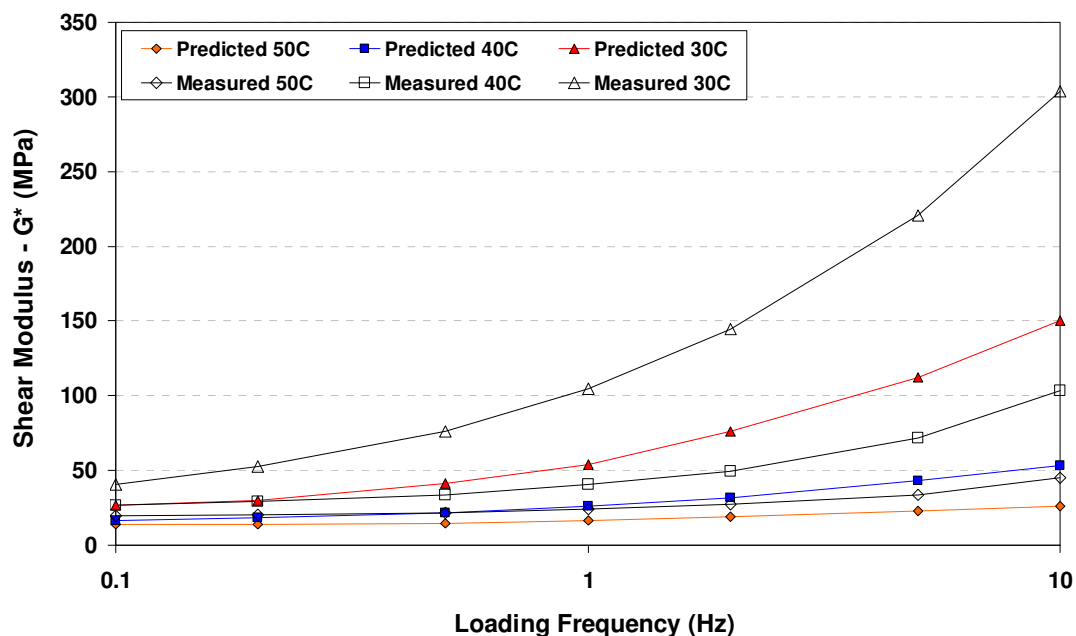
(a)
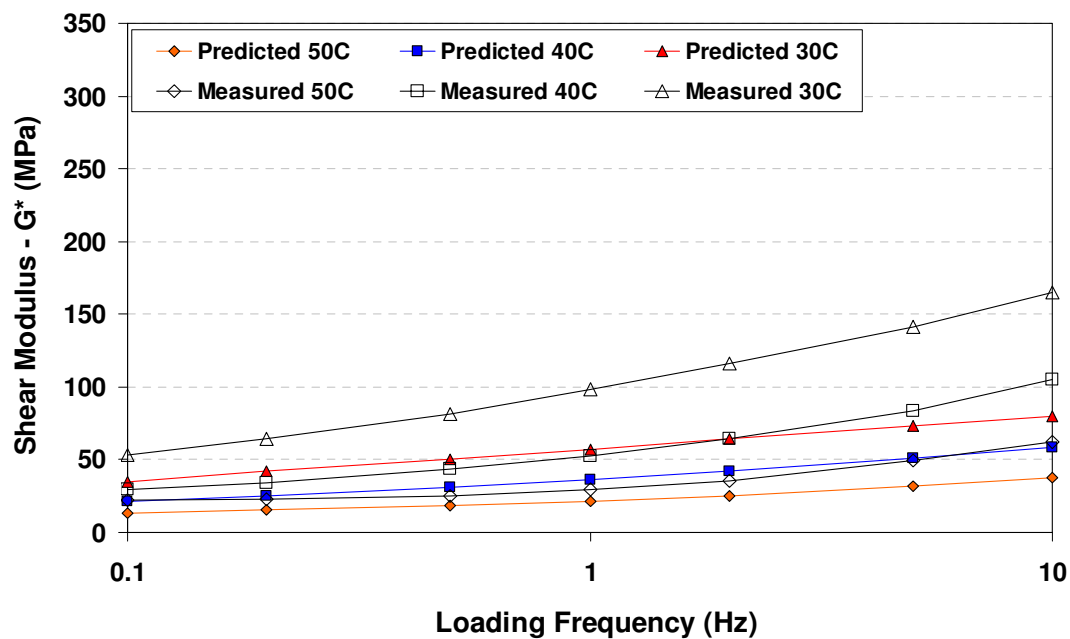
(b)

Figure 5.8 Comparison of laboratory measured and 2D numerical model predicted shear modulus values (a) Asphalt mixture PG 64-28 PM (b) Asphalt mixture RHMA-G.
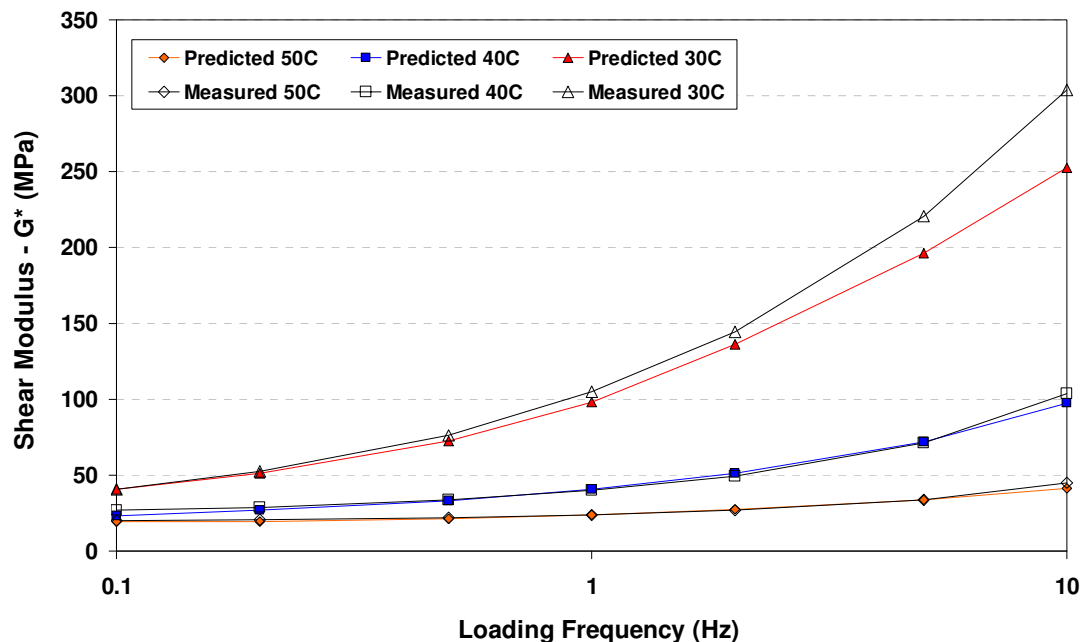
(a)
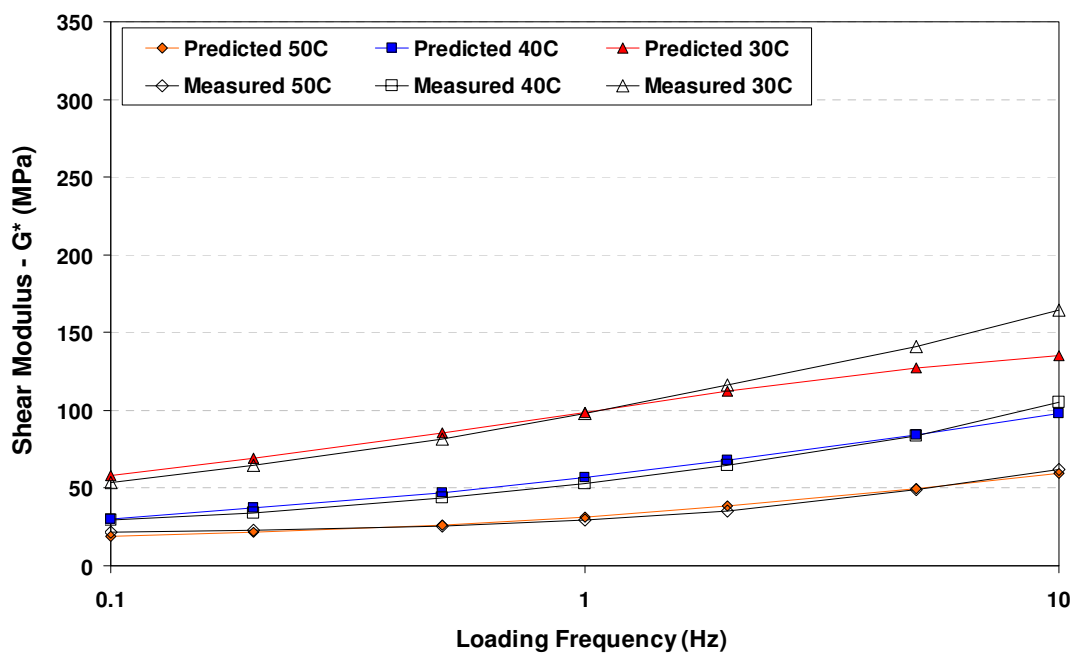
(b)

Figure 5.9 Comparison of laboratory measured and 3D numerical model predicted shear modulus values (a) Asphalt mixture PG 64-28 PM (b) Asphalt mixture RHMA-G.

Figure 5.10 illustrates the distributions for laboratory measured and 2D - 3D numerical model predicted shear modulus values. Although the distributions for 3D numerical model predictions are very close to the laboratory measured values for both asphalt mixture types, prediction error increases at higher loading frequencies and lower temperatures when the mastic is stiffer. It can also be observed from Figure 5.9 that predictions with the highest error levels belong to the lowest temperature (30°C) and highest loading frequencies (2 Hz, 5 Hz and 10 Hz). This result can be explained by the low modulus assumption (55 GPa) for the aggregate domain. As the mastic modulus increases and starts to converge with the aggregate modulus values at low temperatures and high loading frequencies, the 3D numerical models start to underpredict the shear modulus.

The 2D and 3D numerical model predictions given in Figure 5.10 were compared to the laboratory measured values by using three statistical tests, paired t-test, Wilcoxon rank sum test, and Kolmogorov-Smirnov test. Table 5.2 summarizes the results of the statistical tests. The paired t-test results indicated that 95% confidence interval for the mean difference between the 2D predictions and the laboratory measurements for both mixture types did not include zero. This result suggests that there are significant differences between the laboratory measured and 2D numerical model predicted shear modulus values.
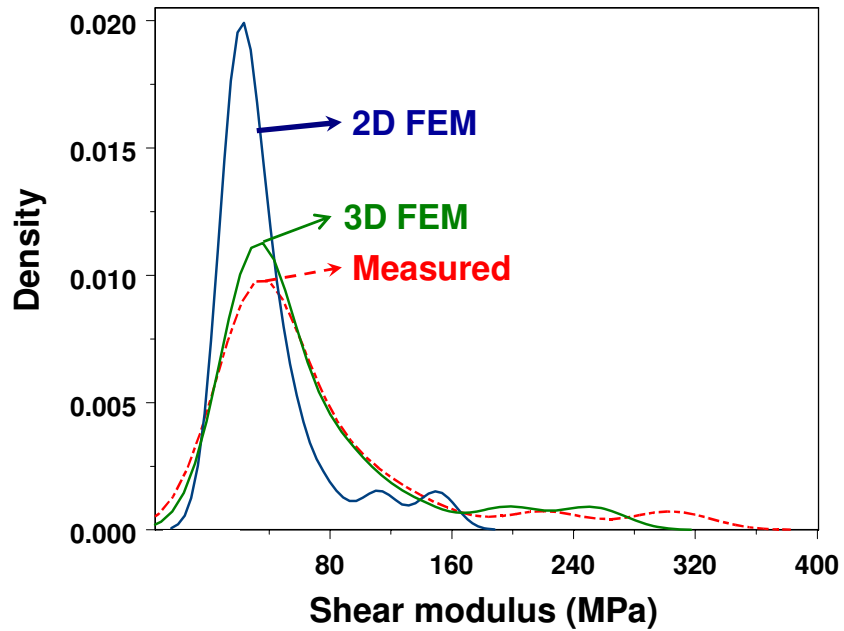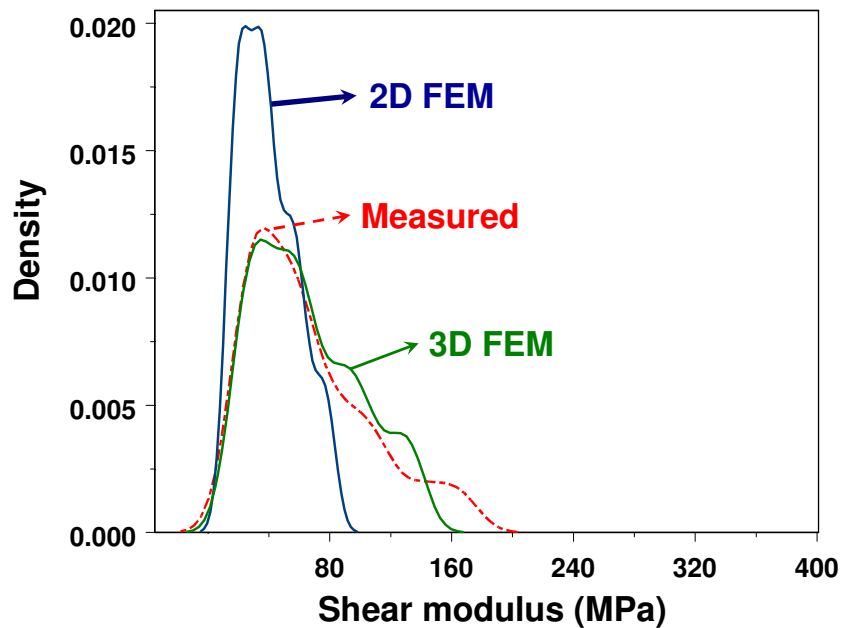
Figure 5.10 Comparing distributions for laboratory measured and 2D - 3D numerical model predicted shear modulus values (a) Asphalt mixture PG 64-28 PM (b) Asphalt mixture RHMA-G.

Table 5.2 Paired t-test, Wilcoxon rank sum test and Kolmogorov-Smirnov statistical test results comparing the 2D and 3D numerical model predictions to laboratory measured values

Compared distributions	CIFMD	p values		
		Paired t-test	Wilcoxon rank sum	Kolmogorov Smirnov
Mix 1 - 2D	14.29, 48.75	0.0011	0.0315	0.0948
Mix 2 - 2D	16.36, 35.90	0.0000	0.0195	0.1963
Mix 1 - 3D	-0.17, 10.70	0.0568	0.8617	1.0000
Mix 2 - 3D	-2.37, 4.85	0.4816	0.9010	1.0000

Note: CIFMD = 95% confidence interval for the mean difference between predictions (2D and 3D) and the laboratory measurements; Mix 1 = PG 64-28 PM; Mix 2 = RHMA-G.

Calculated p-values for all statistical tests are given in Table 5.2. Suppose F_1 and F_2 are two distributions. Possible hypotheses and alternatives concerning these distributions are (Insightful, 2001):

H_0: $F_1(x) = F_2(x)$

H_A: $F_1(x) \neq F_2(x)$

Decision rule: Reject H_0 if p-value<0.05

Fail to reject H_0 if p-value≥ 0.05

Based on the given decision rule, paired t-test and Wilcoxon rank sum test suggest that 2D numerical model predictions are significantly different than the laboratory measurements while the distributions for 3D model predictions are similar to the distributions of laboratory measurements. On the other hand, p-values for the Kolmogorov-Smirnov test indicated that 2D model predictions and laboratory measured values also show similarities. However, it should be noted that Kolmogorov-Smirnov test can be considered to be a more conservative test since it tends to procedure a p-value that is larger than the true one and conservative tests are generally accepted to be lower in

power than less conservative tests (Hayes, 2005). The null hypothesis $[F_1(x) = F_2(x)]$ is failed to reject with 95% confidence interval for comparisons of 3D model predictions and laboratory measurements in all statistical tests. This result suggests that reasonable shear modulus predictions can be made with the 3D micromechanical model proposed in this study.

5.7 SUMMARY AND CONCLUSIONS

In the study presented in this chapter, 2D and 3D micromechanical FE models were developed to predict the shear modulus of two asphalt mixture types, PG 64-28 PM (dense-graded polymer modified mixture) and RHMA-G (gap-graded rubberized mixture). The FE model developed in this study is the first 3D micromechanical model used for evaluating shear resistance of asphalt mixtures at high temperatures. The microstructures of the FMLC mixture specimens were determined by X-ray CT images taken at UCDMC. The asphalt mixture was divided into three phases, air-voids, mastic and aggregates by image processing. The air-void phase was excluded from the model because it has zero resistance. X-ray CT images were processed to create 2D and 3D meshed asphalt mixture model structures. The aggregate and mastic phases were meshed to share nodes on aggregates. Meshed model structures were exported to FE modeling software ABAQUS. Elastic and viscoelastic assumptions were used for modeling the aggregate and mastic subdomains, respectively. Shear modulus predictions for 2D and 3D models were compared to the measured values to determine the effectiveness of each model type for the simulation of FSCH test.

It was concluded that 3D micromechanical FE model is capable of predicting shear modulus at high test temperatures across a range of loading frequencies. 2D numerical models always underpredicted the shear modulus values at all simulation temperatures and loading frequencies because small amount of microstructure for the 2D models decreased the accuracy of numerical predictions. It was also identified that although the sample height was kept constant and sample volume change was avoided during the tests, there were significant aggregate movements in the sample microstructure. Asphalt mixture RHMA-G was exposed to higher levels of vertical displacement than the mixture PG 64-28 PM. The developed micromechanical finite element model presented in this chapter is used in Chapter 6 to investigate the differences between the rutting accumulation mechanisms of RHMA-G and PG64-28PM mixes under HVS trafficking.

CHAPTER 6   INVESTIGATION OF IN-SITU RUTTING MECHANISMS BY X-RAY COMPUTED TOMOGRAPHY IMAGING AND MICROMECHANICAL FINITE ELEMENT MODELING

6.1   INTRODUCTION

The general trend in truck tire technology for heavy freight trucks is to reduce rolling resistance and improve fuel economy, including the switch from bias-ply to radial tires beginning 45 years ago, and continuing with the movement to wide-base single tires over the last 20 years. At the same time, tire inflation pressures have generally been increasing for the same reasons. The combined effects of each of these tire technology changes and increasing inflation pressures and truck traffic volumes have increased the risk of rutting of AC and a need for high performance pavement structures (Al-Qadi and Elseifi, 2008). Therefore, new pavement design and construction specifications have been developed to reduce the risk of early failure of pavement structures (White et al., 2002). Three other trends affecting the design and construction of asphalt mixes are:

- Change of focus from designing and constructing new pavements adding traffic volume capacity to the road network to rehabilitation and maintenance of the existing network;

- Increased use of modified asphalt binders and gap-, open- and stone matrix type aggregate gradations in addition to dense-gradations, as specialized mixes are developed for specific performance requirements in different layers of the pavement and different functional requirements; and

- Increasing use of specifications to reward or penalize the contractor for performance-related construction quality or performance (Epps et al., 2002).

Together, these trends require the use of design methods that consider material properties, structural design (particularly the use relatively thin modified asphalt overlays on concrete and aged existing asphalt layers), and the effects of traffic and climate to deliver the required future performance of the constructed structure.

Mechanistic-empirical (ME) design methods are developed by calibrating critical mechanistic responses of pavement structures calculated using theoretical structural models with responses measured in the field, and then correlating those responses with empirical performance data. The structural models are developed based on generally accepted theories and methods, such as linear elastic theory (LET) and finite element (FE) method, with specific constitutive relations that consider the effects of environmental conditions and traffic loads, and dimensions. The structural models use laboratory test results to characterize the damage in the materials (usually loss of stiffness

or permanent deformation) resulting from the pavement response (stress and/or strain). Structural models are calibrated based on measured pavement performance that is generally determined from accelerated pavement testing (APT) and/or less commonly field test results (Ullidtz et al., 2006). APT is also commonly used to calibrate responses with observed distresses because it offers controlled experiments with the ability to comprehensively and cost-effectively characterize the pavement and measure responses and distress development, or to relate material properties to full-scale performance (Brown, 2004). However, ME design methods use greatly simplified models (such as relating elastic strains to plastic strains) (Ullidtz et al., 2006; MEPDG, 2004; Sousa et al., 1994) that rely on correct conceptual understanding of causal relationships between responses that can be measured in APT or in the field and distress development. There has been considerable theoretical, laboratory testing and modeling work to relate material properties to performance of modified binder mixes and different aggregate gradations. However, the densification and shearing processes that cause rutting of asphalt mixes have not had experimental measurements of the movement of aggregate and changes in air-void content and distribution that explain rutting failure at a microstructure scale. The literature also indicates that greater attention has been paid to the mechanics of thick asphalt layers as opposed to the thinner overlays on existing stiff layers that make up the majority of the applications in California and many other locations.

Asphalt concrete is a composite material which consists of aggregates, air-voids and mastic, and each phase plays a role in development of total accumulated rutting. Asphalt concrete mixes act as continuum materials at low temperatures when the stiffness of the

asphalt binder and the aggregate are close (Weissman et al., 1999). However, at high temperatures, i.e. the critical conditions for rutting deformation accumulation, stiffness of the aggregate can be two to three orders of magnitude higher than the asphalt binder stiffness. As a result, asphalt concrete pavement layers start to act as particulate structures where the contact points between the aggregates become more important in terms of rutting deformation accumulation (Weissman, 1997). Therefore, permanent deformation accumulation mechanisms predicted by using continuum mechanics may not reflect the actual mechanism under the in-situ truck traffic. This has been recognized in recent years and has lead to increased use of multi-phase continuum mechanics and discrete element method approaches (You et al., 2008; You et al., 2009; Braz et al., 1999a; Braz et al., 2000; Warr et al., 1994; Wang et al., 1999; Yin et al., 2008). These methods consider the properties of the aggregate (shape, texture, gradation, modulus), of the asphalt binder (visco-elasticity) and distribution of air voids in the asphalt concrete layers. However, as noted, experimental measurements for validation of these models for permanent deformation under full-scale loading and for thin overlays has not been available to date.

Microstructures of AC laboratory samples have been analyzed by various researchers. Masad et al. (1999; 2002) characterized the air-void distribution in AC samples using the Weibull model and concluded that the method of laboratory specimen compaction significantly influences the air-void size distributions. Masad and Button (2004) developed a procedure to quantify the distribution of aggregate skeleton and air-voids by analyzing images of the internal structure. You et al. (2008; 2009) processed the AC X-ray computed tomography (CT) images to develop 2D and 3D discrete and finite element

models to evaluate the effect of binder, aggregate and air-void interaction on AC performance.

Changes in material microstructure under laboratory testing were also evaluated by various researchers. Braz et al. (1999a; 1999b) analyzed the propagation of cracks under diametral compression testing to determine the effect of AC air-void distributions on cracking performance. Warr et al. (1994) analyzed the 2D transitional and rotational motion of granular particles under laboratory loading by using the images collected by high-speed photography. Wang et al. (1999) used photograph images taken before and after Georgia Loaded Wheel Test loading (GLWT) to determine the 2D permanent strain field of an asphalt concrete specimen. Wang et al. (2007) also calculated the plastic strain field in asphalt concrete laboratory samples accumulated for specimens tested with the Asphalt Pavement Analyzer (APA). It was concluded that permanent deformation of asphalt concrete is localized mainly in the soft mastics due to low mastic stiffness at high test temperatures (60°C). Synolakis et al. (1996) used X-ray CT images that were taken before and after the application of a diametral load on a cylindrical laboratory sample to calculate the plastic displacement field.

In this study, changes in AC microstructure were determined using full-scale test sections and Heavy Vehicle Simulator (HVS) loading, and X-ray CT images taken before and after HVS testing. AC blocks sawn from four HVS test sections were scanned to determine the microstructure of the blocks before testing. 3D distributions of air-voids, location and shape parameters for the aggregates were determined using these images.

Scanned AC blocks were installed back into their original locations using a fast-setting epoxy. HVS tests were conducted at high temperatures (50°C at 50 mm depth) that are critical for rutting until the surface failure was observed. Deformed AC blocks were re-sawn to perform X-ray CT scanning after HVS loading. Deformed and un-deformed 3D air-void and aggregate distributions were compared to determine the changes in air-void content distributions and aggregate positions. Changes in air-void content distributions were used to identify the contribution of densification to total accumulated downward rut, while changes in aggregate positions were used to determine the displacement field under full-scale wheel loading. The primary purpose of this study is to investigate the reasons behind the earlier failure of the rubberized gap graded AC mix when compared to the polymer modified dense graded mix. A step-by-step elimination approach is followed to explain the failure phenomenon.

1. Changes in air void content distributions were determined based on the before and after X-ray CT images. The contribution of densification (air void reduction) to the measured surface rutting was determined based on the measured change in air void content. Transverse profiles of the densification related rutting were compared with the actual surface rutting profiles, which were measured by a laser profilometer. It was observed that the contribution of air void reduction to total downward rut was similar for all test sections. This result suggested that earlier failure of sections with rubberized gap graded mix was actually a result of shear related deformation, not densification.

2. In order to understand the effects of binder properties on rutting performance, shear frequency sweep tests were performed on rubberized and polymer modified mastic samples.

3. The differences between shear related deformation accumulation for rubberized gap graded and polymer modified dense graded mixes were investigated based on the particle movement data that was obtained by processing the before- and after-testing X-ray CT images with a particle tracking algorithm.

4. Because shear related deformation was determined to be critical for rutting failure, a viscoelastic micromechanical finite element model was developed for a shear frequency sweep test to evaluate the differences between particle movements of two mix types under repeated shear loading. This model was also used to identify the dilative behavior of rubberized gap graded and polymer modified dense graded mixes under shear loads.

Results of the analyses showed that the contribution of densification related deformation to total measured surface rutting was similar for all mix and structure types in this study. Binder properties of two mix types did not appear to control the rutting failure according to the shear frequency sweep test results. This result suggested that aggregate properties, gradation and orientation of aggregates were the primary controlling factors for the rutting performance. It was also observed from micromechanical finite element simulations and particle tracking analysis that the gap graded rubberized mix in the study showed more dilative behavior which resulted in larger humps at the edges of the HVS wheelpahts as a result of lateral and upward shear flow. Larger humps increased the

maximum rut depth (top of the hump to the bottom of the downward rut) which consequently resulted in earlier failure for that gap graded rubberized mix.

This study is the first in-situ investigation of micromechanical changes in AC layers under full-scale loading, and provides experimental data for continued development of multi-scale continuum mechanics and discrete element method analysis approaches. Results of the analyses will give important information about the rutting failure mechanisms of gap-graded rubberized and polymer modified dense graded asphalt mixes. The method used in this study can be used to develop additional experimental data for other mix types and under different testing conditions. Changes in air-void distributions and displacement field can also be used to validate and/or calibrate micromechanical finite element or discrete element models.

6.2 OBJECTIVES

The main objectives of the work presented in this chapter were

- Use the X-ray CT imaging method to identify changes in microstructure caused by the rutting process, namely aggregate displacements and changes in air-void content and distribution, under full-scale loading and for different thicknesses of overlay on very stiff underlying layers.

- Use the experimental measurements to perform a first-level assessment of the micro-mechanical phenomena to provide insight into mix performance for mix design and development and understanding of laboratory tests, and information

regarding the mechanics of rutting that can be used to improve micro-mechanical analysis approaches.

6.3   MECHANICS OF RUTTING ACCUMULATION

Pavement rutting can be divided into two parts: rutting of the asphalt surfacing and rutting of the unbound layers. Unbound layers rutting is caused by subsidence caused by the shearing and densification in unbound base, subbase and subgrade layers, and directly affects the total rutting accumulated at the surface. However, on existing pavements that are rehabilitated and where water has not been allowed to pass to the unbound layers, the major part of the rutting (85 to 95 percent) is generally accumulated in the AC layers (Coleri et al., 2008). Rutting in the asphalt layers accumulates with increasing number of load applications and is highly sensitive to variations in the temperature and traffic levels (Metcalf, 1996). Volume change (densification) and shape distortion (shear related deformation) are the two deformation modes that control the rutting accumulation. Volume change is the deformation of a material with equal principal strains in all dimensions. Bulk modulus (K) is the resistance of a material to volume change. Shear distortion can be defined as the deformation without any change in volume. Resistance of a material to shear distortion is represented with the shear modulus (G) (Kim, 2009).

Typically, rutting accumulation rate is higher under initial loading due to the combined effect of densification and shear distortion. The deformation accumulation rate starts to decrease as the layers become stiffer with the reduction in air-voids and reorientation of

aggregates. Sousa et al. (1994) indicated that strain caused by densification will be recovered more than the strain due to the shear distortion when a transient load is released. Thus, the shear distortion component of the total deformation will be more than the portion related to the volume change. However, results of the analysis conducted by using the profilometer measurements indicated that the contribution of densification to total accumulated rutting can be up to 45 percent even after the structure is failed by rutting (White et al., 2002). This result suggests that prediction of the AC rutting performance by only considering the shear resistance of the material may be misleading under specific circumstances. Therefore, the fundamental phenomenon behind the movement of the aggregates at high temperatures should be determined.

6.4   EXPERIMENT PROGRAM

6.4.1   Heavy Vehicle Simulator testing

Full scale accelerated pavement tests are performed by applying a prototype wheel load at or above the actual load levels to a prototype or actual pavement system (Metcalf, 1996). Long-term pavement performance can be determined in a short period of time by evaluating the response of the pavement system to applied loads. Duration of the testing can be reduced by performing the tests at critical conditions. For instance, for rutting performance evaluation, accelerated tests can be conducted at critical field temperatures and loads can be applied without simulating the decrease in temperature during daytime or cold seasons. The rate of deformation can also be increased by decreasing the wheel

speed. Variables which affect the rutting performance of the pavement can be more accurately controlled and monitored during the accelerated tests (Ullidtz et al., 2006).

The HVS is a mobile load frame that uses a full-scale wheel (dual or single) to traffic the pavement test section. The trafficked test section is 8 m long, of which 1 m on each end are used for turnaround of the wheel and are discarded.

In this study, composite, AC over PCC, full-scale pavement sections were constructed for HVS test sections at the Advanced Transportation Infrastructure Research Center (ATIRC) facility at UC Davis (Coleri et al., 2012). Detailed HVS test results are given in Appendix A. Two asphalt mixture types were used in this study (Appendix A), a dense-graded mixture with PG 64-28 polymer modified (PM) binder and a gap-graded mixture with asphalt rubber binder (PG 64-16 base binder and crumb rubber modified), RHMA-G. Both mixes were specified based on Caltrans specifications (Caltrans, 2006a; Caltrans 2006b) for both mix and binder. Nominal maximum aggregate sizes (NMAS) for PG64-28PM and RHMA-G mixtures were 19 mm and 12.5 mm, respectively. Table 6.1 shows the aggregate gradations, asphalt binder content and air-void content of the asphalt mixtures.

Two overlay thicknesses were tested for each of the two mix types placed on the HVS test sections: 64 mm (one lift) and 114 mm (two lifts) for thin and thick AC sections, respectively. All sections had 150 mm aggregate base layers and 178 mm thick PCC layers.

Table 6.1 Aggregate gradation for asphalt mixtures

Sieve size (mm)	Percent Passing (%)	
	Mix PG64-28PM	Mix RHMA-G
25.4	100	100
19	99	100
12.5	87	98
9.5	74	84
4.75	50	34
2.36	36	21
1.18	27	14
0.6	21	10
0.3	16	7
0.15	10	5
0.075	6.2	3.5
Asphalt binder content[a] (%)	5.1	7.6
Air void content[b] (%)	9.9	13.6

[a] Design binder content (by dry weight of aggregate).
[b] As-built average air void content.

The HVS loading program for each section is summarized in Table 6.2. The failure criterion was defined as an average maximum rut (defined as the summation of the downward deformation and "humping" of material sheared to the sides of the wheelpath) of 12.5 mm over the full monitored section. The pavement temperature at 50 mm depth was maintained at 50°C±4°C to assess rutting potential under typical pavement conditions. All trafficking was carried out with a dual-wheel configuration with the centerlines of the two tires spaced 360 mm apart, using radial truck tires inflated to a pressure of 690 kPa, in a channelized (no wander), unidirectional loading mode in which the wheel travels one direction loaded and is lifted off the pavement for the return pass. Channelized trafficking is used to simulate the tracking of radial tires in the wheelpath once a small rut forms, and is more aggressive than field conditions in the initial stages of rutting before tires begin to track in the ruts. Wheel speed for all tests was 8.7 km/h.

Table 6.2 Summary of HVS loading program

| Section | Mix type | As-built Thickness (mm) | Wheel Load (kN) | Temperatures at 50 mm | | Total Repetitions |
				Average (^{o}C)	SD^{a} (^{o}C)	
609HB	PG64-28PM	116	40 60	49.5	1.1	63,750 136,250
610HB	PG64-28PM	72	40 60	49.8	1.0	64,000 137,200
611HB	RHMA-G	118	40	48.7	1.1	18,503
612HB	RHMA-G	74	40	49.7	1.3	90,000

^{a} SD: Standard deviation

6.4.2 Laboratory testing - Frequency sweep at constant height

Mastic samples were prepared and tested to identify the effect of binder properties on overall AC mix rutting performance. Test results were also used for viscoelastic finite element model development (Chapter 5). Binders and aggregates for mastic sample preparation were taken from the plant which provided the asphalt mixtures for construction. Because the NMAS for mastic samples was 1.18 mm and the binder content was very high, mechanical compaction was not performed. However samples were manually compacted in the laboratory with small size 7 kg cylinders. The width and length for the mastic samples were selected to be 100 mm while the height was 15 mm.

Shear frequency sweep at constant height (FSCH) tests were conducted with mastic samples. Tests were conducted with two replicates to eliminate the effects of test results' variability on the developed mastic model. However, it was observed that due to the small NMAS of mastic samples (1.18 mm), differences between replicate test results were negligible.

6.5 GENERAL PROCEDURE FOR X-RAY CT IMAGE DATA COLLECTION FOR HVS SAMPLES

The general procedure followed for X-ray CT image data collection (before-after HVS testing) is illustrated with photographs in Figure 6.1.

The steps followed for X-ray CT image data collection are described as follows:

- Preliminary tests were performed to determine the best adhesive to glue sawn AC blocks back into their original locations. Because sawing changes the boundary conditions around the AC blocks, adhesive type to create the best connectivity between the AC blocks and pavement was selected. The adhesive also needed to have similar material properties as the original AC pavement to avoid non-uniformity around the blocks. Epoxy and asphalt mastic were evaluated using Hamburg Wheel Tracking Device (HWTD) results (Figure 6.1a). Small AC blocks were sawn from the HWTD test samples and glued back with epoxy and mastic. Localized rutting failure was observed around the block that was glued with mastic (Figure 6.2). On the other hand, more uniform rutting deformations were observed on the HWTD sample with epoxy glued block. Fast-setting epoxy was used in the HVS sections for gluing the sawn AC blocks.

- The 3D internal structures of the asphalt mixtures were acquired by X-ray CT imaging at University of California Davis Medical Center (UCDMC). The allowable maximum length of the AC block dimension that can be scanned with a medical scanner was determined by scanning laboratory samples with various dimensions. It was determined that largest dimension of the AC block should not exceed 17 cm (6.7

inches) in order to acquire X-ray CT images with an acceptable level of quality. Square 17 cm AC blocks were sawn from HVS test sections to achieve the maximum volume that could be scanned.

- AC blocks were located so that one half of the block was in the wheelpath while the other half was next to the wheelpath in order to monitor the lateral shear flow. Four blocks were sawn from distributed locations (to avoid localized failures) on each HVS test section (16 blocks from 4 HVS rutting sections) to get the complete deformation profile (Figure 6.3). Locations were different on sections with a thick AC layer to avoid cutting the cables of strain gauges at 50 mm depth.

- Because tack coat was applied on the PCC layer to create bonding between PCC and AC layers during construction, non-stick paper was used to break the bond between PCC and AC layers (Figure 6.1b) under the blocks. This facilitated the removal of sawn AC blocks while avoiding any damage to the blocks during removal.

- AC layers were constructed on top of PCC layer (Figure 6.1c).

- AC block locations were marked on AC layer and blocks were sawn from those previously determined locations (Figure 6.1d).

- 3D internal structures of the asphalt mixtures were acquired by X-ray CT imaging at UCDMC (Figure 6.1e).

- X-ray CT images were processed to obtain aggregate location and shape information. In addition, distributions of air-voids in AC blocks were determined (Figure 6.1f).

- Extended cuts that were created during sawing of the blocks due to the circular shape of the concrete saw were filled with an emulsion-sand mixture to avoid localized failures (Figure 6.1g).

- Scanned AC blocks were installed back in to their original position with fast-setting epoxy (Figure 6.1h).

- HVS test sections were prepared for testing. Boundaries for the HVS wheel paths were drawn on the sections by considering the AC block locations (Figure 6.1i).

- HVS sections were tested (Figure 6.1j).

- Rutted AC blocks were re-sawn after trafficking (Figure 6.1k). In order to perform sawing with high precision, blocks were first sawn with a perimeter larger than the original block. Original blocks were sawn with high precision using a stationary saw.

- After test-AC blocks were re-scanned at UCDMC and images were processed to acquire the new 3D aggregate and air-void distributions (Figure 6.1l).

Figure 6.1 The general procedure followed for CT image data collection (before-after HVS testing).
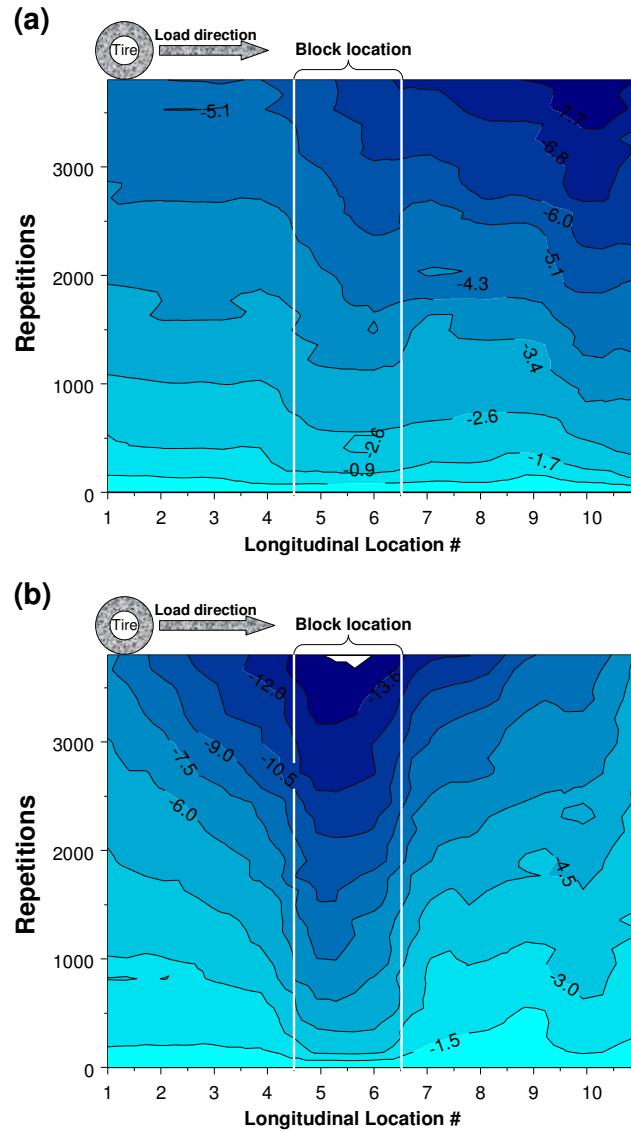
Figure 6.2 HWTD test results (a) For the AC block that was glued with epoxy (b) For the AC block that was glued with mastic.
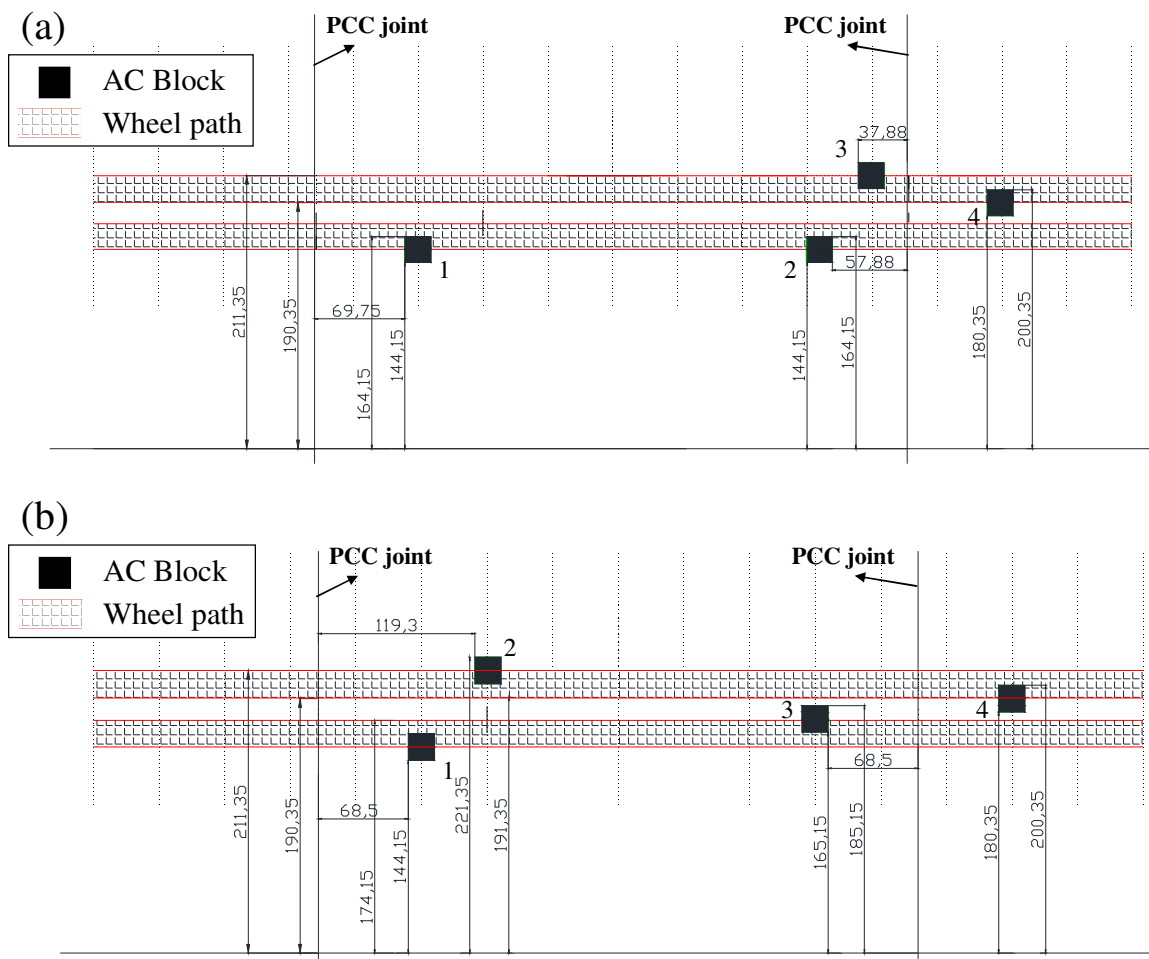
Figure 6.3 Locations for the AC blocks (scaled - Dimensions in cm) (a) Sections 609HB and 611HB with thick (114 mm) AC layer (b) Sections 610HB and 612HB with thin (64 mm) AC layer.

6.6 X-RAY CT IMAGE ACQUISITION AND PROCESSING FOR HVS SAMPLES

The X-ray CT scanner at UCDMC reconstructs the 3D spatial distribution of the attenuation coefficients of the scanned materials. Three dimensional images of the specimen are generated by combining a series of 2D images generated by the scanner. The quality of the 3D image depends on the X-ray CT image resolution. In this study,

horizontal planar images were acquired at 1 mm intervals while the resolution cell for the other two dimensions was determined to be 0.24 mm. At each sampling point within the sample volume, each pixel from a CT image measures a value that is related to the density and atomic number of the material at that particular point. These measured values are then converted to grayscale values (Simpleware, 2010). The gray scale intensities for the aggregates, air voids and mastic range from -1000 to 3095, but these values were rescaled to the range from 0 to 255. Because aggregates are denser than mastic and air voids, they occupy the higher portion of the intensity scale. Low density air voids are at the lowest intensity portion while mastic intensity is between aggregate and air void intensities.

6.6.1 *Development of 3D air-void distributions*

Simpleware software (Simpleware, 2010) was used to create masks for the air void domain based on measured intensity groups. Air void percentages for each asphalt mixture sample were determined by using the standard CoreLok method (AASHTO, 2009) (Table 6.1). The total volume of each specimen was calculated for the complete intensity range, 0 to 255. The upper limit for the air void intensity range was determined by trial and error to match the measured air void contents. The average air-void intensity range for the PG64-28PM blocks was determined to be 0-119 with a calculated average air void content of 9.9 % while the average range for RHMA-G blocks was 0-102 with a calculated average air void content of 13.6 %. After the thresholds for the air void domain were determined, masks with specific colors were assigned to clearly visualize

the distribution of air void domain in the total block volume. Figure 6.4 illustrates the air void distributions for block 1 (See Figure 6.3) of all HVS test sections.

Developed 3D images were further processed to obtain the distribution of air voids with depth. First, AC blocks were divided into 2.93 mm thick volumes in the vertical direction. Volumetric air void content for each volume was calculated with Simpleware software (Simpleware, 2010) to determine the distribution of air voids within the depth of the AC blocks. Figure 6.5a shows the distribution of air-voids with depth for the thick asphalt sections, also showing the construction lift. It can be observed that air-void content in the middle depth of each lift is lower than the bottom and top of the lift, most likely the result of greater temperatures being retained longer in the middle of the lift and less interference with aggregate rotation from stiff horizontal boundaries. It can also be seen that the bottom lift is better compacted than the top lift. This maybe a result of the reheating and additional compaction of the bottom lift provided during the compaction of the top lift and/or the high confinement provided by the stiff PCC layer during the compaction of the bottom lift.
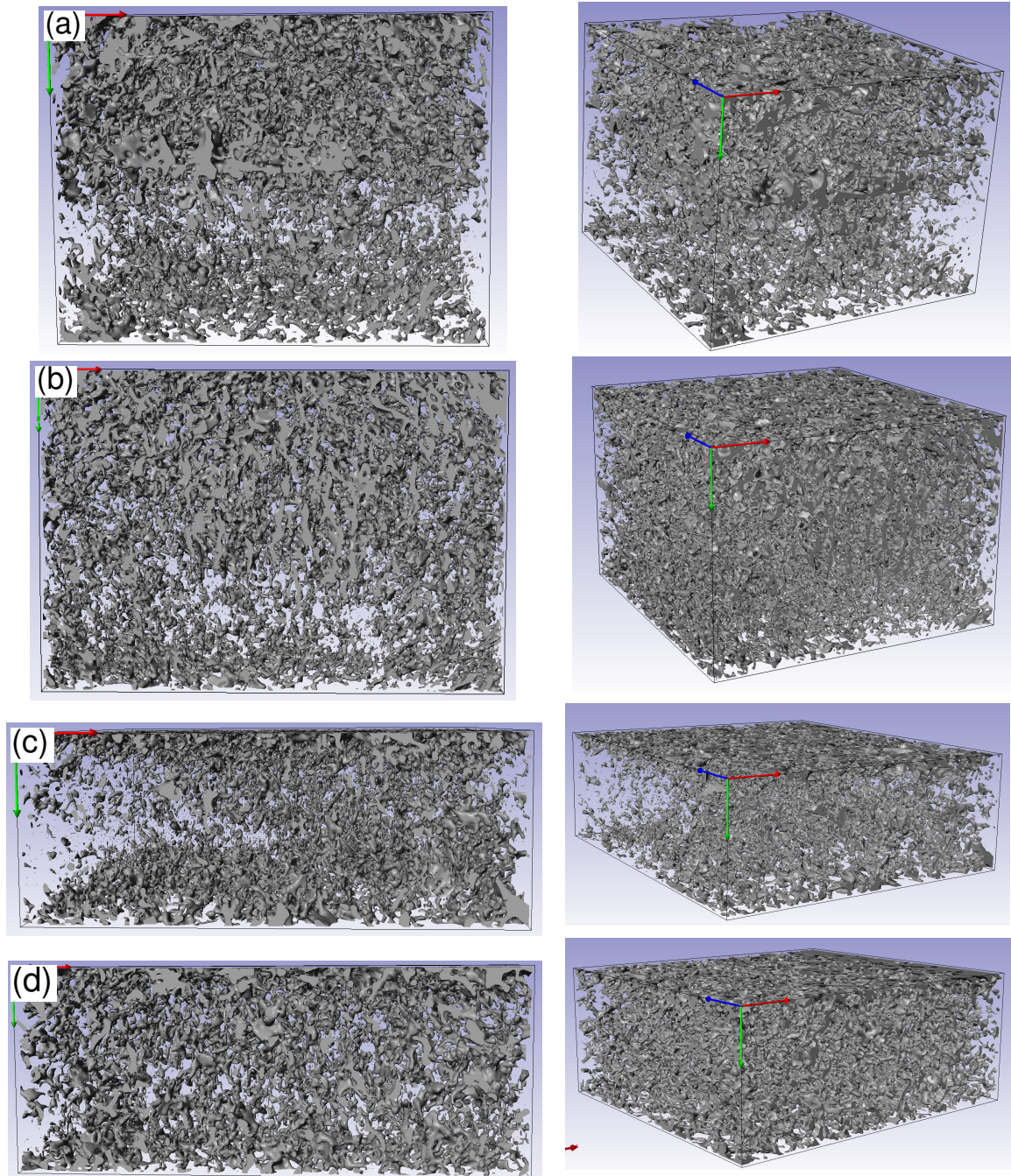
Figure 6.4 Distributions of air voids in AC blocks (colored volumes are air-voids) (a) Block 1 - Section 609HB - PG64-28PM - 114mm from two perspectives (b) Block 1 - Section 611HB - RHMA-G - 114mm from two perspectives (c) Block 1 - Section 610HB - PG64-28PM - 64mm from two perspectives (d) Block 1 - Section 612HB - RHMA-G - 64mm from two perspectives.
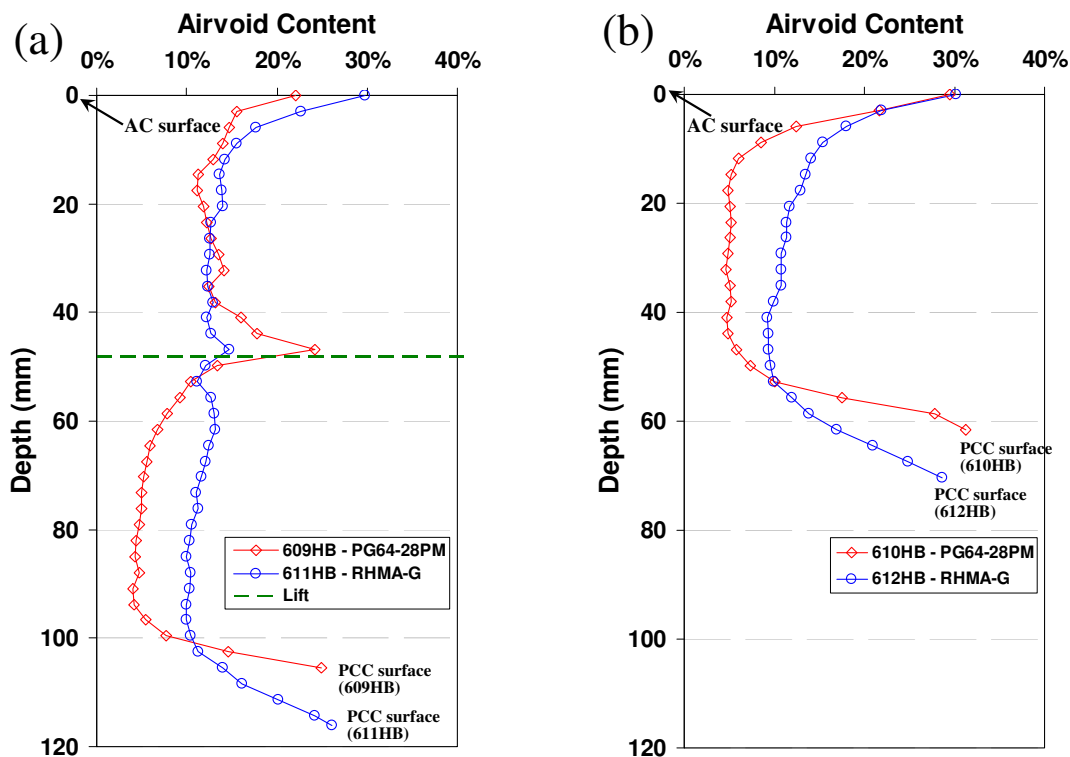
Figure 6.5 The distribution of air void contents with depth for block 1 of all HVS test sections (a) Section 609HB - PG64-28PM - 114mm and Section 611HB - RHMA-G - 114mm (b) Section 610HB - PG64-28PM - 64mm and Section 612HB - RHMA-G - 64mm.

Figure 6.5b shows the distribution of air void contents for the thin (64 mm) AC blocks. Distributions appeared to be similar to the distributions obtained for the bottom lift of thick sections except for higher air void contents observed at the top and bottom of thin AC blocks. Air void content distributions for the thick and thin AC blocks also show that due to the larger NMAS for the PG64-28PM mix, air void contents at the bottom of each lift appear to be relatively larger than the RHMA-G blocks. However, in the middle depth of each lift, PG64-28PM blocks have significantly lower air void contents.

6.6.2   Development of 3D aggregate distributions

Imaris Version 7.2 software was used in this study to create masks for the aggregate domain based on measured intensity groups. Intensity ranges for the aggregates were determined based on the X-ray CT images. Surfaces and volumes for aggregates were created by Imaris in order to visualize the range of interest of a volume object. Figure 6.6 illustrates the procedure for the creation of aggregate volumes and surfaces, which was as follows:

- Prepare X-ray CT image stacks using the software ImageJ Version 1.43 (Figure 6.6a).
- Import image stacks to Imaris and create 3D images from the stack of 2D images (Figure 6.6b)
- Determine the intensity range that will create the aggregate volumes that are close to the actual aggregates.
- Create 3D aggregate volumes for before and after trafficking-AC blocks (Figure 6.6c).
- Split discrete aggregates that appear unified in the image.
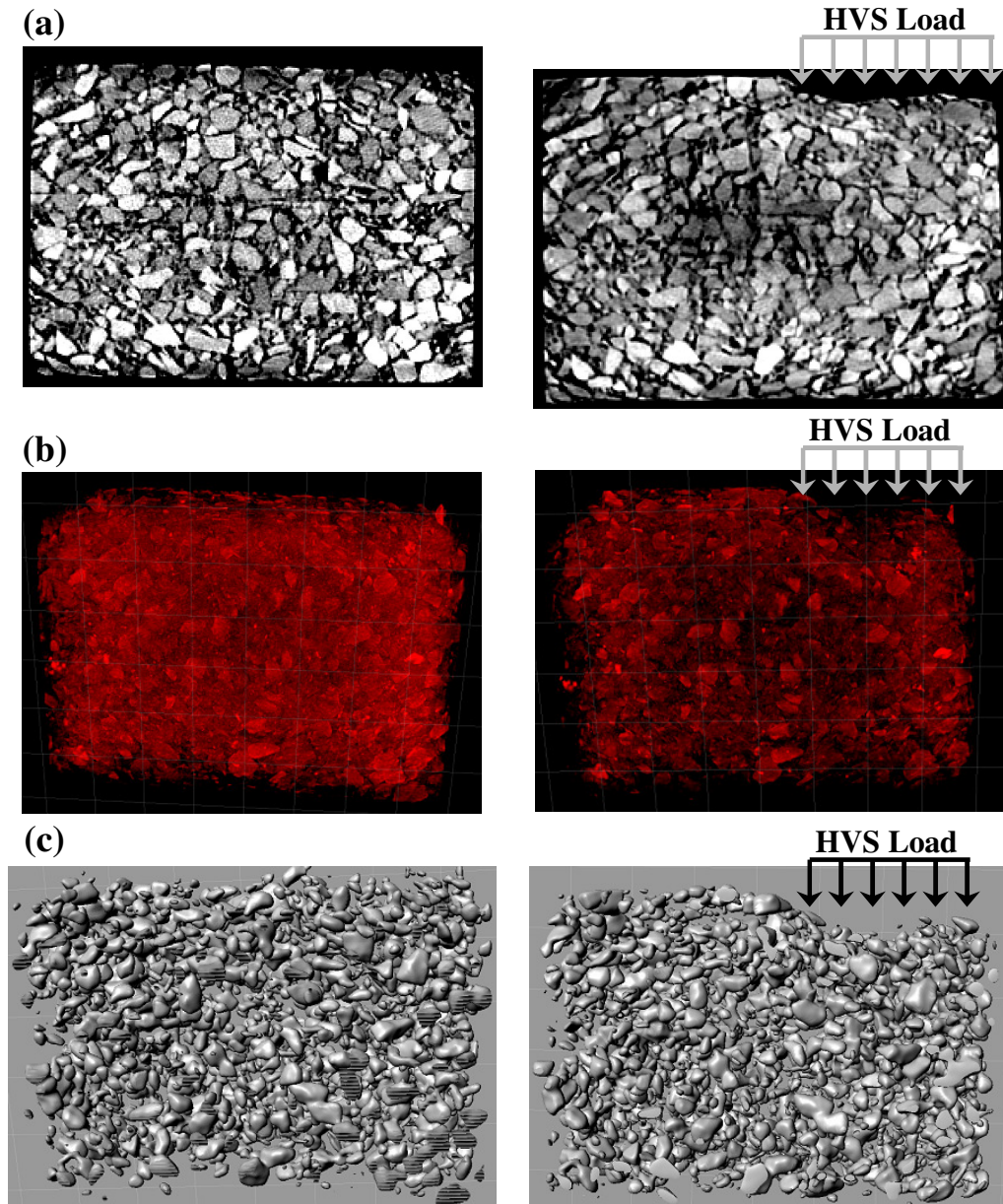
Figure 6.6 The procedure followed for aggregate domain creation (a) Unprocessed 2D X-ray CT image used for the development of image stacks (Left: Before HVS trafficking - Right: After HVS trafficking) (b) 3D images developed from X-ray CT image stacks (Left: Before HVS trafficking - Right: After HVS trafficking) (c) 3D aggregate volumes (Left: Before HVS trafficking - Right: After HVS trafficking)

Note: Direction of HVS traffic is out of the page.

The particle tracking algorithms of Imaris were used to determine the displacement field in AC blocks. Aggregate and spot tracking options of Imaris were evaluated to decide on the best method for the identification of displacement field. The aggregate tracking option basically determines the coordinates for the volume center of each aggregate for before and after trafficking. Based on the measured coordinates, vectors were created between before and after trafficking coordinates. These vectors basically show the permanent displacement field in the AC blocks.

The "spot object" feature of Imaris was also used for the development of the displacement fields. Adjacent voxels, which is a volume element representing a value on a regular grid in 3D space, with close intensity values were combined to form spots in before- and after-trafficking images. Similar to aggregate tracking, coordinates for each spot in before- and after-trafficking images were determined and used for displacement vector development. The major advantage of using spots for tracking is due to large number of vectors that can be created in AC block volumes. With this method, the displacement field can be more effectively produced to visualize the general shear and densification related flow under HVS trafficking. It is also not necessary to assign geometrical shape parameters for the shape identification in the spot object option, unlike the aggregate tracking option, which reduces the probability of having false-tracking. Figure 6.7 shows the differences between the two algorithms. It can be observed that the displacement field and the plastic shear flow can be clearly visualized when spots object is used. On the other hand, the general displacement trend cannot be clearly captured

However, increasing the load did not have any significant effect on the rutting accumulation rate. Earlier failure was observed for the thick RHMA-G section (611HB). The average maximum rut depth is approximately two times greater than the downward rut depth for both of the PG64-28PM sections, and nearly three times greater for both of the RHMA-G sections, indicating that shearing of material to the side of the wheelpath is as important a contributor or more important than the downward rut.
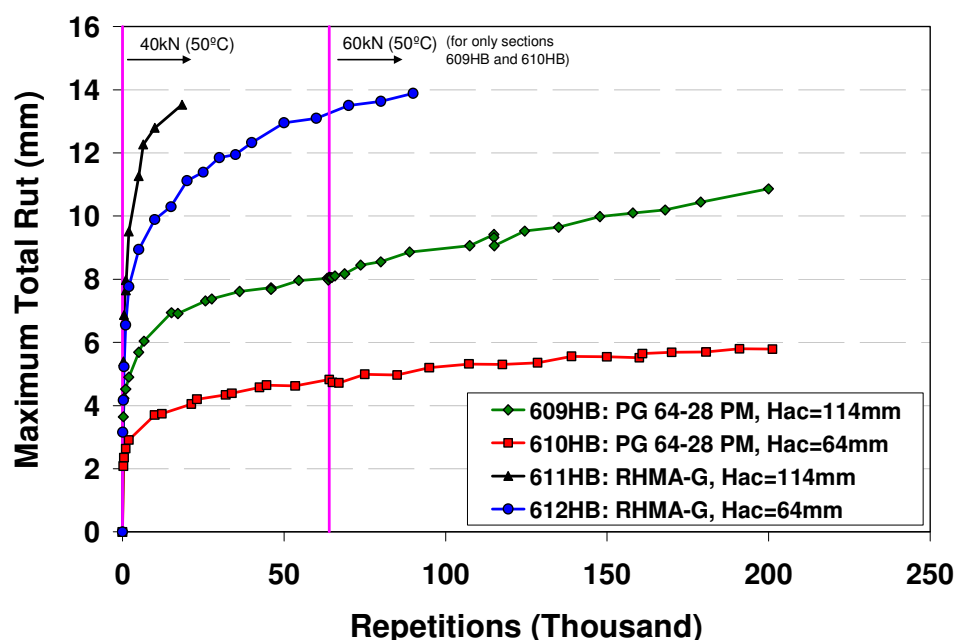
Figure 6.8 Comparison of average maximum rut.

Profilometer measurements were also taken on the AC blocks at many load intervals. Figure 6.9 shows the block surface deformation at the end of HVS testing. It can be observed that part of hump (right next to HVS tire) and rut (under HVS tire) created by HVS loading were captured by the profilometer on the AC blocks to be able to compare the shear flow and densification with X-ray CT imaging.
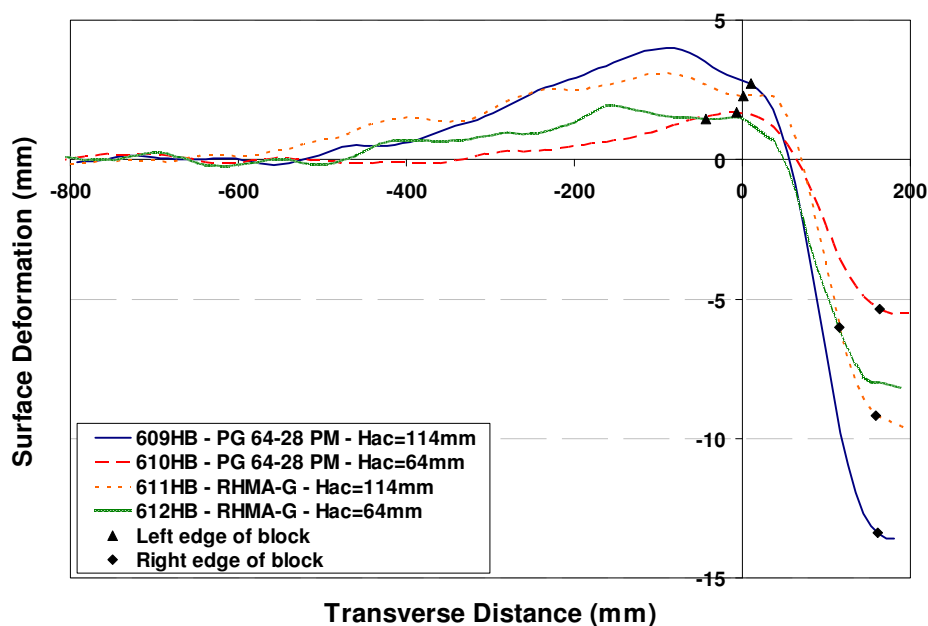
Figure 6.9 Final surface profile on AC blocks.

6.7.2   *Changes in 3D air-void distributions with HVS loading-Investigation of vertical profile*

Changes in air void content distributions with HVS trafficking were investigated by comparing the X-ray CT images taken before and after testing. The purpose was to determine the contribution of densification (air void reduction) to total downward surface rut along the depth of the AC layer. Figure 6.10 shows the changes in air void contents after HVS trafficking for the AC block of section 609HB - PG64-28PM with 114mm thickness. In order to determine the change in air void content, air void content distributions, similar to Figure 6.5, for both before and after trafficking images were calculated for hump (right next to HVS tire) and wheelpath locations. Before-trafficking air void content distributions were subtracted from the after trafficking distributions to calculate the change in air void content distributions. The areas under change in air void

content curves for the unit volume thickness (2.93 mm) were calculated to determine the distribution of densification related rutting along the thickness of the AC layers.
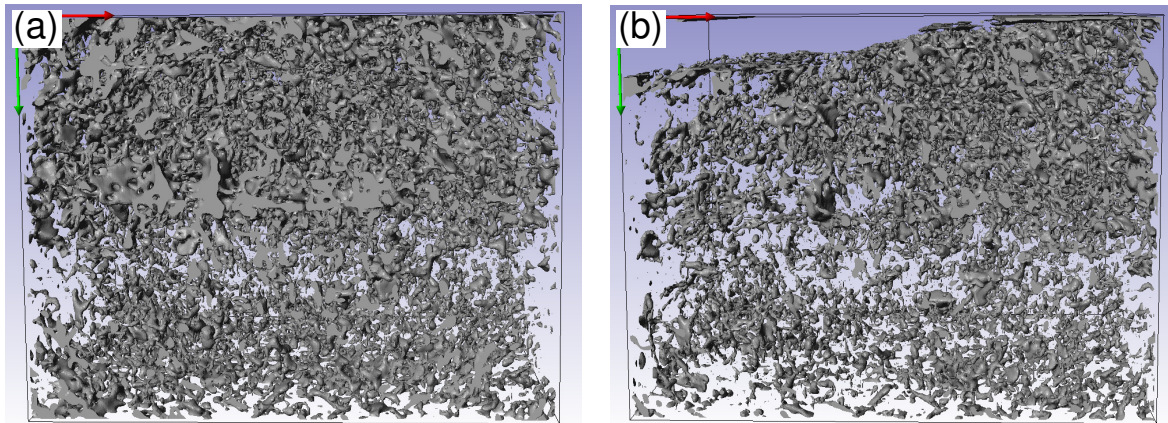
Figure 6.10 The changes in air void contents after HVS trafficking for the AC block of section 609HB - PG64-28PM 114mm thick (colored volumes are air-voids) (a) Before trafficking (b) After trafficking.

Note: Direction of HVS traffic is out of the page, wheelpath on left half of images.

Figure 6.11 shows the calculated distributions for rutting caused by densification for block 1 of all HVS test sections. It can be observed that sections with RHMA-G mix (611HB and 612HB) experienced more uniform densification related rutting, which was a result of the uniform constructed air void content distributions (see Figure 6.5). For sections constructed with PG64-28PM mix, high air void contents at the bottom of each lift caused large densification related rutting. In order to determine the contribution of densification related rutting to total downward rut, rut depths in Figure 6.11 were summed up and compared with the measured downward rut on AC blocks (Table 6.3). In addition, the contribution of densification at the bottom 8.7 mm of each lift to total downward rut was calculated. Results show that although average air void contents of

RHMA-G were 37 percent higher than PG 64-28PM, the contribution of air void reduction to total downward rutting was close for all test sections. This result suggests that earlier failure of sections with RHMA-G mix was actually a result of the shear related deformation. Displacement fields for each section will be analyzed to investigate the reasons behind the faster shear failure for RHMA-G mixes.

Results further indicated that 43 percent of densification for the thick-PG64-28PM section accumulated at the bottom 8.7 mm of top and bottom construction lifts while this number increased to 67 percent for the thin-PG64-28PM section. This result suggests that localized compaction problems related to large NMAS can cause large densifications around these poorly compacted locations.
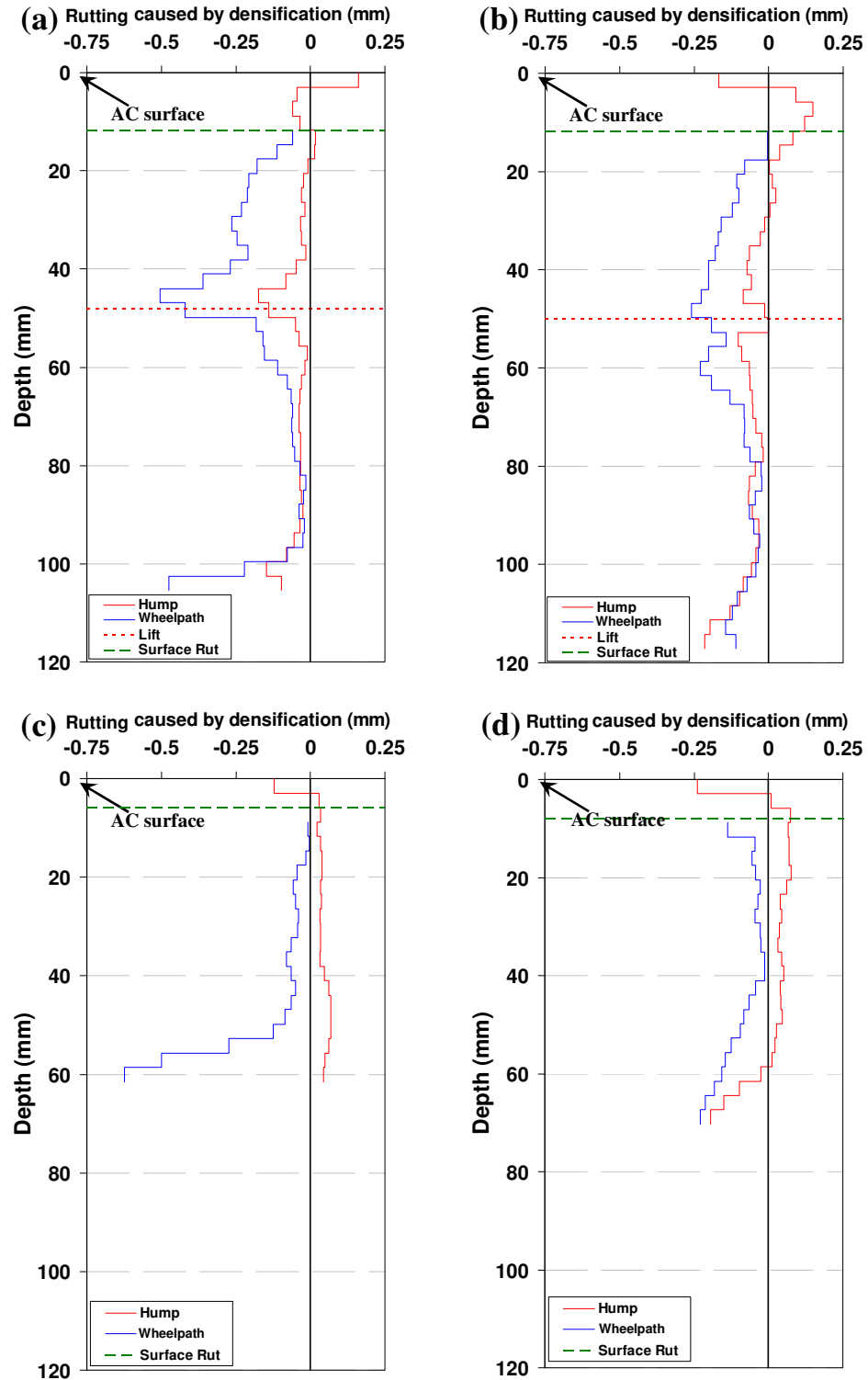
Figure 6.11 Calculated distributions of rutting caused by densification for block 1 of all HVS test sections (a) Section 609HB - PG64-28PM - 114mm (b) Section 611HB - RHMA-G - 114mm (c) Section 610HB - PG64-28PM - 64mm (d) Section 612HB - RHMA-G - 64mm.

Table 6.3 Contribution of densification related rutting to overall downward rut in the wheelpath.

Section	Thickness (mm)	Mix Type	Downward rut (mm)	Densification rut (mm)	Densification lift[a] (mm)
609HB	114	PG 64-28PM	13.42	5.19	2.25
610HB	64	PG 64-28PM	5.37	2.11	1.41
611HB	114	RHMA-G	9.22	4.07	0.94
612HB	64	RHMA-G	6.02	1.89	0.62

[a] Densification lift: Total densification related rutting at the bottom 8.7 mm of each lift.

6.7.3 Changes in 3D air-void distributions with HVS loading-Investigation of horizontal profile

The changes in air void content profiles were determined by comparing the air void content distributions of AC blocks before and after HVS testing. 3D image of AC blocks were divided into 2.93 mm thick volumes along the horizontal direction. The volumetric air void content for each volume was calculated with Simpleware software (2010) to determine the distribution of air voids within the AC blocks in the horizontal direction. The calculated change in air void content percentages for each unit volume were multiplied by the height of the volume slice to calculate the air void content related surface deformation. Changes in block surface profile with HVS trafficking were also determined by taking surface profilometer measurements on the blocks before and after testing.

Four blocks were sawn from each HVS test section (16 blocks from 4 HVS rutting sections) to get the complete deformation profile (Figure 6.3). AC blocks were distributed over the HVS test sections to avoid localized failure problems around the blocks. Because sections with thick AC layers have strain gauges at 50 mm depth, only one block was

sawn from the upper wheel path of the thick-AC sections (609HB and 611HB) in order not to cause any damage to the strain gauge cables. Thus, only half of the inner wheelpath profiles were analyzed in this study for the thick-AC sections.

Profilometer-measured (total) and air void related surface deformation, calculated from X-ray CT images, profiles are given in Figure 6.12. It can be observed that a significant amount of densification occurs under the wheelpaths. In addition, air voids were observed to be translated laterally by the shear stresses caused by HVS trafficking. On each block, the locations close to the humps (next to the wheelpath) were exposed to smaller densification related downward deformations while even upward movements were observed for sections with thinner AC layers (Figure 6.12c and Figure 6.12d) as a result of the shear related air void movement.
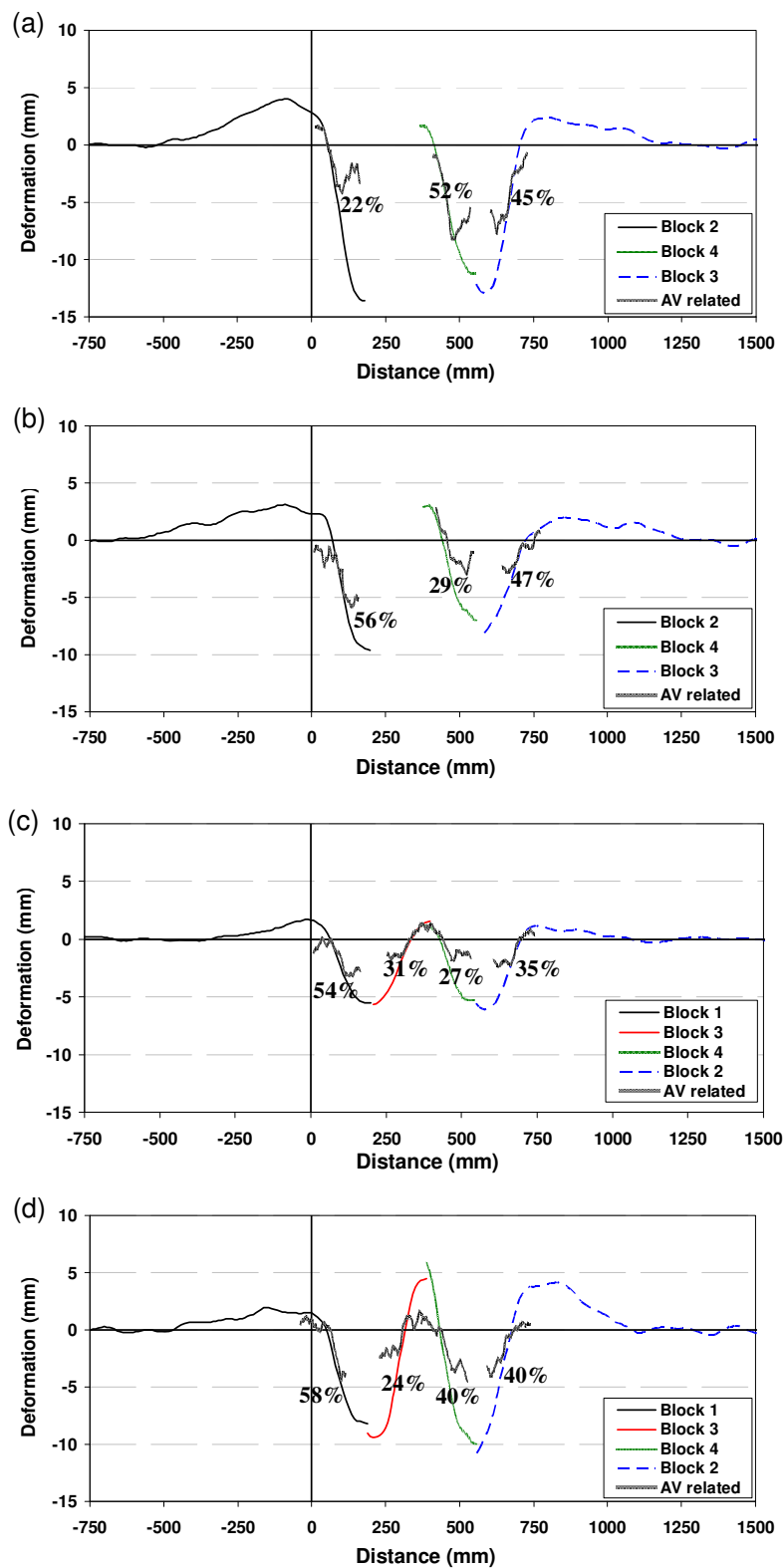
Figure 6.12 Comparison of profilometer-measured and air void related surface deformation profiles (a) PG64-28PM - Hac=114mm (b) RHMA-G - Hac=114mm (c) PG64-28PM - Hac = 64mm (d) RHMA-G - Hac= 64mm.

The contribution of air void reduction related deformation (densification) to the total accumulated surface deformation was determined by comparing the profiles given in Figure 6.12. The air void reduction related deformation in the wheelpath, was isolated from the complete block densification profile to calculate the average air void reduction related rutting under the HVS wheel. The ratio of densification related deformation to the total surface downward deformation was determined for each block and is shown as a percentage on the profile curves in Figure 6.12. The average contribution of densification related deformation to the total surface deformation was determined to be 40, 44, 37 and 41 percent for thick-PG 64-28PM, thick-RHMA-G, thin-PG 64-28PM and thin-RHMA-G sections, respectively. This result shows that significant part of the measured downward rut was actually a result of the densification. In addition, although the average air void content of RHMA-G blocks was 37 percent higher than PG 64-28PM blocks according to the CoreLok measurements, the contribution of air void reduction to total downward rutting was close for both mix types at both thicknesses.

The rutting performance of the HVS test sections was determined by collecting profilometer data at specific intervals throughout the tests. The measured average downward rut depth, defined as the downward deformation compared to the original pavement surface, averaged along the test section, for all test sections is given in Figure 6.13. The wheel load for the two sections with the PG64-28PM mix (609HB and 610HB) was increased from 40 kN to 60 kN at around 64,000 repetitions. However, increasing the load did not have any significant effect on the rutting accumulation rate. Earlier failure was observed for the thick RHMA-G section (611HB).
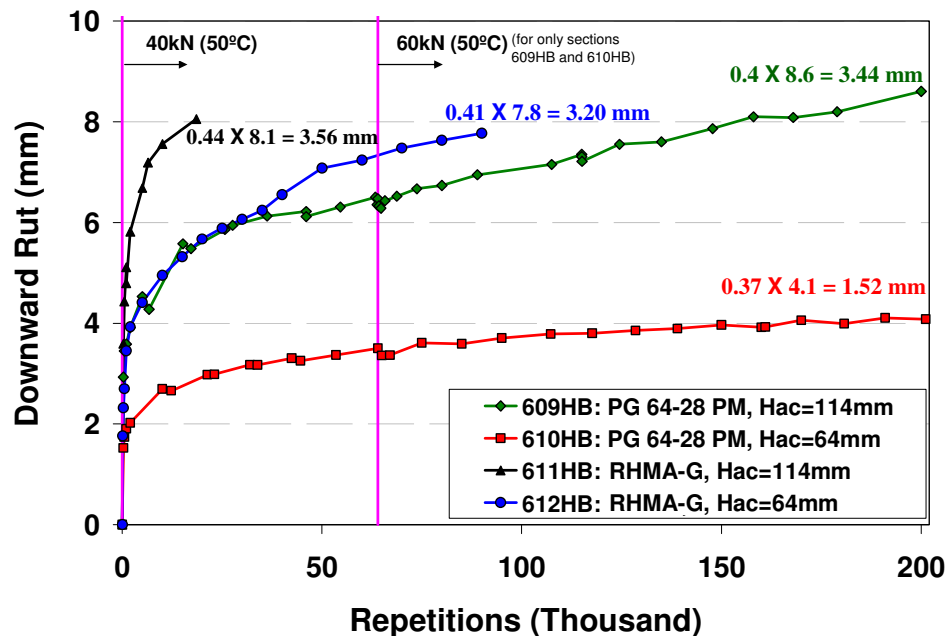
Figure 6.13 Comparison of downward rut.

The densification related portion of the measured downward rut was determined by multiplying the measured downward rut at the end of HVS tests with the calculated densification percentages (see Figure 6.13). Because at the start of the HVS testing, air voids will quickly dissipate under the HVS wheel, this reduction in air void content can be assumed to directly affect the initial phase of the rutting accumulation.

Figure 6.14 shows the repetitions at which densification related surface deformation was completely accumulated (called the "densification limit"). The rest of the deformation accumulated after the densification limit is reached will be mostly related to shear related particle movement. It can be observed that densification related deformation was accumulated within the first 1000 repetitions. Although earlier failure was observed for the thick-RHMA-G section, downward rut at the densification limit was close for all test

sections. In other words, it is not possible to predict the future rutting performance of the sections from the densification because it was approximately the same. Shear related deformation appears to control the long term rutting performance of the test sections while densification was just an initial contributor at the very earlier stages of the trafficking. For that reason, shear related particle movement in the AC blocks needs to be analyzed to describe the failure mechanisms of different mix and structure types of this study.
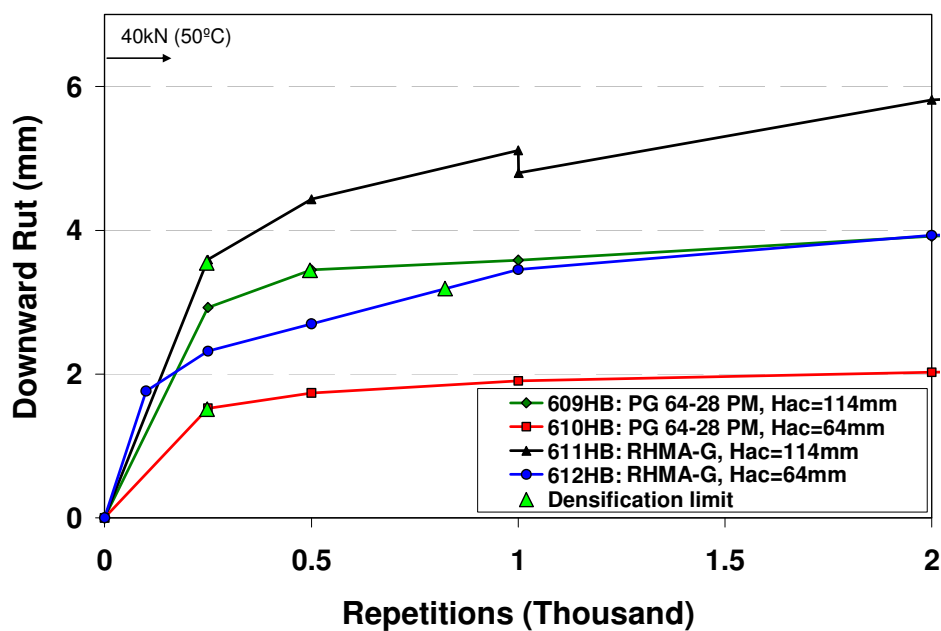
Figure 6.14 The effect of densification on downward rut at the initial stages of the HVS tests.

6.7.4   Changes in 3D aggregate distributions with HVS loading - Particle tracking

After the formation of the 3D aggregate structures from the X-ray CT images, the "spot particle" tracking algorithm of Imaris was used to determine the displacement field in AC blocks. Adjacent voxels, which is a volume element representing a value on a regular grid in 3D space, with close intensity values were combined to form spots in before and after trafficking X-ray CT images. Coordinates for each spot in before and after trafficking AC blocks were determined and used for displacement vector development. Spots that were furthest from the HVS load (at the bottom of the block) were assumed to be stationary after HVS trafficking. These spots were used as reference points to match before and after trafficking images. It should be noted that no significant differences between the displacement fields were observed when different spots (furthest from the HVS load) were used as reference. This result suggested that movements of the spots that are furthest from the HVS load were negligible and they can be used as reference points for particle tracking.

Figure 6.15 shows the distribution of displacement vectors for one of the outer tire edge blocks for all HVS test sections. Two shear flow patterns can be observed for thick sections (609HB and 611HB), one flow to the hump and the other to the opposite direction under the tire. For thin sections, only shear flow to the hump part was observed. In addition, significant shear related upward movement can be observed at the upper part of the humps for the sections constructed with the RHMA-G mix. This movement caused larger humps which consequently increased the maximum deformation (top of the hump

to bottom of the rut) for these sections. This result can be accepted to be the major cause of earlier failure for these sections.

Figure 6.15 Distribution of displacement vectors for one of the outer tire edge blocks of all HVS test sections (Front view) (a) Section 609HB - PG64-28PM - 114mm (b) Section 611HB - RHMA-G - 114mm (c) Section 610HB - PG64-28PM - 64mm (d) Section 612HB - RHMA-G - 64mm.

Note: Direction of HVS traffic is out of the page.

In order to quantitatively evaluate the upward shear movement, first displacement vectors in the hump of the blocks were isolated from the wheelpath. Then, displacement vectors at the bottom half of the isolated hump block were excluded for upward shear flow evaluation. The projections of the displacement vectors onto the XY plane were determined and used to calculate the angle between this projected vector and the positive

X axis. This calculated angle value was assumed to be an indicator for the type and extent of shear flow at the humps.

Rose histograms, which is a polar plot showing the distribution of values grouped according to their numeric range, were used to present the angle distributions for each block. Results are given in Figure 6.16. It can be observed that there is very little upward movement observed for the thick-PG64-28PM (Figure 6.16a) section. On the other hand, a significant amount of upward movement was observed for the thick-RHMA-G section (Figure 6.16b).

When the histograms for the thin-PG64-28PM (Figure 6.16c) and thin-RHMA-G (Figure 6.16d) sections were compared, again a higher level of upward movement was observed for the section with RHMA-G mix. This result suggests that RHMA-G mixes are more prone to upward shear movements and can be considered to show more dilative behavior when compared to PG64-28PM mixes. In order to determine the effect of layer thickness on upward shear movement, rose histograms for thick and thin sections were separately compared for the same mix type. Result show that sections with thinner AC layers are more prone to upward shear movement when compared to thicker sections. However, the effect of layer thickness on measured angles does not appear to be as significant as the effect of mix type.
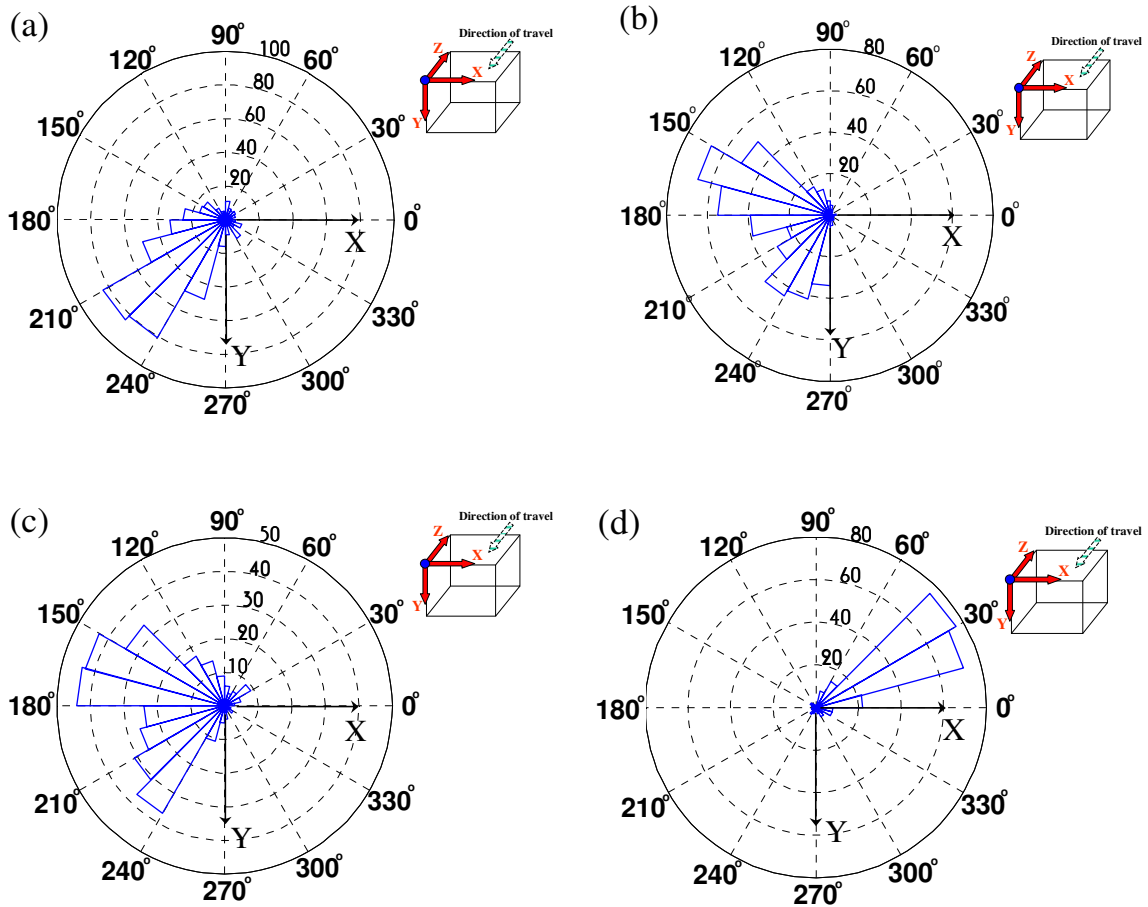
Figure 6.16 Rose histograms showing the distributions of calculated angles (a) Section 609HB - PG64-28PM - 114mm (b) Section 611HB - RHMA-G - 114mm (c) Section 610HB - PG64-28PM - 64mm (d) Section 612HB - RHMA-G - 64mm.

Note: For the AC block of Section 612HB - RHMA-G - 64mm, different from the other sections, HVS trafficking was applied on the left side of the block (See Figure 6.15).

In order to determine the pattern of the displacement field in the direction of traffic (Z direction), top-view for the AC block displacement field is given in Figure 6.17. A significant shear flow pattern can be observed in the direction of traffic (Z direction) for sections constructed with RHMA-G mix. In addition, larger displacement vectors in the

direction of traffic were observed at the hump part of the thin-RHMA-G section (612HB).

Large shear flow in the direction of traffic can be accepted to be another contributor to earlier failure of sections constructed with RHMA-G mix (611HB and 612HB). The movement in the direction of traffic can be related to the fact that the HVS wheel is pushed, as opposed to being a traction wheel. The movement in the Z direction would likely be in the opposite direction for a traction wheel. This suggests that the passing of traction and pushed wheels on a truck would produce potentially important shear reversals in the wheel paths and to some degree in the humps. The differing performance of the two mixes in the Z direction is a result of the differences between the aggregate shape, gradation and size of two mix types. In addition, high air void content for the RHMA-G mix might have induced the excessive shear flow. In other words, although high air void content for the sections constructed with RHMA-G mix was expected to cause larger densification related rutting and earlier failure related to this densification, the actual reason behind the earlier failure was determined to be the gap gradation and small aggregate size resulting in greater shear flow.
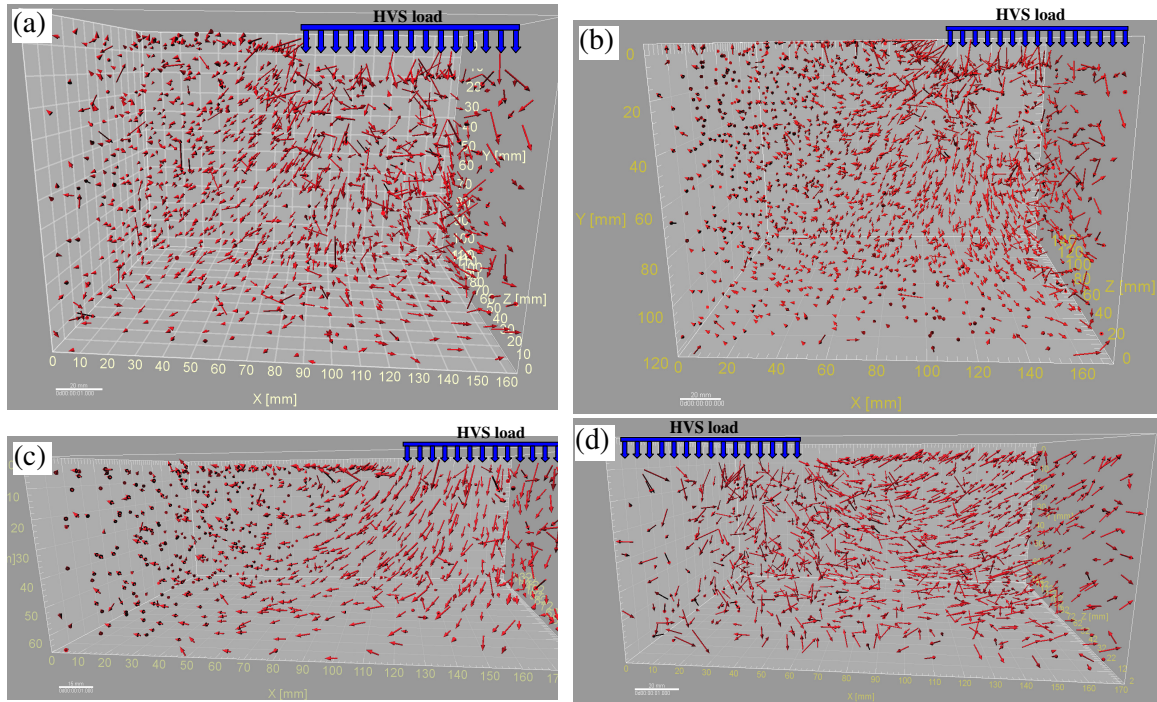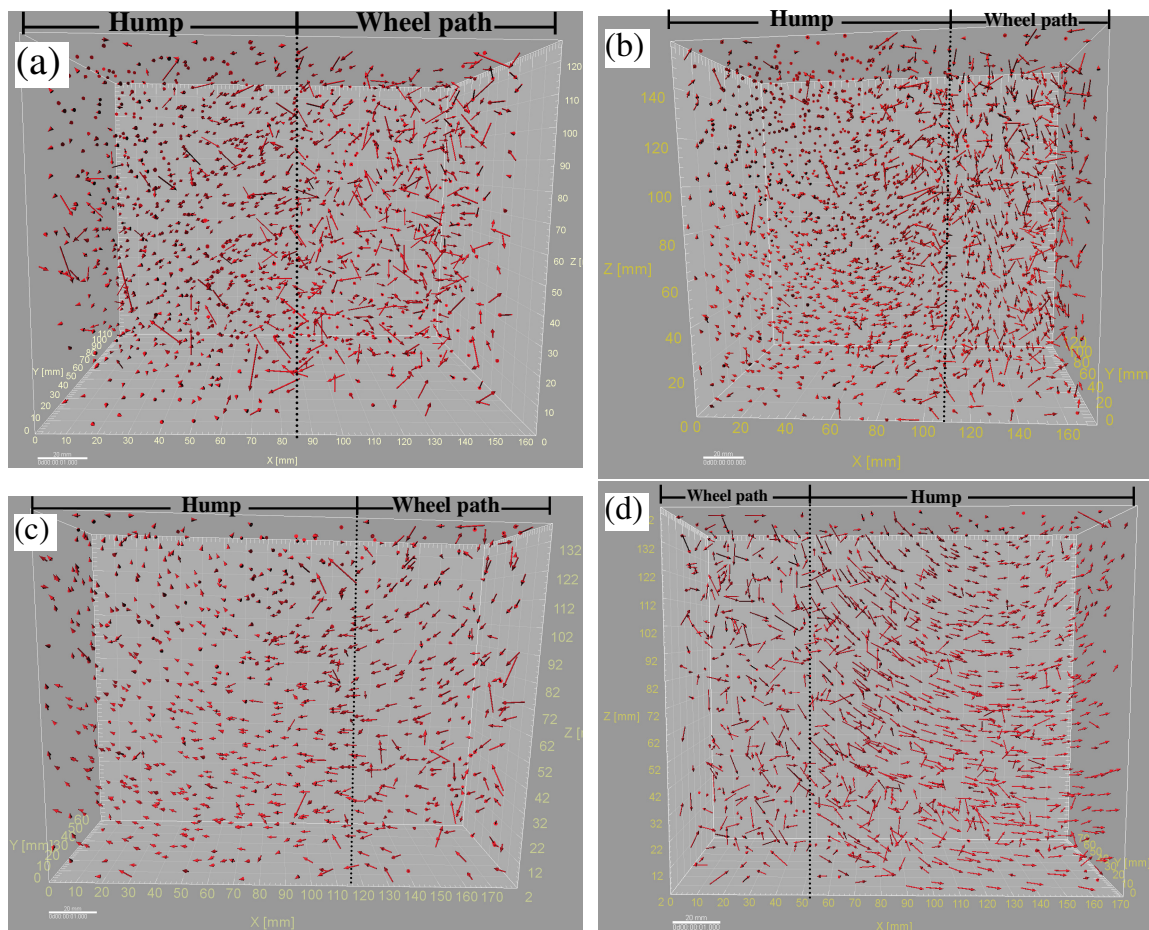
Figure 6.17 Distribution of displacement vectors for block 1 of all HVS test sections (Top view) (a) Section 609HB - PG64-28PM - 114mm (b) Section 611HB - RHMA-G - 114mm (c) Section 610HB - PG64-28PM - 64mm (d) Section 612HB - RHMA-G - 64mm.

Note: Direction of HVS traffic is from top to bottom.

6.7.5   Laboratory test results

Because shear related deformation was determined to be the major contributor to measured surface rutting, the effects of aggregate and binder properties on the shear related deformation needed to be identified. In order to understand the effects of binder properties on rutting performance, FSCH were performed on RHMA-G and PG64-28PM

mastic samples. Binders and aggregates for mastic sample preparation were taken from the plant which provided the asphalt mixtures for construction. As a result of the high binder content used for mastic sample preparation, air void content for the mastic samples was determined to be negligible. Thus, results of the mastic sample tests were assumed to provide only the actual shear performance of asphalt mastic without any air voids. In addition, test results were further used for micromechanical finite element model development, which provided important information about the aggregate movement under FSCH testing in this study.

FSCH tests were conducted with mastic samples at seven loading frequencies, 0.1 Hz, 0.2 Hz, 0.5 Hz, 1 Hz, 2 Hz, 5 Hz, and 10Hz, and three temperatures, 30oC, 40oC and 50oC under a controlled shear strain level of 0.2 %. Figure 6.18 illustrates the mastic test results. Results showed that although earlier rutting failure was observed for the HVS test sections constructed with RHMA-G mixes, higher shear resistance was observed for the RHMA-G mastic samples at all loading frequencies and temperatures. This result suggests that earlier failure of RHMA-G mix under HVS testing was not a result of the low shear resistance of the mastic. Thus, by deduction, earlier failure can be attributed to the gap gradation and smaller aggregate size induced excessive shear flow. In order to evaluate the aggregate movement pattern under shear testing, 2D micromechanical finite element models were developed for both mix types.
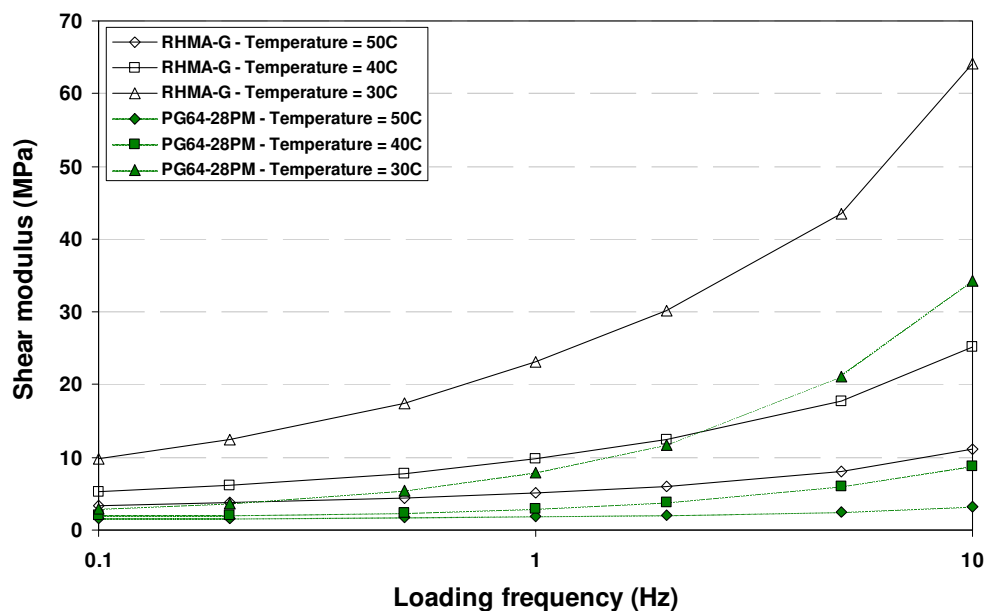
Figure 6.18 FSCH test results for the RHMA-G and PG64-28PM mastic samples.

6.8 MICROMECHANICAL FINITE ELEMENT MODELING FOR SHEAR PERFORMANCE EVALUATION

The viscoelastic micromechanical finite element model given in Chapter 5 was used for simulation of particle movement under shear testing. Aggregates were assumed to be stiff-elastic materials while a linear viscoelastic model, developed from FSCH mastic tests, was used to simulate the mastic behavior. Temperature dependency of the mastic was defined by using Williams-Landel-Ferry (WLF) equation (Williams et al., 1955). Time dependency of mastic phase was simulated based on a generalized Maxwell-type viscoelastic model. The model consists of two basic units, a linear elastic spring and a linear viscous dash-pot. Various combinations of these spring and dashpot units define the type of viscoelastic behavior. One spring and five Maxwell elements in parallel were used for the mastic model. To predict the global viscoelastic behavior of the asphalt

mixture, time-temperature dependent finite element analysis was conducted by combining the elastic aggregate, viscoelastic mastic and empty air void subdomains.

FSCH tests were simulated by applying a cyclic shear load at the upper loading platen that is glued to asphalt sample while maintaining the sample height constant during this loading. The bottom loading platen was fixed in the test setup that was used for this study. For the 2D finite element simulation, a constant sinusoidal shear strain of 0.2% was applied. Since the specimen height was 48 mm for asphalt mixture samples, cyclic displacement-based loading (strain controlled) was applied by fixing the peak upper platen movement at 0.096 mm for all cases. Simulations were conducted at a target temperature of 50°C because the HVS tests were conducted, at that temperature. In order to determine the loading frequency of finite element model simulations, strain gauge outputs from HVS test sections were analyzed. The average HVS loading frequency for the 8.7 km/hr wheel speed, calculated from a transverse strain gauge was determined to be 0.2Hz and used as the cyclic loading frequency for the FSCH test simulations. Because the standard FSCH test is an unconfined test, confining pressures were not applied around the sample walls (AASHTO, 2003).

Figure 6.19 shows the distributions of Von Mises stresses in 2D AC models. It can be observed that larger stresses needed to be applied for the PG64-28PM mix than the RHMA-G mix to achieve the same peak horizontal movement of 0.096 mm at the upper loading platen. This result suggests that PG64-28PM mix is more resistant to shear forces. Because analysis for the change in air void content distributions for the HVS AC

blocks showed that shear related deformation directly controls the long term rutting performance of the test sections, faster rutting failure would be expected to happen for the RHMA-G mix with significantly lower shear resistance.

(a)

(b)
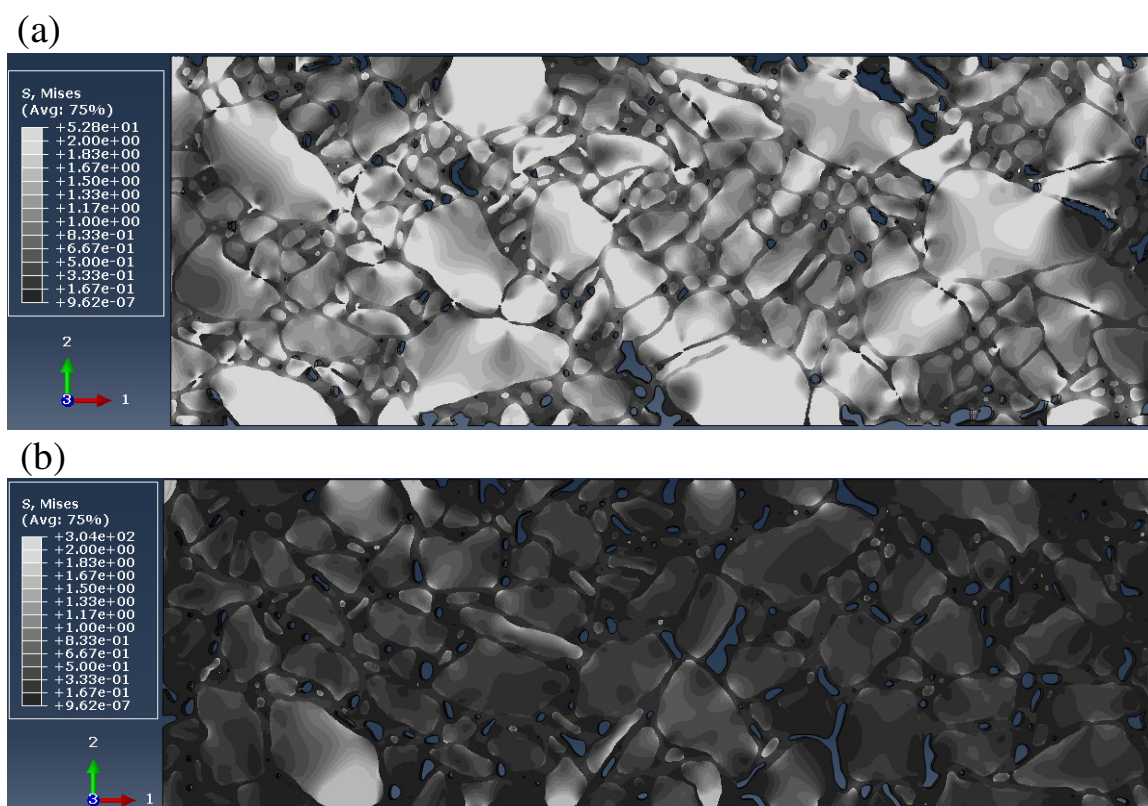
Figure 6.19 Distribution of Von Mises stresses in 2D AC models (a) PG64-28PM mix (b) RHMA-G mix.

In order to evaluate the dilative behavior of RHMA-G and PG64-28PM mixes, distributions of vertical displacement vectors (U2) for both mix types were given in Figure 6.20. Vectors in white color are showing the upward movement while black vectors represent the movement in the downward direction. Shear load was applied at the top of the samples in positive direction 1 (left to right) while constant sample height was

maintained. Although the sample height was kept constant to avoid the sample volume change during the tests, significant vertical movements were observed in the sample microstructure. RHMA-G mix was exposed to higher levels of internal vertical displacements than the PG64-28PM mix. This result points out a more dilative behavior for the RHMA-G mix which also caused large upward shear movements and resulted in larger humps on HVS test sections constructed with the RHMA-G mix. In addition, vertical displacement vectors were observed to be more uniformly distributed in the RHMA-G mix while localization of positive and negative direction vectors was observed for the PG64-28PM mix. The greater aggregate interlock in the PG64-28PM mix, as a result of the dense gradation and larger aggregate sizes, resulted in greater aggregate interaction which consequently caused the more efficient dissipation of shear stresses and created larger shear resistance. The lack of this interlocking effect for the RHMA-G mix caused the earlier failure on HVS test sections.

(a)

(b)
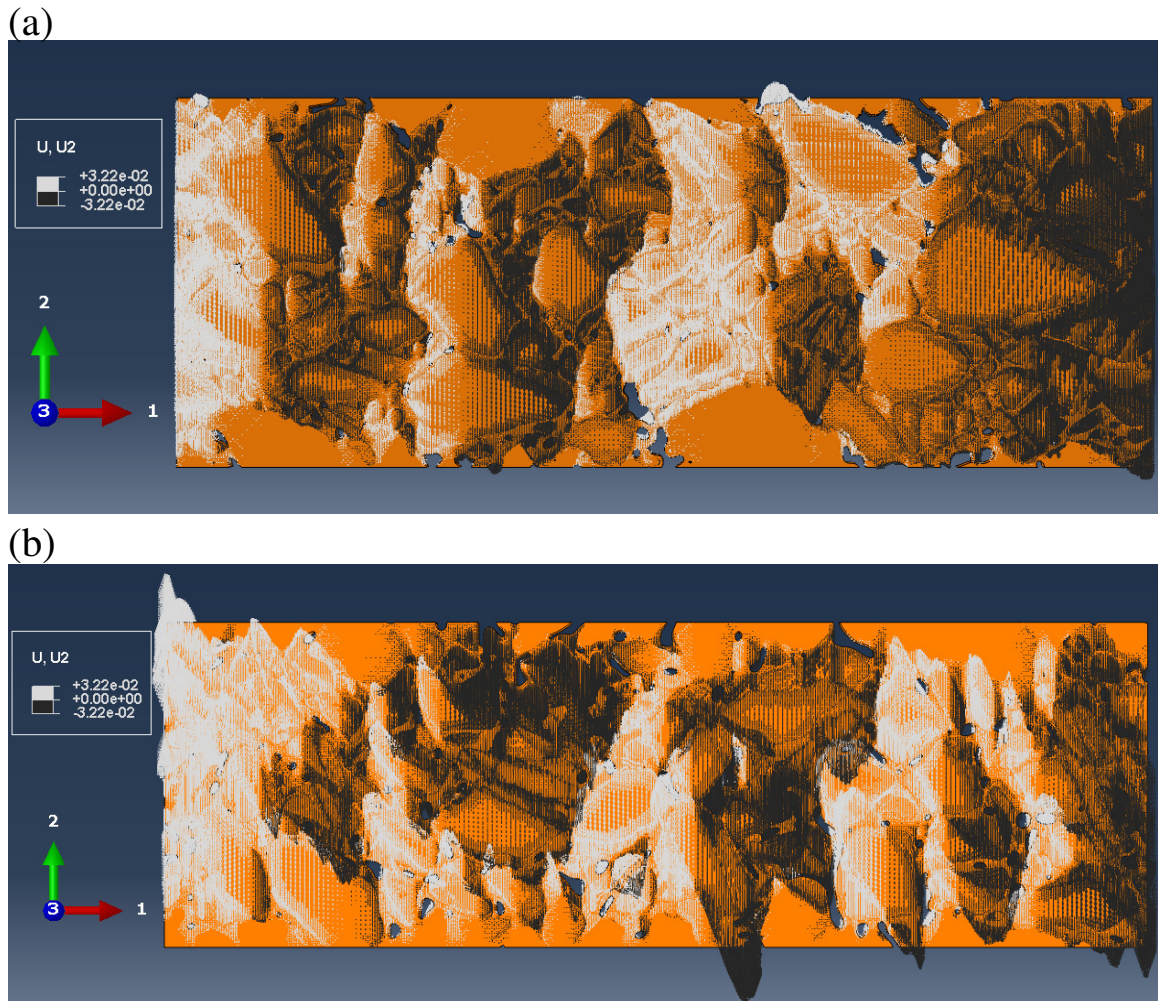
Figure 6.20 Distributions of vertical displacement vectors (U2) (a) PG64-28PM mix (b) RHMA-G mix.

6.9   CONCLUSIONS

In this study, a micromechanical investigation was performed to evaluate the differences between the rutting accumulation mechanisms of RHMA-G and PG64-28PM mixes for two layer thicknesses. Deformed and un-deformed 3D air-void and aggregate distributions determined from X-ray CT imaging were compared to evaluate the changes in air-void content distributions and aggregate positions under HVS trafficking. In order

to understand the effects of binder properties on rutting performance, shear frequency sweep tests were performed on rubberized and polymer modified mastic samples. A viscoelastic finite element model was also developed to investigate the aggregate movement and interlocking properties under applied shear forces.

Results of this study can be summarized as follows.

1. Sections constructed with RHMA-G mixes had more uniform air void content distributions due to the smaller NMAS. Thus, these sections experienced more uniform densification related rutting while sections constructed with PG64-28PM mixes had more localized densifications.

2. 43 percent of densification for the thick-PG64-28PM section accumulated at the bottom 8.7 mm of top and bottom construction lifts while this number increased to 67 percent for the thin-PG64-28PM section. This result suggests that localized compaction problems related to large NMAS for the PG64-28PM mix can cause large densifications around these poorly compacted locations.

3. Two shear flow patterns were observed for thick sections (609HB and 611HB), one flow to the hump and the other to the opposite direction under the tire. For thin sections, only shear flow to the hump at the sides of the wheelpath was observed.

4. A significant shear flow pattern in the direction of traffic (Z direction) was observed for sections constructed with RHMA-G mix. In addition, larger displacement vectors in the direction of traffic were observed at the hump of the thin-RHMA-G section. The movement in the direction of traffic can be related to the fact that the HVS wheel is pushed, as opposed to being a traction wheel. This greater shear flow in the

direction of traffic can be accepted to be another contributor to earlier failure of sections constructed with RHMA-G mix.

5. Changes in air void microstructure in AC blocks under HVS trafficking showed that significant part of the measured surface rut, on the order of 40 percent, was actually a result of the densification. The average contribution of densification related deformation to the total surface deformation was determined to be 40, 44, 37 and 41 percent for thick-PG 64-28PM, thick-RHMA-G, thin-PG 64-28PM and thin-RHMA-G sections, respectively. In addition, although the average air void content of the RHMA-G blocks was 37 percent higher than the PG 64-28PM blocks according to the CoreLok measurements, the contribution of air void reduction to total downward rutting was similar for all test sections.

6. Integration of the HVS surface rutting measurements and densification percentages showed that densification related deformations for all HVS test sections were accumulated within the first 1000 repetitions. Although earlier failure was observed for the thick-RHMA-G section, downward rut at the densification limit was close for all test sections. Thus, shear related deformation appears to control the long term rutting performance of the test sections while densification was a contributor at the very earlier stages of trafficking.

7. Displacement vectors developed by comparing the X-ray CT images of AC blocks taken before and after HVS testing showed that significant shear related upward movement occurs at the upper part of the humps for the sections constructed with the RHMA-G mix. This movement caused larger humps which consequently increased

the maximum deformation for these sections. This result can be accepted to be the major cause of earlier failure for these sections.

8. FSCH tests performed with mastic samples revealed that RHMA-G mastic is more resistant to shear forces at all loading temperatures and frequencies. This result suggests that earlier failure of RHMA-G mix under HVS testing was not a result of the low shear resistance of the mastic.

9. Viscoelastic micromechanical finite element analysis showed that although shear resistance of the PG64-28PM mastic samples were significantly lower than the RHMA-G mastic samples, PG64-28PM mix appears to be more resistant to shear related deformation. This higher resistance is a result of the denser gradation and larger aggregate size for the PG64-28PM mixes.

10. Comparison of the vertical displacement fields for the 2D micromechanical finite element models showed that RHMA-G mix was exposed to higher levels of vertical displacements than the PG64-28PM mix. This result points out a more dilative behavior for the RHMA-G mix which also caused large upward shear movements and resulted in larger humps on HVS test sections constructed with the RHMA-G mix.

11. Vertical displacement vectors of the 2D finite element models were observed to be more uniformly distributed in RHMA-G mix while localization of positive and negative direction vectors was observed for PG64-28PM mix. More aggregate interactions in PG64-28PM mix, as a result of the dense gradation and larger aggregate sizes, allowed the aggregates to act in unison which consequently caused the more efficient dissipation of shear stresses and created greater shear resistance.

The lesser amount of this interlocking effect for RHMA-G mixes caused the earlier failure on HVS test sections.

CHAPTER 7   CONCLUSIONS AND RECOMMENDATIONS

7.1 CHALLENGES TO THIS THESIS STUDY

Micromechanical finite element models provide useful information in understanding the interactions between aggregate, air void and binder phases of composite asphalt concrete materials. The response of the asphalt concrete material under various loading frequencies, temperatures and boundary conditions can be evaluated based on the model outputs. However, such models require extensive meshing effort and massive numbers of nodes to describe the complex structure of the composite asphalt concrete material. As a result of the required complex mesh structure, excessive computational effort may be necessary to create the mesh structure and run the model.

Based on the experience gained from the developed micromechanical finite element model for a laboratory shear test, given in Chapter 5, possible computational time (with a

new generation computer with 12 CPUs) for a 3D viscoelastic micromechanical finite element model simulating the HVS trafficking was estimated to be around four months for a single case with one load level, temperature and loading frequency while it is not computationally possible to simulate the visco-elastic-plastic response of the pavement by applying thousands of HVS load repetitions for a single case with the capacity of today's computers. This result suggests that it is not computationally efficient to identify the 3D micromechanical response of HVS test sections by micromechanical finite element modeling.

Reasonable model run times can be achieved for 2D micromechanical finite element models. However, it was observed from 2D and 3D micromechanical model simulations that, due to the absence of aggregate interactions in the third dimension, 2D models always under predict the material performance and do not appear to be effective alternatives that can be used to explain the in-situ rutting failure phenomenon. Thus, reliable predictions can only be made by using 3D models for the estimation of shear performance.

Due to the described challenges, in this study, an empirical investigation was undertaken to measure the changes in asphalt concrete microstructure with HVS trafficking by comparing the X-ray CT images taken before and after HVS testing. Deformed and un-deformed 3D air-void and aggregate distributions were compared to determine the changes in air-void content distributions and aggregate positions. The primary purpose was to investigate rutting failure phenomenon by analyzing the interactions between

aggregate, binder and air void phases. Viscoelastic micromechanical finite element models developed for a laboratory shear test were also used to evaluate the shear resistance of different mix types.

7.2   RECOMMENDED CHANGES IN RSST-CH SPECIMEN DIMENSIONS

An innovative approach based on bootstrapping and Monte Carlo simulations was introduced to quantify the precision and bias in RSST-CH laboratory test results for different sized specimens and determine the effects of this precision and bias on predicted rutting performance. In addition, the required number of replicates in an experimental design for RSST-CH testing was determined based on the parameter PSS5000 and using the proposed ANOVA approach. It was concluded that when three or more replicate tests were used for testing, the effect of size-related bias on the variability of parameter PSS5000 will be at acceptable levels.

Results indicated that significant bias existed between the predicted rut depths of different specimen sizes as a result of the increasing shear resistance of asphalt concrete specimens with increasing volume. It was also observed that increasing the specimen size significantly decreases test variability. This conclusion is also coherent with the general theoretical background on specimen size induced variability for composite materials. It was further concluded that increasing testing temperature also increases the test results variability due to the increased difference between aggregate and mastic stiffness at high temperatures.

Based on the test results and analysis presented in Chapter 3, specimen size requirements for dense graded mixes were determined. For mixes with NMAS 9.5 mm, RSST-CH specimens should be close to Size 3 (172 x 143 x 58 mm) with length-to-height ratio of at least 3. An acceptable level of variability at temperatures 45°C and 55°C can only be achieved with Size 3 specimens. For mixes with NMAS 19 mm, Size 4 (229 x 192 x 77 mm) is recommended for RSST-CH testing at temperatures 45°C and 55°C. However, Size 3 specimens can also be used at 45°C since the level of variability for these specimens is tolerable at that temperature. It is worth mentioning in this regard that volumes for Size 3 and Size 4 specimens are 1.6 and 3.8 times larger than the volume for standard RSST-CH specimens, respectively.

7.3   A NEW RELIABILITY BASED RUTTING DESIGN METHOD

Estimating the variability in fundamental pavement design inputs and integrating this variability into the general performance prediction procedures is generally considered a required component of modern ME pavement design. Since all public agencies would like to have control over the risk that they take, design reliability levels and the corresponding costs for each level of reliability should be determined. However, the methods used for the incorporation of variability into the design procedures are generally not computationally efficient due to large numbers of simulations required to produce a robust predicted outcome distribution.

In Chapter 4, a reliability based design procedure was developed by evaluating the reliability based on the variability in laboratory test results, layer thicknesses, stiffnesses and measured in-situ performance. With the proposed method, the effects of input design parameters variability on predicted performance can be determined by evaluating the calculated distributions of calibration coefficients. By the use of calculated calibration coefficient distributions, the need for performing computationally intensive calculations within the design software for reliability evaluation is eliminated.

Results indicated that variability in measured rut depths (performance variability) of the HVS test sections causes high levels of variability in the calculated calibration coefficients. In addition, distributions of calibration coefficients calculated by using measured rut depths (performance variability) are very similar to calibration coefficient distributions calculated by using thickness and stiffness (construction) variability for most of the HVS test sections. This result suggests that variability in performance can be effectively predicted by using the variability in thickness and stiffness for HVS test sections.

On other hand, it was observed that precision of laboratory test results did not have much effect on predicted rutting performance when the effect of laboratory variability is simulated with construction or performance variability because high level of variability in measured performance, thickness and stiffness mask the effect of laboratory variability on calculated calibration coefficient distributions.

7.4   INVESTIGATION OF RUTTING FAILURE PHENOMENON AT A MICROMECHANICAL LEVEL

A micromechanical investigation was performed in Chapters 5 and 6 to evaluate the differences between the rutting accumulation mechanisms of RHMA-G and PG64-28PM mixes for two layer thicknesses. In Chapter 6, deformed and un-deformed 3D air-void and aggregate distributions determined from X-ray CT imaging were compared to evaluate the changes in air-void content distributions and aggregate positions under HVS trafficking. In order to understand the effects of binder properties on rutting performance, shear frequency sweep tests were performed on rubberized and polymer modified mastic samples. The viscoelastic micromechanical finite element model developed in Chapter 5 was also used to investigate the aggregate movement and interlocking properties under applied shear forces.

Changes in air void microstructure in AC blocks under HVS trafficking showed that significant part of the measured surface rut, on the order of 40 percent, was actually a result of the densification. This result suggested that although the average air void content of the RHMA-G blocks was 37 percent higher than the PG 64-28PM blocks according to the CoreLok measurements, the contribution of air void reduction to total downward rutting was similar for all test sections. Thus, shear related deformation appears to control the long term rutting performance of the test sections while densification was a contributor at the very early stages of trafficking.

Displacement vectors developed by comparing the X-ray CT images of AC blocks taken before and after HVS testing showed that significant shear related upward movement occurs at the upper part of the humps for the sections constructed with the RHMA-G mix. This movement caused larger humps which consequently increased the maximum deformation for these sections. This result can be accepted to be the major cause of earlier failure for these sections. A significant shear flow pattern in the direction of traffic (Z direction) was also observed for sections constructed with RHMA-G mix. This greater shear flow in the direction of traffic can be accepted to be another contributor to earlier failure of sections constructed with RHMA-G mix.

FSCH tests and viscoelastic micromechanical finite element analysis showed that although shear resistance of the PG64-28PM mastic samples were significantly lower than the RHMA-G mastic samples, PG64-28PM mix appears to be more resistant to shear related deformation. This higher resistance is a result of the denser gradation and larger aggregate size for the PG64-28PM mixes. More aggregate interactions in PG64-28PM mix, as a result of the dense gradation and larger aggregate sizes, allowed the aggregates to act in unison which consequently caused the more efficient dissipation of shear stresses and created greater shear resistance. The lesser amount of this interlocking effect for RHMA-G mixes caused the earlier failure on HVS test sections.

7.5   RECOMMENDATIONS FOR FUTURE RESEARCH

Although the results obtained in this study provide a great deal of insight, further study is required to extend the analysis. The following recommendations are made for future research on rutting performance prediction and evaluation of asphalt concrete mixes based on the conclusions and limitations of this thesis work.

Although the results obtained in Chapter 3 give useful information about the effects of laboratory test results precision and bias on predicted rutting performance, further study is required to extend the analyses. Test results for mixes with different binder contents, binder types, air-void contents and gradations (gap-graded, open-graded) should also be analyzed to determine the effects of each variable on precision and bias of RSST-CH results. In addition, the reason behind the increased measured shear resistance for larger size specimens should be investigated by performing finite and/or discrete element simulations. Three dimensional stress and strain distributions for different sized specimens should be calculated to evaluate the effects of specimen size on laboratory test results precision and bias. Differences between the stress and strain distributions of cylindrical and rectangular prism shaped specimens under identical testing conditions should also be determined to evaluate the specimen geometry induced bias on test results.

The reliability based rutting design methodology given, in Chapter 4, should be validated by performing a field performance study. FWD tests should be conducted at various locations of a highway section to determine the variability of stiffness for all pavement layers. In addition, pavement layer thickness variability across the section should be

measured by coring and/or ground penetrating radar. Rut depths should be measured at different time points by using Laser profilometers. Rut depths, thicknesses and stiffnesses from these in-situ measurements should be combined with data from weather and weigh-in-motion (WIM) stations to calibrate laboratory models. The ability of construction variability to define performance variability should be checked for this particular highway section. Based on the results of field study, the levels of variability in pavement rutting performance for a highway section can be identified. In addition, the effectiveness of using stiffness and thickness variability to evaluate overall in-situ performance variability can be determined. A reliability based design procedure can be developed by combining the results of this field performance study with the results given in this thesis.

The viscoelastic micromechanical finite element model developed in Chapter 5 should be used to identify the effects of different test and material parameters on shear resistance. The effects of air-void distributions and aggregate shape and texture parameters on mix shear resistance should be determined based on the developed model. The effects of confining pressure on predicted shear modulus should also be determined by using this 3D micromechanical FE model. Results of the simulations performed with and without confining pressure can be compared with the HVS test results to identify the level of improvement in predictions with the inclusion of confining pressure to the laboratory tests.

The empirical evaluation method presented in Chapter 6 should also be used to identify the rutting performance and failure mechanism of other mix types under different testing

conditions. The effects of aggregate shape on rutting performance should be determined by using the aggregate shape parameters that can be obtained from X-ray CT images. Most of the current ME rutting performance prediction procedures rely on the assumption that distribution of the elastic strain values at a few depths for an asphalt pavement layer calculated by using continuum mechanics should be highly correlated with the distribution of the in-situ permanent strains. The validity of this assumption for different mix and structure types can be checked by comparing the predicted and measured displacement and strain fields. This comparison will help to understand the deficiencies in current methods that have been used for performance simulation. Based on the comparisons, critical strain locations in AC layers (particularly in pavements with different kinds of asphalt layers on top of each other) can be determined for rutting failure modeling.

Results of the analyses from Chapter 6 showed that although RHMA-G mastic is more resistant to shear forces at all loading temperatures and frequencies, sections constructed with RHMA-G mix failed earlier due to the gap-gradation and small aggregate size. In the light of this observation, rutting performance of dense-graded terminal blend asphalt rubber mixes should be investigated by the empirical X-ray CT imaging method proposed in this study and micromechanical finite element modeling. Dense-gradation and stiff binder may create a mix with high rutting performance according to the conclusions derived from Chapter 6.

Particle movement and air void distribution data obtained in Chapter 6 can also be used to calibrate or validate discrete element models (DEM). A DEM model simulating the in-situ construction compaction for different mix types can be developed. This DEM model can be calibrated using the construction air void content distributions. Based on the calibrated DEM model, the effects of various compaction variables, temperature, aggregate shape, NMAS, binder type etc., on the distribution of air voids can be determined. Results can be used to develop new construction and design specifications. DEM models for simulation of rutting performance can be calibrated based on the particle movement and air void reduction data. Calibrated models can be used to identify the changes in rutting failure mechanisms when different asphalt layer thicknesses are used. With this method, optimization of design thicknesses for relatively soft overlays used for reflective cracking that will give adequate rutting performance can be determined.

APPENDIX A   HVS RUT TESTING - COMPOSITE PAVEMENTS

This appendix presents the HVS test results of a study that has been completed for the Strategic Highway Research Program 2 (SHRP2) by the University of California Pavement Research Center (UCPRC). The study, based on a work plan approved by SHRP2, included the identification of an appropriate site for the experiment, the design and construction of a test track, an accelerated loading test using the HVS to assess rutting behavior, and a series of laboratory tests. The objectives of the general research are to investigate the design and construction of new composite pavement systems, and specifically not those resulting from the rehabilitation of existing pavements. The objective of the research presented in this Appendix is to determine the rutting performance of AC layers on top of PCC layers at critical temperatures and traffic loads.

The test track is located at the UC Davis ATIRC test facility. The test track is 41 m by 14.6 m (135 ft by 48 ft) divided into nine test sections. The pavement structure consists of the existing subgrade/subbase material overlying bedrock, with 150 mm (6 in.) of

imported aggregate base. Two AC mix types were used in this study, dense-graded AC with PG 64-28 polymer modified (PM) binder and gap-graded AC with asphalt rubber binder, PG 64-16 (RHMA-G). Both mixes are specified using Caltrans specifications for both mix and binder. AC layer thicknesses for HVS rutting test sections were selected to be 64mm. (2.5 in.) and 114 mm. (4.5 in.). Thus, in this study, a total of four sections were tested for rutting performance evaluation.

Excavation and grading of subgrade was performed on November, 2008. Aggregate base placement followed subgrade preparation. An asphalt prime coat meeting Caltrans specifications section 93-1.01 was applied in December 2008 to the 250 yd^2 (225 m^2) aggregate base to minimize winter rain damage prior to PCC paving in 2009. Concrete layer was constructed on August 2009. Asphalt concrete layer was placed on the test track on October 2009. Field-mixed, laboratory-compacted (FMLC) asphalt concrete specimens were prepared on site adjacent to the test track for laboratory testing.

The first phase of HVS testing commenced in January 2010 and was completed in April 2010. This testing compared early rutting performance at elevated temperatures (pavement temperature of 50°C at 50 mm [122°F at 2.0 in.]), using a 40 kN (9,000 lb) load on a standard dual wheel configuration and a unidirectional trafficking mode. For sections with PM 64-28 PM mix, section 609HB and section 610HB, load was increased to 60kN (13,500 lb) after 64,000[th] repetitions to reach rutting failure.

A.1 HVS TEST CRITERIA AND CONDITIONS

A.1.1 *Protocols*

Heavy Vehicle Simulator (HVS) test section layout, test setup, trafficking, and measurements followed standard University of California Pavement Research Center (UCPRC) protocols *(Jones 2005)*.

A.1.2 *Pavement instrumentation and monitoring methods*

Instrumentation for the HVS rutting tests is shown in Figure A.1, and included the following types and collection intervals:

- Laser profilometer, a portable beam with a traveling laser collecting 260 points across its 2.3-m length, used to measure transverse surface profile across the wheelpath, with measurements taken at each 0.5-m station and at load repetition intervals selected to provide characterization of the rut development.
- Thermocouples, to measure ambient and pavement temperature, with measurements taken at Stations 4 and 12 and for ambient temperature at one-hour intervals during HVS operation.
- AC strain gauges, with measurements taken at locations shown in Figure A.1 and at load repetition intervals selected to provide characterization of the rut development.
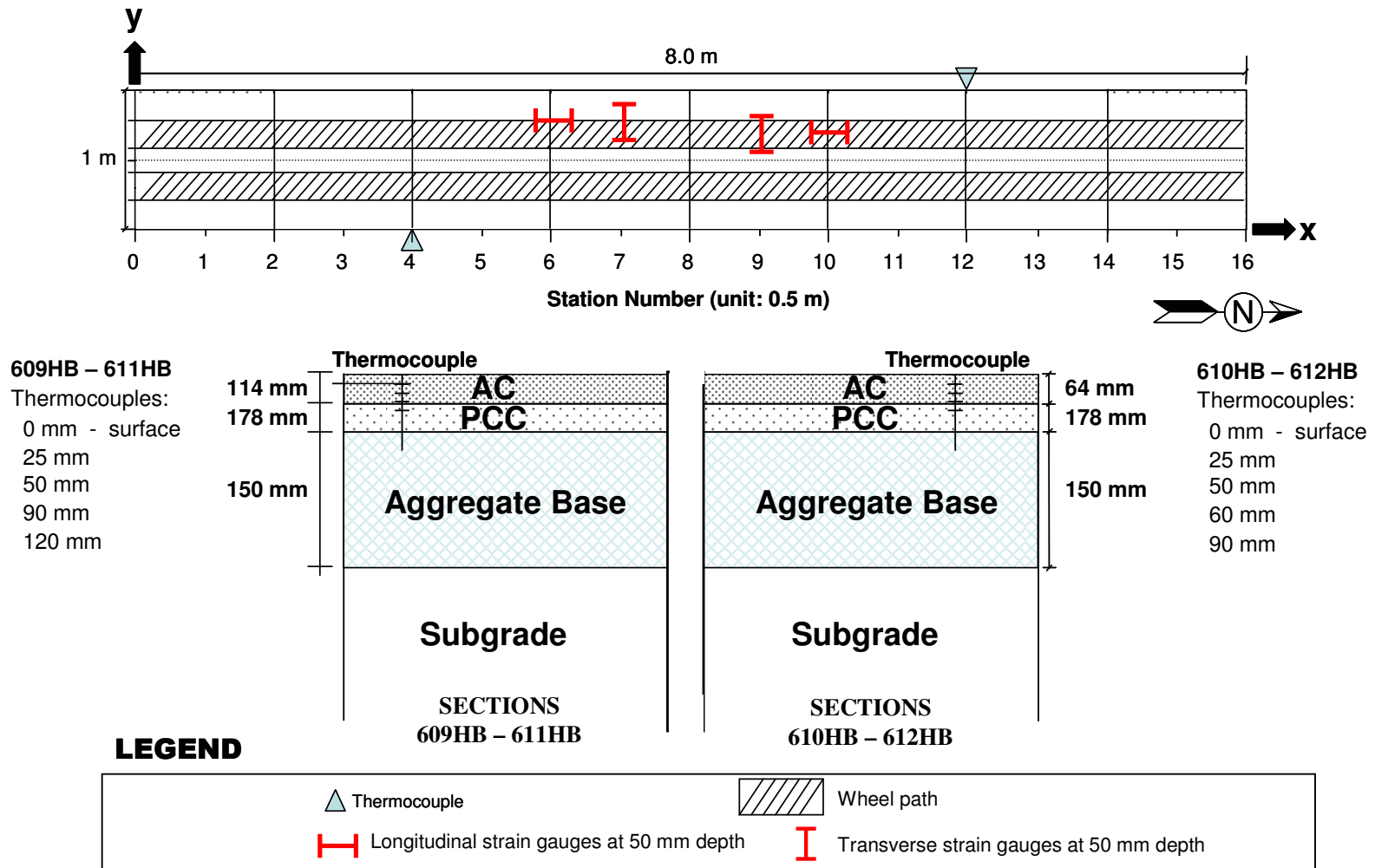
Figure A.1 HVS rutting test section layout and location of thermocouples.

www.manaraa.com

Surface and in-depth deflections were not measured during the HVS rutting tests. As can be seen in Figure A.1, HMA strain gauges at 50 mm depth were used to collect pavement response in the asphalt overlays throughout the HVS tests. These strain gauges were located under the wheelpath and at the edge of the wheelpath to provide information about the response of the asphalt overlay to the shearing action of the tires. Results for the strain gauge measurements are given in this appendix in the section Asphalt Strain Gauge Results. Pavement cells on which HVS rutting test sections were performed are shown in Figure A.2. The purpose of the HVS rutting tests was to evaluate the effects of overlay thickness on rutting performance for thin overlays on concrete slabs. For this reason, two overlay thicknesses were tested for each of the two mix types placed on the UC Davis test sections.
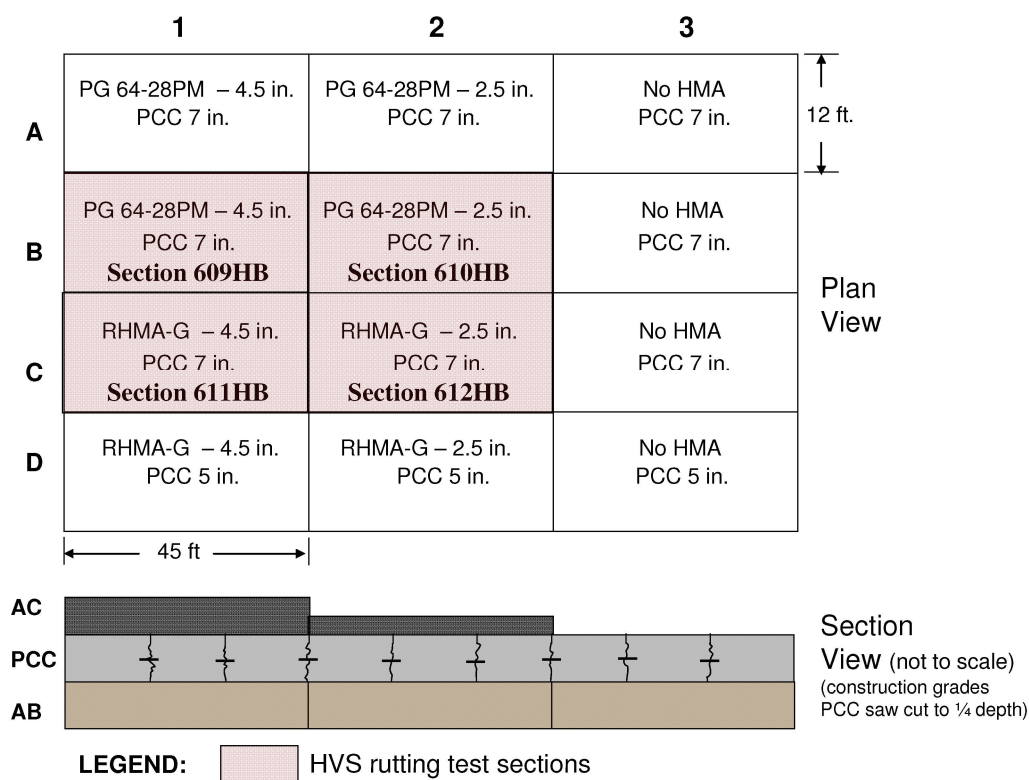
	1	2	3
A	PG 64-28PM − 4.5 in. PCC 7 in.	PG 64-28PM − 2.5 in. PCC 7 in.	No HMA PCC 7 in.
B	PG 64-28PM − 4.5 in. PCC 7 in. **Section 609HB**	PG 64-28PM − 2.5 in. PCC 7 in. **Section 610HB**	No HMA PCC 7 in.
C	RHMA-G − 4.5 in. PCC 7 in. **Section 611HB**	RHMA-G − 2.5 in. PCC 7 in. **Section 612HB**	No HMA PCC 7 in.
D	RHMA-G − 4.5 in. PCC 5 in.	RHMA-G − 2.5 in. PCC 5 in.	No HMA PCC 5 in.

12 ft. Plan View

45 ft

Section View (not to scale) (construction grades PCC saw cut to ¼ depth)

LEGEND: HVS rutting test sections

Figure A.2 Pavement cells with HVS rutting tests.

A.1.3 *Test section failure criterion*

The failure criterion was defined as an average maximum rut of 12.5 mm (0.5 in.) over
the full monitored section (Station 3 to Station 13). Testing was continued past a 12.5-
mm average rut depth until the rutting accumulation rate stabilized.

A.1.4 *Environmental conditions*

The pavement temperature at 50 mm (2.0 in.) depth was maintained at 50°C±4°C
(122°F±7°F) to assess rutting potential under typical pavement conditions. Heaters were
operated inside the temperature control box to maintain the pavement temperature. The
pavement surface received no direct rainfall as it was protected by the temperature
control unit. The sections were tested predominantly during the wet season, however,
measures were taken to keep water from entering the pavement structure inside the
temperature control box, and there was an extensive drainage system placed around the
entire set of pavement test sections. In addition, plastic sheets were placed on the surface
to keep water out of the pavement.

A.1.5 *Test schedule*

The schedule of HVS trafficking and number of loads on each section is shown in Table
A.1.

Table A.1 Test duration for HVS rutting tests

Section	Mix type	Design Thickness (mm)	As-built Thickness (mm)	As-built Air-void (%)	Start Date	Finish Date	Total Repetitions
609HB	PG64-28 PM	114	116	9.8	1/28/2010	2/26/2010	200,000
610HB	PG64-28 PM	64	72	10.0	3/4/2010	3/23/2010	201,200
611HB	RHMA-G	114	118	13.8	3/29/2010	4/2/2010	18,503
612HB	RHMA-G	64	74	13.4	4/13/2010	4/27/2010	90,000

A.1.6 *Loading program*

The HVS loading program for each section is summarized in Table A.2. All trafficking was carried out with a dual-wheel configuration with the centerlines of the two tires spaced 360 mm (14.2 in.) apart, using radial truck tires (Goodyear G159 - 11R22.5- steel belt radial) inflated to a pressure of 690 kPa (100 psi), in a channelized (no wander), unidirectional loading mode in which the wheel travels one direction loaded and is lifted off the pavement for the return pass. Channelized trafficking is used to simulate the tracking of radial tires in the wheelpath once a small rut forms, and is more aggressive than field conditions in the initial stages of rutting before tires begin to track in the ruts. Wheel speed for all tests was 8.7 km/h (5.4 mph).

Table A.2 Summary of HVS loading program

| Section | Mix type | As-built Thickness (mm) | Wheel Load[1] (kN) | Temperatures at 50 mm (2 in.) | | Total Repetitions |
				Average (°C)	SD[2] (°C)	
609HB	PG 64-28 PM	116	40 60	49.5	1.1	63,750 136,250
610HB	PG 64-28 PM	72	40 60	49.8	1.0	64,000 137,200
611HB	RHMA-G	118	40	48.7	1.1	18,503
612HB	RHMA-G	74	40	49.7	1.3	90,000
				Total		**509,703**

[1] 40 kN = 9,000 lb. 60 kN = 13,500 lb
25.4 mm = 1 inch,   *Fahrenheit = Celsius*9/5+32*

[2]SD: Standard deviation

A.2 HVS TEST DATA SUMMARY

A.2.1 *Introduction*

The results of the HVS rut tests were summarized and a first-level analysis was performed. In assessing rutting performance, the temperature at 50 mm depth of the asphalt concrete and the temperature gradient are two important temperature parameters controlling the stiffness of the asphalt concrete which was used to compute plastic strain. Permanent deformation at the pavement surface (rutting) was monitored with the Laser Profilometer at the surface and strain gauges at 50 mm depth in the asphalt in the sections with thicker HMA overlays (strain gauges placed between the two lifts of HMA used to construct the overlay). The Laser Profilometer is a stand-alone moveable beam with a traveling downward-shooting vertical laser, which is used to take surface profiles transverse to the direction of the HVS wheel track. Transverse profiles are taken at 0.5-m (1.15-ft) intervals along the test section. The following rut parameters were determined

from the surface profile measurements taken with the Laser Profilometer, as illustrated in Figure A.3:

- Average maximum rut depth,
- Average deformation,
- Location and magnitude of the maximum rut depth, and
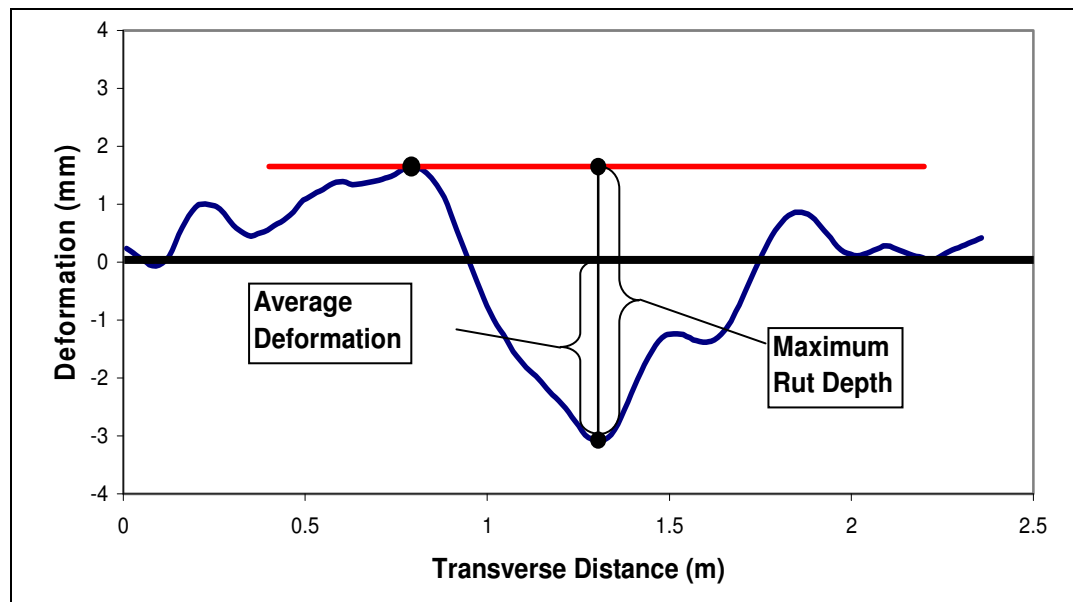- Rate of rut development.

Figure A.3 Illustration of maximum rut depth and average deformation of a leveled profile.

The Laser Profilometer provides sufficient information to evaluate the evolution of permanent surface deformation of the entire test section at various loading stages. The rut depth figures in this appendix show the average values over the entire section (Stations 3 through 13) as well as values for half-meter interval locations between Stations 3 and 8

and Stations 9 and 13. These two additional data series were plotted to illustrate any differences along the length of the section. The permanent deformation will be further characterized after a forensic investigation (test pits and cores) on each section when all testing on the test track has been completed, which will occur after the end of the SHRP R21 project, and will be completed with Caltrans funding. Tire pressure was constant at 690kPa (100 psi) for all test sections.

The data from each HVS test is presented separately, with the presentation of each test following the same format. Data plots are presented on the same scale to facilitate comparisons of performance.

A.2.2 *Section 609HB: Mix: PG 64-28 PM, HMA thickness: 114 mm*

A.2.2.1 Test summary

Loading commenced on January 28, 2010, and ended on February 26, 2010. A total of 200,000 load repetitions were applied and 36 datasets were collected across the duration of the testing. Testing was interrupted for six days (February 13, 2010 through February 19, 2010) due to an oil leak caused by a broken O-ring in the carriage. The HVS loading history for Section 609HB is shown in Figure A.4.
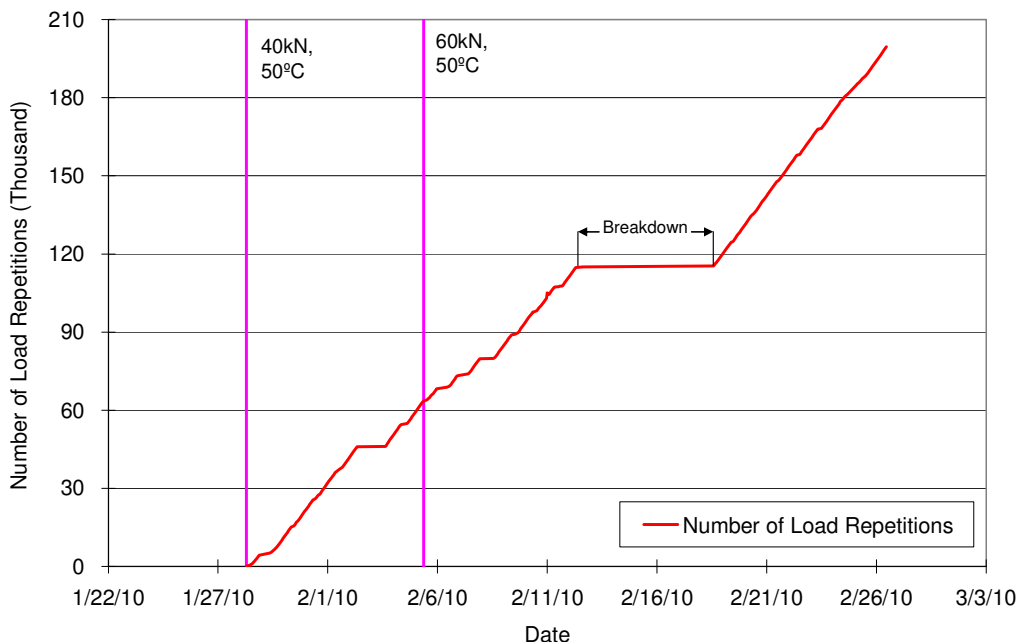
Figure A.4 609HB - PG 64-28 PM - 114 mm: Load history.

A.2.2.2 Outside air temperatures

Outside air temperatures are summarized in Figure A.5. Vertical error bars on each point on the graph show daily temperature range. Temperatures ranged from 1.4°C to 20.9°C (34.5°F to 69.6°F) during the course of HVS testing, with a daily average of 10.6°C (51.1°F), an average minimum of 6.7°C (44.1°F), and an average maximum of 15.5°C (59.9°F).

A.2.2.3 Air temperatures in the temperature control unit

During the test, air temperatures inside the temperature control unit ranged from 15.6°C to 52.9°C (60.1°F to 127.2°F) with an average of 41.1°C (106°F) and standard deviation of 2.6°C (4.7°F). The daily average air temperatures recorded in the temperature control

unit, calculated from the hourly temperatures recorded during HVS operation, are shown in Figure A.6. Vertical errors bars on each point on the graph show daily temperature range.
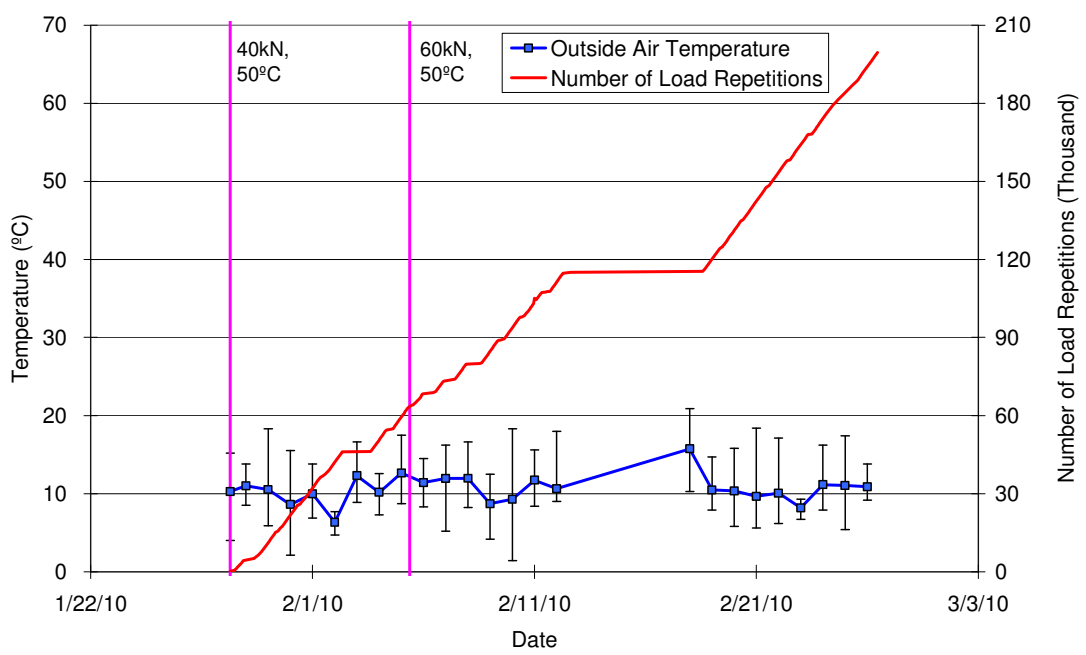

Figure A.5 609HB - PG 64-28 PM - 114 mm: Daily average outside air temperatures.

A.2.2.4 Temperatures in the asphalt concrete layers

Daily averages of the surface and in-depth temperatures of the asphalt concrete layers are listed in Table A.3 and shown in Figure A.7. Pavement temperatures decreased slightly with increasing depth in the pavement, which was expected as there is usually a thermal gradient between the top and bottom of the asphalt concrete pavement layers.
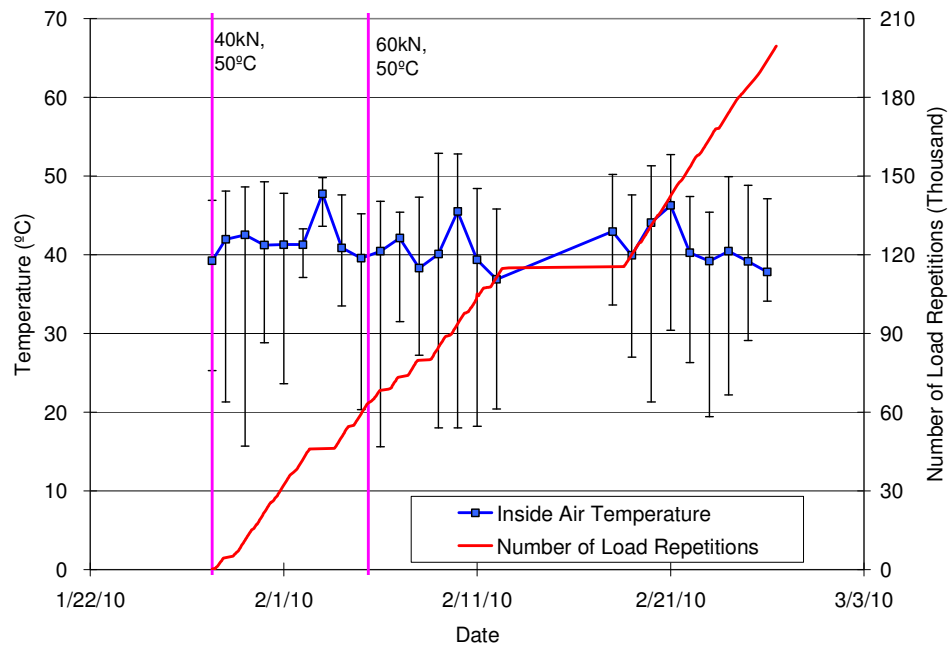
Figure A.6 609HB - PG 64-28 PM - 114 mm: Daily average inside air temperatures.

Table A.3 609HB - PG 64-28 PM - 114 mm: Temperature summary for air and pavement

Temperature	Average (°C)	Std Dev (°C)	Average (°F)	Std Dev (°F)
Outside air	10.6	1.8	51.1	3.2
Inside air	41.1	2.6	106.0	4.7
Pavement surface	47.8	2.0	118.0	3.6
- 25 mm below surface	49.7	1.3	121.4	2.4
- 50 mm below surface	49.5	1.1	121.1	2.0
- 90 mm below surface	48.6	0.9	119.5	1.7
- 120 mm below surface	47.5	0.9	117.4	1.7
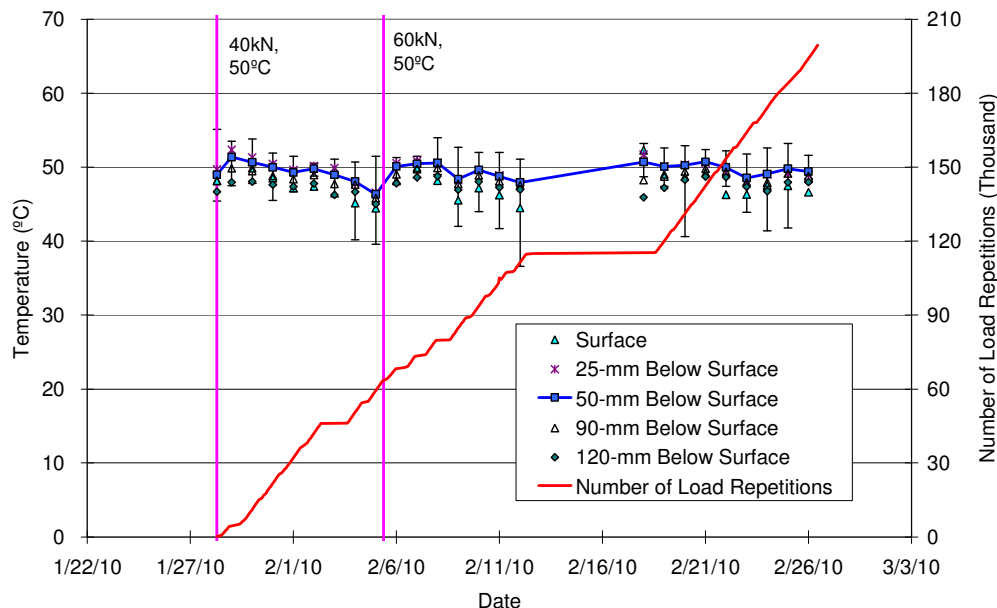
Figure A.7 609HB - PG 64-28 PM - 114 mm: Daily average temperatures at pavement surface and various depths.

A.2.2.5 Permanent surface deformation (Rutting)

Figure A.8 shows the average transverse cross section measured with the Laser Profilometer at various stages of the test.

During HVS testing, rutting usually accumulates at a faster rate initially due to fast reduction of air-voids (densification), and then it typically diminishes as trafficking progresses until reaching a steady state. This initial phase is referred to as the "embedment" phase. Figure A.9 and Figure A.10 show the development of permanent deformation (average maximum rut and average deformation, respectively) with load repetitions as measured with the Laser Profilometer for the test section, with an embedment phase only apparent at the beginning of the experiment (i.e., first 15,000

repetitions). Error bars on the average reading indicate that there was high variation along the length of the section which was a result of the HMA blocks removed for CT image evaluation. (For details see the section Air-Void Content Distribution in HMA layers from Image Analysis). Figure A.11 shows the distribution of rutting along the test section after data for Stations 4, 10, 11, and 13, which are close to CT blocks, were excluded from the dataset. It can be observed that variability significantly decreases after excluding data for those four biased stations. Figure A.12 shows a contour plot of the pavement surface at the end of the test (200,000 repetitions), also indicating localized permanent deformation near the block locations. In addition, a slightly deeper rut was recorded in one of the wheel tracks, which was attributed to the positioning of the HVS on the crossfall on the section. After completion of trafficking, the average maximum rut depth and the average deformation were 10.9 mm (0.43 in.) and 5.5 mm (0.22 in.), respectively. The maximum rut depth measured on the section was 17.1 mm (0.67 in.), recorded at Station 4, close to one of the CT blocks.
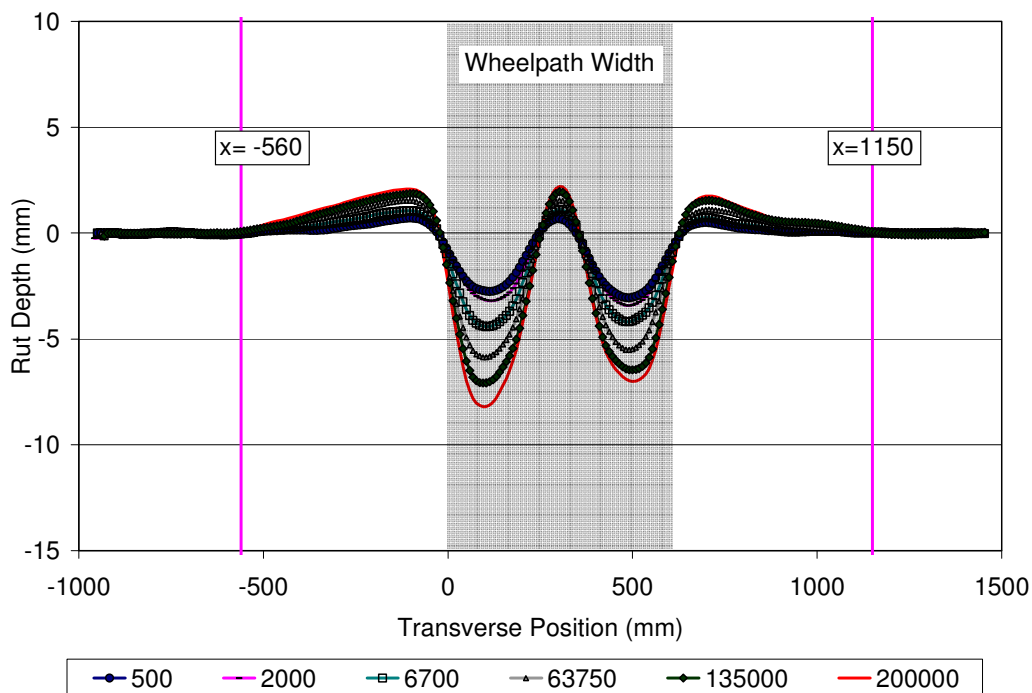
Figure A.8 609HB - PG 64-28 PM - 114 mm: Profilometer cross section at various load repetitions.
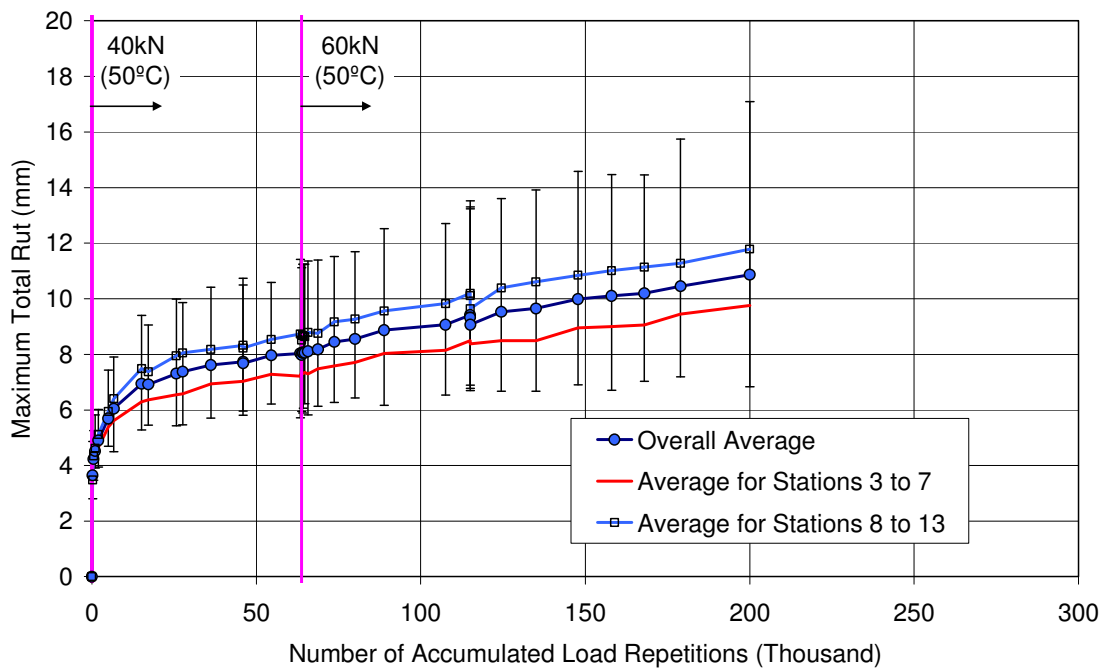

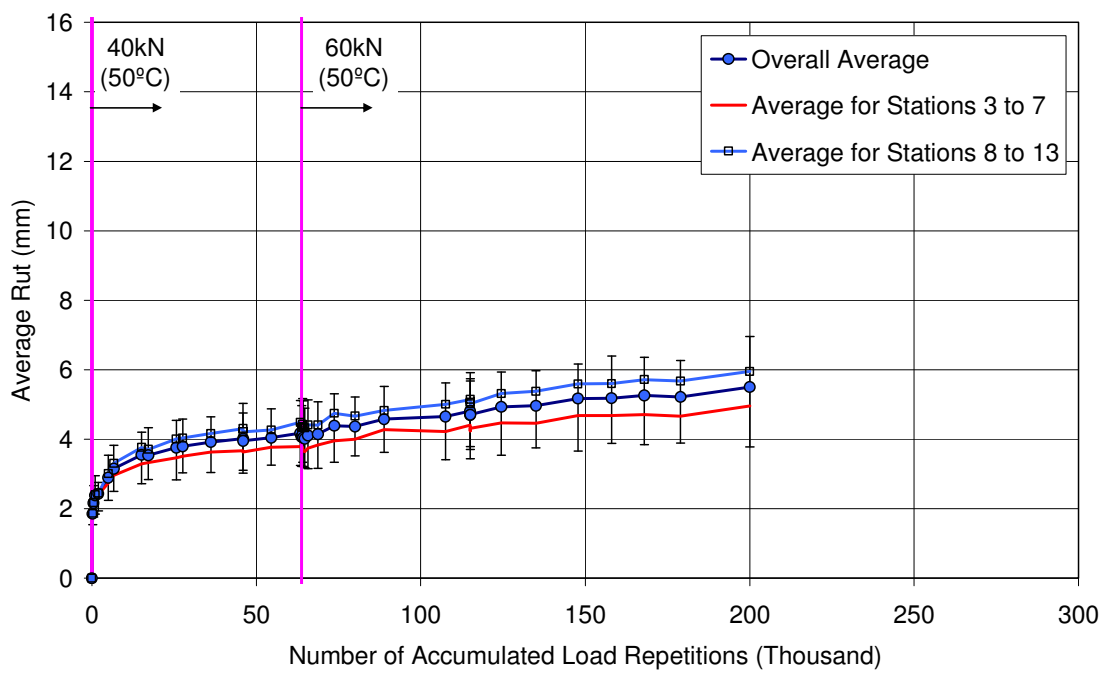Figure A.9 609HB - PG 64-28 PM - 114 mm: Average maximum rut.

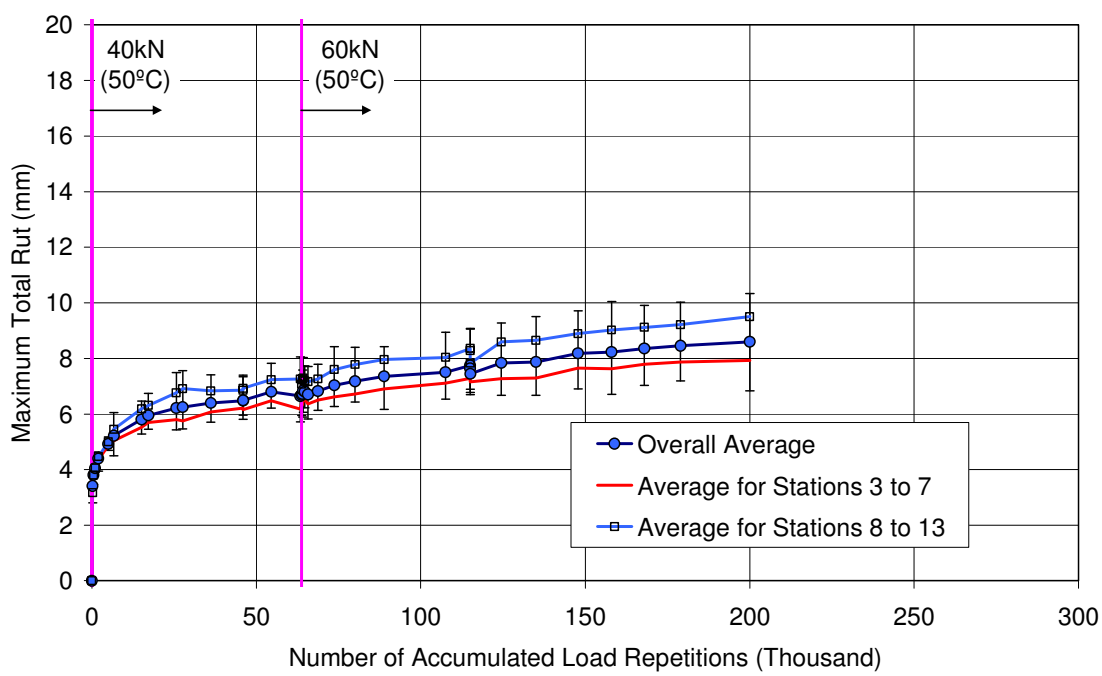Figure A.10 609HB - PG 64-28 PM - 114 mm: Average deformation.

Figure A.11 609HB - PG 64-28 PM - 114 mm: Average maximum rut after excluding data for Stations 4, 10, 11, and 13 that are close to CT blocks.
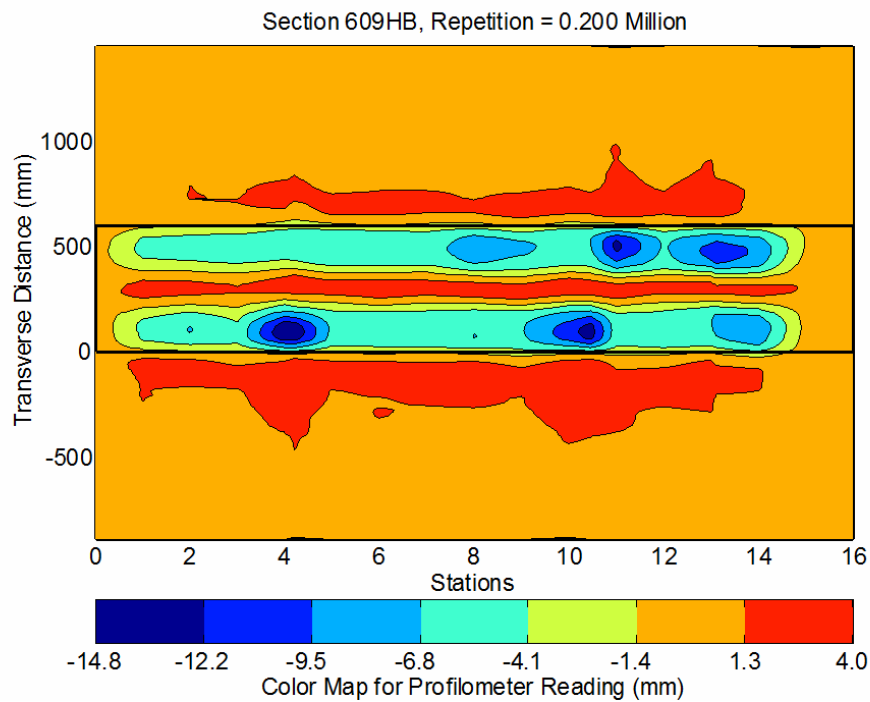
Figure A.12 609HB - PG 64-28 PM - 114 mm: Contour plot of permanent surface deformation at end of test.

A.2.2.6 Visual Inspection

Apart from rutting, no other distress was recorded on the section. Figure A.13 is a

photograph taken of the surface at the end of the test.

Figure A.13 609HB - PG 64-28 PM - 114 mm: Section photograph at test completion.

A.2.3   *Section 610HB: Mix: PG 64-28 PM, HMA thickness: 64 mm*

A.2.3.1 Test summary

Loading commenced on March 4, 2010, and ended on March 23, 2010. A total of 201,200 load repetitions were applied and 31 datasets were collected. The HVS loading history for Section 610HB is shown in Figure A.14. No breakdowns occurred during this test.
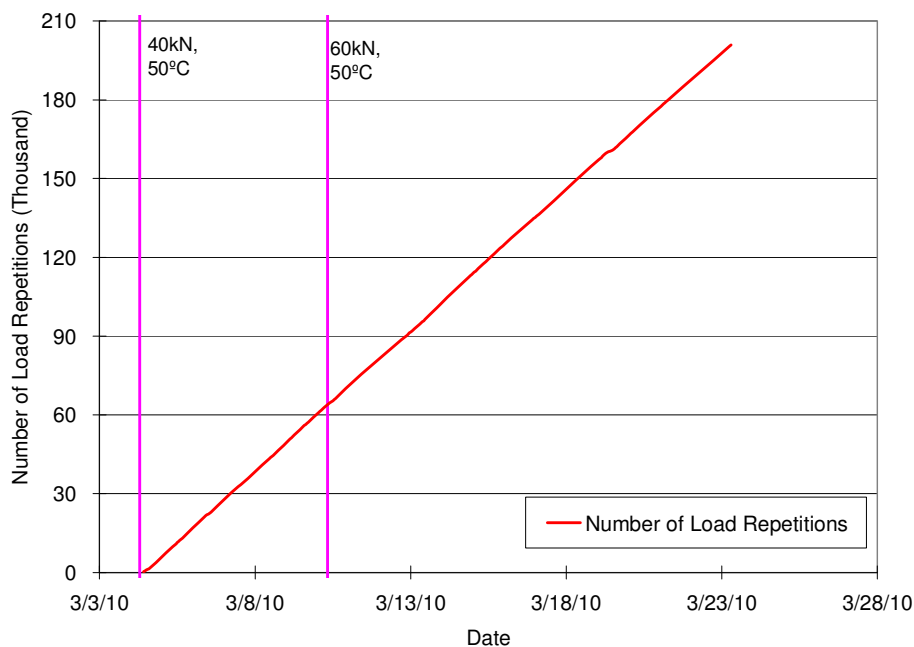

Figure A.14 610HB - PG 64-28 PM - 64 mm: Load history.

A.2.3.2 Outside air temperatures

Outside air temperatures are summarized in Figure A.15. Vertical error bars on each point on the graph show daily temperature range. Temperatures ranged from 1.0°C to 28.5°C (33.8°F to 83.3°F) during the course of HVS testing, with a daily average of

12.0°C (53.6°F), an average minimum of 5.4°C (41.7°F), and an average maximum of 20.1°C (68.1°F).

A.2.3.3 Air temperatures in the temperature control unit

During the test, the measured air temperatures inside the temperature control unit ranged from 16.3°C to 52.3°C (61.3°F to 126.1°F) with an average of 40.4°C (104.8°F) and standard deviation of 1.9°C (3.5°F). The daily average air temperatures recorded in the temperature control unit, calculated from the hourly temperatures recorded during HVS operation, are shown in Figure A.16. Vertical errors bars on each point on the graph show daily temperature range.
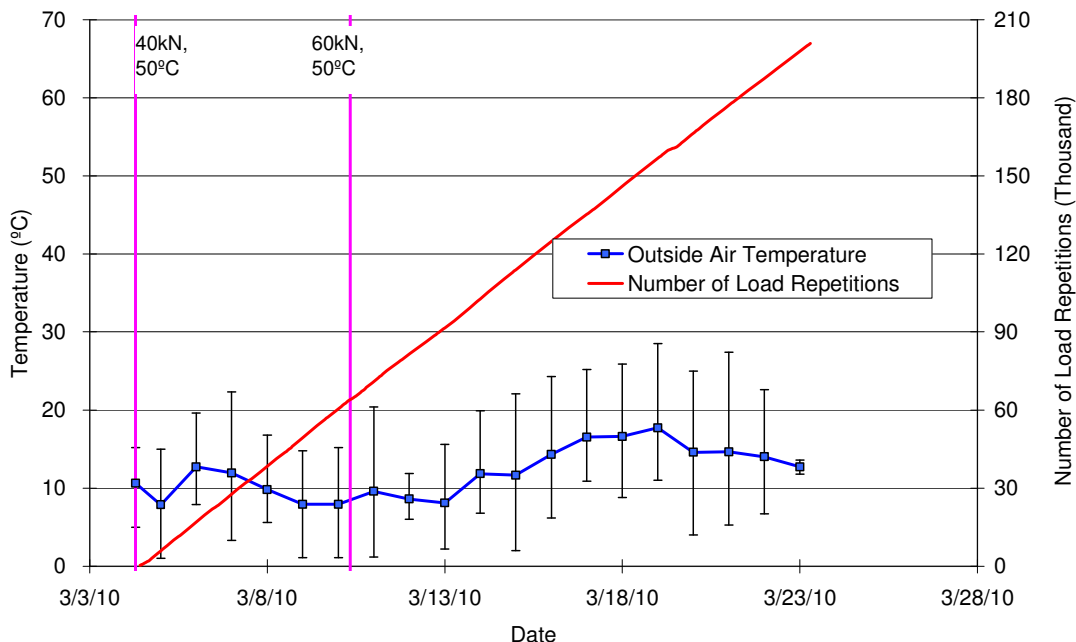

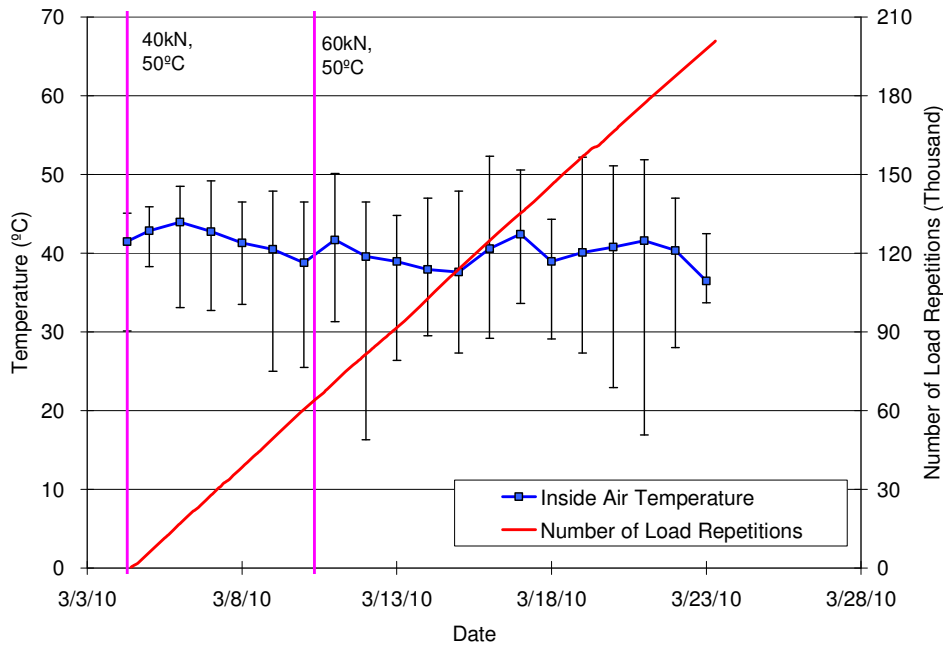Figure A.15 610HB - PG 64-28 PM - 64 mm: Daily average outside air temperatures.

Figure A.16 610HB - PG 64-28 PM - 64 mm: Daily average inside air temperatures.

A.2.3.4 Temperatures in the asphalt concrete layers

Daily averages of the surface and in-depth temperatures of the asphalt concrete layers are listed in Table A.4 and shown in Figure A.17. Pavement temperatures decreased slightly with increasing depth in the pavement, as expected. Average pavement temperatures at all depths of Section 610HB were similar to those recorded on the section 609HB.

Table A.4 610HB - PG 64-28 PM - 64 mm: Temperature summary for air and pavement

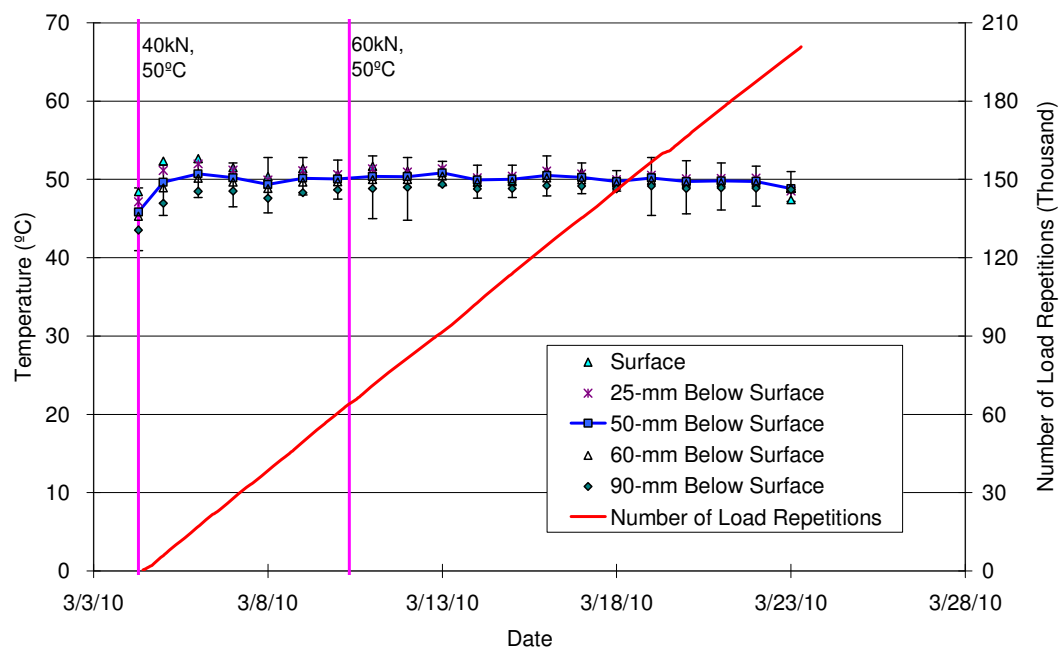| Temperature	610HB			
	Average (°C)	Std Dev (°C)	Average (°F)	Std Dev (°F)
Outside air	12.0	3.1	53.6	5.7
Inside air	40.4	1.9	104.8	3.5
Pavement surface	50.5	1.2	122.9	2.2
- 25 mm below surface	50.4	1.1	122.8	1.9
- 50 mm below surface	49.8	1.0	121.7	1.9
- 60 mm below surface	49.5	1.1	121.0	1.9
- 90 mm below surface	48.4	1.3	119.2	2.3

Figure A.17 610HB - PG 64-28 PM - 64 mm: Daily average temperatures at pavement surface and various depths.

A.2.3.5 Permanent surface deformation (Rutting)

Figure A.18 shows the average transverse cross section measured with the Laser Profilometer at various stages of the test.

Figure A.19 and Figure A.20 show the development of permanent deformation (average maximum rut and average deformation, respectively) with load repetitions as measured with the Laser Profilometer for the test section. Error bars on the average reading indicate that the level of variability caused by the CT blocks is less than the variability for Section 609HB. This is a result of the epoxy material used on Section 610HB to glue CT blocks to pavement. Figure A.21 shows the distribution of rutting along the test section after data for Stations 4, 5, 11, and 13, which are close to CT blocks, are excluded from the dataset. It can be observed that excluding data for those four biased stations does not cause any significant change in variability and average accumulated rutting.

Results for the section 609HB are also shown for comparative purposes in Figure A.19 and Figure A.20. It can be observed that rutting accumulation rates after the embedment phase are similar for both sections. However, high level of densification at the embedment stage resulted in higher rutting for the section 609HB. Because both pavements are constructed from the same mix type, the only reason for higher rutting can be the differences in HMA layer thicknesses. In order to identify the effect of thickness on accumulated rutting, rutting measurements were converted to permanent shear strain (PSS) by dividing the measured rutting by the HMA layer thickness of each section. Figure A.21 shows that PSS curves for Sections 609HB and 610HB are close to each

other. This result indicates that accumulated rutting for these two sections is a function of thickness. It should be noted that this result is most likely to be a result of the underlying concrete layer which minimizes permanent deformation at the unbound layers. A similar result may not be observed when the section does not have any concrete layer under the HMA.

Figure A.27 shows a contour plot of the pavement surface at the end of the test (201,200 repetitions). After completion of trafficking, the average maximum rut depth and the average deformation were 5.8 mm (0.23 in.) and 2.9 mm (0.11 in.), respectively. The maximum rut depth measured on the section was 6.9 mm (0.27 in.) recorded at Station 4.
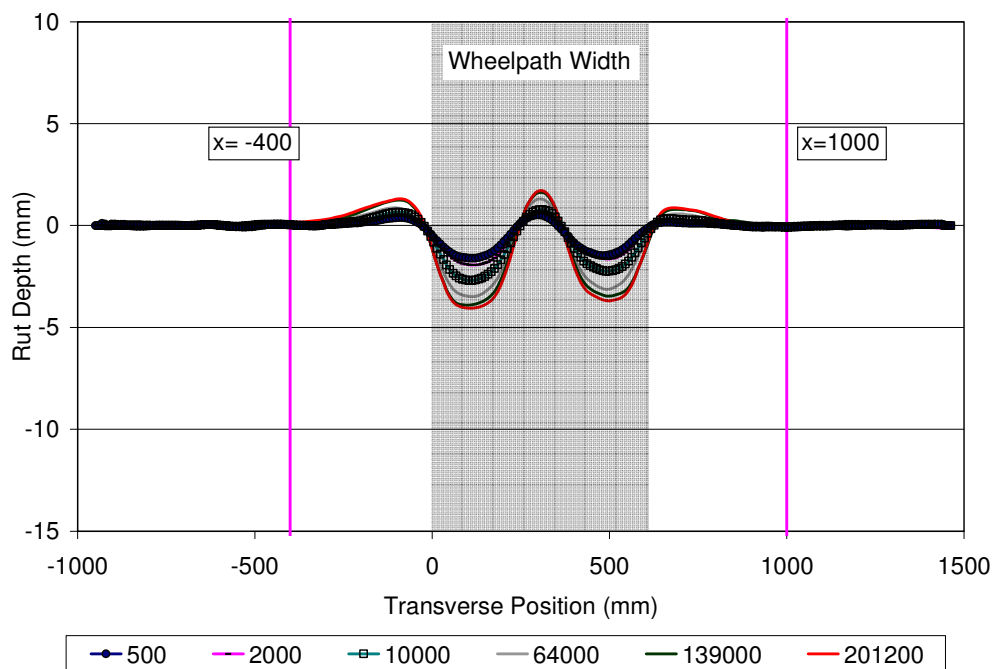

Figure A.18 610HB - PG 64-28 PM - 64 mm: Profilometer cross section at various load repetitions.

A.2.3.6 Visual inspection

Apart from rutting, no other distress was recorded on the section at the end of testing.

Figure A.24 is a photograph taken of the surface at the end of the test.
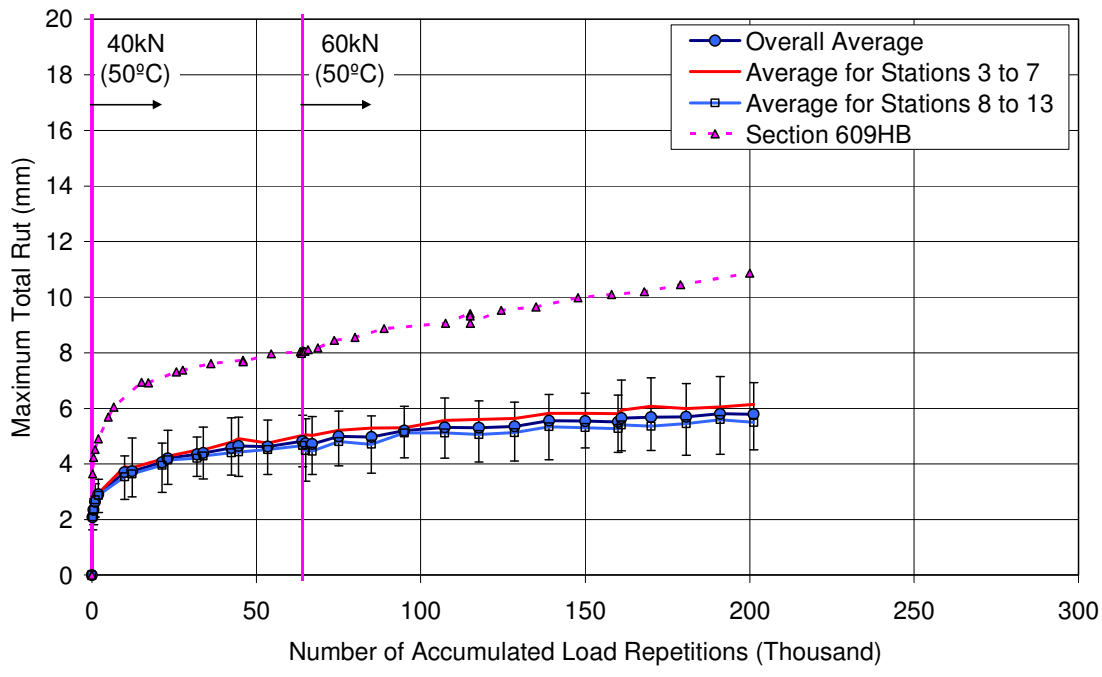

Figure A.19 610HB - PG 64-28 PM - 64 mm: Average maximum rut.
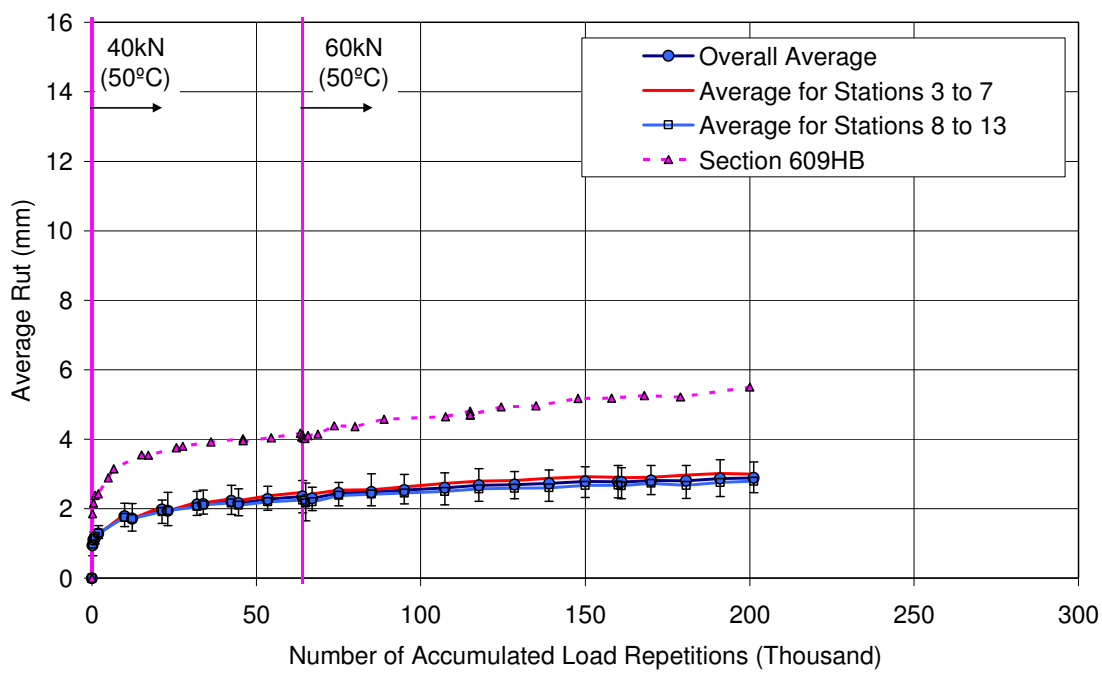
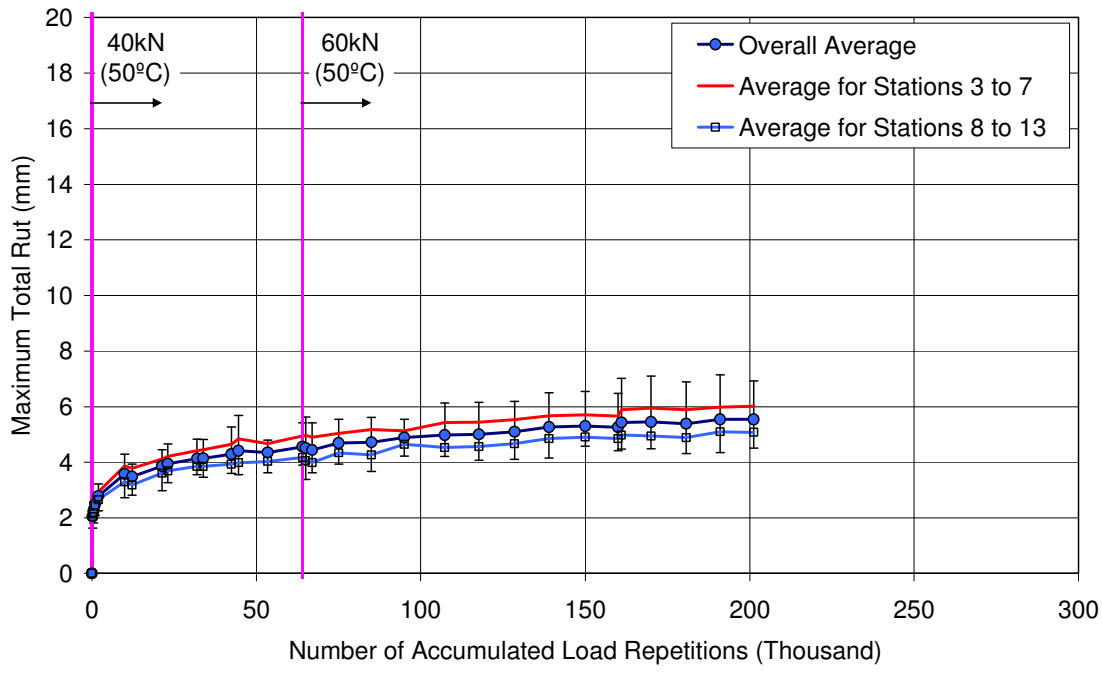Figure A.20 610HB - PG 64-28 PM - 64 mm: Average deformation.

Figure A.21 610HB - PG 64-28 PM - 64 mm: Average maximum rut after excluding data for Stations 4, 5, 11, and 13 that are close to CT blocks.
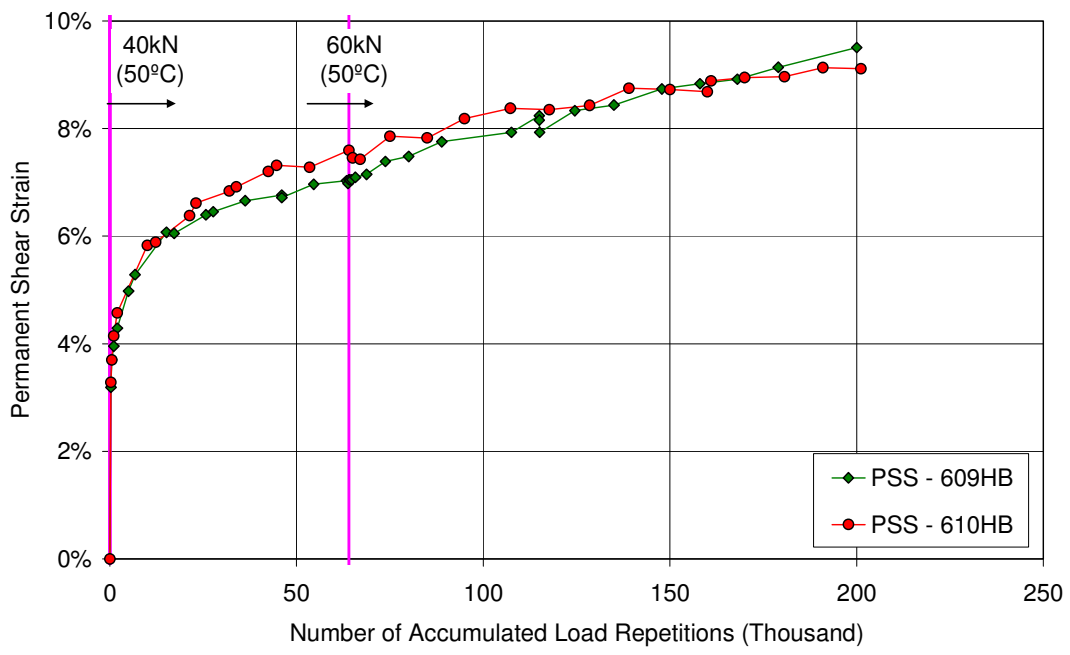
Figure A.22 Comparison of PSS for Sections 609HB - PG 64-28 PM - 114 mm and 610HB - PG 64-28 PM - 64 mm.
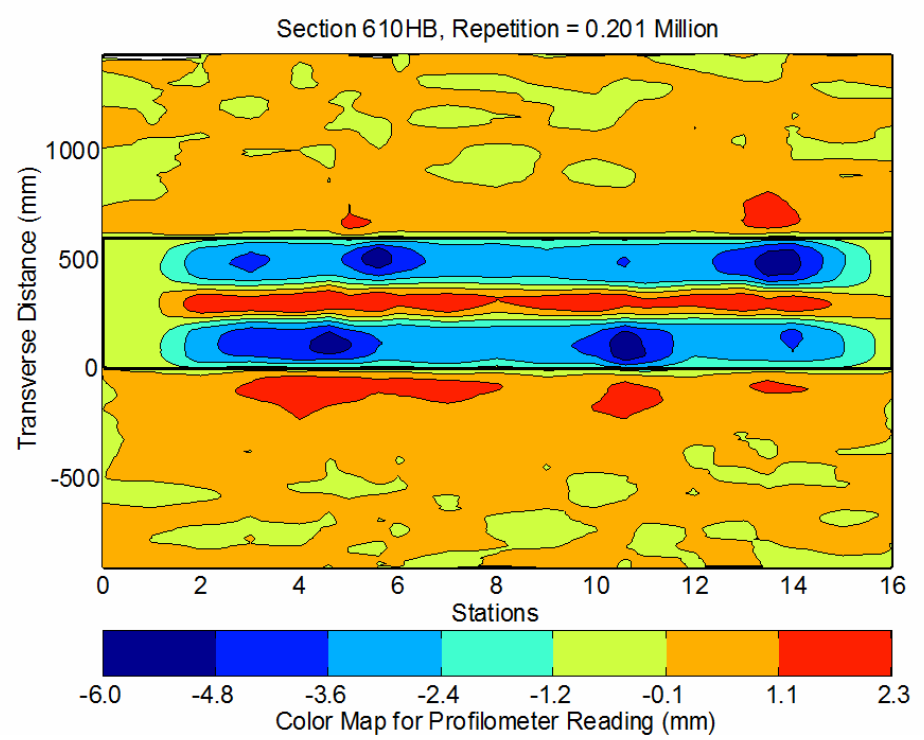

Figure A.23 610HB - PG 64-28 PM - 64 mm: Contour plot of permanent surface deformation at end of test.

Figure A.24 610HB - PG 64-28 PM - 64 mm: Section photograph at test completion.

A.2.4 *Section 611HB: Mix: RHMA-G, HMA thickness: 114 mm*

A.2.4.1 Test summary

Loading commenced on March 29, 2010, and ended on April 2, 2010. A total of 18,503 load repetitions were applied and 10 datasets were collected. Early failure was observed for the section when compared to Sections 609HB and 610HB. The HVS loading history for Section 611HB is shown in Figure A.25. Although the failure criterion (12.5 mm rut depth) was reached after 6,400 repetitions, testing was continued until the rutting accumulation rate stabilized.
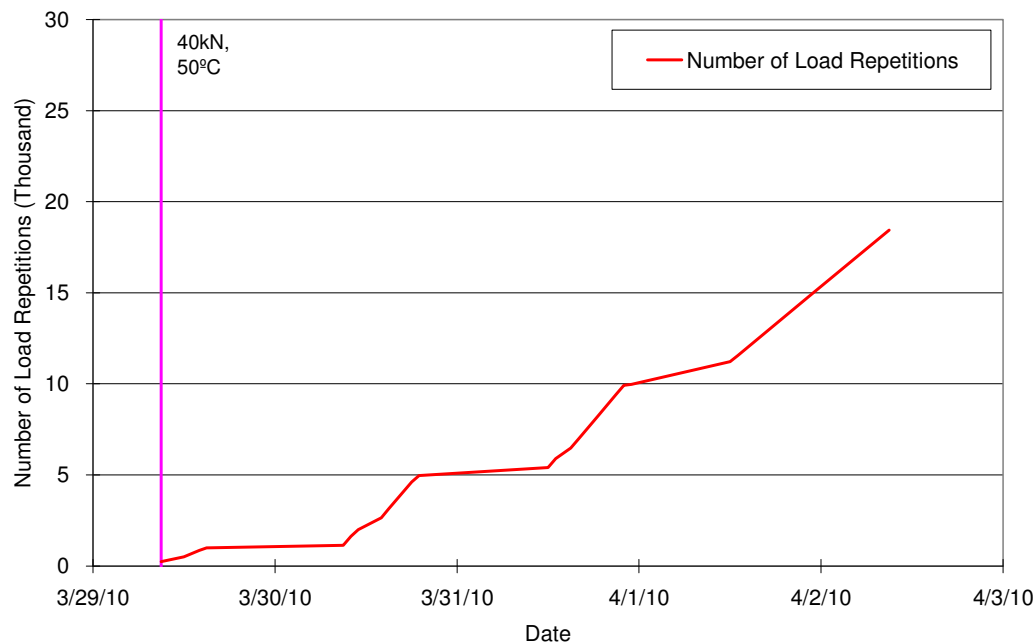
Figure A.25 611HB - RHMA-G - 114 mm: Load history.

A.2.4.2 Outside air temperatures

Outside air temperatures are summarized in Figure A.26. Vertical error bars on each point on the graph show daily temperature range. Temperatures ranged from 5.2°C to 21.5°C (41.4°F to 70.7°F) during the course of HVS testing, with a daily average of 13.0°C (55.4°F), an average minimum of 9.4°C (49°F), and an average maximum of 16.2°C (61.2°F).

A.2.4.3 Air temperatures in the temperature control unit

During the test, air temperatures inside the temperature control unit ranged from 16.1°C to 45.1°C (61°F to 113.2°F) with an average of 35.2°C (95.4°F) and standard deviation of 3.6°C (6.5°F). The air temperature was adjusted to maintain a pavement temperature of 50°C±4°C (122°F±7°F). The daily average air temperatures recorded in the temperature control unit, calculated from the hourly temperatures recorded during HVS operation, are shown in Figure A.27. Vertical errors bars on each point on the graph show daily temperature range.

A.2.4.4 Temperatures in the asphalt concrete layers

Daily averages of the surface and in-depth temperatures of the asphalt concrete layers are listed in Table A.5 and shown in Figure A.28. Pavement temperatures decreased slightly with increasing depth in the pavement, as expected. Average pavement temperatures at all depths of Section 611HB were similar to those recorded on the Sections 609HB and 610HB.
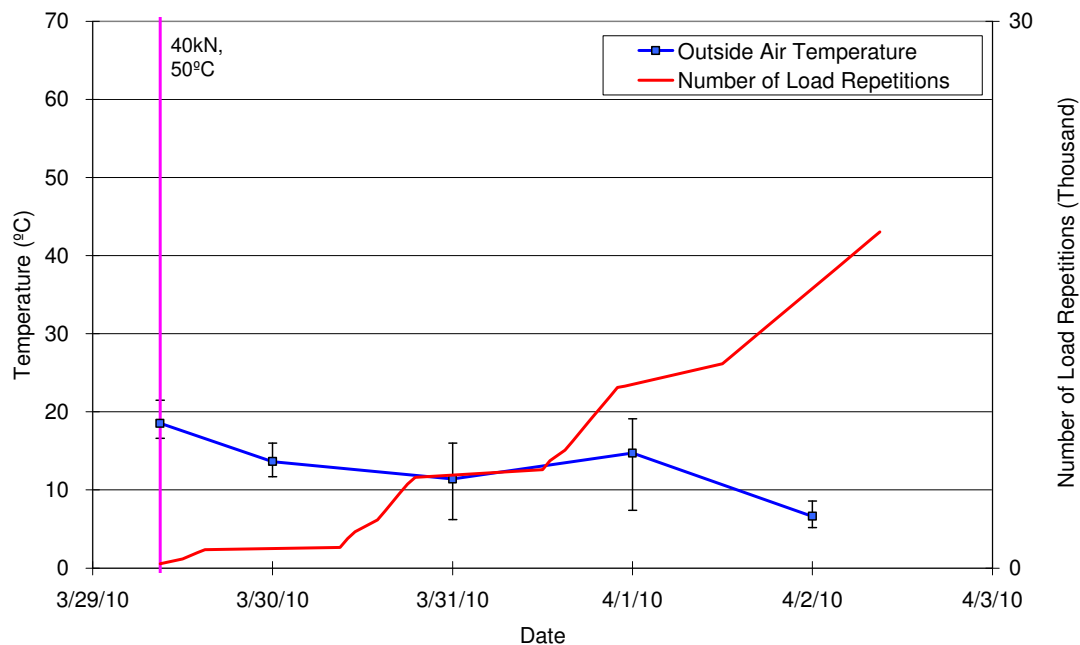
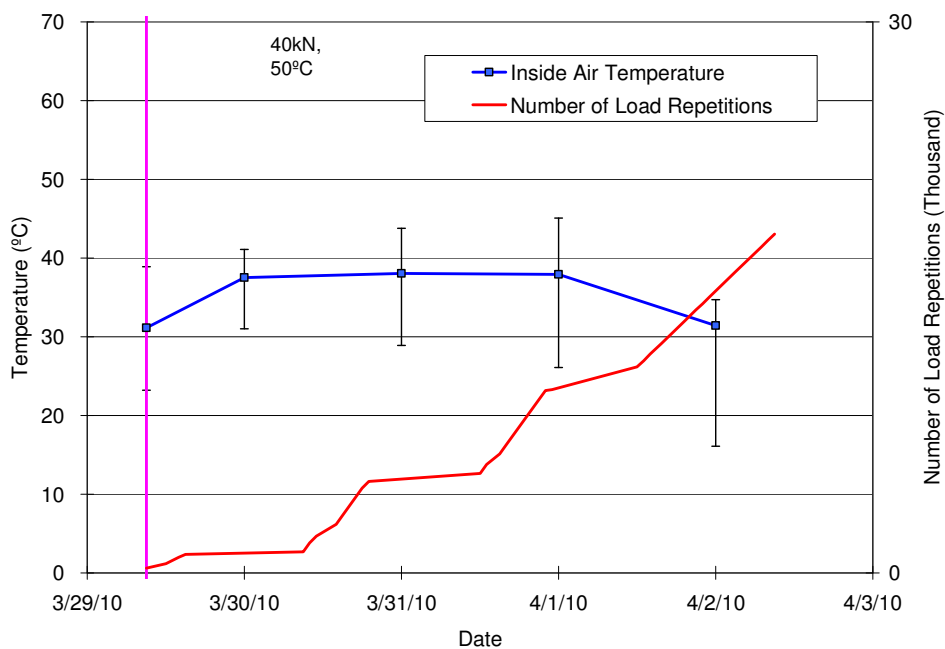Figure A.26 611HB - RHMA-G - 114 mm: Daily average outside air temperatures.

Figure A.27 611HB - RHMA-G - 114 mm: Daily average inside air temperatures.

Table A.5 611HB - RHMA-G - 114 mm: Temperature summary for air and pavement

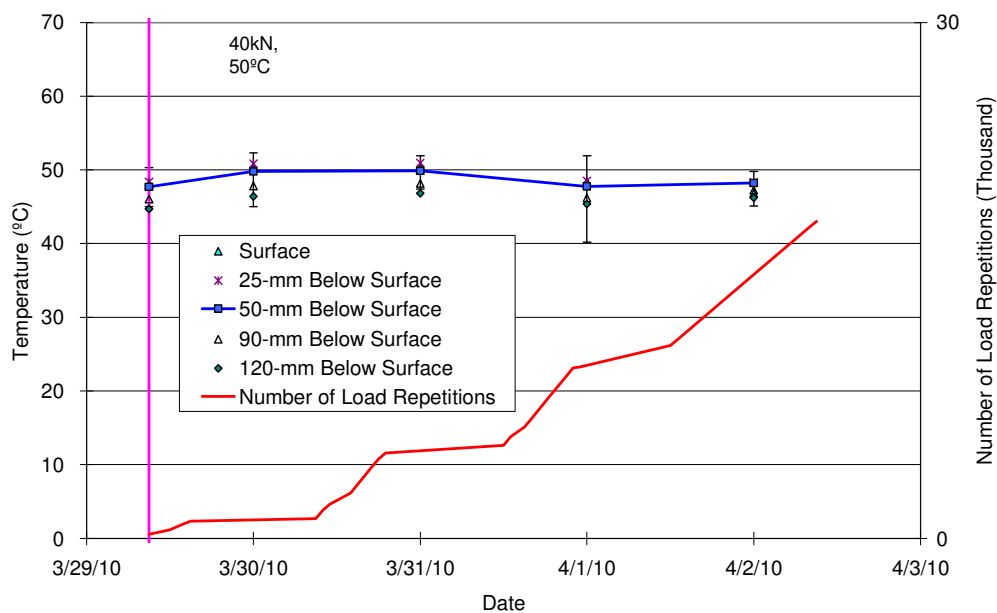| Temperature	611HB			
	Average (°C)	Std Dev (°C)	Average (°F)	Std Dev (°F)
Outside air	13.0	4.4	55.4	7.9
Inside air	35.2	3.6	95.4	6.5
Pavement surface	48.8	1.5	119.8	2.8
- 25 mm below surface	49.4	1.4	120.9	2.4
- 50 mm below surface	48.7	1.1	119.6	1.9
- 90 mm below surface	47.1	1.0	116.8	1.7
- 120 mm below surface	45.9	0.9	114.6	1.5

Figure A.28 611HB - RHMA-G - 114 mm: Daily average temperatures at pavement surface and various depths.

A.2.4.5 Permanent surface deformation (Rutting)

Figure A.29 shows the average transverse cross section measured with the Laser Profilometer at various stages of the test. This plot clearly shows the increase in rutting and deformation over the duration of the test.

Figure A.30 and Figure A.31 show the development of permanent deformation (average maximum rut and average deformation, respectively) with load repetitions as measured with the Laser Profilometer for the test section. It can be observed that early failure occurred after 18,503 repetitions. Error bars on the average reading indicate that the level of variability caused by the CT blocks is less than the variability for section 609HB. This is a result of the epoxy material used on section 611HB to glue CT blocks to pavement. Figure A.32 shows the distribution of rutting along the test section after data for Stations 4, 10, 11, and 12, which are close to CT blocks, were excluded from the dataset. It can be observed that excluding data for those four biased stations did not cause any significant change in variability and average accumulated rutting.

Figure A.33 shows a contour plot of the pavement surface at the end of the test (18,503 repetitions). After completion of trafficking, the average maximum rut depth and the average deformation were 13.5 mm (0.53 in.) and 5.5 mm (0.22 in.), respectively. The maximum rut depth measured on the section was 16.2 mm (0.64 in.) recorded at Station 12.

A.2.4.6 Visual inspection

Apart from rutting, no other distress was recorded on the section. Figure A.34 shows photograph taken of the surface at the end of the test.
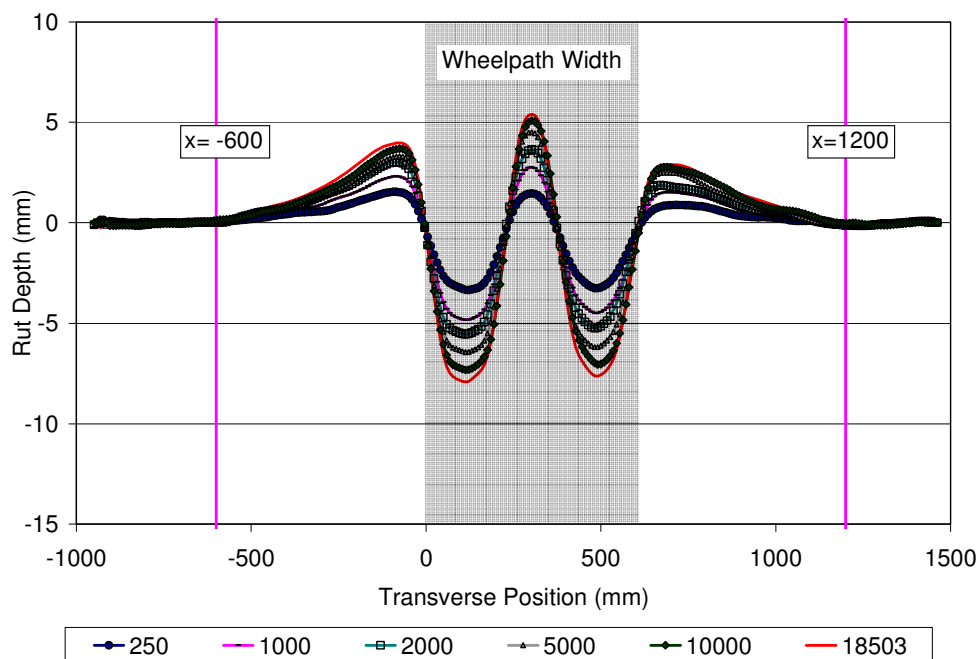

Figure A.29 611HB - RHMA-G - 114 mm: Profilometer cross section at various load repetitions.

Figure A.30 611HB - RHMA-G - 114 mm: Average maximum rut.

Note: Section 609HB - PG 64-28 PM - 114 mm
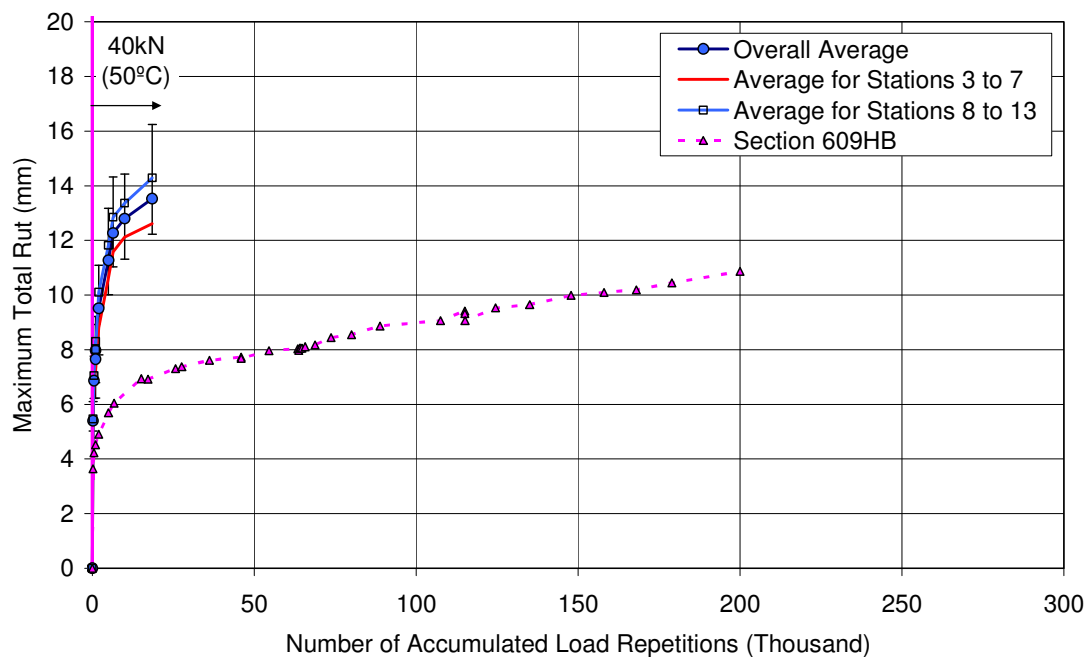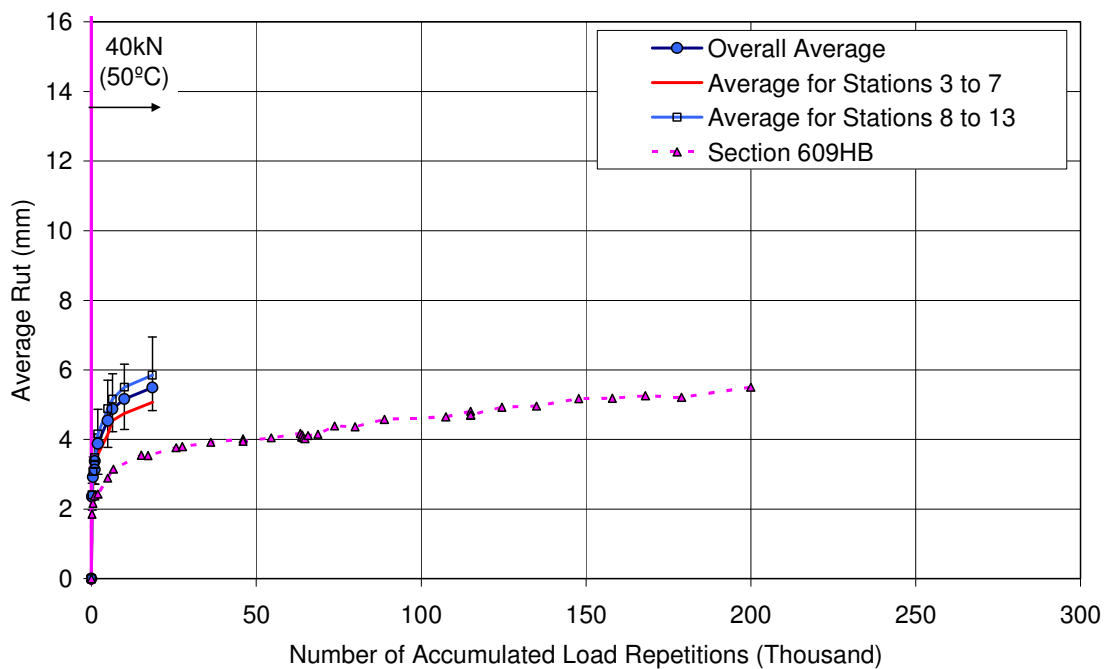

Figure A.31 611HB - RHMA-G - 114 mm: Average deformation.

Note: Section 609HB - PG 64-28 PM - 114 mm
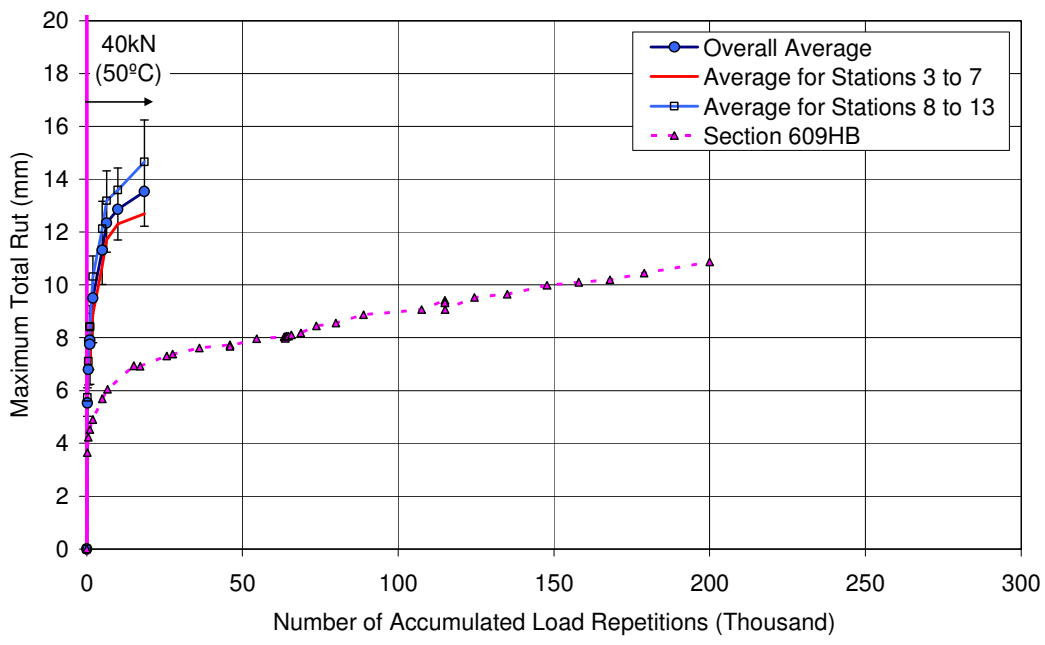
Figure A.32 611HB - RHMA-G - 114 mm: Average maximum rut after excluding data for Stations 4, 10, 11, and 12, which are close to CT blocks.

Note: Section 609HB - PG 64-28 PM - 114 mm
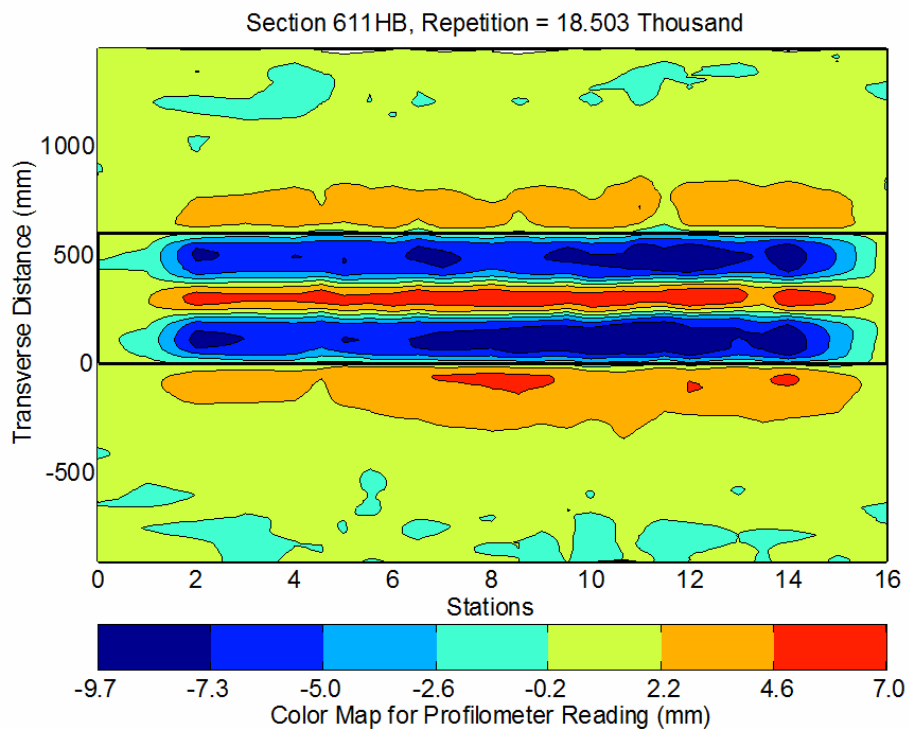
Figure A.33 611HB - RHMA-G - 114 mm: Contour plot of permanent surface deformation at end of test.

Figure A.34 611HB - RHMA-G - 114 mm: Section photograph at test completion.

A.2.5 *Section 612HB: Mix: RHMA-G, HMA thickness: 64 mm*

A.2.5.1 Test summary

Loading commenced on April 13, 2010, and ended on April 27, 2010. A total of 90,000 load repetitions were applied and 19 datasets were collected. Considerably more load repetitions (90,000) were applied to Section 612HB compared to Section 611HB. Although the failure criterion (12.5 mm rut depth) was reached after 40,000 repetitions, testing was continued until the rutting accumulation rate stabilized. The HVS loading history for Section 612HB is shown in Figure A.35.
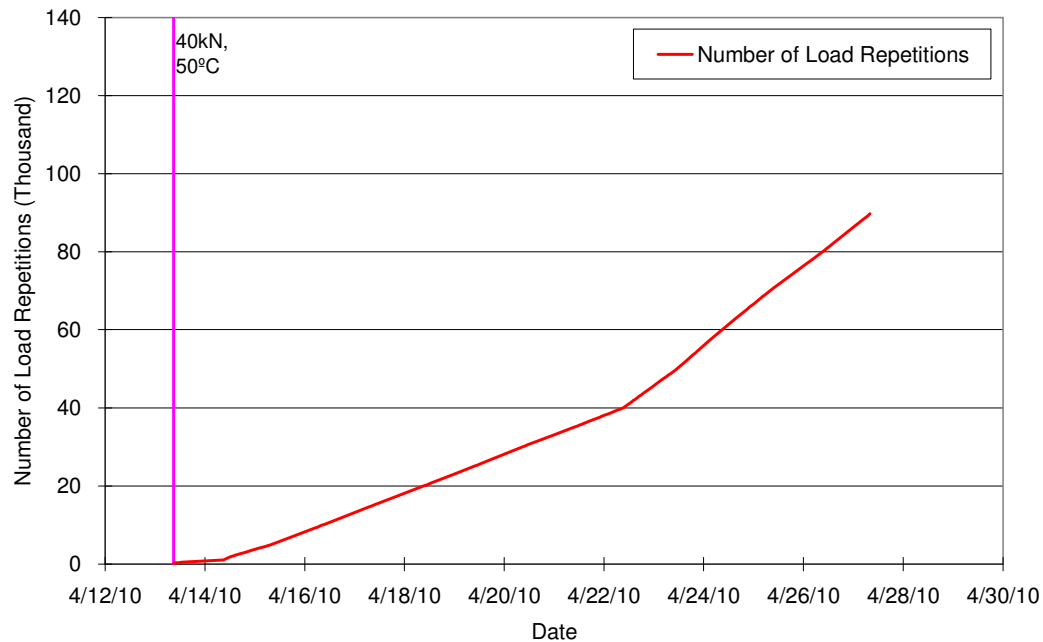
Figure A.35 612HB - RHMA-G - 64 mm: Load history.

A.2.5.2 Outside air temperatures

Outside air temperatures are summarized in Figure A.36. Vertical error bars on each point on the graph show daily temperature range. Temperatures ranged from 5.4°C to 30.7°C (41.7°F to 87.3°F) during the course of HVS testing, with a daily average of 15.0°C (59.1°F), an average minimum of 8.4°C (47.1°F), and an average maximum of 23.4°C (74.1°F).

A.2.5.3 Air temperatures in the temperature control unit

During the test, air temperatures inside the temperature control unit ranged from 14.7°C to 51.6°C (58.5°F to 124.9°F) with an average of 37.0°C (98.5°F) and standard deviation of 3.2°C (5.8°F). The air temperature was adjusted to maintain a pavement temperature of 50°C±4°C (122°F±7°F) at 50 mm depth throughout the test. The daily average air temperatures recorded in the temperature control unit, calculated from the hourly temperatures recorded during HVS operation, are shown in Figure A.37. Vertical errors bars on each point on the graph show daily temperature range.
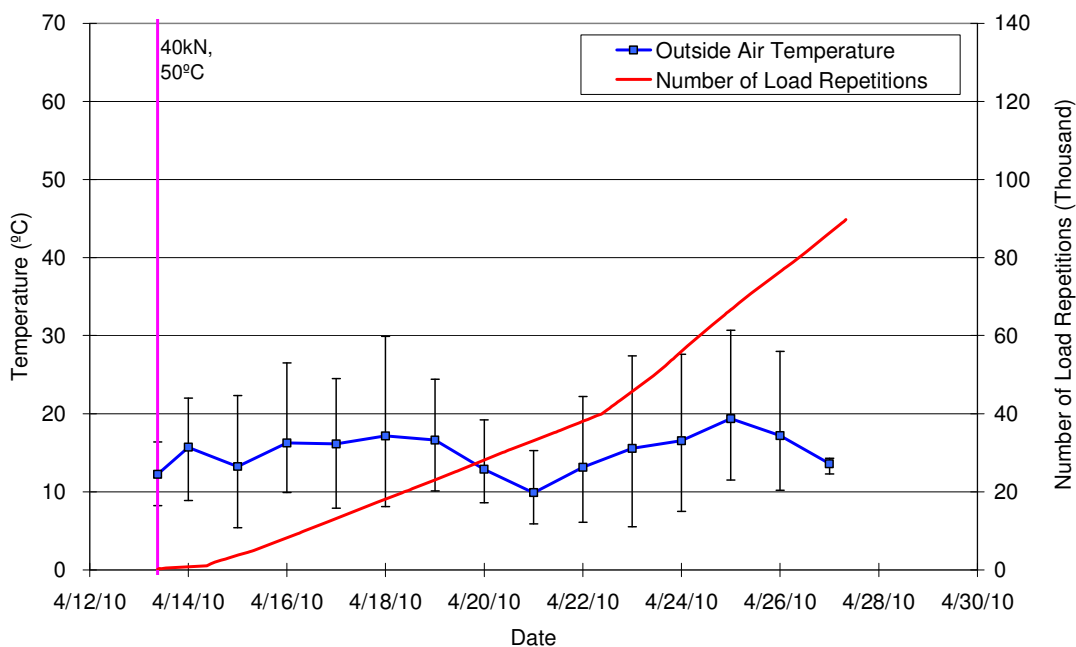
Figure A.36 612HB - RHMA-G - 64 mm: Daily average outside air temperatures.
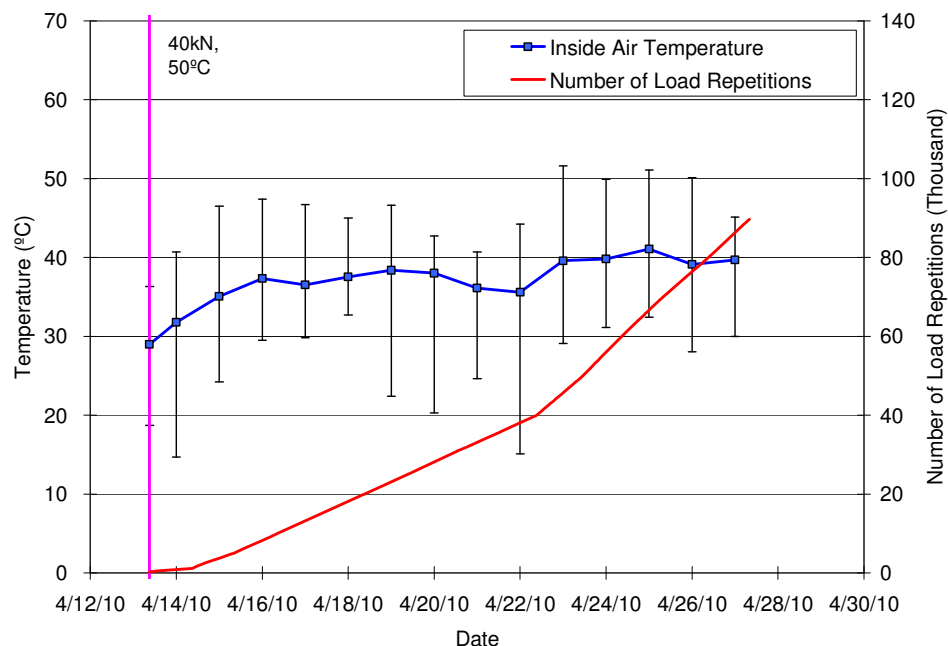
Figure A.37 612HB - RHMA-G - 64 mm: Daily average inside air temperatures.

A.2.5.4 Temperatures in the asphalt concrete layers

Daily averages of the surface and in-depth temperatures of the asphalt concrete layers are listed in Table A.6 and shown in Figure A.38. Pavement temperatures decreased slightly with increasing depth in the pavement, as expected. Average pavement temperatures at all depths on Section 612HB were similar to those recorded on the other sections.

Table A.6 612HB - RHMA-G - 64 mm: Temperature summary for air and pavement

Temperature	612HB			
	Average (°C)	Std Dev (°C)	Average (°F)	Std Dev (°F)
Outside air	15.0	2.4	59.1	4.4
Inside air	37.0	3.2	98.5	5.8
Pavement surface	51.3	1.3	124.4	2.3
- 25 mm below surface	50.7	1.2	123.3	2.2
- 50 mm below surface	49.7	1.3	121.4	2.4
- 60 mm below surface	49.3	1.4	120.7	2.5
- 90 mm below surface	48.1	1.6	118.6	2.8

Figure A.38 612HB - RHMA-G - 64 mm: Daily average temperatures at pavement surface and various depths.

A.2.5.5 Permanent surface deformation (Rutting)

Figure A.39 shows the average transverse cross section measured with the Laser Profilometer at various stages of the test. This plot clearly shows the increase in rutting and deformation over the duration of the test.
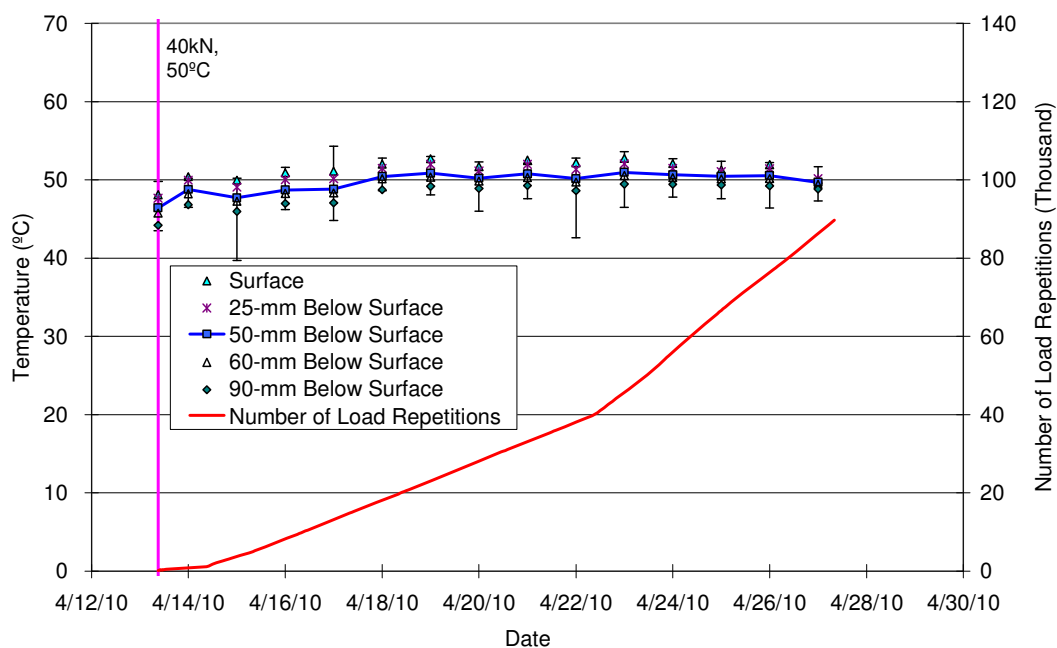
Figure A.40 and Figure A.41 show the development of permanent deformation (average maximum rut and average deformation, respectively) with load repetitions as measured with the Laser Profilometer for the test section. Error bars on the average reading indicate that the level of variability caused by the CT blocks is less than the variability for Section 609HB. This is a result of the epoxy material used on section 612HB to glue CT blocks to pavement. Figure A.42 shows the distribution of rutting along the test section after data for Stations 4, 5, 11, and 13, which are close to CT blocks, were excluded from the dataset. It can be observed that excluding data for those four biased stations did not cause any significant change in variability and average accumulated rutting.

Results for the section 611HB are also shown for comparative purposes in Figure A.40 and Figure A.41. It can be observed that rutting accumulation rates after the embedment phase are similar for both sections. However, high level of densification at the embedment stage resulted in higher rutting for the Section 611HB. Because both pavements were constructed from the same mix type, the only reason for higher rutting can be the differences in HMA layer thicknesses. In order to identify the effect of thickness on accumulated rutting, rutting measurements were converted to permanent shear strain (PSS) by dividing the measured rutting by the HMA layer thickness of each section. Figure A.43 shows that PSS accumulation rate for Section 612HB was faster than the rate for Section 611HB.

Figure A.44 shows a contour plot of the pavement surface at the end of the test (90,000 repetitions). After completion of trafficking, the average maximum rut depth and the

average deformation were 13.9 mm (0.55 in.) and 4.4 mm (0.17 in.), respectively. The maximum rut depth measured on the section was 19.9 mm (0.78 in.) recorded at Station 13.
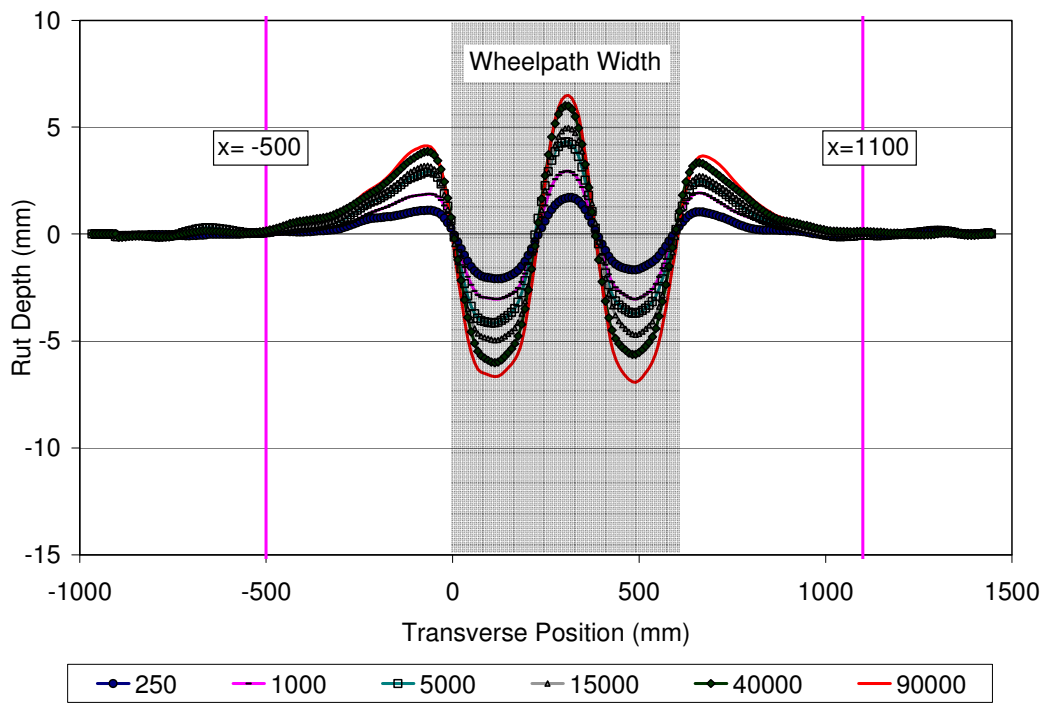
Figure A.39 612HB - RHMA-G - 64 mm: Profilometer cross section at various load repetitions.
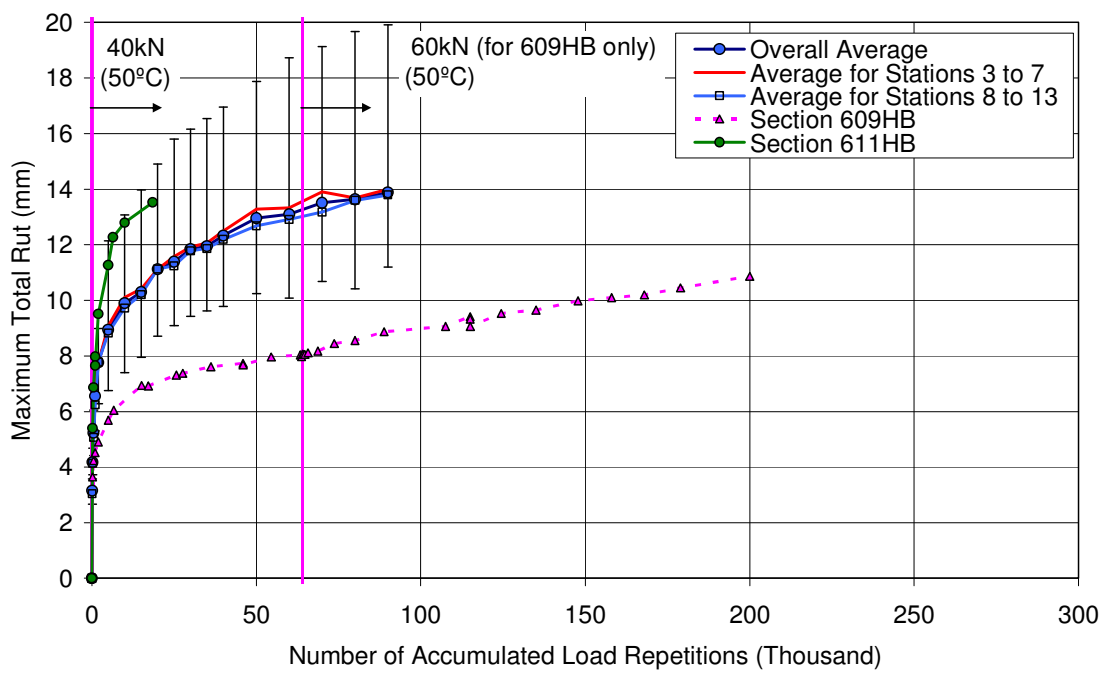
Figure A.40 612HB - RHMA-G - 64 mm: Average maximum rut.

Note: Section 609HB - PG 64-28 PM - 114 mm; Section 611HB - RHMA-G - 114 mm.
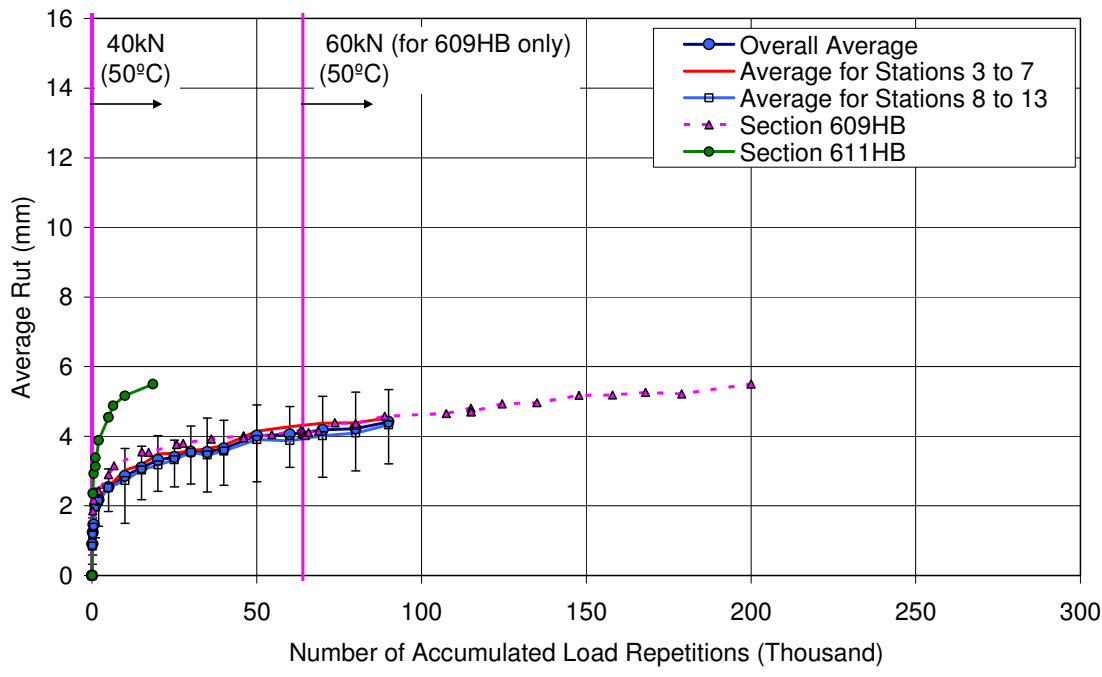
Figure A.41 612HB - RHMA-G - 64 mm: Average deformation.

Note: Section 609HB - PG 64-28 PM - 114 mm; Section 611HB - RHMA-G - 114 mm.
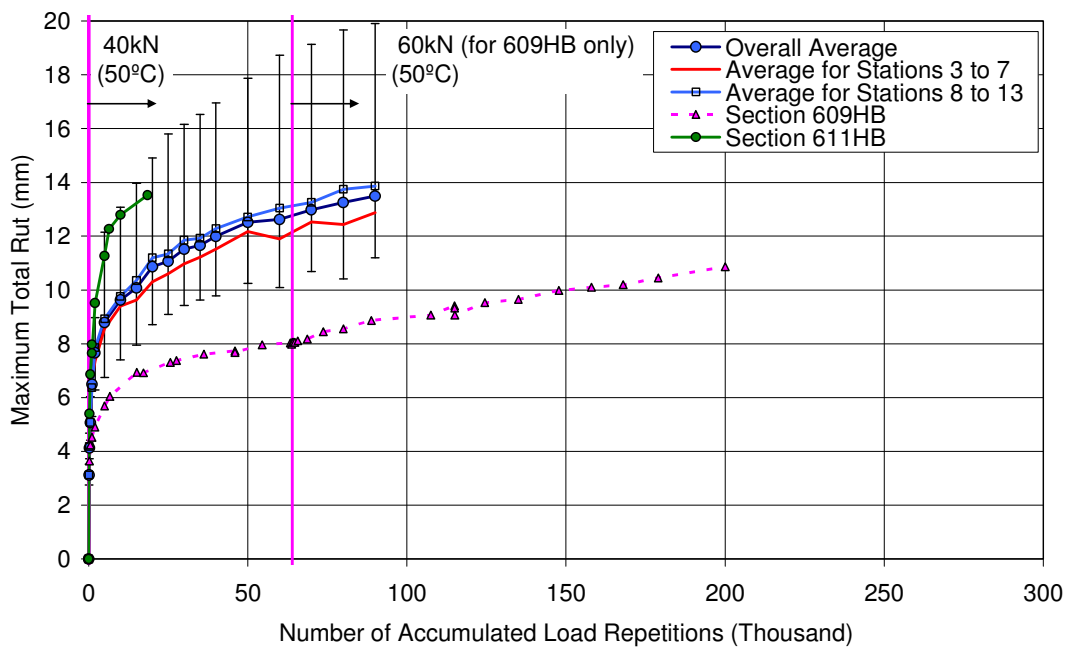
Figure A.42 612HB - RHMA-G - 64 mm: Average maximum rut after excluding data for stations 4, 5, 11 and 13 that are close to CT blocks.

Note: Section 609HB - PG 64-28 PM - 114 mm; Section 611HB - RHMA-G - 114 mm.
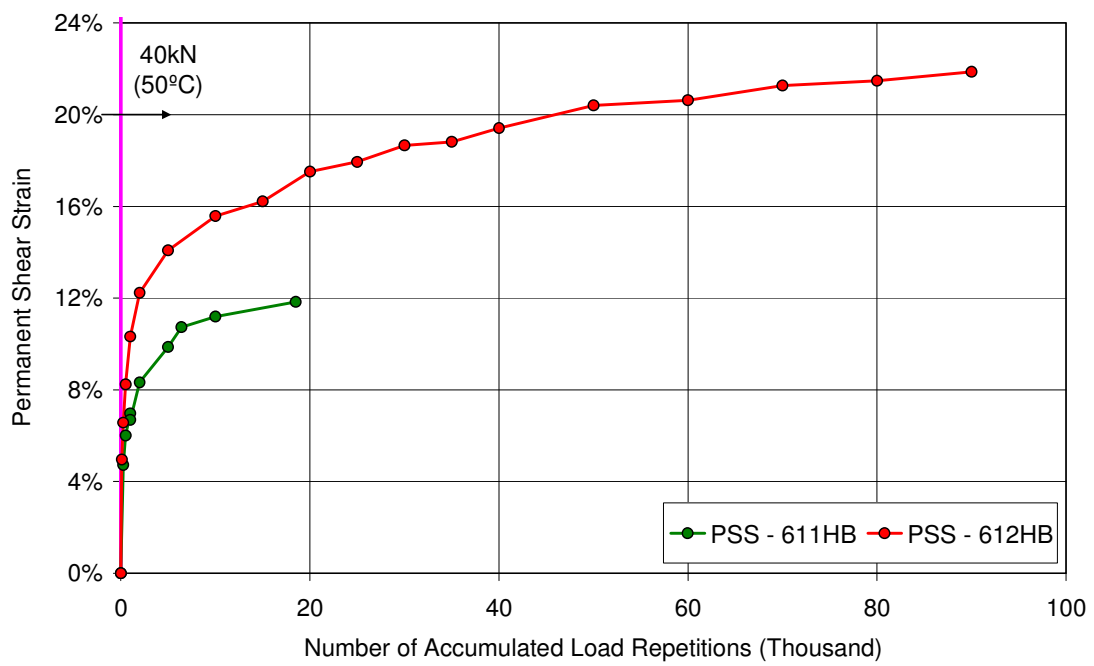
Figure A.43 Comparison of PSS for Sections 611HB - RHMA-G - 114 mm and 612HB - RHMA-G - 64 mm.
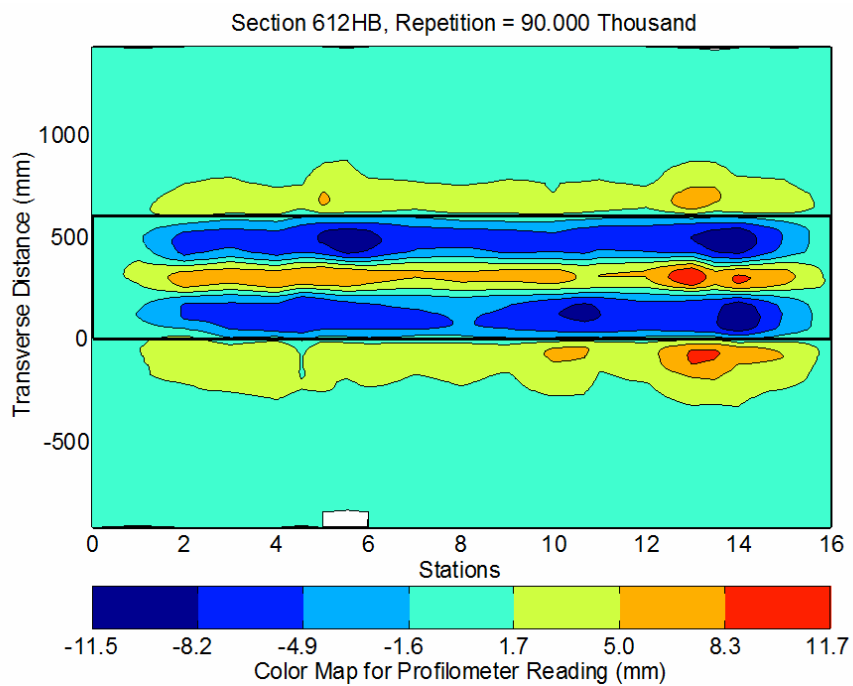
Figure A.44 612HB - RHMA-G - 64 mm: Contour plot of permanent surface deformation at the end of the test.

A.2.5.6 Visual inspection

Apart from rutting, no other distress was recorded on the section. Figure A.45 is a photograph taken of the surface at the end of the test.
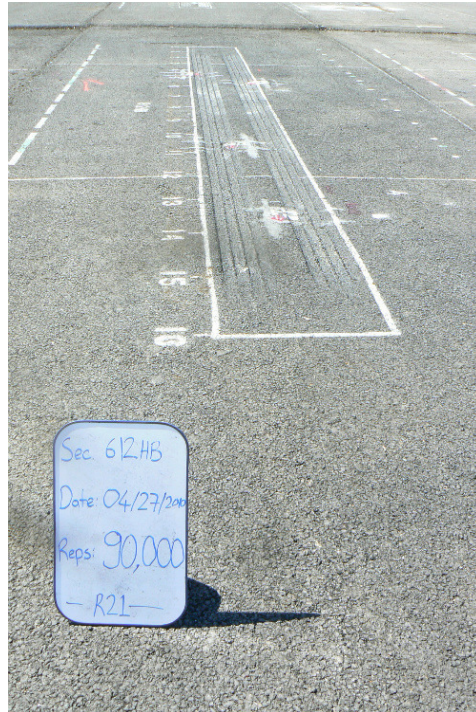
Figure A.45 612HB - RHMA-G - 64 mm: Section photograph at test completion.

A.3 TEST RESULTS SUMMARY

Rutting performance of the four sections is shown in Figure A.46 (average maximum rut) and Figure A.47 (average deformation). It can be seen that larger rut depths were measured for sections with thicker HMA layers for both mix types (609HB and 611HB), and that there was a greater difference between mix types than thicknesses for the two mixes included in the experiment. The wheel load for the two sections with the PG 64-

28PM mix (609HB and 610HB) was increased from 40 kN to 60 kN at around 64,000 repetitions. However, increasing the load did not have any significant effect on the rutting accumulation rate. Early failure was observed for the thick RHMA-G section (611HB).

The results shown in Figure A.47 for average deformation, which is the measure of the downward rut compared to the original pavement surface, indicate that there was less than 6 mm (0.25 in.) of downward deformation of material under the wheels. The maximum rut depth, which considers both downward deformation and "humping" of material sheared to the sides of the wheelpath, is approximately two times greater than the average rut depth for both of the PG 64-28PM sections, and nearly three times greater for both of the RHMA-G sections, indicating that shearing of material to the side of the wheelpath is as important a contributor or more important than the downward rut.
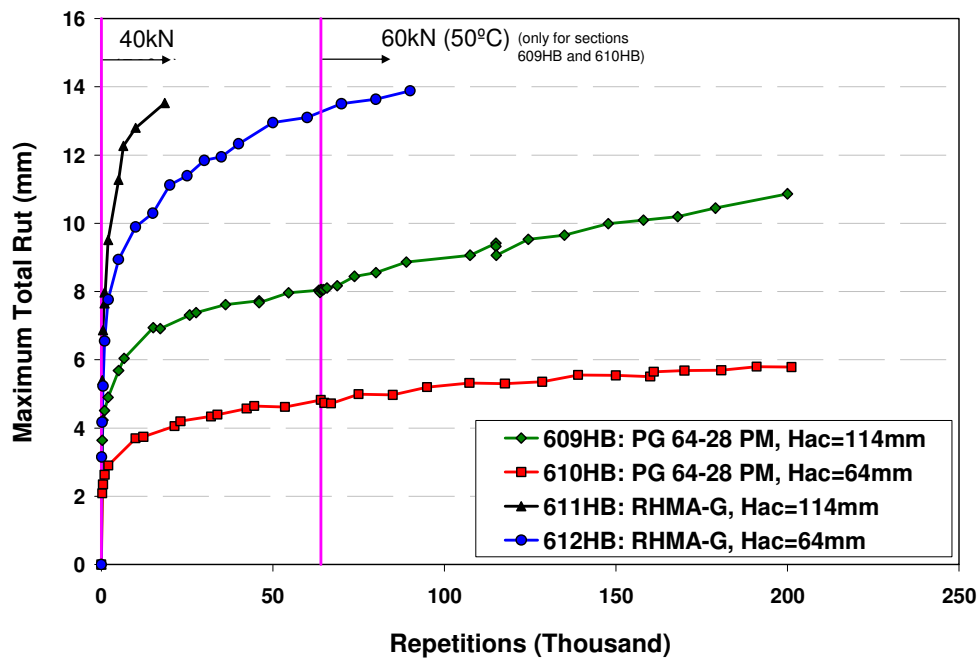
Figure A.46 Comparison of average maximum rut.
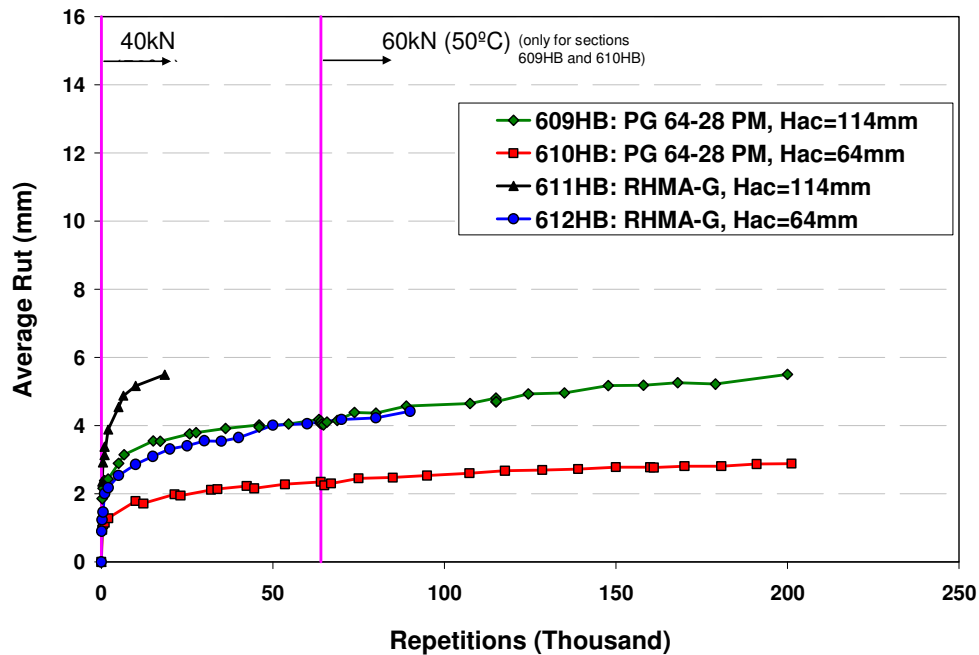
Figure A.47 Comparison of average deformation.

In order to identify the effect of thickness on accumulated rutting, rutting measurements were converted to permanent shear strain (PSS), similar to the PSS determined in the laboratory repeated shear test, by dividing the measured average maximum rut by the HMA layer thickness of each section. Figure A.48 shows the PSS curves for all sections. It can be observed that the PSS curves for the two thicknesses of the PG 64-28PM mix (Sections 609HB and 610HB) are very close. This result indicates that accumulated rutting for these two sections is approximately a linear function of thickness for the thickness range in this experiment in which the HMA thicknesses are less than 125 mm (5 in.). This result is compatible with results of visco-elastoplastic finite element simulations of rut depth for different asphalt overlay thicknesses on concrete pavement performed during the SHRP I A-003A project (Sousa et al. 1994). The simulation showed a typical increase in rut depth with increasing asphalt thickness at an approximately 1:1 ratio up to a thickness of approximately 200 mm (8 in.) for a given asphalt response to repeated shear loading, and a diminishing effect of asphalt thickness at greater thicknesses, assuming uniform temperature and properties through the full depth of the asphalt and full bonding with the concrete. This result is most likely due to the effects of the underlying concrete layer on shear stress distributions at the edges of the tires, which reduce permanent deformation in the asphalt. A similar result may not occur when the section does not have a concrete layer under the HMA. A less consistent result was observed for the RHMA-G sections (611HB and 612HB), where the thinner section rutted at a faster rate relative to thickness than did the thicker section.
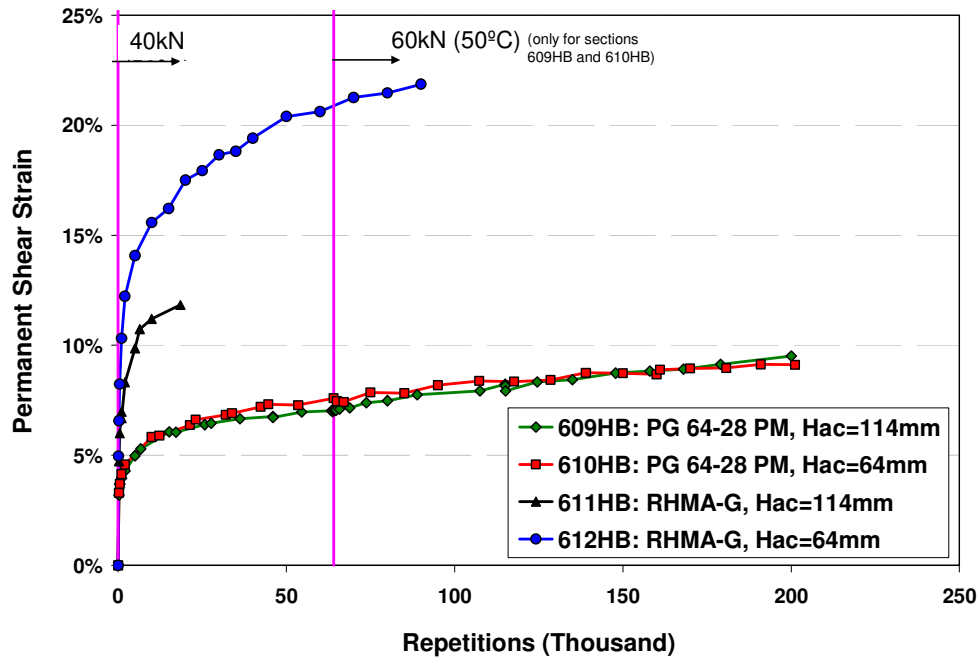
Figure A.48 Comparison of PSS for all HVS rut test sections.

Key findings from the HVS rutting study include:

1. Maximum rut depths for same trafficking were observed to increase for thicker HMA overlays for both mix types, with the PG 64-28PM mix showing an approximately 1:1 relationship between rut depth development and thickness, and a greater than 1:1 relationship, although less consistent, for the RHMA-G mix.

2. The downward deformation in the wheelpath was approximately equal to the upward deformation of material at the sides of the wheelpath for the PG 64-28PM mix. For the RHMA-G mix, the upward deformations at the sides of the wheelpath were greater than the downward wheelpath deformation.

3. Increasing the wheel load for Sections 609HB and 610HB from 40 kN to 60 kN at around 64,000 repetitions did not appear to have any significant effect on the rutting accumulation rate.

REFERENCES

AASHTO. (2002). *AASHTO 2002 Pavement Design Guide*. AASHTO Provisional Standards, Washington, D.C.

AASHTO. (2003). *Standard Method of Test for Determining the Permanent Shear Strain and Stiffness of Asphalt Mixtures Using the Superpave Shear Tester (SST): Designation T 320.* AASHTO Provisional Standards. Washington, D.C.

AASHTO. (2009). *Bulk Specific Gravity and Density of Compacted Asphalt Mixtures Using Automatic Vacuum Sealing Method: Designation T 331.* AASHTO provisional standards, Washington, D.C.

ABAQUS. (2004). *User's Manual, Version 6.5.* Hibitt, Karlsson and Sorenson, Pawtucket, R.I.

Al-Qadi I., and Elseifi M. (2008). New Generation of Wide-Base Tires: Impact on Trucking Operations, Environment, and Pavements. In *Transportation Research Record: Journal of the Transportation Research Board*, No.2007, Transportation Research Board of the National Academies, Washington, D.C., pp. 120–130.

Bates, D.M., and Watts, D.G. (1988). *Nonlinear Regression Analysis and Its Applications.* Wiley, New York.

Baumgaertel, M., and Winter, H.H. (1989). Determination of Discrete Relaxation and Retardation Time Spectra from Dynamic Mechanical Data. In *Rheologica Acta*, Vol. 28, pp. 511–519.

Bejarano, M., Jones, D., Morton, B., and Scheffy, C. (2005). *Reflective Cracking Study: Initial Construction, Phase 1 HVS Testing, and Overlay Construction.* Report Prepared for the California Department of Transportation (Caltrans) Division of Research and Innovation by the University of California Pavement Research Center, Davis and Berkeley. UCPRC-RR-2005-03.

Braz, D., Da Motta, L.M.G., and Lopes, R.T. (1999a). Computed Tomography in the Fatigue Test Analysis of an Asphaltic Mixtures. In *Journal of Applied Radiation and Isotopes*, No. 50_4, pp. 661–671.

Braz, D., Lopes, R.T., and Da Motta, L.M.G. (1999b). Analysis of the Percentage Voids of Test and Field Specimens Using Computerized Tomography. In *Journal of Nuclear Instruments and Methods in Physics Research Section A*, No. 422_1, pp.942–948.

Braz D., Da Motta, L.M.G., and Lopes, R.T. (2000). Computed Tomography: Evaluation of Stability Tests and Indirect Tensile Strength of Field Asphaltic Mixtures. In *Journal of Nondestructive Testing and Evaluation International*, 33, No. 8, pp.517–522.

Brown, S.F. (2004). Accelerated Pavement Testing in Highway Engineering. *Proceedings of the Institution of Civil Engineers and Transportation*, 157(3), pp.173-180.

California Department of Transportation (Caltrans) Division of Maintenance. Maintenance Program, Pavement Management Information Branch. (1995). *State of the Pavement.* California Department of Transportation, Sacramento.

California Department of Transportation (Caltrans). (1999). *Standard Specifications*. State of California Business, Transportation and Housing Agency, Department of Transportation.

California Department of Transportation (Caltrans). (2006a). *Highway Design Manual 2006 Update Chapter 630 Flexible Pavement.* Caltrans, Sacramento, CA.

California Department of Transportation (Caltrans). (2006b). *Use of Rubberized Asphalt Concrete for New Construction.* Memorandum, Caltrans, Sacramento, CA.

California Department of Transportation (Caltrans) Division of Maintenance. (2007). *California State of the Pavement Report.* Publication Caltrans. California Department of Transportation.

Coleri, E., Tsai, B.W., and Monismith, C.L. (2008). Pavement Rutting Performance Prediction by Integrated Weibull Approach. In *Transportation Research Record: Journal of the Transportation Research Board*, No. 2087, Transportation Research Board of the National Academies, Washington, D.C., pp. 120–130.

Coleri, E., Wu, R., Signore, J.M., and Harvey, J.T. (2012) Rutting Performance Evaluation of Rubberized Gap-Graded and Polymer Modified Dense Graded Mixes under HVS Testing. Submitted for *Publication and Presentation to Transportation Research Board Annual Meeting*, National Research Council, Washington, D.C.

Cross, S.A., and Brown, E.R. (1992). Selection of Aggregate Properties to Minimize Rutting of Heavy Duty Pavements. Effects of Aggregates and Mineral Fillers on Asphalt Mixture Performance. *ASTM STP 1147. American Society for Testing and Materials*, Philadelphia, PA.

Dai, Q. L., and You, Z. (2007). Prediction of Creep Stiffness of Asphalt Mixture with Micromechanical Finite-Element and Discrete Element Models. In *Journal of Engineering Mechanics*, No.133(2), pp.163–173.

Dai, Q., and You, Z. (2008). Micromechanical Finite Element Framework for Predicting Viscoelastic Properties of Heterogeneous Asphalt Mixtures. In *Journal of Materials and Structures,* No.41(6), pp.1025–1037.

Dai, Q. (2010). Prediction of Dynamic Modulus and Phase Angle of Stone-Based Composites Using Micromechanical Finite Element Approach. In *Journal of Materials in Civil Engineering*, ASCE, No.22 (6), pp.618-627.

Deacon, J.A, Harvey, J., Guada, I., Popescu, L., and Monismith, C.L. (2002). Analytically Based Approach to Rutting Prediction. In *Transportation Research Record: Journal of the Transportation Research Board,* No.1806. Transportation Research Board of the National Academies, Washington D.C.

Dynatest International (2001). *Elmod 5.0 Quick Start Manual*. Dynatest International, Stark, FL 35 p.

Efron, B. (1979). *Bootstrap Methods: Another Look at the Jacknife.* The Annal of Statistics. Vol. 7: pp. 1-26.

Einstein, A. (1906). Eine Neue Bestimmung Der Moleküldimensionen. *Annalen Der Physik.* Vol. 19, pp. 289-306, Vol. 34, pp.591-592. English Translation in "Investigations on the Theory of Brownian Motion.", *Dover*, 1956, pp. 36-62.

Epps, J.A., Hand, A., Seeds, S., Schulz, T., Alavi, S., Ashmore, C., Monismith, C.L., Deacon, J.A., Harvey, J.T., and Leahy, R. (2002). *Recommended Performance-Related Specification for Hot Mix Asphalt Construction: Results of the WesTrack Project*. NCHRP Report 455, Transportation Research Board, Washington, D.C.

Epps Martin, A., and Park, D.-W. (2003). Use of the Asphalt Pavement Analyzer and Repeated Simple Shear Test at Constant Height to Augment Superpave Volumetric Design. In *Journal of Transportation Engineering,* ASCE, No.129 (5), pp.522–530.

Federal Highway Administration. (1994). *Motor Vehicle Accident Costs*. Technical Advisory. FHWA, U.S. Department of Transportation.

Gitman, I., Askes, H., and Sluys, L. (2007). Representative Volume: Existence and Size Determination. In *Journal of Engineering Fracture Mechanics* 74, pp.2518 - 2534.

Harr, M.E. (1987). *Reliability Based Design in Civil Engineering*. McGraw-Hill, Inc., New York.

Harvey, J.T., Deacon, J.A., Taybali, A.A., Leahy, R.B., and Monismith, C.L. (1997). A Reliability-Based Mix Design and Analysis System for Mitigating Fatigue Distress. *Proceedings of the 8th International Conference on Asphalt Pavements*. International Society for Asphalt Pavements, Univ. of Washington, Seattle, pp.301–324.

Harvey, J.T., Guada, I., and Long, F. (1999). *Effects of Material Properties, Specimen Geometry, and Specimen Preparation Variables on Asphalt Concrete Tests for Rutting*. Final Report for the Federal Highway Administration Office of Technology Applications, Washington, D. C.

Harvey, J.T., Lu, Q., Lea, J.D., Ullidtz, P., Wu, R., and Basheer, I. (2010). Features of Mechanistic Empirical Asphalt Pavement Models for New Design and Rehabilitation in California. *Proceedings of the 11th International Conference on Asphalt Pavements*. International Society for Asphalt Pavements, Nagoya, Japan.

Hashin, Z. (1983). Analysis of Composite Materials: A Survey. In *Journal of Applied Mechanics, No.*50, pp.481-505.

Hayes, A.F. (2005). *Statistical Methods for Communication Science*. Mahwah, NJ: Lawrence Erlbaum Associates.

Insightful. (2001). *S-Plus 6 for Windows Guide to Statistics, Volume 1*. Seattle: Insightful.

Jiang, Y., Selezneva, O., Mladenovic, G., Aref, S., and Darter, M. (2003). Estimation of Pavement Layer Thickness Variability for Reliability-Based Design. In *Transportation Research Record: Journal of the Transportation Research Board,* No.1849, Transportation Research Board, Washington D.C., pp.156 -165.

Jones, D., Wu, R., and Harvey, J.T. (2006). *Reflective Cracking Study: First-level Report on HVS Testing on Section 586RF - 45 mm MB15-G Overlay*. Report Prepared for California Department of Transportation, University of California Pavement Research Center.

Kandhal, P.S., and Mallick, R.B. (2001). Effect of Mix Gradation on Rutting Potential of Dense-Graded Asphalt Mixtures. In *Transportation Research Record: Journal of the Transportation Research Board,* No.1767*,* Transportation Research Board, National Research Council, Washington, D.C., pp.146- 151.

Kandhal, P.S., and Cooley, L.A. (2003). *Accelerated Laboratory Rutting Tests: Evaluation of the Asphalt Pavement Analyzer.* National Cooperative Highway Research Program, NCHRP, Report 508.

Kim, H.B., and Lee, S.H. (2002). Reliability-Based Design Model Applied to Mechanistic Empirical Pavement Design. *Korean Society of Civil Engineers*, v.6, No.3, pp.263-272.

Kim, Y.R. (2009). Modeling of Asphalt Concrete. McGraw-Hill Construction, ASCE Press, USA.

Kutner, M.H., Nachtsheim, C.J., Neter, J., and Li, W. (2005). *Applied Linear Statistical Models.* Fifth ed. McGraw-Hill; Boston.

Lea, J.D. (2009). *The Effect of Spatial Variability on the Reliability of Pavements.* Doctoral dissertation. University of California, Davis, CA.

Li, G., Li, Y., Metcalf, J.B., and Pang, S.S. (1999). Elastic Modulus Prediction of Asphaltic Concrete. In *Journal of Materials in Civil Engineering*, No.11 (3), pp.236–241.

Masad, E., Muhunthan, B., Shashidhar, N., and Herman, T. (1999). Internal Structure Characterization of Asphalt Concrete Using Image Analysis. In *Journal of Computing in Civil Engineering*, No.13_2, pp.88–95.

Masad, E., Jandhyala, V.K., Dasgupta, N., Somadavan, N., and Shashidhar, N. (2002). Characterization of Air Void Distribution in Asphalt Mixes Using X-Ray Computed Tomography. In *Journal of Materials in Civil Engineering*, No.14_2, pp.122–129.

Masad E., and Button J. (2004). Implications of Experimental Measurements and Analysis of the Internal Structure of Hot-Mix Asphalt. In *Transportation Research Record: Journal of the Transportation Research Board,* No.1891, Transportation Research Board, Washington D.C., pp.212-220.

Mechanistic Empirical Pavement Design Guide (MEPDG). (2004). *Part 3, Design Analysis, Chapter 3, Design of New and Reconstructed Flexible Pavements*. ARA, Inc., ERES Consultants Division, Champaign, Illinois.

Metcalf, J. (1996). *Application of Full-Scale Accelerated Pavement Testing*. National Cooperative Highway Program, Synthesis of Highway Practice 235.

Monismith, C.L., Ogawan, N., and Freeme, C.R. (1975). Permanent Deformation Characteristics of Subgrade Soils Due to Repeated Loading. In *Transportation Research Record: Journal of the Transportation Research Board,* No.537. Transportation Research Board, National Research Council, Washington, D.C., pp.1-17.

Monismith, C.L., Deacon, J.A., and Harvey, J.T. (2000). *Westrack: Performance Models for Permanent Deformation and Fatigue.* Report to Nichols Consulting Engineers, Chtd. Pavement Research Center, Institute of Transportation Studies, University of California, Berkeley.

Natu, G.S., Guada, I., and Tayebali, A.A. (2002). Evaluation of the Sensitivity of Repeated Simple Shear Test at Constant Height Based on Rutting Characteristics of Westrack Fine Mixes, Aggregate Contribution to Hot Mix Asphalt (HMA) Performance. *ASTM STP 1421, American Society for Testing and Materials*. West Conshohocken, PA.

NCHRP. (2004). *Guide for Mechanistic-Empirical Design of New and Rehabilitated Pavement Structures*. National Cooperative Highway Research Program, Report 1-37A.

Papagiannakis, T., Abbas, A., and Masad, E. (2002). Micromechanical Analysis of the Viscoelastic Properties of Asphalt Concretes. In *Transportation Research Record: Journal of the Transportation Research Board,* No.1789, Transportation Research Board, National Research Council, Washington, D.C, pp. 113-120.

Prozzi, J.A., Gossain, V., and Manuel, L. (2005). Reliability of Pavement Structures Using Empirical-Mechanistic Models. *CD-ROM Proceedings of the 84th Annual Meeting of the Transportation Research Board*. Washington, DC, January 9-13.

Rayleigh, L. (1892). On the Influence of Obstacles Arranged in a Rectangular Order Upon the Properties of the Medium. *Philosophical Magazine,* No.34, pp.481.

Rice, J. (1995). *Mathematical Statistics and Data Analysis.* Second ed., Duxbury Press.

Romero, P., and Masad, E. (2001). Relationship between the Representative Volume Element and Mechanical Properties of Asphalt Concrete. In *Journal of Materials in Civil Engineering*. Vol. 13, No. 1, pp. 77-84.

Rothenburg, L., Bogobowicz, A., and Haas, R. (1992). Micromechanical Modeling of Asphalt Concrete in Connection with Pavement Rutting Problems. *Proceedings of the 7th International Conference on Asphalt Pavements*, No.1, pp.230–245.

Simpleware. (2010a). *ScanIP and +ScanFE Software Developed by Simpleware Ltd, Innovation Centre, Rennes Drive*. Exeter EX4 4RN, United Kingdom.

Simpleware. (2010b). *Converting 3D Images into Models - ScanIP Software +FE Module +CAD Module Tutorial Guide*. Simpleware LTD. Innovation Centre Exeter, United Kingdom.

Sousa, J.B., Deacon, J.A., Weissman, S.L., Leahy, R.B., Harvey, J.T., Paulsen, G., Coplantz, J.S., and Monismith, C.L. (1994). *Permanent Deformation Response of Asphalt Aggregate Mixes*. Report SHRP-A-415, Strategic Highway Research Program, National Research Council, Washington D.C., 437 pp.

Start, M.R., Kim, J., and Berg, W.D. (1998). Potential Safety Cost-Effectiveness of Treating Rutted Pavements. In *Transportation Research Record: Journal of the Transportation Research Board,* No.1629, Transportation Research Board, National Research Council, Washington, D.C, pp. 208-213.

Synolakis, C.E., Zhou, Z., and Leahy, R.M. (1996). Determination of Internal Deformation Field in Asphalt Cores Using X-Ray Computer Tomography. In *Transportation Research Record*, No.1526 , Washington, D.C., pp. 135-141.

Timm, D.H., Newcomb, D.E., and Galambos, T.V. (2000). Incorporation of Reliability into Mechanistic-Empirical Pavement Design. In *Transportation Research Record: Journal of the Transportation Research Board,* No.1730, Transportation Research Board, National Research Council, Washington, D.C, pp. 73-80.

Tsai, B.W., Kannekanti, V.N., and Harvey, J.T. (2004). Application of Genetic Algorithm in Asphalt Pavement Design. In *Transportation Research Record: Journal of the Transportation Research Board,* No.1891, Transportation Research Board, National Research Council, Washington, D.C, pp.112-120.

Ullidtz, P., Harvey, J.T., Tsai, B.W., and Monismith, C.L. (2006). *Calibration of Incremental-Recursive Flexible Damage Models in CalME Using HVS Experiments.* Report Prepared for the California Department of Transportation (Caltrans) Division of Research and Innovation by the University of California Pavement Research Center, Davis and Berkeley. UCPRC-RR-2005-06.

Ullidtz P., Harvey, J.T., Tsai, B.W., and Monismith, C.L. (2008). Calibration of Mechanistic–Empirical Models for Flexible Pavements Using California Heavy Vehicle Simulators. In *Transportation Research Record: Journal of the Transportation Research Board,* No. 2087, Transportation Research Board, National Research Council, Washington, D.C, pp. 20-28.

Velasques, R.A. (2009). *On the Representative Volume Element of Asphalt Concrete with Applications to Low Temperature.* Dissertation, University of Minnesota.

Wang, L.B., Frost, J.D., and Lai, J.S. (1999). Non-Invasive Measurement of Permanent Strain Field Resulting from Rutting in Asphalt Concrete. In *Transportation Research Record: Journal of the Transportation Research Board,* No.1687, Transportation Research Board, National Research Council, Washington, D.C, pp. 85-94.

Wang, Y., Wang, L.B., Harman, T., and Li, Q. (2007). Noninvasive Measurement of Three Dimensional Permanent Strains in Asphalt Concrete with X-Ray Tomography Imaging. In *Transportation Research Record: Journal of the Transportation Research Board,* No.2005, Transportation Research Board, National Research Council, Washington, D.C, pp. 95-103.

Warr, S., Jacques, G.T.H., and Huntley, J.M. (1994). Tracking the Translational and Rotational Motion of Granular Particles: Use of High Speed Photography and Image Processing. In *Journal of Powder Technology,* No.81, pp.41–56.

Weissman, S. L. (1997). *The Mechanics of Permanent Deformation in Asphalt-Aggregate Mixtures: A Guide to Laboratory Test Selection*. Symplectic Engineering Corp.

Weissman, S.L., Harvey, J.T., Sackman, J.L., and Long, F. (1999). Selection of Laboratory Test Specimen Dimension for Permanent Deformation of Asphalt Concrete Pavements. In *Transportation Research Record: Journal of the Transportation Research Board,* No. 1681, Transportation Research Board, National Research Council, Washington, D.C, pp.113–120.

White, T., Haddock, J., Hand, A., and Fang, H. (2002). *Contributions of Pavement Structural Layers to Rutting of Hot Mix Asphalt Pavements.* NCHRP Report No. 468, National Cooperative Highway Research Program, Transportation Research Board, National Research Council, National Academy Press, Washington, D.C.

Williams, M.L., Landel, R.F., and Ferry, J.D. (1955). The Temperature Dependency of Relaxation Mechanisms in Amorphous Polymers and Other Glass Forming Liquid. In *Journal of the American Chemical Society*, Vol. 77, No. 14, pp.3701-3707.

Yin, H.M., Buttlar, W.G., Paulino, G.H., and Di Benedetto, H. (2008). Assessment of Existing Micromechanical Models for Asphalt Mastics Considering Viscoelastic Effects. In *Journal of Road Materials and Highway Design*, No.9, pp.31-57.

You, Z. (2003). *Development of A Micromechanical Modeling Approach to Predict Asphalt Mixture Stiffness Using Discrete Element Method.* Department of Civil and Environmental Engineering, published by UMI, a Bell & Howell Information Company, Ann Arbor, MI University of Illinois at Urbana-Champaign, 512 pp.

You, Z., Adhikari, S., and Dai, Q. (2008). Three-Dimensional Discrete Element Models for Asphalt Mixtures. In *Journal of Engineering Mechanics*, Vol. 134, No. 12, American Society of Civil Engineers (ASCE).

You, Z., Adhikari, S., and Kutay, M.E. (2009). Dynamic Modulus Simulation of the Asphalt Concrete Using the X-Ray Computed Tomography Images. In *Journal of Materials and Structures*, No.42(5), 617–630.

Zhou, F., Chen, D.H., Scullion, T., and Bilyeu, J. (2003). Case Study: Evaluation of Laboratory Test Methods to Characterize Permanent Deformation Properties of Asphalt Mixes. In *International Journal of Pavement Engineering,* Vol. 4, No. 3, pp. 155-164.

Zhou, F., Hu, S., and Scullion, T. (2006). *Integrated Asphalt (Overlay) Mixture Design, Balancing Rutting And Cracking Requirements*. Texas Transportation Institute Research Report No. 0-5123-1, 162pp.

Zhu, H., and Nodes, J.E. (2000). Contact Based Analysis of Asphalt Pavement with the Effect of Aggregate Angularity. In *Journal of Mechanics of Materials, No.*32(3), pp.193-202.